UNIVERSITÀ DEGLI STUDI DI NAPOLI FEDERICO II

DEPARTMENT OF CHEMICAL, MATERIALS AND INDUSTRIAL PRODUCTION ENGINEERING
(DICMAPI)

Ph.D. in INDUSTRIAL PRODUCT AND PROCESS ENGINEERING

XXXVI cycle

MICROENVIRONMENT-MEDIATED CELL CONTROL. A MULTI-MODAL MICROFLUIDIC PLATFORM FOR CARDIOMYOCYTES STATE REGULATION

Supervisor

Prof. Paolo Antonio Netti

Advisor

Raffaele Vecchione, PhD Eng.

Coordinator

Prof. Andrea D'Anna

PhD Candidate

Denise Pagliara

2020/2024

Table of contents

Abstract

Comprehending the influence of the microenvironment on cell health is crucial for an in-depth understanding of human wellness. This knowledge underscores the necessity of examining how cells adapt and react to their surroundings, particularly through the lens of epigenetic modulation of their behavior. Autophagy, a pivotal epigenetic pathway, plays a significant role in controlling various physiological and pathological processes, including those of the cardiovascular field. The cellular microenvironment in cardiac tissue, characterized by factors such as nutrient availability, mechanical and topographical interaction with the surroundings, is fundamental in the induction and progression of autophagy and to control the consequent cell state. In the context of cardiac health, tissue engineering represents a unique approach to study and potentially modulate cardiac cells wellness. In this PhD work, a microfluidic platform was designed to replicate critical signals of the cardiac microenvironment. A multilayer setup enabled the integration of equi-biaxial mechanical stimulation on a deformable membrane with fluid flow micro-channels for nutrient delivery. Photolithography was used to create topographical cues on the membrane surface, so that a micro-pattern, radially arranged in a circular fashion, was fabricated to align cells in the direction of stretching, mimicking physiological cell arrangement. The device's functionality was initially verified through COMSOL simulations and subsequently tested with fluorescent labeling to demonstrate equi-biaxial mechanical stimulation and fluid flow interaction. HL-1 rat atrial cardiomyocytes seeded on the platform were able to align with the micro-pattern, migrating along its direction under continuous equi-biaxial deformation. Cells exhibited enhanced beating activity with high coordination upon cyclic deformation on the patterned membrane. Autophagy induction was observed under cyclic deformation coupled with micro-patterned alignment. Notably, enhanced autophagy induction was demonstrated, but, at the final phase of the autophagy flux, a blockage in the fusion and final degradation was observed. However, the patterned arrangement and mechanical deformation significantly enhanced autophagy, as evidenced by a higher total number of vacuoles, compared to the autophagy in non-patterned HL-1 cells. The read-out of autophagy level correlated with a vital cell state, as confirmed by live-dead assays. This suggests that the proposed platform can establish a link between cell state and autophagy under specific cardiac microenvironment signals, such as cyclic mechanical deformation with aligned cell populations. This approach opens avenues for innovative characterizations and therapeutic strategies targeting autophagy pathways, potentially improving treatment outcomes for heart diseases and modifying underlying epigenetic pathways.

List of abbreviations

ALS *Amyotrophic Lateral Sclerosis*

AMPK *Adenosine Monophosphate-activated Protein Kinase*

AP *Action Potential*

ATG *Autophagy Transcription Gene*

ATF6 *Activating Transcription Factor 6*

ATP *Adenosine triphosphate*

BafA1 *Bafilomycin A1*

BMP-2 *Bone Morphogenic Protein 2*

Ca^{2+} *Calcium ions*

CaM *Calmodulin*

CaMKII *Calmodulin-dependent protein kinase II*

CFD *Computational Fluid Dynamics*

CMs *Cardiomyocyte*s

CMA *Chaperone-mediated Autophagy*

colMA *Methacrylayed collagen*

Crtl1 *Cartilage link protein 1*

cTnT *Cardiac Troponin T*

CVDs *Cardiovascular diseases*

DOX *Doxorubicin*

ECM *Extracellular matrix*

ECs *Endothelial cells*

ER *Endoplasmic Reticulum*

ESCs *Embryonic Stem cells*

FAK *Focal Adhesion Kinase*

FAs *Focal Adhesions*

FBS *Fetal Bovine Serum*

GAGs *Glycosaminoglycans*

gelMA *Methacrylayed gelatin*

GFP *Green Fluorescent Protein*

HBSS *Hank's Balanced Salt Solution*

HF *Heart Failure*

hiPSCs *Human-induced Pluripotent Stem Cells*

hMSCs *Human Mesenchymal Stem Cells*

HoC *Heart-on-a-chip*

HSC70 *Heat Shock 70 kDa Protein 8*

HIFs *Hypoxia-Inducible Factors*

HUVEC *Human Umbilical Vein Endothelial Cells*

I/R *Ischemia/Reperfusion*

IF *Immunofluorescence*

IPA *Isopropyl Alcohol*

IRE1α *Inositol-Requiring Kinase 1α*

iPSCs *Induced-Pluripotent Stem cells*

LAMP-2A *lysosome-associated membrane protein type 2A*

LC3 *Microtubule-associated Protein Light Chain 3*

μP *Microfluidic Platform*

mRFP *Monomeric Red Fluorescent Protein*

mRFP-GFP tfLC3 *mRFP-GFP tandem fluorescent-tagged LC3*

MSCs *Mesenchymal Stem Cells*

mTOR *Mechanistic Target of Rapamycin*

mTORC1/mTORC2 *mTOR complex 1 and 2*

P/S *Penicillin/Streptomycin*

PBS *Phosphate Buffer Saline*

PDGF *Platelet-Derived Growth Factor*

PDMS P*olydimethylsiloxane*

PE *Phosphatidylethanolamine*

PEDOT:PSS *Poly(3,4-ethylene dioxythiophene) polystyrene sulfonate*

PEG *Poly(ethylene glycol)*

PERK *Protein Kinase RNA-activated (PKR)-like ER kinase*

PFA *Paraformaldehyde*

PI *Propidium Iodide*

PLGA *Poly Lactic-co-Glycolic Acid*

PMMA *Polymethyl Methacrylate*

POMaC *Poly(octamethylene maleate (anhydride) citrate)*

PPy *Polypyrrole*

PtdIns3K *Phosphatidylinositol 3-kinase*

ROI *Region Of Interest*

SEM *Scanning Electron Microscopy*

sI/R *simulated ischemia/reperfusion*

SMCs *Smooth Muscle cells*

TAZ *Transcriptional coactivator with PDZ-binding motif*

TEM *Transmission Electron Microscopy*

TFEB *Transcription Factor EB*

TGF-β1 *Tranforming Growth Factor -b1*

TSC1/TSC2 *Tuberous Sclerosis Complex 1 and 2*

UBL *Ubiquitin-like Proteins*

ULK *Unc-51-like kinase family*

UPR *Unfolded Protein Response*

VE-cadherin *Vascular Endothelial-cadherin*

VEGF *Vascular Endothelial Growth Factor*

YAP *Yes-associated protein*

List of figures

Chapter 1:

Chapter 2:

Chapter 3:

Chapter 4:

List of tables

Chapter 2:

List of equations

Chapter 2:

Chapter 3:

Chapter 1:
State of the art

1.1 Genetics and epigenetics for cell control

Nowadays, worldwide healthcare management costs are continuously rising, prompting concentrated efforts in the study, design and testing of new drugs, vaccines, surgical procedures, and medical devices. The final goal is to preserve wellness and extend human lifespan under the best possible conditions. A broad knowledge around the pursuit of an optimum in terms of wellness is still missing and further investigations are needed to uncover how to reach this target. Research is currently focused on recapitulating many biologic processes from a laboratory-scale perspective. Since cells are the morphological and functional elementary units of the human body, they are extensively used to explore biological processes.

Genetics is a field of biology that studies the genes and the genetic variability of living organisms. It bases its investigation on the genome, which is the collection of organism genes considered as maps. The sequence of these genes gives rise to the genotype, and its manifestation is the phenotype.

Epigenetics, situated between genotype and phenotype, encompasses every change that affects the phenotype without altering the genotype of the organism. This includes hereditable modifications that leave footprints impacting the functional behavior of cells and changing genic expression without modifying the DNA sequence [1].

Genetic approaches are widely used to control cell behavior with the aid of genetic engineering, that is a technology conceived to isolate and manipulate genic material to confer new characteristics to the target cells. Despite its ground-breaking potential, genetic engineering is limited by high-cost equipment needs and ethical claims [2]. In this scenario, epigenetic manipulation addresses many of these concerns. In fact, cells are considered controllable entities since, from fetal development to adult homeostasis and pathological phenomena, epigenetic events regulate cell functionalities in response to external factors [3].

1.2 Influence of the environment on epigenetic pathways

Epigenetic mechanisms play a crucial role in the regulation of cell genes, operating at the level of transcription, post-transcription, protein translation and post-translation. The primary actors in epigenome modifications include DNA methylation, histone modifications and non-coding RNAs [4–6]. DNA methylation involves the covalent binding of methyl groups to cytosine ring within phosphate-linked cytosine-guanine (CpG) dinucleotides complex. This methylated complex leads to chromatin condensation, preventing transcription and gene expression. Histone modifications, occurring on the tails of histones, the core protein component of chromatin, include changes such as the addition or removal of histones and acetyl groups, directly influencing DNA transcription. Non-coding RNAs, including miRNAs, piRNAs, endogenous siRNAs, and long non-coding RNAs are a cluster of RNAs not encoding functional proteins and playing a vital role in tumor suppression, apoptosis, proliferation and migration.

Different environmental cues, such as lifestyle factors, physical activity, psychological stress, aging strongly affect epigenetic pathways [7]. Sets of genes are in fact activated or silenced in response to these cues, influencing the development and adaptation of the organism in combination with environmental factors.

For instance, DNA methylation is strongly affected by prenatal diet deprivation, leading to lower methylation of genes essential for insulin metabolism [8], folate metabolism and choline availability [9], potentially impacting health and longevity. Conversely, moderate dietary restriction and maintenance of essential nutrient availability have been associated with the extension of the human lifespan [10]. Natural components in the diet, like resveratrol, activate sirtuin 1, contributing to the delay or reversal of age-related changes through action on DNA methylation [10].

Exercise is another relevant factor positively controlling human metabolism, DNA methylation in adipose tissue [11] and skeletal muscle [12], as well as the distribution of histone markers in histone modification pathways. miRNAs play a role in controlling genes related to myoblast proliferation, differentiation, muscle regeneration in skeletal muscle. Exercise decreases the overexpression of miRNAs in the liver, crucial in lipogenesis and triacylglycerol production. Long term exercise has been shown to enhance cognitive functions and therapeutic interventions based on running wheel exercise have demonstrated recovery from cognitive deficits after traumatic brain injury due to miRNA-related mechanisms [13].

In addition, the interaction of the human body with environmental factors and chemicals is evident. Metals such as nickel, cadmium, and arsenic induce altered methylation of cytosine

residues, leading to oxidative DNA damage [14]. Exposure to particulate matter from air pollution strongly contributes to DNA hypomethylation in patients with cancer and cardiovascular diseases [15].

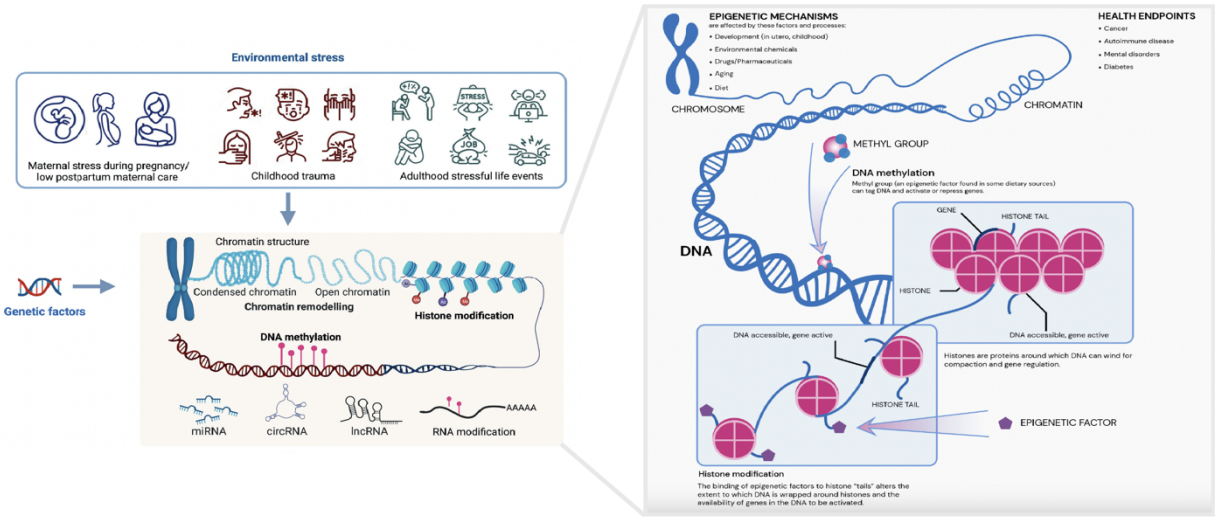

Figure 1 – The epigenetic activity is tightly related to the environmental control. Different environmental factors can influence the stress response, from childhood to adulthood, by directly acting on the epigenetic activity, which involves chromatin assembly, histone modifications, DNA methylation and non-coding RNA changes. Images readapted from [16] and https://www.xcode.life/genetics/epigenetic-testing/.

1.3 The microenvironment control on cell behavior

Likewise, cells *in vivo* are enveloped in a complex and dynamic interplay of biochemical and biophysical cues, collectively forming the cell microenvironment (*Fig. 2*). This microenvironment serves as a structural support for cell organization and assembly, heavily relying on the dynamic presentation of biochemical and biophysical cues and their combinations, with effect on cell behavior control.

In its most general representation, the cell microenvironment comprises the extracellular matrix (ECM) and its proteins [15] (collagens and elastin, fibronectin, laminin, tenascin), homotypic and heterotypic neighboring cells, cytokines and hormones, nano- and micro-topographies due to cell arrangement and ECM physical structure. Additionally, mechanical forces associated with tissue resistance to surrounding stimuli and physiological fluids motion contribute to the ECM complexity. These components directly influence cell functions and serve as external determinants of epigenetic pathways, either acting individually or synergistically to regulate cellular activities.[17]

1.3.1 The Extracellular Matrix

The ECM gives an important contribution to cell survival, since it is the physical scaffold for cells and regulate their functionalities including proliferation, migration and viability. In the bone, the ECM composition, due to collagen type I and mineral compounds along with osteocalcin, osteonectin and fibronectin play a pivotal role in preserving osteoblasts phenotype. The ensemble of ECM bulk proteins gives osteoinductive, osteoconductive and osteogenic characteristics to the bone tissue [18]. The bulk ECM composition consists of insoluble and interlocked macromolecules secreted by cells, providing structural support and biochemical and biophysical properties to the tissue. This intricate composition effectively regulates cell behavior.

Biochemical cues within ECM influence cell guidance by presenting adhesion ligands to cell membrane receptors. ECM proteins, like collagen, fibronectin, vitronectin, laminin, glycosaminoglycan (GAGs) and hyaluronic acid are functionally deputed to the exposure of adhesion ligands to cells. Among the others, integrins act as receptors mediating cell-ECM interaction, essential for the transduction of microenvironmental cues for cell survival, spreading, migration and proliferation [19]. Lack of cell attachment to a structural ECM trigger programmed cell death, i.e. the apoptosis process. In epithelial cells, this apoptotic status contributes to the loss of activation of intracellular pathways towards cell survival, promoting the enhancement of cancerous cells and metastasis formation [20]. ECM proteins are also reservoirs for soluble signaling molecules like growth factors, sequestering and storing them in non-covalent electrostatic and hydrogen-bonding interactions. Examples include collagen II, with binding sites for transforming growth factor β1 (TGF-β1) [21] and bone morphogenic protein 2 (BMP-2) [22], and fibronectin for vascular endothelial growth factor (VEGFs) and platelet-derived growth factor (PDGFs) [23]. The spatial localization, stability and activity of these growth factors are controlled by ECM arrangement in various physiologic processes such as skin repair, vascularization and bone homeostasis.

The ECM is also providing a microenvironmental control over cells from a biophysical perspective. Structural features and arrangement of macromolecules are crucial for tissue function and cell behavior. For instance, the orientation and alignment of collagen I fiber guide cell migration throughout direct interaction and consequent spatial arrangement of cell adhesion ligands and the underlying matrix [24,25]. Yim et al. showed a reduction in the expression of integrin subunits in human mesenchymal stem cells (hMSCs) cultured on nanogrooved topography with characteristic dimension of 350 nm [26]. With this geometry, cellular

cytoskeleton displayed an elongated shape with an aligned organization, contrasting the random network arrangement observed in cells on a control surface. In another work, Carthew et al. investigated the impact of engineered microstructures on mesenchymal stem cells, revealing that specific micropillar designs influence osteogenesis by modulating nuclear deformation and chromatin organization through cell cytoskeletal tension, with implications on cell fate control [27].

1.3.2 Substrate Mechanical Properties

Mechanical properties of the cell microenvironment play a key role in governing the growth and organization of cells in different tissue types. Neural tissue, characterized by very soft and low elastic moduli values, is influenced by the macroscopic ensemble of cerebrospinal fluid, soft membranes of the brain, and spinal cord fibers [28]. In contrast, bone tissue is stiff and its mechanical properties range in high elastic moduli values, providing a high resistance to mechanical loads [29]. From a cellular perspective, various cell types tend to exhibit directional motion when exposed to a gradient in substrate stiffness, a phenomenon known as durotaxis [30]. For instance, Ng et al. [31] demonstrated that substrate rigidity influences collective migration in epithelial wound healing assays by modulating cell-cell contacts throughout cell adhesion molecules known as cadherins. This mechanoresponsive behavior is dependent on myosin II, a family of motor proteins involved in cellular movement and shape maintenance in non-muscle cells. The collective mechanoresponsive behavior of cells is further supported by the work of Sunyer et al. In their study they compared individual human mammary epithelial cells (MCF-10A) with clusters of the same cell type plated on a stiffness gradient [32], observing that multicellular clusters exhibited durotaxis even when isolated cells did not. The study demonstrated that collective durotaxis involved long-range force transmission across the cluster through cadherin-based contacts.

1.3.3 Physical Cues

In addition to signals originating from ECM and biologic interactions with the environment, cells within their natural context encounter, detect, and react to a diverse array of physical stimuli, including strain and stress, as well as electrical, magnetic, acoustic, and thermal fields. For instance, in the vasculature, blood cells undergo shear stress and shear strain due to blood flow. Cells in the heart and lungs primarily experience cyclical tensile stress and strain fields,

while those in cartilage and bone mainly encounter compressive stress and strain during body movement, along with additional shear stresses resulting from fluid flow.

The study of Vion et al. demonstrated that the interplay between flow-induced shear stress and VEGF-A treatment in endothelial cells established front-rear polarity and alignment of endothelial cells [33], highlighting the intricate relationship between flow levels and VEGF-A concentrations.

In vitro, uniaxial cyclic stretching induces osteogenic differentiation of mesenchymal stem cells (MSCs). Zhang et al. [34] observed an alignment of hMSCs perpendicular to the stretching direction, with the degree of alignment intensifying with increased magnitude and frequency of uniaxial cyclic stretching. This stretching also augmented the accessibility of gene loci linked to the regulation of cell morphogenesis and osteogenesis, along with the corresponding transcriptional activities.

Beyond stress and strain fields, cells are responsive to various physical fields such as electrical, magnetic, acoustic, and thermal fields. Small electric fields have been shown to be potent signals for guiding and promoting the migration of human-induced pluripotent stem cells (hiPSCs). Notably, applied electric fields can induce the migration of hiPSC clusters that typically remain stationary in a three-dimensional environment, suggesting potential applications in enhancing stem cell therapy, particularly when controlled cell migration and integration with host tissue are crucial [35]. Brief electric stimulation was also explored for its effect on the cardiogenic potential of hiPSCs, leading to enhanced gene expression of cardiac transcription factors and contractile muscle proteins. Cardiomyocytes derived from electrically stimulated hiPSCs express cardiac-specific markers, undergo calcium cycling, and respond to adrenergic stimuli [36].

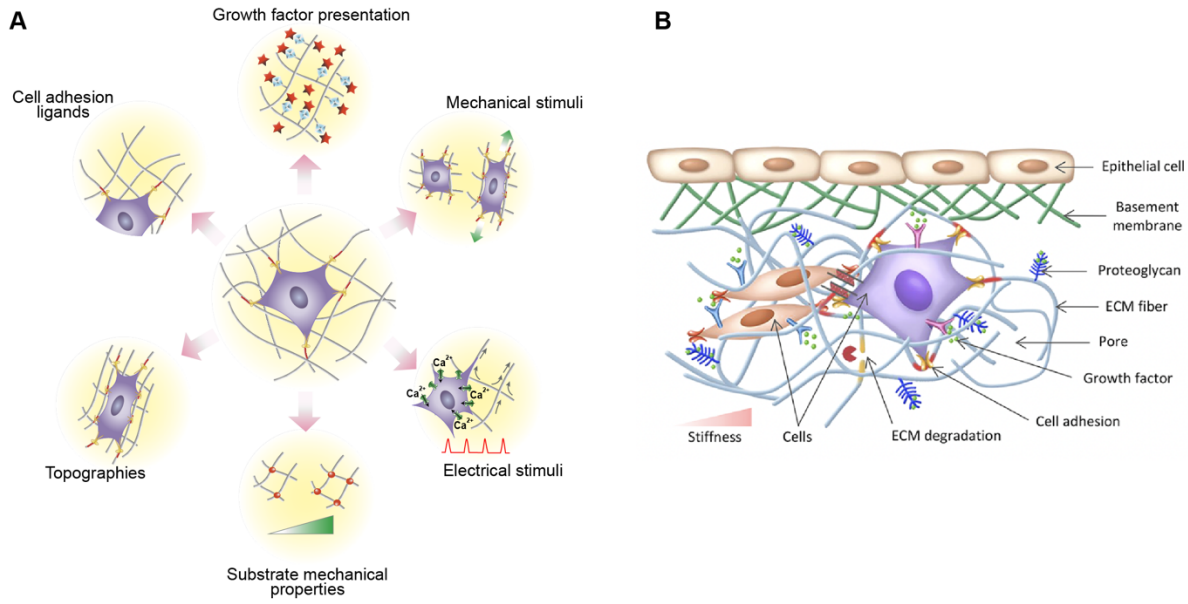

Figure 2 – The microenvironment control on cell behavior is influenced by a set of signals. A) The stimuli primarily act through the cell-ECM interplay, in the growth factors and ligands presentation to the cells, the mechanical and topographical identity of the surroundings, and throughout the application of physical fields, like electrical stimuli. B) Cells in their 3D assembly are surrounded by an intricate and complex environment made by cells, basement membrane, ECM proteins and signals. Image adapted from [17].

1.4 Autophagy

The aforementioned signals within the microenvironment machinery exert physiological effects on cells either alone or simultaneously, influencing cell survival. However, the impact of microenvironment on cell behavior can be dual, posing threats or enhancing cell health. An example of the manifestation of extracellular signals on cell epigenome control can be found in the context autophagy, an essential catabolic mechanism commonly adopted by cells in response to internal and external insults to either preserve or impair cell survival.

In mammalian cells, three defined types of autophagy exist: macro-autophagy, micro-autophagy and chaperone-mediated autophagy. These mechanisms enable cells to ultimately degrade or recycle worthless metabolites and by-products of cellular processes by transporting them to the lysosome [37,38]. In micro-autophagy, cytoplasmic content enters the lysosome through invagination of the lysosomal membrane and there are distinct mechanisms for cargo recognition and uptake. For example, endosomal micro-autophagy involves the engulfment of soluble cytoplasmic contents and proteins through the invagination of late endosomal membranes. Chaperone-mediated autophagy (CMA) selectively targets specific proteins for lysosomal degradation. In CMA, substrates contain a pentapeptide targeting motif (KFERQ-like motif) recognized by chaperone proteins like heat shock 70 kDa protein 8 (HSC70), which deliver them to the lysosomal membrane. The lysosome-associated membrane protein type 2A (LAMP-2A) facilitates the translocation of the target protein into the lysosomal lumen, where degradation occurs by lysosomal proteases.

Differently from the above-mentioned autophagy processes, in which the degradation cargoes are engulfed or bound to translocation proteins towards the lysosome, macro-autophagy (or simply called autophagy) involves the sequestration of cargo, organelles or portions of the cell cytoplasm in double-membraned vesicles called autophagosomes. Macro-autophagy phases include induction and nucleation of the double membrane, its elongation and closure, fusion with the lysosome, and the final step of degradation. Autophagosomes form *de novo* by expansion and do not originate from cell organelles. The initiation points for autophagosome formation are dispersed across multiple sites throughout the cytoplasm. For simplicity, since the

macro-autophagy is the most studied and described autophagy type, it will be referred to simply as *autophagy*.

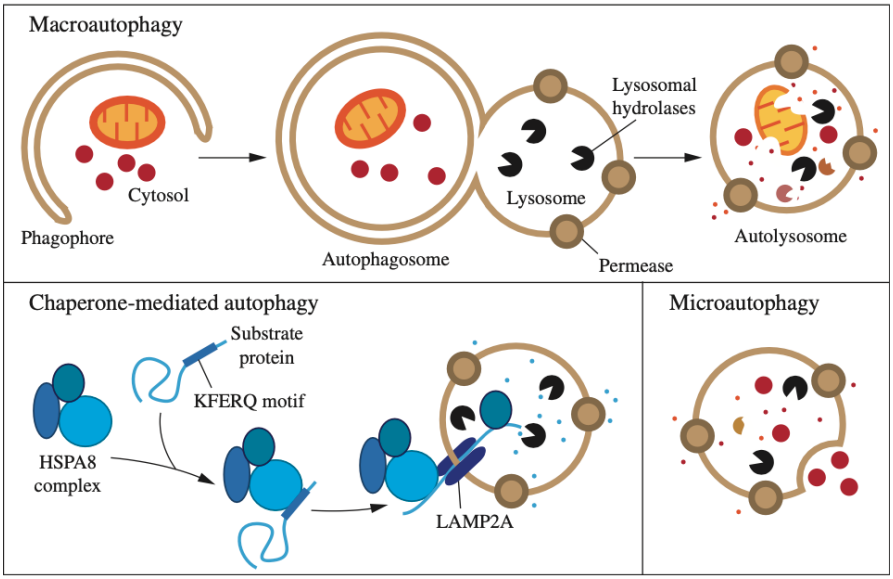

Figure 3 – The three types of autophagy in mammalian cells for the degradation of worthless components and byproducts. Macroautophagy involves the creation of new cytosolic vesicles, which enclose and deliver cellular material to the lysosome for breakdown. In contrast, chaperone-mediated autophagy transports specific unfolded proteins directly across the lysosomal membrane for degradation. Microautophagy, on the other hand, entails the direct engulfment of cellular components by the lysosomal membrane through invagination. All three forms of autophagy culminate in the dismantling of the enclosed cargo, with the resultant breakdown products being released back into the cytosol for recycling by the cell. Readapted from [38].

1.4.1 Autophagy Phases

Although the origin of autophagosomes remains unclear, it is widely accepted that specialized subdomains of the endoplasmic reticulum (ER) serve as the primary location for autophagosome formation [39]. In mammalian cells, autophagy induction is regulated by a kinase complex comprising Unc-51-like kinases (ULK1 or ULK2), autophagy transcription gene 13 (ATG13) and RB1-inducible coiled coil 1 (RB1CC1 or FIP200). This complex is highly dependent on the nutrient status of the cell. After the initiation phase, the membrane assembles and starts to expand, forming the primary double membrane known as the phagophore. It originates from various cellular structures, including the plasma membrane, ER, Golgi apparatus, and mitochondria. Phagophore nucleation is facilitated by the recruitment of the ATG14-containing class III phosphatidylinositol 3-kinase (PtdIns3K) complex, with BECN1 being a crucial component for autophagy regulation. The antiapoptotic protein BCL2 inhibits autophagy by

binding to BECN1 and preventing its interaction in the PtdIns3K complex [40,41]. The elongation of the phagophore is guided by two ubiquitin-like (UBL) protein conjugation systems. The ATG12-ATG5 conjugation, followed by binding to ATG16L1, leads to phagophore membrane growth. Another UBL complex is the ATG8/LC3 system (microtubule-associated protein light chain 3). In particular, LC3 is expressed as a cytosolic protein and in autophagy induction conditions is cleaved by ATG4 into LC3-I, then it is conjugated to lipid phosphatidylethanolamine (PE) by ATG12-ATG5 complex, becoming LC3-II. This lipidation is enhanced in the case of nutrient starvation and external stresses exposure with LC3-II found on both the internal and external interfaces of the autophagosome. The transmembrane protein ATG9 is essential for phagophore elongation, localizing in trans-Golgi network and late endosomes under normal conditions and colocalizing with autophagosome during starvation [42]. The wrapping of the membrane around the cargo creates the closed autophagosome, with sizes ranging from 0.5 to 1.5 μm [43], and its outer membrane is deputed to the fusion with the lysosome resulting in autolysosome formation. Fusion is mediated by a subset of small GTPase proteins such as Rab7 and Rab2A, which bind to endosomes and lysosomes and ensure proper positioning between autophagosomes and lysosomes. Motor adaptor proteins link the autophagy players to motor proteins associated with the cell cytoskeleton, allowing autophagosomes to move towards the perinuclear region via microtubules, while lysosomes travel to the cell periphery. This antagonistic movement is the key element for their gathering and fusion [44]. Once the autophagosome fuses with the lysosome, the inner membrane and its cargo undergo degradation in the acidic lumen of the lysosome environment with the help of lysosomal hydrolases. Subsequently, lysosomal permeases export the degradation products back into the cytoplasm, where they are then utilized by the cell for biosynthetic processes or to generate energy.

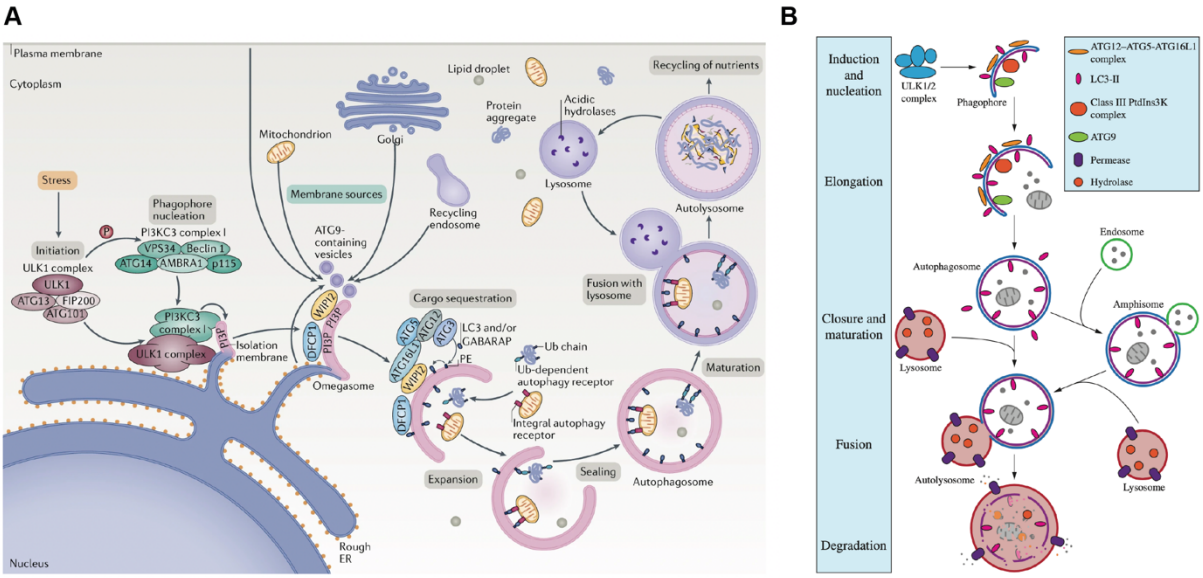

Figure 4 – The main characters of the autophagy process. A) The autophagy initiation is related to the recall of a group of components, essential for the phagophore formation. Image adapted from [45]. B) After the initiation different proteins and actors are involved in the various steps of autophagic flow. Image from [38].

1.4.2 Pathways For The Regulation And Induction Of Autophagy

Autophagy serves as a housekeeping mechanism, actively engaged at basal level to preserve the integrity of organelles and proteins within the cell. In addition to this role, autophagy acts as a cellular mechanism responsive to various external stresses, including nutrient starvation, hypoxia, and the accumulation of damaged proteins and organelles. In addition, it plays a key role in eliminating intracellular pathogens and associated defective proteins, contributing significantly to the control of inflammation processes. The autophagy is controlled by multiple signaling pathways, each activated under different cellular conditions.

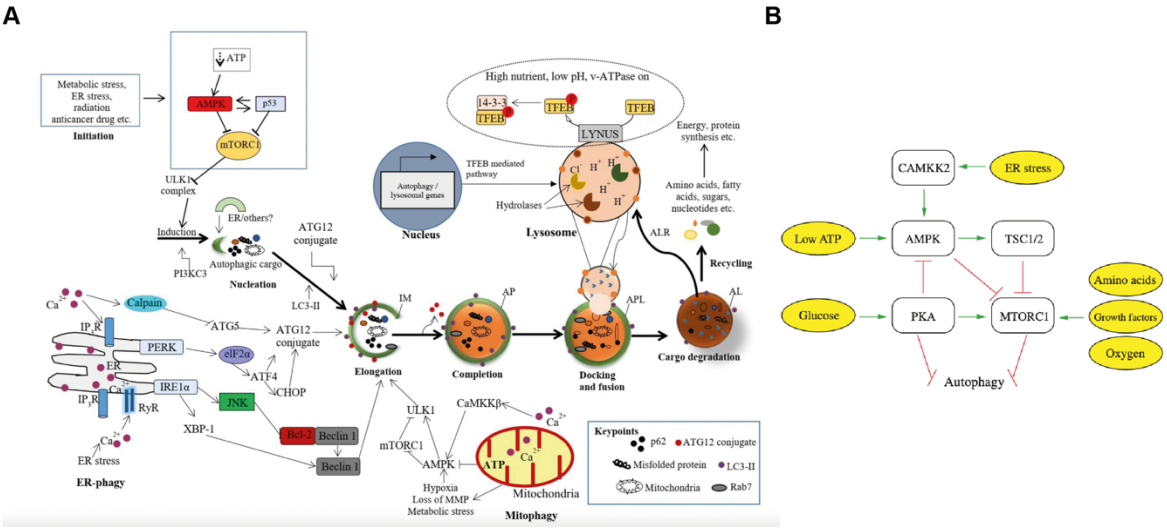

Figure 5 – The autophagy is triggered by various pathway depending on the extracellular factor affecting the cell. A) mTORC1 inhibition of autophagy triggers the ULK1 complex recruitment and the following cascade of events leading to autophagy degradation. Image from Ref. [46]. B) Schematic representation of the main signals enhancing the autophagy induction. Adapted from [38].

1.4.2.1 mTOR pathway

The mechanistic target of rapamycin (mTOR) pathway is a central player in nutrients sensing and energy status within the cell [47]. This kinase is the core of two complexes, mTOR complex 1 and 2 (mTORC1 and mTORC2), accomplishing two distinct roles. mTOR's function is directly linked to nutrient availability and key second messengers of the nutritional state, such as insulin. It actively blocks autophagic catabolism by promoting the uptake of extracellular nutrients. Under normal conditions with stationary level of nutrients, mTORC1 is active and inhibits autophagy by phosphorylating and suppressing the ULK1 complex, crucial for the autophagy initiation. In conditions of low nutrients availability, mTORC1 is inactivated due to a lack of stimulatory signals like amino acids and growth factors, along with the activation of inhibitory pathways of AMPK under low-energy levels. Inhibition of mTORC1 leads to the dephosphorylation and activation of the ULK1 complex, initiating the autophagic process through phagophore formation. On the other hand, the role of mTORC2 pathway in autophagy is more indirect compared to mTORC1, but still significant in regulating cell catabolic processes. Its activation is related to the levels of growth factors rather than nutrients and indirectly affects autophagy through the activation of Akt protein kinase B. Akt phosphorylates and inhibits the TSC1-TSC2 complex, a negative regulator of mTORC1, leading to the activation of mTORC1 and subsequent inhibition of autophagy. Moreover, mTORC2 not only impacts autophagy activation by means of mTORC1 but also interacts with SGK1 and PKC pathways downstream of altered mitochondrial permeability [48].

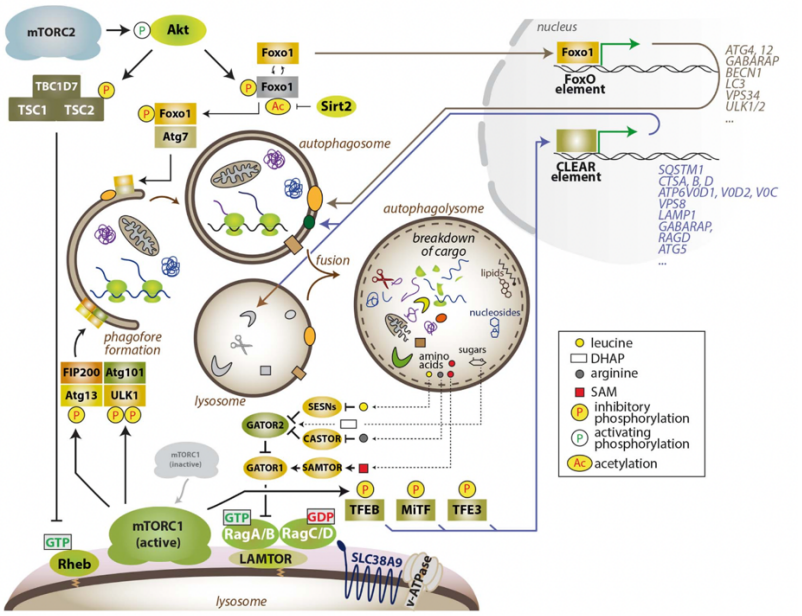

Figure 6 – The mTOR autophagy axis. The mTOR–autophagy axis is crucial for cellular regulation, with mTORC1 inhibiting autophagy initiation and limiting degradative capacity. Inhibition of mTORC1 activates autophagy and enhances cellular degradation by activating genes involved in these processes, while reducing the cell's demand for energy and nutrients. MTORC2 and certain kinases restrict autophagic flux and lysosomal function, while the regulation of FoxO transcription factors affects the expression of genes critical for autophagy and lysosomal catabolism. Image adapted from Ref. [49].

1.4.2.2 Endoplasmic Reticulum Stress-induced pathway

Another pathway influencing autophagy induction in response to extracellular stress is the one related to the ER stress-induced unfolded protein response (UPR) arising in conditions of imbalance of cellular homeostasis [50]. ER stress occurs when the ER's protein-folding capacity is saturated, such in case of aberrant aggregation of misfolded or mutant proteins, variation in ATP levels, accumulation of viral proteins and toxins, or in the presence of nutrient deprivation, hypoxia and alterations in Ca^{2+} levels. In response to these stress conditions, cells activate an adaptive cascade of events within the UPR to alleviate the ER stress and enhance protein-folding capacity. The three main UPR pathways involve inositol-requiring kinase 1α (IRE1α), protein kinase RNA-activated (PKR)-like ER kinase (PERK) and activating transcription factor 6 (ATF6). These pathways, upon activation, strongly influence amino acid metabolism, protein folding control, ER stress response, and autophagic activation. Autophagy, in this context, serves to recycle misfolded proteins and damaged ER components. The UPR pathway plays a pivotal role in the preservation of cellular homeostasis by alleviating ER stress, preventing cell death. However, its dysregulation has been implicated in the progression of neurodegenerative diseases, including Parkinson's disease [51,52].

1.4.2.3 Hypoxia-induced autophagy

Hypoxia-induced autophagy is a cellular response triggered by low oxygen levels, aiding in the maintenance of cellular energy levels and the removal of damaged cellular components, thereby contributing to cell survival in low-oxygen environments [53,54]. Hypoxia-inducible factors (HIFs) are the primary mediators of the cellular response to hypoxia. In particular, HIF-1α is rapidly degraded in normal oxygen levels (normoxia), while it is stabilized and accumulates in the cell in hypoxia increasing conditions. This accumulation leads to nucleus translocation and dimerization with HIF-1β, activating the transcription of genes involved in autophagy induction such as BNIP3, which hampers the interaction between the anti-apoptotic protein Bcl-2 and the key autophagic protein Beclin-1, ultimately promoting autophagy. This autophagy pathway interacts with other cellular stress responses, including ER stress and mTOR pathways. If hypoxia persists and progresses to anoxia, a condition of complete lack of oxygen, autophagy becomes crucial for recycling intracellular components to generate essential metabolic substrates and energy, since the ATP production is hindered. If anoxia persists and autophagy is not sufficient to maintain cellular homeostasis, cells may undergo apoptosis, a response primarily mediated by the activation of Bcl-2 family proteins [55]. Understanding cellular responses to hypoxia is crucial, particularly in conditions such as stroke, myocardial infarction, and tumor microenvironments, where anoxic conditions are common.

1.4.2.4 Ca^{2+}-mediated pathway

Calcium ions (Ca^{2+}) function as versatile second messengers in various cellular processes and their involvement in autophagy is complex. Ca^{2+} is released into the cytosol from the ER throughout ion channels of the plasma membrane. Elevated cytosolic Ca^{2+} levels can induce autophagy in different pathways [56,57]. Ca^{2+}/calmodulin-dependent kinase kinase β (CaMKKβ) is an enzyme actively released in response to increased cytosolic Ca^{2+} concentrations. Its phosphorylation leads to the activation of AMP-activated protein kinase (AMPK), which, in turn, initiates autophagy by activating the ULK1 complex or inhibiting mTOR pathway. Transcription Factor EB (TFEB), a master regulator of lysosomal biogenesis and autophagy gene expression, is activated by calcineurin, a Ca^{2+}/calmodulin-dependent phosphatase. Calcineurin phosphorylates TFEB, leading to its nuclear translocation and the activation of autophagy genes. In addition, Ca^{2+} levels influence the interaction between Beclin 1 and Bcl-2. Disruption of this interaction serves as an inducer of autophagy. Likewise, mitochondrial autophagy (mitophagy) is highly regulated by Ca^{2+} uptake. An abundance of mitochondrial Ca^{2+} concentrations can lead to mitochondrial disfunction, triggering the induction of autophagy.

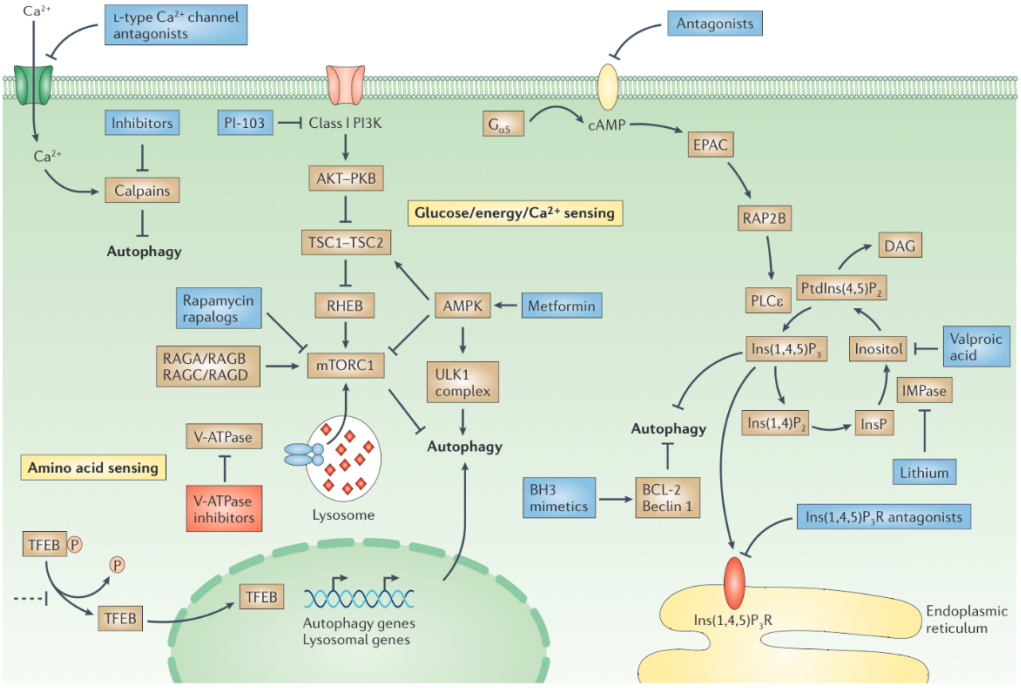

Figure 7 – The Ca^{2+}-dependent autophagy axis. Ca^{2+} plays a pivotal role in autophagy induction by modulating various signaling pathways. An increase in intracellular Ca^{2+} can activate autophagy through pathways involving AMPK activation and mTOR inhibition. Additionally, Ca^{2+} can stimulate autophagy via calcineurin-dependent dephosphorylation of TFEB, promoting its nuclear translocation and the transcription of autophagy-related genes. Thus, Ca^{2+} acts as a critical second messenger in regulating autophagic processes. Image revised from [58].

1.5 The role of autophagy in pathologies and diseases

Autophagy plays a pivotal role in a variety of human pathologies, acting as both protective mechanism and contributor to disease progression.

1.5.1 Neurodegenerative diseases

In neurodegenerative diseases such as Alzheimer's, Parkinson's and Huntington's diseases, the progressive loss of neuron structure and function is the cause of the pathologic state, often attributed to the accumulation of misfolded proteins and damaged organelles [59]. In this context, autophagy is a key factor in enhancing the clearance of toxic aggregates, such as amyloid-β in Alzheimer, α-synuclein in Parkinson's and huntingtin in Huntington's disease. This protective mechanism aims to prevent the toxic accumulation of these aggregates and protect neurons from degeneration. Conversely, an impairment of autophagy is often associated with disease

progression, leading to increased aggregation and neuronal toxicity. Damaged mitochondria are also a common feature in neurodegenerative diseases, along with increased oxidative stress and neuronal death. Mitophagy, a selective autophagic process directed to mitochondria degradation, becomes crucial for misfunctioning mitochondria elimination. In addition to these factors, neurodegenerative diseases exhibit neuroinflammation induction, where glial cells are activated and their autophagic pathways modulate the inflammatory response [60,61].

1.5.2 Cancer

In cancer, autophagy plays a dual role, acting both as a tumor suppressor and a survival mechanism for cancer resistance [62,63]. Playing the role of housekeeping of damaged organelles and proteins, autophagy serves as a protective mechanism to reduce oxidative stress and chronic inflammation, known contributors to cancer initiation and progression. Additionally, autophagy aids in maintaining cellular homeostasis, preventing the accumulation of damaged DNA, and thereby preserving genome stability to inhibit tumorigenesis. In established cancers, autophagy improves cancer cell survival under stress conditions such as hypoxia, nutrient starvation and chemotherapy. Additionally, autophagy serves as resisting factor against therapies, by organelles and proteins degradation as metabolic substrate for energy availability.

1.5.3 Infections and Viruses

Autophagy plays a significant role also in the defense against infections and viruses, contributing to the elimination of pathogens, regulation of immune response and modulation of inflammation [64,65]. In the autophagic pathways cells directly engulf and degrade pathogens introduced into the intercellular space, a process known as xenophagy. Here, autophagy serves as a defense mechanism against viral and bacterial infections within cells, facilitating their clearance. In the immune response modulation, autophagy is involved in the adaptive process of processing and presenting antigens to immune cells, thereby enhancing the development of adaptive immunity. In addition, by removing or down-regulating pro-inflammatory cytokines, autophagy plays a role in limiting chronic inflammation.

1.5.4 Cardiovascular Diseases (CVDs)

Autophagy is also determinant in the pathogenesis and progression of cardiovascular diseases (CVDs), impacting the health of the heart and blood vessels in various ways depending on the stage and severity of the disease [66]. For instance, in atherosclerosis, moderate autophagy induction in endothelial cells, smooth muscle cells and macrophages contributes to stabilizing plaques and controlling inflammation, slowing down disease progression. However, abnormal autophagy destabilizes plaques formation and intensifies the inflammatory state, leading to the disease development.

In myocardial ischemia/reperfusion (I/R) injury, increased autophagy provides cardio-protection during myocardial ischemia, but excessive autophagy during reperfusion can damage and induce death in myocardial cells.

In heart failure (HF), a condition characterized by progressive weaking of the heart, myocardial hypertrophy and diminished contractility, the role of autophagy is complex and not fully understood [67]. While inhibiting autophagy contributes to adverse cardiac remodeling leading to myocarditis and cardiomyopathy [68], excessive autophagy can be detrimental, leading to the degradation of vital components and cell death [69]. This dual nature of autophagy in HF suggests that it initially aids in adapting to the disease, but excessive autophagy in later stages may contribute to HF.

The increasing significance of studying autophagy's role in cardiovascular diseases has become unequivocal due to the global health concerns posed by these diseases, which remain a leading cause of mortality. The focus on cardiovascular health and autophagy correlation is emphasized by the dependency of heart’s function on myocardial cells healthy state. These cells rely on autophagy and cellular rejuvenation to sustain their activity and to resist various stress factors. Triggers like inflammation, reduced oxygen supply, lipid oxidation, ER stress, and the production of reactive oxygen species (ROS) can initiate the autophagic process. Autophagy operates in a dual way in this context: it not only recycles damaged organelles, preventing apoptosis, but also supplies essential resources for protein production and cellular upkeep under external stresses perturbations. This unraveling is necessary to the onset, progression, and the potential treatment of cardiovascular diseases, emphasizing the growing importance of understanding autophagy in cardiovascular health research.

1.6 Cardiac Physiology

The heart tissue is a complex and specialized structure crucial for the organ's main pumping function, comprising three types of tissue that alternate in the whole organ: the myocardium, endocardium, and epicardium [70,71].

The endocardium, lining the inner part of the heart, consists mainly of endothelial cells, providing a smooth surface that aids blood flow, minimizes resistance to the flow and prevents clot formation. The underlying connective tissue consists of elastin and collagen fibers, giving flexibility and strength to withstand the blood flow and the contraction force of the heart. In addition, its integrity is crucial for the normal electrical activity of the heart tissue, being in this way an essential part of the cardiac conduction system.

The epicardium, the outermost layer of the heart, protects and supports the heart, featuring epithelial cells, connective tissue, nerves, blood vessels, which supply the necessary oxygen and nutrients to the myocardium, and fat, providing a lining effect, shielding the myocardium and storing energy for the metabolic sustenance.

The myocardium is the middle layer between endocardium and epicardium and contains cardiomyocytes responsible for heart contraction. Cardiomyocytes (CMs) have a striated appearance due to sarcomeres, the contractile units, consisting of basic filaments, i.e. actin and myosin, and regulatory proteins, i.e. troponin and tropomyosin. The sarcoplasmic reticulum is essential in the tuning of intracellular Ca^{2+} levels and contraction. Sarcomeres allow muscle contraction by sliding its main filaments. CMs are interconnected by intercalated discs, facilitating electrical and metabolic communication, ensuring synchronized hearth muscle contraction.

The heart's primary function is to pump blood throughout the whole body, driven by the contractile machinery of the myocardium. The core of the myocardial contractile machinery lies in the sarcomeres and is governed by the sliding filament mechanism. During the contraction evolution, by exploiting ATP for energy requirement, myosin heads bind to actin filaments and pull them closer, with a consequent shortening of the sarcomere and contraction of the muscle cell. The triggering of the contraction resides in the electrical signal propagation of the action potential (AP), which travels along the cell membrane and stimulates the release of Ca^{2+} from the sarcoplasmic reticulum into the cell cytoplasm. Ca^{2+} binds troponin, leading to a conformational change that cause the release of tropomyosin away from the actin binding sites and allowing the interaction of myosin with actin. CMs are connected by intercalated discs and interact each other by means of gap junctions, allowing the direct electrical coupling between

cells. This also ensures that the contraction is propagated and synchronized throughout the myocardium, leading to effective heart pumping.

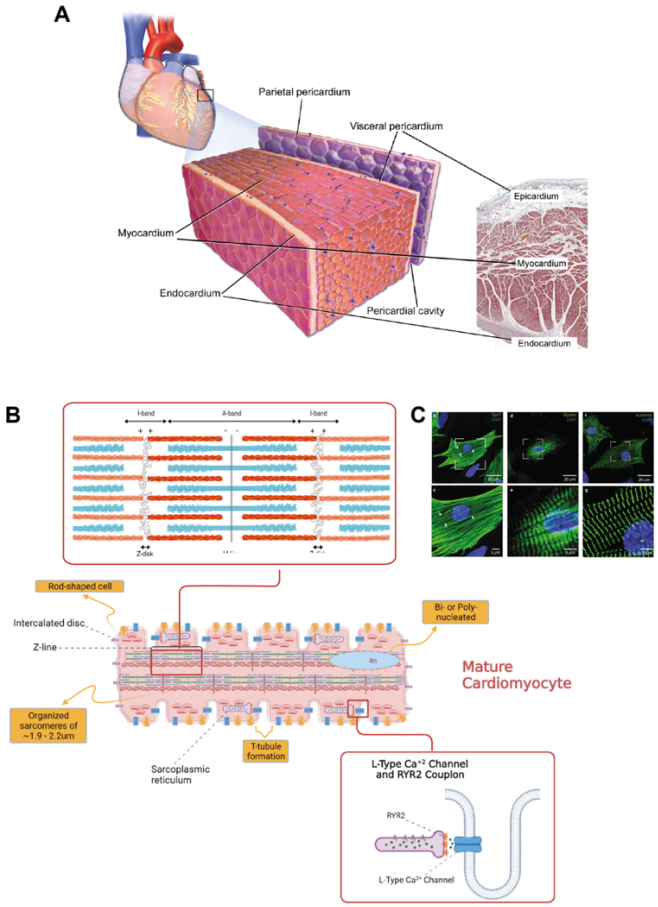

Figure 8 – Cardiac tissue structure. A) The heart is made by three important layers, from the inner part to the outer part: endocardium, myocardium and epicardium. Each of them has a singular cell composition and orientation of fibers. B) The substructure of the contractile unit of the heart tissue can be found in the cardiomyocytes basic assembly, the sarcomere. C) Neonatal rat cardiomyocytes labeled to show troponin T (b, c), myosin (d, e) and α-actinin (f, g). Panel made by images adapter from [7273,74].

1.6.1 The microenvironment cues control on cardiac functionalities

The functional mechanism of the heart operates across a wide range of spatial and temporal scale. For instance, the contractility of cardiac muscle cells is influenced by actin filaments that, linked to myosin, generate, and withstand mechanical forces during the contraction and relaxation, maintaining the structural integrity of the cardiac muscle cells. In addition, the alignment of cardiac cells is essential for correct mechanical and electrical coupling at tissue level. The ECM, such as the underlying basement membrane, acts as scaffold for cell alignment, shaping the muscular layer of the heart. Likewise, the interstitial network between cardiac cells,

comprising collagen fibers and elastin bundles, has structural and connective properties in the interaction with adjacent neural and vascular tissues. Therefore, the biochemical, electrical, and mechanical signals, acting synergistically to maintain heart functionality, are linked across various biological scales. Understanding these main cues and how they act to control cardiac cells is crucial for uncovering new strategies for *in vitro* recapitulation of the heart microenvironment and engineering heart tissue functionality.

1.6.1.1 3D cellular and spatial organization

While CMs make up most of the heart's volume, they represent only a third of the cell count, with fibroblasts being crucial cell type in forming the interstitial ECM and influencing its development and diseases progression. Nerve fibers and cells are another key cell type, intricately embedding the heart and playing a vital role in its conduction system. The complex vascular network is also essential for oxygen and nutrients delivery: the dense and branching capillary network runs adjacently to the cardiac muscle fibers, with limited and efficient distances for oxygen diffusion. The engineering of human heart tissue also requires the unraveling of the cardiac hierarchical structure. The ventricle tissue consists of myocytes organized in separate layers with variable orientations, which are rearranged in a total helical and anisotropic configuration. Due to this structure, the muscle possesses different electrical and mechanical properties that changes from the endocardium to the epicardium, and from the base to the apex of the whole heart. This results in contractility, excitability, and force generation, attributed also to the variable interconnection between adjacent CMs, which communicate not only longitudinally front-to-rear but also side-to-side in the transverse direction [75,76].

1.6.1.2 Cell-ECM biochemical interaction

The cardiac architecture and its complexity are due to the convoluted 3D organization of the cell assembly but also to the characteristic ECM network composed of collagen, elastin and an interconnected basement membrane. Its role encompasses the necessity to structurally sustain the heart and vascular wall and to physically orientate the CMs, providing a linking point between cells and elasticity during the stretching phase. The mechanical continuity between the cells is provided by the mutual connections of collagen, whose disruption can impair myocardial performance and propagate the stretching between contiguous cells. The ECM plays a crucial role also in CM's proliferation. Some studies have highlighted the importance of the presence

of hyaluronan in the build-up of an environment favorable for cell growth due to its hydrating properties [77]. On this point, the protein HapIn1 or Cartilage link protein 1 (Crtl1), which binds to hyaluronan, seems to enhance the proliferation activity of myocardial cells. Studies on Crtl1 depletion in zebrafish, in which abnormal hyaluronic acid deposition and low proliferation of CMs were observed, confirm the significant role of hyaluronan in heart development [78]. Utilizing components of the ECM to stimulate pluripotent stem cells has been effective in producing a range of cardiovascular and hematopoietic cells, including progenitors, endothelial cells (ECs), smooth muscle cells (SMCs), and CMs [79]. Notably, in animal models, such as murine embryonic stem cells (ESCs) and induced pluripotent stem cells (iPSCs), when cultured on collagen IV-coated surfaces, there is evidence of the development of these cells into FLK1+ mesodermal progenitor cells. These progenitors can differentiate into ECs, as indicated by their expression of characteristic markers such as CD31 and vascular endothelial-cadherin (VE-cadherin). Furthermore, these FLK1+ cells can also transform into CMs, as demonstrated by the presence of sarcomeric myosin and troponin C, and into SMCs, distinguished by their specific contraction patterns [79–81]. The control of CMs' behavior and stem cell differentiation are significantly influenced by the ECM primarily through the action of integrin receptors. These receptors, upon binding to ECM ligands, change their conformation, initiating a series of downstream signaling processes. For instance, it has been proven that cardiac differentiation is affected by the interaction between collagen type I and β1 integrin: when this interaction is blocked, abnormal embryoid bodies develop along with decreased beating activity and reduced cardiac gene expression [82]. Furthermore, fibronectin increases the phosphorylation of integrins, impacting signaling pathways like RhoA-PI3K/Akt-ERK1/2, which is involved in mouse ESCs proliferation [83]. Eukaryotic cells are also highly responsive to calcium and calmodulin (CaM), a calcium-binding messenger protein: calmodulin-dependent protein kinase II (CaMKII) is a structural kinase that manages the interaction with cytoskeleton, by means of the laminin at the cell-ECM interface [84]. Ca^{2+}/CaM binding to CaMKII and an increase in Ca^{2+} level in the cell cytoplasm lead to the phosphorylation and inhibition of the interaction of the kinase with the F-actin, heading to cytoskeletal disassembly [85,86]. ECM proteins also regulate the activity of soluble growth factors, crucial for their distribution and presentation to the cells. Proteins like heparan sulfate proteoglycan on the ECM surface can bind growth factors such as fibroblast growth factor (FGF) and VEGF, activating various differentiation pathways such as the one involving TGF-β [87]. While the ECM's role in modulating cellular biochemical pathways is established through its interactions with integrins and various soluble factors, the mechanical identity of the ECM is also crucial for the tissue assembly.

1.6.1.3 Topographic control on cardiac cell behavior

The heart tissue is characterized by its intricate structure, encompassing features ranging from nanoscale dimensions, such as actin and myosin filaments, to microscale features, like fibrils. Cardiac cells are highly elongated and organized in parallel lines of microfibrils in their physiologic state, allowing for effective coordination of anisotropic myocardial contraction and propagation of electric signals. In fact, adult CMs are characterized by high aspect ratio, resulting in parallel sarcomere arrays and polarized gap junctions from end to end. The *in vitro* recapitulation of these organized structures is challenging, requiring micro- and nano-topographies to mimic the physiologic dynamic organization of cell complexes responsible for translating these physical cues. Cardiac cells exhibit contact guidance, in response to specific micro- and nano-patterns on substrates by aligning themselves along the underlying features. This phenomenon influences the arrangement and conformation of key cardiac cells structures, migration and proliferation rates, and contraction propagation. For instance, the alignment of CMs on pattern is influenced by the width of the surface features, resulting in enhanced cell area, elongation, and sarcomere length [88], which is an indicator of cardiac maturity, with adult CMs typically showing longer sarcomere than immature CMs derived from iPSCs [89]. Cx43, a gap junction protein essential for the electrophysiological function of CMs, is located at the ends of mature cardiac cells, facilitating strong contractile forces and electrical conduction. Several studies have reported high expression and end-to-end polarization of Cx43 on patterned substrates, serving as markers of mature contractile function development (*Fig. 9*) [90,91]. Topographical cues also boost the expression of markers associated to cardiomyogenesis, as demonstrated by the differentiation of hiPSC CMs cultured on aligned poly(caprolactone) (PC) [92] and poly lactic-co-glycolic acid (PLGA) [93] scaffolds. This differentiation is accompanied by enhanced gene expression related to structural and calcium-handling proteins translation. Moreover, the expression of contractile and electrophysiological activity factors is heightened when interacting with topographical cues. CMs on micro-patterned surfaces exhibit better calcium transient synchronicity [94] and stronger contraction forces [95]. Aligned and elongated cells on micropatterned scaffolds demonstrate higher contraction velocities, beating rates, and amplitudes [96] compared to cells on random scaffolds. Given the demonstrated crucial role of topographies in CMs behavior and the multi-scale hierarchical structures of native tissue, a hierarchical topography offers enhanced insights into how cells respond to surface physical characteristics across different scales, from micro to nano levels. In the work of Ahn et al., CMs maturation was found to be enhanced by implementing a hierarchical structure that combines

nano-pillars and micro-wrickles [97]. Nano-pillar structures with a lower aspect ratio effectively boosted focal adhesion (FAs) expression, leading to increased expression of cardiac troponin T (cTnT), an indicator of cardiac maturation. The combination of supra-cellular micro-wrinkles and low-aspect ratio nano-pillars notably enhanced cardiac maturation, by effectively constraining cells within grooves and promoting controlled FAs confinement on nano-pillars.

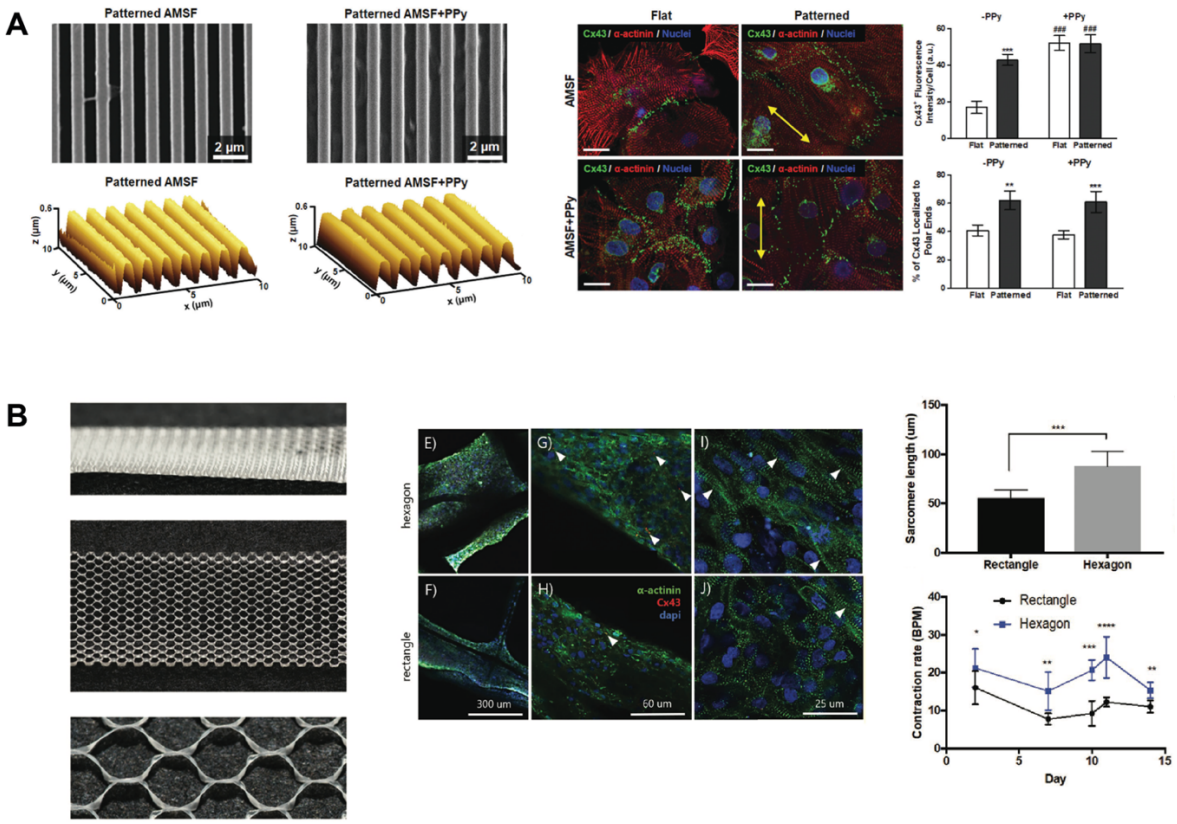

Figure 9 – The topography control over cardiac cells behavior. A) Nanopatterned substrates made by conductive silk-polypyrrole demonstrated structural arrangement and development of the contractile machinery. Illustrative images show CMs marked with fluorescent staining for Cx43, α-actinin and nuclei. Cells positioned on nanopatterned surfaces demonstrate extended and orderly shapes. Yellow arrows point to the orientation of the nanopattern. [98] B) Detailed microstructures allowed to iPSC-CMs adhere to both hexagonal and rectangular fiber scaffolds. Confocal microscopy reveals Cx43 expression, as well as a higher sarcomere density, improved alignment, and greater length in hexagonal scaffolds compared to rectangular ones [96].

1.6.1.4 Cell-ECM mechanical interaction

The ECM regulatory role is largely expressed through physical forces. During embryonic development, ECM molecules undergo self-assembly into more complex structures, including collagen fibrils, bundles, nets of basement membrane collagens and hydrogels. These structures bind to cell surface integrins, acting as the receptor machinery for CMs anchoring to the basement membrane. In this way, the ECM provides the structural scaffold for the tissue, relying on the stiffness of its network to balance cell-generated contractile forces. Variations in the mechanical properties of the ECM influence and alter the resistance to cell tension, thereby impacting the balance of mechanical forces in the cytoskeleton. The ability of cells to respond to physical signals coming from the adhesion substrate is termed mechanotransduction, involving the conversion of physical stimuli into molecular signaling [99]. The primary elements facilitating the transmission of mechanical signals from the ECM to cells are the integrin receptors on the cell surface. Integrins, consisting of α and β subunits, are dimeric proteins that bridge ECM proteins outside the cell with cytoplasmic proteins, playing a crucial role in linking the cell's cytoskeleton to the ECM. Cardiac myocytes express various types of integrin receptors that bind specific ECM components. This binding leads to the clustering and activation of receptors on the membrane cytoplasmic side, involving kinases such as src kinase and focal adhesion kinase (FAK). These molecular events contribute to the formation of FA complexes, essential for cellular anchoring to the ECM. Hence, integrins exhibit the ability to build an inside-out and outside-in signaling. Ligand affinity and receptor clustering can be controlled through the binding of intracellular signaling molecules, while receptor-ligand binding modulates intracellular signaling in the cytoplasmic domain. In addition, the ensemble of vinculin, talin, integrin and laminin form the attachment complex found at the costamere, situated between Z-lines of CMs. These connections facilitate the transmissions of contractile forces between CMs and the ECM and *vice versa*, forming a vital bridge from the external cellular environment directly to the Z-line within the sarcomere.

CMs possess two primary types of mechanical sensors: biophysical and biochemical sensors. In mechanotransduction, the sensing machinery of CMs plays the role of balance element between internal and external forces to maintain cellular structure. Biophysical sensors involved in this regulation are founded in the structural element of the ECM and the ECM-cytoskeleton connection, particularly integrins. Structural proteins on the cell surface, such as acto-myosin stress fibers, α-actin, and myosin, interact with filamentous actin, generating forces that eventually influence the nuclear membrane shape and balance. When the force exerted on these

proteins, it reaches a threshold and triggers the recruitment of molecules from the attachment complex at the costamere, including talin, vinculin, paxillin and FAK. This recruitment initiates intracellular signals for various activation pathways. In particular, the FAK phosphorylation causes myosin proteins to move along the actin-myosin fibers, leading to conformational changes in mitochondria, sarcomeres, and nuclear membrane, which ultimately lead to regulation of gene expression, translation pathways and mitochondrial function [100,101]. Besides the crucial role of biophysical sensors in CMs mechanotransduction, different biochemical sensors regulate the CMs fate in response to mechanical stress events. One component of the biochemical sensors family includes the Ras-like small GTP-binding proteins. These proteins play a in switching between GTP- and GDP-bound forms of Ras, influencing their interaction with downstream signaling molecules, including those crucial for cardiogenesis, heart development, and management of calcium channels [102]. In CMs, Rap2 has been confirmed as a key controller of mechanosensitive events by acting on the Yes-associated protein (YAP) and transcriptional coactivator with PDZ-binding motif (TAZ). The mechanical properties of the microenvironment activate Rap2 via specific biochemical pathways, making it a key converter of mechanical to biochemical signals. This mechanism works upstream of the Hippo-YAP/TAZ pathway, crucial in heart biogenesis and regeneration. In this pathway, when cells are exposed to growth-inhibiting signals, the cascade of involved kinases leads to the final phosphorylation and inactivation of YAP and TAZ, resulting in their cytoplasmic retention and degradation. Instead, when the Hippo pathway is inhibited by growth-promoting signals, YAP and TAZ dephosphorylation induces their retention in the cell nucleus, where they bind to TEAD family transcription factors to promote genes involved in proliferation, migration and survival [103,104]. Regarding the role of YAP and TAZ in mechanotransduction processes, it has been proven that increased ECM stiffness is linked to nuclear localization of these factors [105]. High stiffness promotes cell spreading and actin cytoskeleton tension and RhoA GTPase contributes to this process by affecting actin polymerization under the sensing of ECM stiffness through FAs.

Adherent cells experience physical forces due to tension from mechanical stretching, which is attributed not only to increased ECM stiffness during tissue growth or pathological states but also to external stretching forces from tissue strains or under shear flow conditions. As described earlier, cell stretching leads to changes in behavior through YAP/TAZ-dependent mechanisms, also interacting with the Hippo pathway to regulate cell functions [106–108]. Recent research has connected the endogenous role of YAP in an adaptive hypertrophic response to acute pressure overload, aiding in wall stress reduction, cardiomyocyte protection, and delaying HF onset [109]. In particular, YAP is activated during acute pressure overload in CMs via RhoA-dependent

mechanism. Partial deletion of YAP leads to reduced cardiac hypertrophy, alongside apoptosis, fibrosis, and dysfunction after transverse aortic constriction. In the presence of static stretch, when mechanical forces are low, YAP/TAZ are suppressed by F-actin-capping and severing proteins, a mechanism activated for the enhancement of F-actin turnover during migration and contraction [110]. Removing these proteins results in the reactivation of YAP/TAZ, leading to nuclear localization and cell proliferation. Static stretching can also reduce the mechanical constraints on nuclear pores, enhancing the nuclear trafficking of YAP/TAZ [111]. Cyclic stretching also plays a crucial role in mechanotransduction pathways as reported by Yamashiro et al., showing that in vascular cells it activated YAP via the thrombospondin-1/Rap2 pathway, contributing to vascular remodeling. In fact, thrombospondin-1 forms FAs through integrins and influences YAP by encompassing the Rap2 GTPase activity, strongly responding to cyclic blood flow and pressure [112]. In a recent work it has also been proven that cyclic stretching of CMs promotes their maturation. Under tensile forces, cellular Ca^{2+} ion channels activation led to increased membrane Ca^{2+} influx and greater AP duration, alongside an increase of YAP expression upon tensile force [113].

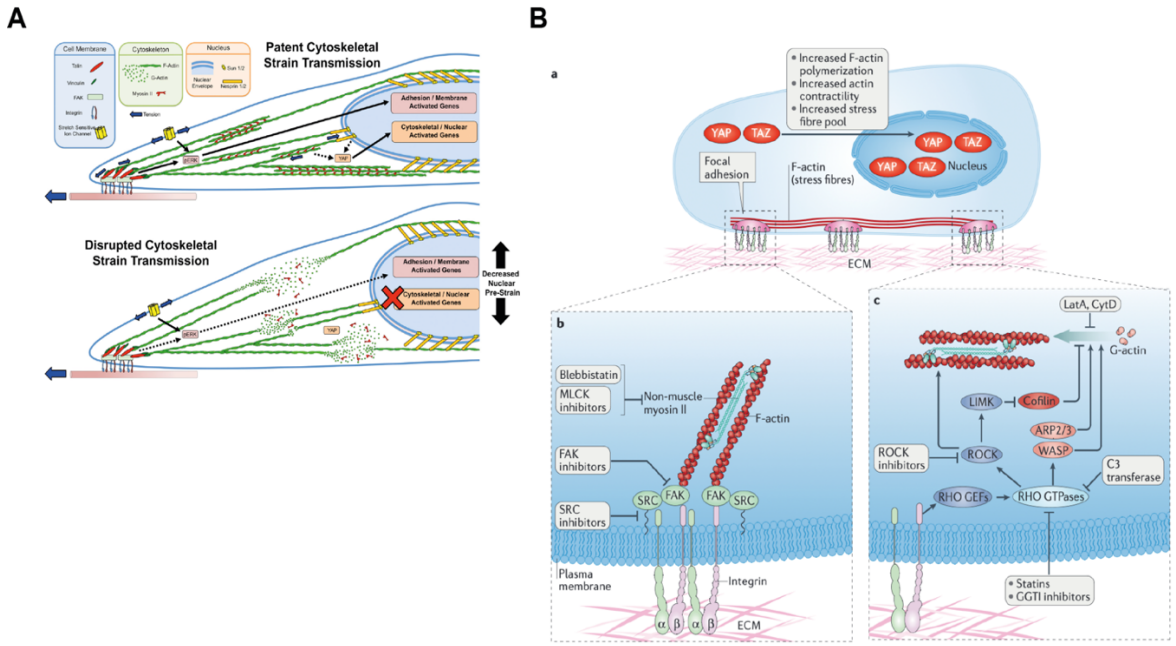

Figure 10 – The mechanotransduction players in the cell-ECM mechanical interaction. A) Mechanoactivation can be initiated through mechanisms involving mechano-transduction modules linked to the cell membrane or via modules that mediate mechanotransduction through the transfer of strain from the cytoskeleton to the nucleus. Inhibition of ROCK results in reduced nuclear prestrain and actin depolymerization. Consequently, this disrupts the transfer of strain from the cytoskeleton to the nucleus essential for YAP activation [107]. B) Cell-ECM adhesion complexes initiate force-induced conformational changes, leading to an increase in actin polymerization and stress fiber contractility, which activates YAP and TAZ. A stiffer matrix promotes integrin

clustering and the activation of kinases like FAK and SRC, enhancing stress fiber growth, stability, and contractility, further activating YAP and TAZ. Focal adhesion signaling also activates RHO GTPases, influencing actin regulatory proteins or promoting F-actin polymerization via ROCK activation. ROCK enhances actomyosin contractility [103].

1.7 *In vitro* cardiac tissue: tissue engineering approaches

In the quest to unravel various physiologic and pathologic processes involved in heart tissue homeostasis or disease, cardiac tissue engineering represents a promising field. It focuses on developing functional cardiac tissues that closely mimic the heart's natural macro- and micro-environment. The goal is to employ biomimetic strategies that emulate the heart's biochemical, mechanical, and structural aspects, as well as the interactions between cells and cardiac tissue. Ultimately, the aim is to realize an accurate apparatus for tissue growth from a physiologic standpoint, allowing the validation of the functional and therapeutic potential of these *in vitro* cardiac tissues. On-chip technologies seek to replicate organ microenvironments by integrating microfluidics, biomimetic materials and sensing technologies. Through accurate emulation of the heart's microenvironment, these tissue engineering approaches enable more effective treatment strategies. This advancement holds the potential to move towards personalized medicine, addressing the widespread injuries and facilities associated with cardiovascular diseases.

1.7.1 Biomaterials for cardiac tissue engineering

In cardiac tissue engineering, materials must withstand the heart's cyclic mechanical stretching and electrical activity while ensuring biocompatibility for cell proliferation and survival. Polydimethylsiloxane (PDMS) has been favored in early cardiac-on-a-chip models due to its affordability, ease of fabrication, transparency with consequent optical accessibility, controllable mechanical properties, sterilizability, oxygen permeability and compatibility with surface modifications. In the platform developed by Thavandiran et al., they used a bottom-up approach combined with computational methods to build cardiac microtissues in a PDMS structure made of parallel pillars, inducing correct ECM organization with stress-mediated alignment and patterned expression of sarcomeric filaments [114]. In another work, an array of pillars, obtained by casting PDMS in master acrylic cavities, allowed the alignment of cardiac tissue constructs in the so-called I-wire system, generating a macrotissue that simulates the

spatial organization of native cardiac tissue constructs [115]. Despite its advantages and widespread use in tissue engineering, PDMS is not suitable for sustaining large deformations and is known for the uncontrolled absorption of small molecules on its surface, which can impair cell culture viability. On the other hand, elastomers and polyesters are increasingly popular in tissue engineering applications due to their physiologically relevant stiffness, ability to endure cyclic stretching, and suitable degradation rates, making them excellent candidates for scaffolding purposes. Their hydrolytic degradation into metabolism-related monomers, such as glycerol and citric acid, also renders them ideal for transplantation applications. Soft polyesters, such as poly(octamethylene maleate (anhydride) citrate) (POMaC), have found extensive use in *in vitro* cardiac engineering. In the work of Zhao et al., POMaC wires allowed the organization of aligned mature cardiac microtissue for on-line noninvasive recording of contractile activity in a conjunct atrial-ventricular axis of differentiation [116]. Hydrogels, derived from both natural and synthetic sources, are commonly used in cardiac tissue engineering. Poly(ethylene glycol) (PEG) hydrogels, known for their soft mechanical behavior, can be easily shaped into complex micro-structures using precision techniques such as stereolithography and photopolymerization [117]. Materials like methacrylayed gelatin (gelMA) [118] and collagen (colMA) [119] are common for cardiac applications due to their photocrosslinking properties. Alginate, valued for its biocompatibility, low toxicity, and quick solidification in calcium-rich environments, is ideal for *in situ* biomaterial formation. Agarwal et al. developed two effective micropatterning techniques such as microcontact printing and micromolding, for soft alginate substrates, leading to distinct patterns and topographies that facilitated the formation of anisotropic cardiac and vascular smooth muscle tissues, demonstrating their potential in muscular contractility assays [120]. In addition, integrating electroconductive polymers like polypyrrole (PPy) [98] and poly(3,4-ethylene dioxythiophene) polystyrene sulfonate (PEDOT:PSS) [121] into cardiac tissue engineering approaches represents a promising development. These polymers offer adjustable conductivity, closely mimicking the cardiac tissue microenvironment and realizing conductive cellular networks for electrical signal propagation, essential for the proper functioning of cardiac tissues.

1.7.2 Cardiac tissue engineering platforms

The heart, functioning as an electromechanical pump, relies on the uniform layer-by-layer alignment of CMs to improve the contractility function of the tissue and blood circulation. To recreate cardiac tissue *in vitro*, it becomes crucial to engineer cells and anisotropic structures that mimic the heart's apparatus. Heart-on-a-chip (HoC) techniques are the ensemble of approaches exploited by the tissue engineering community to recapitulate the heart functionalities by means of artificial and synthetic tools. HoC has employed various cell types, such as neonatal rat CMs, human ESCs, and hiPSCs, to replicate this complex biological structure and function. CMs cultured in traditional 2D Petri dishes do not fully replicate the complex *in vivo* interactions found in the heart, such as those between cells and the ECM. On one hand, 3D culture techniques are more effective in this respect, offering greater cell viability, maturity, and contractile forces. 3D printing has gained particular attention due to the possibility to build specific geometrical structures, alongside the uniform printing of cells within hydrogel-based bioinks, thus better mimicking the architecture of native cardiac tissues and enhancing the physiological relevance of these engineered constructs [122]. On the other hand, HoC techniques leverage microfluidic technology, a key driver in chip development, allowing for nano- and micro-structural control over the building of a biomimetic cardiac environment. This approach facilitates the development of cell-scale stimulators and read-out, essential for mimicking the cellular and extracellular aspects of the heart and its response to cues coming from the surroundings [123].

Fluid perfusion is crucial for HoC because of the necessity to provide a certain nutrient level and remove waste materials of cell metabolism, mirroring the mechanism in the human circulatory system. The perfusion microenvironment offers significant advantages over simple 2D cultures by maintaining an environment that mimics a normal human heart. This also includes the need to sustain optimal oxygen levels and physiological pH. For instance, PDMS-based microfluidic devices can effectively control oxygen concentration, generating a gradient that is vital for cell culture. A study by Rexius-Hall et al. demonstrated that the presence of an oxygen gradient led to distinctive effects compared to tissues subjected to uniform oxygen levels [124]. For example, tissues exhibited characteristics associated with arrhythmogenic conditions, such as a slower calcium transient, reduced propagation velocity, and uneven expression of Cx43. Another study by Liu et al. utilized a bioelectronic HoC model with immortalized mouse atrial HL-1 cells to explore the effects of acute hypoxia on cardiac function [125]. The system used

arrays of platinum nanopillars as intracellular probes to register the electrophysiological response to hypoxia, monitoring pulse rates and wavefront propagation.

External stimuli, particularly electrical and mechanical stimuli in heart tissue recapitulation, significantly enhance contractile function, metabolism and calcium regulation. Accordingly, the use of electrical stimulation is effective in improving the maturity and beating patterns of CMs. Radisic et al. developed a platform that integrated 3D cell cultivation with electrical stimulation to mature heart tissues derived from hPSCs [126]. The degree of maturation was evaluated by observing the myofibril ultrastructural organization, by quantifying the conduction velocity and propagation of Ca^{2+}. Moreover, the combination of microgrooves and electrical stimulation in a high-throughput platform for HoC is able to reproduce the sarcomere structure and synchronized contractions, with CMs maturation and efficacy in response to cardiotoxicity and cardioprotection [127]. Mechanical stretching is crucial in CMs elongation and functionality. Already in the early 2000s, 3D aligned myocardial tissues derived from neonatal rat CMs, combined with collagen and growth factors, were grown in a casting ring-shaped mold to create a condensed tissue and then were transferred in a stretch apparatus to continue culture under uniaxial stretch [128]. The mechanical stimulation was able to produce a tissue with contractile and electrophysiological characteristics similar to those of native tissues. In a more recent study, a microscale cell stimulator was developed to deliver both mechanical and electrical stimuli [129]. The platform was composed by a pneumatic layer for stretching, a conductive layer of carbon nanotubes and PDMS for electrical stimulation and a fluidic layer for cell feeding. This multi-signal microfluidic device effectively mimicked the *in vivo* microenvironment, allowing for the study of cellular responses to combined stimuli that, when applied to hMSCs, were instrumental in promoting the activation of cardiac myocyte markers.

This dissertation on the engineering approaches for cardiac tissue mimicking sheds light on the role of tissue engineering in the design of new strategies to control CMs behavior and to unravel the main mechanisms that make the heart a functioning machinery. Among the reported applications, despite their seeming simplicity, 2D cell culture methods demonstrated to have several advantages. They are cost-effective and yield consistent results, making them ideal candidate for various research purposes, like imaging and high-throughput screening for efficient and fast drug testing. In these models, CMs and cardiac ECs often exhibit higher proliferation rates compared to those in 3D cultures. These advantages are particularly useful in studies exploring the effects of the microenvironment on cardiac cell function and behavior, where handling different stimuli in the same platform should be effortless, with high

reproducibility of the effect of single or combined signals on the treated cell culture. In addition, the management of topographic and stretching cues in a 3D microenvironment remains still challenging. Moreover, characterizing the correspondence between CMs behavior and level of applied microenvironment signals is difficult in such complex constructs. Hence, in the perspective of define the cell status in response to different microenvironment signals, it could be useful to manage 2D surfaces that allow for a more consistent and uniform exposure of cells to signals and treatments, for accurate dose-response characterization and studies.

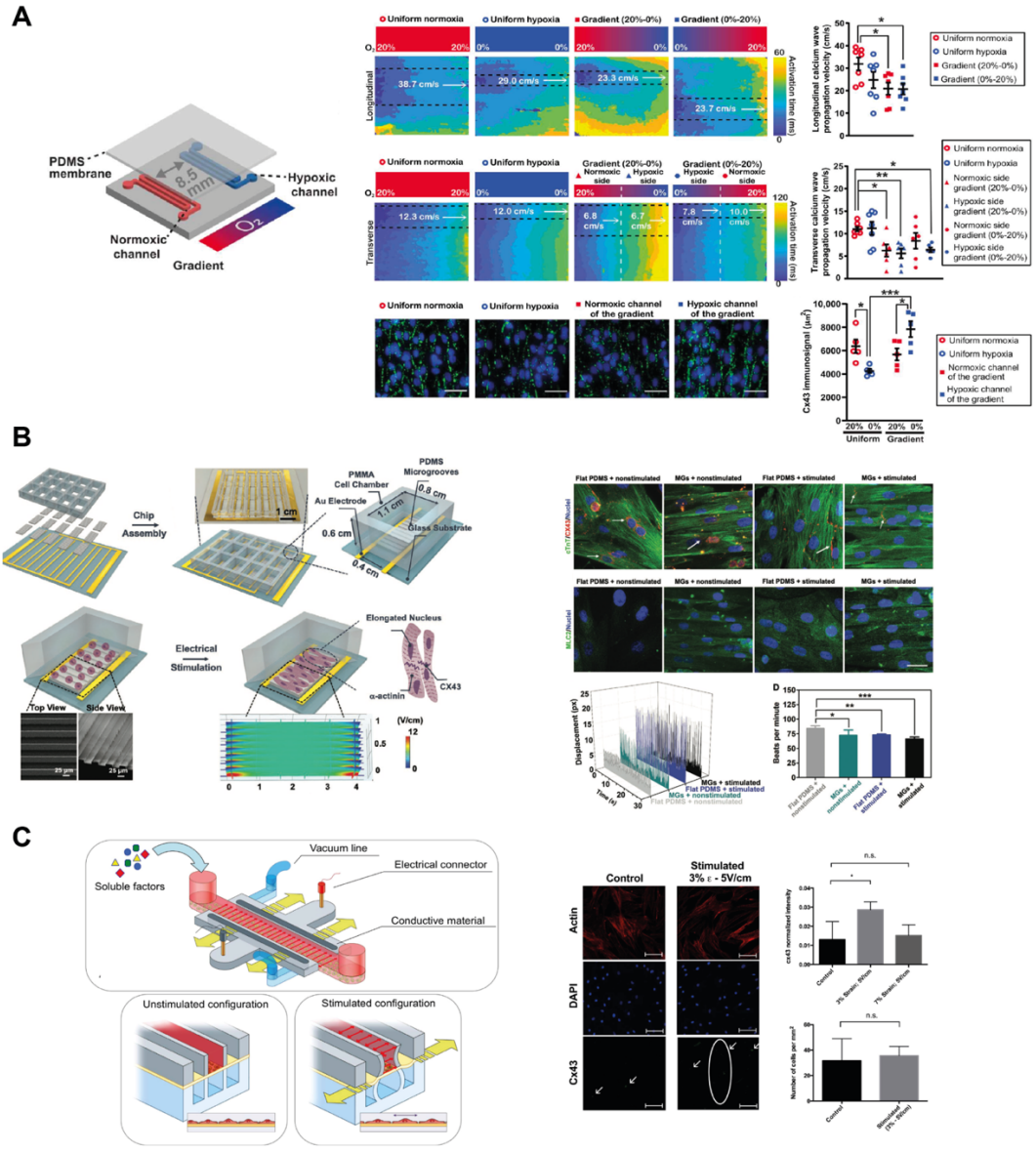

Figure 11 – Examples of tissue engineering approaches to *in vitro* cardiac tissue reproduction. A) Microfluidic devices made from PDMS are capable of precisely regulating oxygen levels, creating a gradient essential for cell culture. Rexius-Hall and colleagues showed that an oxygen gradient results in unique outcomes compared to tissues exposed to consistent oxygen concentrations. Specifically, tissues under gradient conditions displayed traits indicative of arrhythmogenic conditions, including delayed calcium transients, decreased

propagation speed, and irregular Cx43 expression. Images adapted from [124]. B) Integrating microgrooves with electrical stimulation on a high-throughput HoC platform successfully mimics sarcomere structure and coordinated contractions, leading to cardiomyocyte maturation and effective response to cardiotoxic and cardioprotective conditions. Results showed adapting images from [127]. C) The platform of Pavesi et al. introduced a microscale cell stimulator designed to administer both mechanical and electrical stimuli. This platform featured a pneumatic layer for stretching, a conductive layer made of carbon nanotubes and PDMS for electrical stimulation, and a fluidic layer for nourishing cells. In the microfluidic device when applied to human mesenchymal stem cells (hMSCs), these stimuli were crucial in activating markers characteristic of cardiac myocytes [129].

1.8 Control of the microenvironment for autophagy induction in cardiac cells

As mentioned earlier, comprehending the influence of the cellular microenvironment on autophagy induction is essential for the investigation of cellular response to diverse internal and external stimuli. This aspect is fundamental in comprehending how cells adapt and react to their surroundings in the epigenetic expression of autophagy induction. The cellular microenvironment encompasses a range of factors that, in the case of cardiac tissues, mostly includes nutrient availability, oxygen levels, ECM and surroundings mechanical interaction. These factors can significantly condition the induction and progression of autophagy.

Exploring this in the cardiovascular field opens different scenarios for novel strategies to maintain an optimal physiologic state or to treat pathological conditions, as alterations in autophagy can contribute to the progression of cardiovascular diseases, such as in HF or ischemic injury.

Tissue engineering in the context of cardiac health offers a unique tool to study and potentially modulate autophagy in cardiac tissue. By creating engineered platforms that closely mimic the natural heart microenvironment, researchers can more accurately investigate how autophagy is regulated under various conditions. This approach could lead to innovative therapeutic strategies targeting autophagy pathways, potentially improving treatment outcomes for various heart diseases and aiming to modify the underlying epigenetic pathways.

1.8.1 Microenvironment-mediated autophagy induction in cardiac cells

Nutrients starvation significantly triggers autophagy, particularly in cardiac conditions like myocardial infarction (MI), advanced heart failure (HF), cardiac remodeling, and pathological aging. These heart diseases commonly involve nutrient deprivation, impacting CMs activity. It has been reported that autophagy has a physiological function in early life stages and has potential implications for organism health [130]. In a study, a transgenic mouse model was used to examine the role of autophagy *in vivo*, revealing that autophagy was induced in the heart in response to the sudden nutritional shift experienced in post-birth. Neonatal mice lacking the autophagy ATG5 exhibited early death, likely due to nutrient insufficiency, while autophagy was found to play a critical role in maintaining amino acid levels and energy homeostasis, suggesting that it is important for the adaptation to post-natal nutritional changes. Also, in the adult heart, autophagy is critical in maintaining cardiac function, especially under starvation conditions. Inhibition of autophagy leads to significant cardiac dysfunction, underscoring its importance in providing amino acids for energy. Studies on adult mice demonstrated that, by using bafilomycin A1 (BafA1) to inhibit autophagy, reduced autophagy disrupted amino acid levels in the myocardium and decreased ATP content, contributing to cardiac dysfunction [131]. The ubiquitin-proteasome system, another degradation pathway for proteins elimination, was also enhanced under starvation conditions in the heart and further augmented by autophagy inhibition with BafA1, leading to the conclusion that protein clearance pathways under starvation play a crucial role in cardiac tissues under stress. Investigations on isolated adult rat ventricular CMs confirmed the role of autophagy in cell survival, especially under nutrient-deprived conditions. In fact, the use of autophagy inhibitors, 3-MA and leupeptin, reduced survival, impacting on cellular necrosis and ATP depletion [132]. Therefore, autophagy in CMs under glucose deprivation acts as a compensatory mechanism for survival and, when this autophagic response fails, the fate of CMs aims towards necrosis and death. A noteworthy study highlighted the dynamics of autophagy in acute doxorubicin (DOX) cardiotoxicity, which is an anti-neoplastic drug used in the treatment of a broad range of solid human cancers that has high dose-dependent side effects, including cardiomyopathy and HF [133]. Autophagy function was impaired under DOX treatment, due to the inactivation of AMPK and ULK1 phosphorylation, hindering autophagosome formation. However, prior starvation, by inducing autophagy, restored myocardial ATP levels and improved cardiac function. This suggests a protective role of autophagy against DOX cardiotoxicity, and fasting or restrict caloric regimen could be a possible strategy to prevent the cardiotoxic effect of DOX. Autophagy is also critical during I/R-

related damages [134,135]. Cardiac HL-1 cells treated with simulated ischemia/reperfusion (sI/R) have impaired autophagic flux during ischemia and are only partially restored during reperfusion. In addition, autophagy is protective against I/R injury, with pharmacological inhibition or downregulation of autophagic pathways related to cell apoptosis, concluding that up-regulation of autophagy, for instance with rapamycin, can be a therapeutic intervention post-ischemia if accomplished in short times.

In addition to common stimulation pathways, recent research has revealed that autophagy is involved in converting mechanical forces arising from the surrounding microenvironment into biological responses. Autophagy has now been recognized for its role in response to physical stimuli. For instance, shear stress, a force arising from fluid flow acting on cell surfaces, significantly influences autophagy, particularly for cells exposed to fluid dynamics like endothelial and endocardial cells. Studies show that high shear stress promotes autophagy in endothelial cells. This type of fluid flow is protective against atherosclerosis, reducing endothelial cell apoptosis, senescence, and inflammatory cytokine production [136]. The protective mechanism of high shear stress-induced autophagy involves downregulating endothelial cell death and activating specific microRNAs [137].

In the presence of stretching, i.e. when passive deformation arises from tissues or cells under external forces, autophagy activation, for example in muscles during physical activities, plays a vital role in maintenance muscle health, ensuring effective control of mitochondrial quality [138]. The benefits of physical exercise, such as extending lifespan and offering protection against cardiovascular diseases, are well-established. Cardiac cells, when exposed to conditions like myocardial infarction, systemic hypertension and pulmonary embolism, undergo increased mechanical stress. For these reasons, research has extensively studied the impact of mechanical forces on autophagic processes in cardiac cells. These studies, both *in vivo* and *in vitro*, reveal that mechanical tension can induce autophagy in heart cells. For instance, experiments with neonatal rat CMs showed autophagy initiation due to mechanical loading [139,140]. Furthermore, cases of myocardial infarction [141] and scenarios of pressure overload in hearts, such as those occurring in transverse aortic constriction [142], also demonstrated an increase in autophagic activity. The role of autophagy in cardiac cells under mechanical stress is multifaceted and context-dependent. While autophagy offers protective benefits to CMs during ischemia[141,143], its inhibition can enhance cardiac function following reperfusion in I/R scenarios [143]. Simultaneously, autophagy activation can mitigate ventricular hypertrophy caused by transverse aortic constriction, improving heart function [144,145]. However, excessive autophagy in failing hearts may lead to the death of CMs [146,147]. This complexity underscores the dual role of

autophagy, acting both as protective and potentially harmful process depending on its intensity and duration.

1.8.2 Platforms for the induction and control of autophagy

Microfluidic chips are tools for progressive biochemical testing, known for their rapid analysis, real-time monitoring, high integration and their ability to perform high-throughput screening in a compact format, within scales ranging from millimeters to micrometers. They are particularly effective for precise operations like single-cell analysis, observing cell behavior and isolating cancer cells. Their time-saving, multifunctional nature offers significant advantages over conventional methods, promoting the development of precision medicine and enhancing medical research. As anticipated earlier, autophagy is crucial in cell physiology and the development of various diseases. For this reason, it can serve as an important biomarker for detecting disease progression or assessing the effectiveness of different treatments.

1.8.2.1 Autophagy detection techniques

Transmission electron microscopy (TEM) has been a pivotal method for observing autophagy, as it allows the direct visualization of key autophagy structures such as phagocytic vesicles, autophagosomes, and autolysosomes (*Fig. 12A*). The advantage of this detection technique is the possibility to dynamically capture the morphological changes in autophagic flow progression [148]. However, TEM's efficacy is limited by the need for meticulous sample preparation and the user-dependent interpretation of results. Despite the promising technique, TEM acquisitions represent only a part of the larger autophagy structures, leading to potential inaccuracies in size and number estimation. Consequently, TEM is best used in conjunction with other methods to more accurately reflect cellular autophagy levels.

LC3 is a protein that attaches to phagocytic vesicle membranes, binding to PE. In the cytoplasm, it is present as LC3-I, while it transforms into LC3-II upon autophagy initiation, attaching to autophagosome membranes. The level of LC3-II is directly proportional to the number of autophagosomes, making it a key indicator of autophagy activity. Currently, LC3 activity is traceable by using fluorescence microscopy, particularly through the employment of green fluorescent protein (GFP)-tagged LC3. This approach allows for the visual tracking of autophagy in cells by mirroring the behavior of LC3. GFP-LC3 allows the monitoring of autophagic flux by observing vacuolar delivery and cleavage of GFP-LC3. In fact, the acid-

sensitivity of GFP means that the fluorescence signal fades in the acidic environment of autophagic lysosomes, indicating the formation of the autolysosomes. Beside the GFP-LC3 reporter, the monomeric red fluorescent protein (mRFP)-GFP-LC3 double fluorescence indicator is a more complete reporter that exploits the mRFP stability in an acidic environment to assess the autophagic flux in tandem with GFP-LC3 [149,150]. In fact, the acidic environment inside the lysosome quenches the GFP fluorescent signal, having a much less effect on mRFP, giving an interpretation of merged images in which yellow puncta (i.e. RFP and GFP) indicate autophagosomes, while red puncta (i.e. RFP only) are autolysosomes. In this way, autophagic flux results are enhanced when both yellow and red puncta are increased in the cell cytoplasm; block in autophagic flux results in the increment of only yellow puncta without the enhancement of red puncta (*Fig. 12B*). Therefore, while the monitoring of autophagosomes is guided by the observation and quantification of fluorescent-tagged LC3, such in the case of GFP-LC3, the monitoring of autophagic flux can be easily assessed by tandem mRFP-GFP-LC3 reporter.

Changes in the levels of autophagy-related proteins, such as Parkin, LC3 I/II, p62 and ubiquitin, can be assessed through Western blot analysis or enzyme-linked immunosorbent assay (ELISA) for quantitative detection of various autophagy markers (*Fig. 12C*).

These methods for detecting autophagy, while diverse, have limitations and cannot fully capture the dynamic nature of autophagy, consequently it is crucial to employ a combination of these methods for a comprehensive analysis of autophagy. Developing techniques or platforms that can real-time monitor the morphological and metabolic changes in the vesicles during autophagy is therefore a significant area of ongoing research.

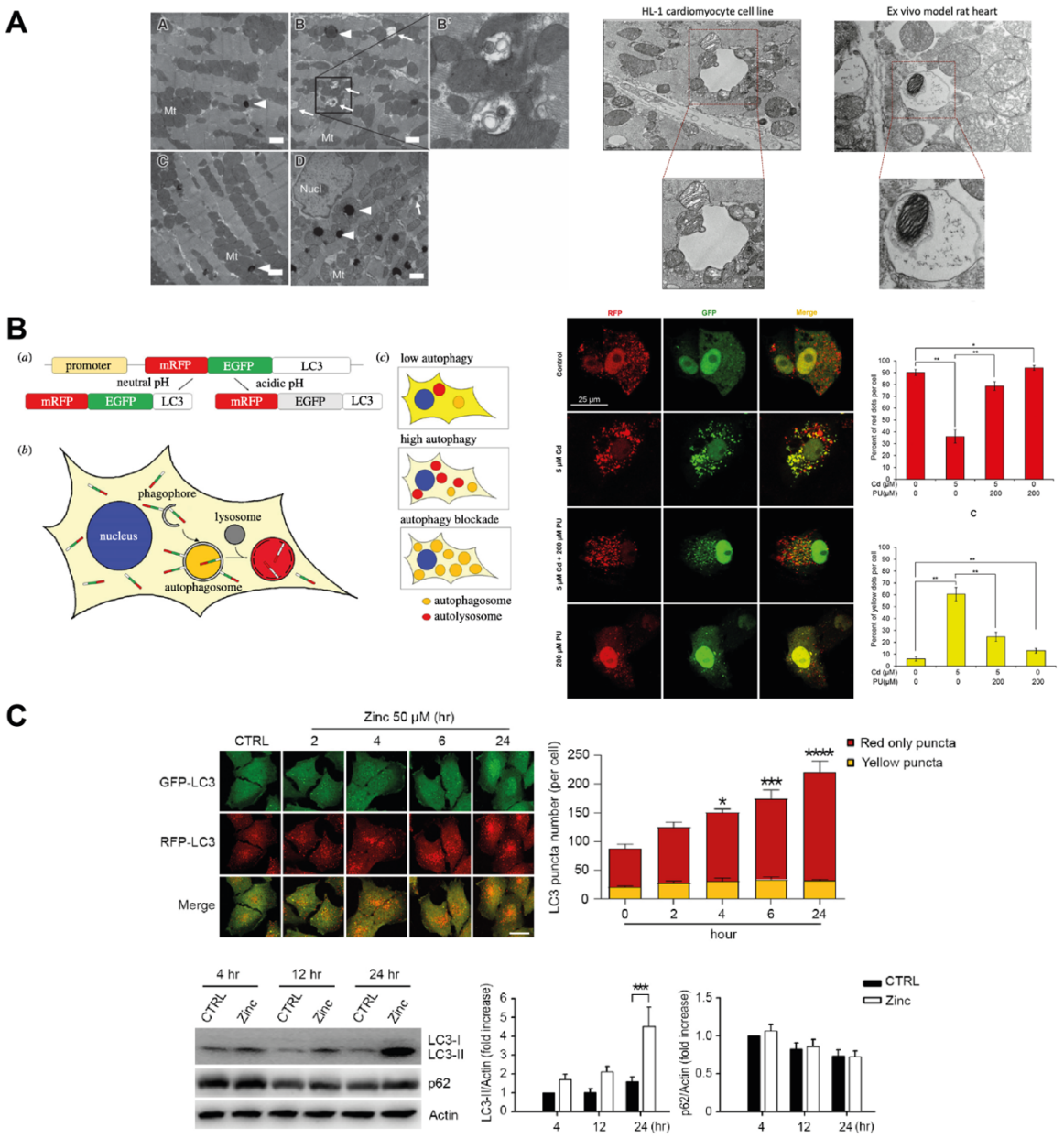

Figure 12 – Techniques for autophagy detection. A) Transmission electron microscopy (TEM) allows to detect the ultrastructure of autophagy vesicles. On the left, arrowheads and arrows indicate lysosomes (electron-dense spherical bodies) and autophagic vacuoles in treated and non-treated diabetic heart [151]. On the right, HL-1 cardiomyocyte cell subjected to ischemia and reperfusion (I/R). Mitochondria undergoing macroautophagy and micromitophagy are shown in the panel. Mitochondria directly fused with the lysosomal membrane for degradation, while mitochondrion inside a lysosome is also seen on the right, providing an example of mitophagy in an *ex vivo* model of rat myocardial infarction [152]. B) Autophagy detected by transfection with a reporter carrying GFP and mRFP working principle. GFP and mRFP coupling allows to detect autophagosomes, while the degradation of GFP and the mRFP resistance to lysosome acidic environment allows to detect autolysosomes [153]. On the right, an example of autophagic vesicles detection and quantification in mouse hepatocytes undergoing cadmium (Cd) toxicity and puerarin (PU) treatment [154]. C) Coupling of fluorescence detection and western blot to quantify the LC3 and p62 production in glioma cells exposure to zinc [155].

1.8.2.2 Microfluidic platforms for the autophagy induction in different cell types

In recent years, there is growing interest in using microfluidic platform (μP) to study autophagy-related phenomena and diseases, given the emerging benefits of μP and the increasing understanding of autophagy in physiologic and pathologic processes. While this area is still in its early stages, some investigations are already underway.

In one of the early studies in the field, an innovative microfluidic approach for conducting highly parallel immunofluorescence (IF) experiments was carried out on human fibroblasts and lysosomal storage disorders cell lines, using LAMP1 and LC3 staining [156]. This method not only economizes antibody usage but also ensures uniform experimental conditions for accurate comparisons, in a quantification accompanied by confocal imaging. The experiments focused on the response of the cells to nutrient starvation and, by using YFP-LC3 as a marker, the authors observed autophagosomes dynamics over a 7-hour period. The platform, controlled by Labview program for automatic handling of fluxes, proved efficient in reducing time intervals for acquisitions, while providing detailed data on autophagy progression. In another study, a chip was designed to analyze cancer cell-stroma interactions at a single-cell level [157]. By marking MDA-MB-231 breast cancer cells and mouse fibroblasts with a GFP-LC3 reporter, the focus of the work was on the role of autophagy in cancer-stroma communication by trapping individual tumor cells in the μP for co-culture with adjacent fibroblasts. The study assessed the role of TGF-β1 in inducing autophagy in fibroblasts in a tumor stroma microenvironment, by paracrine secretion mechanism. In groundbreaking research by Osaki et al., a 3D human motor organoid unit model was developed using MP for the study of amyotrophic lateral sclerosis (ALS) [158]. The work involved the co-culturing of motor neuron spheroids from a patient with sporadic ALS, including motor neurons and astrocytes, and muscle fiber bundles. This model simulated the human physiological environment to explore ALS pathogenesis and drug screening. By testing drugs like bosutinib and rapamycin, they observed a neuroprotective effect of the drugs, with reduced muscle contractions, less motor neuron degradation, decreased apoptosis, by enhancing motor neuron autophagy. A bioengineered model of glioblastoma was developed in a microfluidic device for eventual drug screening analysis [159]. The objectives of the work were to compare cell responses to chemotherapy in 2D cultures and in the bioengineered model, then study the role of autophagy in glioblastoma cell death and evaluate cell invasion as a metric of drug efficacy. The platform included the co-culture of cells of the tumor, stroma and vascular system. Autophagy in glioblastoma cells after treatment with TMZ and Simva was assessed using microfluidics for the introduction of the chemotherapy agents. Immunostaining for LC3

and p62 highlighted that TMZ induced autophagy, while Simva inhibited autophagic flux. Additional experiments compared chemotherapy-treated cells with and without the Atg7 gene, to study the role of autophagy in apoptosis induction, and the results showed that autophagy had a minor effect on apoptosis in this model, suggesting that autophagy is acting in parallel with apoptosis in glioblastoma cells treated with chemotherapy agents.

1.8.2.3 Microfluidic platforms for the autophagy induction in cardiovascular system applications

In cardiovascular research, understanding autophagy remains a crucial topic, as it plays an important role in cellular homeostasis and in response to external stressors. Microfluidic systems allow for high-throughput and real-time analysis, making them indispensable for investigating autophagy-related mechanisms and potential therapeutic targets in cardiac health and diseases. For instance, endothelial dysfunction is a key factor in cardiovascular diseases, often linked to ischemic conditions and nutrient deprivation, and this impairment of basal functionality is marked by reduced nitric oxide production, which represents the most important bioactive vasodilation factor. Endothelial aging, marked by diminished vasodilation and increased inflammatory factors, leads to cardiovascular diseases through reduce nitric oxide availability. Autophagy in endothelial cells, triggered by serum deprivation, helps overcome ischemic damage by breaking down cellular components for energy. In the work of Pestana et al., researchers used a microfluidic device to model endothelial response to shear stress and nutrient deprivation [160]. Metabolomic analysis revealed significant changes in metabolites under these conditions, indicating that autophagy modulation can protect endothelial energy metabolism during ischemia. In another study, the research focused on the protective role of hiPSC-derived endothelial cell-extracellular vesicles (hiPSC-EC-EV) in arterial restenosis, a complication arising during vascular reconstructive procedures [161]. hiPSC-EC-EV alleviated arterial restenosis in mice by enhancing endothelial cell functions and inhibiting apoptosis through the activation of the autophagy signaling pathway. Moreover, miR-126 in TNF-α-treated HUVECs resulted in increased levels of the autophagy marker LC3-II and a decrease in p62 expression, alongside with a suppression of mTOR. This indicates that miR-126 plays a role in restoring impaired autophagy under inflammatory conditions (*Fig. 13A*). Different studies faced the possibility to replicate 3D angiogenesis-on-a-chip, particularly Lee et al. discussed the possibility to investigate autophagic activity in endothelial cells during angiogenic sprouting [162]. Single-cell RNA sequencing analysis revealed two distinct patterns of autophagy activation in

different regions of the sprouts, potentially linked to cell proliferation control. Interestingly, autophagosomes formation was more prevalent in the basement region, while autophagosome-lysosome fusion occurred mainly in the leading position. The two autophagic modes seemed to be defined by the variations in cellular microenvironment, depending on the location on the sprout and on cellular content, alongside with exposure to damaged substances from high cell cycle activity and glycolysis. Hence, the research pointed that cells might regulate different gene sets to trigger these autophagy modes in response to their specific microenvironmental conditions (*Fig. 13B*). In heart health, it was demonstrated that basal autophagy maintains cell homeostasis and heart function, but excessive autophagy could lead to HF, particularly in hypertrophied hearts. It was also demonstrated that mechanical stress induces autophagy in CMs independently of Angiotensin II, via the AT1 receptor, and, in the same work, a stretching platform showed that p38MAP kinase pathway, but not ERK or JNK pathways, is crucial for the stress-induced autophagy (*Fig. 13C*) [163]. The mTOR signaling activation in left ventricular volume overload models, which can cause eccentric hypertrophy, was evaluated at different stages: acutely, during the compensated disease phase and at a later stage of aortic regurgitation. The study of Drolet et al. discovered that mTORC1 was activated following severe left ventricular volume overload due to aortic valve regurgitation [164]. Rapamycin, an mTORC1 inhibitor, was found to partially prevent the development of left ventricular hypertrophy during eccentric remodeling. However, prolonged treatment with rapamycin did not inhibit mTORC2. The levels of autophagy-related proteins LC3 in the left ventricle post-aortic regurgitation remained consistent, whereas LC3-I levels increased both immediately after aortic regurgitation and in later stages of the disease. Additionally, p62 levels remained stable in the initial and intermediate stages but increased in later stages of the disease. To simulate the mechanical stress experienced by CMs in severe aortic regurgitation, which causes diastolic wall stress and cell stretching, mTORC1 activation in HL-1 under biaxial cyclic mechanical stretch was simulated *in vitro*, exploiting a deformation platform for 2D culture systems (*Fig. 13D*).

These findings on the use of μPs to investigate autophagy in cardiac tissues underscore the significance of these tools in comprehending cell behavior in response to microenvironmental variations, comprising pharmacological, dietary, and mechanical insults for the cell physiology. MPs provide a controlled, precise environment for examining cellular responses, especially in cardiac tissues, in which understanding the role of autophagy in response to stressors is crucial. They offer the ability to closely mimic physiological conditions, leading to more accurate and relevant insights into autophagy's role in cardiac health and disease.

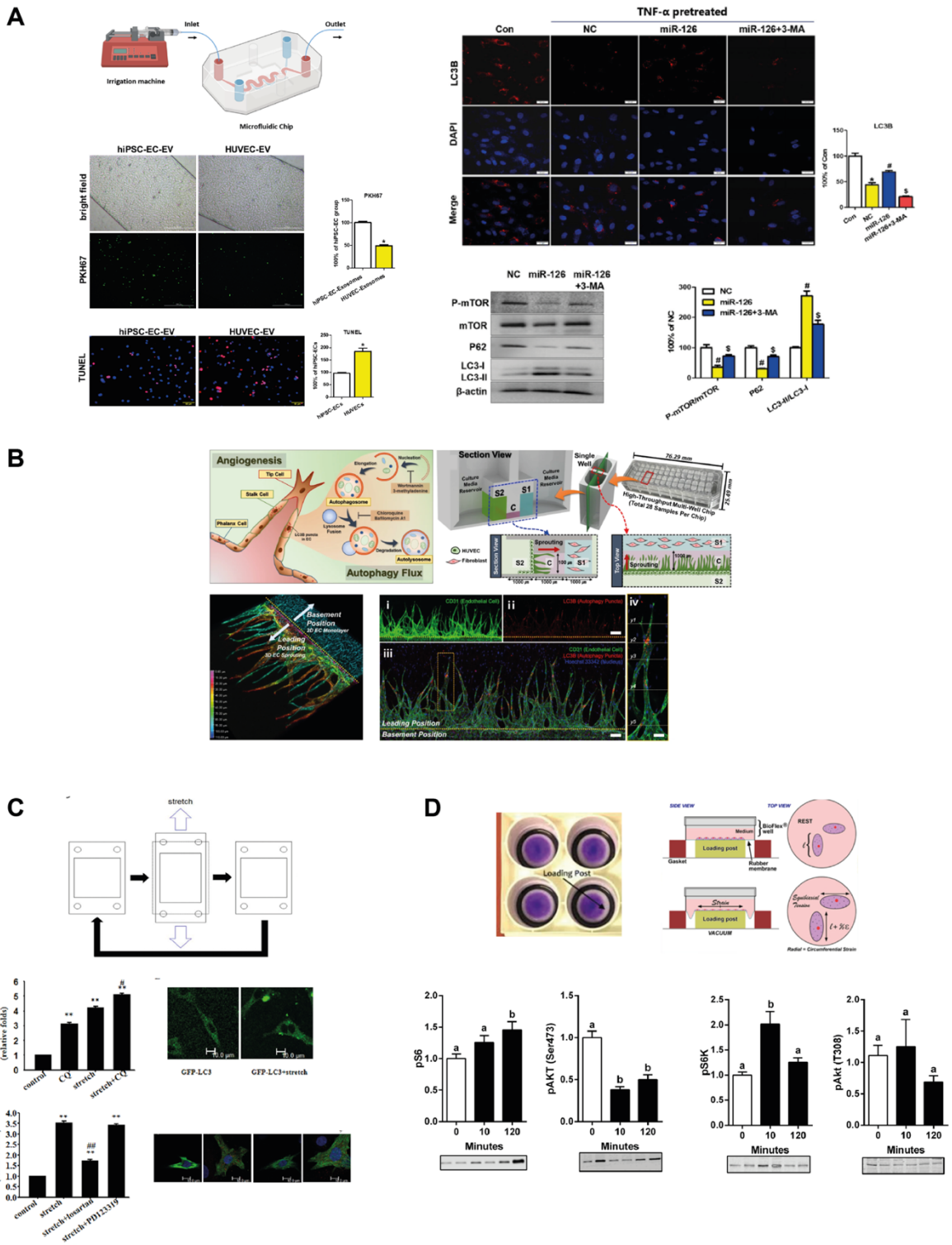

Figure 13 – Examples of the autophagy induction and analysis in μPs. A) The protective effects of human induced pluripotent stem cell-derived endothelial cell extracellular vesicles (hiPSC-EC-EV) on arterial restenosis. hiPSC-EC-EV mitigated arterial restenosis in mice by activating the autophagy signaling pathway. Additionally, in TNF-α-treated HUVECs, miR-126 led to elevated levels of the autophagy LC3-II and a reduction in p62 expression, along with inhibition of mTOR [161]. B) Lee et al. [162] identified two distinct autophagy patterns in endothelial cells during angiogenesis, with autophagosome formation prevalent at the sprout's base and autophagosome-lysosome fusion at the tip, suggesting autophagy is modulated by the

cellular microenvironment and its specific challenges. C) Mechanical stress triggers autophagy in CMs without the involvement of Angiotensin II, acting through the AT1 receptor. Additionally, it was found that the p38MAP kinase pathway plays a key role in the induction of autophagy by mechanical stress, as evidenced by experiments using a stretching platform [163]. D) Biaxially stretched CMs induced the activation of mTORC1. In the left ventricle following aortic regurgitation, the concentration of autophagy-related protein LC3 remained unchanged, while the levels of LC3-I increased both immediately after the onset of aortic regurgitation and during the disease's advanced phases. Furthermore, p62 levels were consistent in the early and middle stages of the condition but saw an elevation in the disease's later stages [164].

1.9 Aim of the work

This PhD dissertation will explore and elucidate the role of the microenvironment in controlling final state of CMs cell line. Microfluidic tools were developed and utilized to introduce a set of signals to the studied cell culture. As previously explained, the microenvironment plays a crucial role in determining the fate, behavior and health of cells. Consequently, the microenvironment can be exploited to enhance the healthy state of cells and the impact of the signals can be investigated using a tailored μP. The result will provide a set of correspondences between stimuli and cell state, aiming to build a conditioning program for the cell culture, like a training schedule. The role of the microenvironment will be unraveled by primarily utilizing microfluidic engineering tools, leading to the design of a "gym-on-a-chip" system.

The first part of the thesis will outline the approach used to build up the device, which was designed to introduce physiologically relevant stimuli found in the cardiac tissue microenvironment, such as biochemical, mechanical, and topographical signals. Various fabrication techniques were employed to achieve the isolated or combined implementation of these signals in the same platform, mimicking the native cardiac microenvironment.

Subsequently, the device was employed to characterize the response of rat CMs cell line (HL-1) to the aforementioned microenvironment signals. The cellular response was analyzed in terms of key aspects of cell behavior, including survival after nutrient feeding, alignment to topography, migration upon mechanical stimulation/topography, and Ca^{2+} handling in response to mechanical stretching/topography. The platform effectively controlled HL-1 cells by introducing these signals individually or simultaneously.

In this scenario, autophagy, a cellular degradative and recycling process, serves as a key indicator of cellular health and response to environmental cues. As autophagy naturally responds to external insults in the human body, it acts as a read-out mechanism, reflecting how cells perceive and adapt to changes in their surroundings. There is currently a gap in the literature regarding studies thoroughly exploring the direct correlation between autophagy and the state of the cell following a set of microenvironment stimuli. This gap is crucial for future research, providing deeper insights into cellular mechanisms and potential therapeutic targets, particularly in diseases where cellular microenvironments are significantly, or even pathologically, altered. Additionally, beyond known insults such as nutrient starvation, there is a lack of investigations in the literature regarding the autophagy response of cardiac cell lines to topographic signals and their combination with mechanical stretching, despite their importance for CMs physiology and performance in the cardiac tissue.

For these reasons, the response of HL-1 cardiac cells to microenvironment signals was also characterized in terms of autophagy expression. Beyond known insults, such as nutrient starvation, the role of topographic and mechanical stimulation and their combination in autophagy induction provided additional information about cell state following microenvironment alterations. The healthy state of the cells was proven by employing a live-dead assay to determine whether the introduced signals had detrimental or vital effects on the CMs cell culture.

The ability to “read” cell health through autophagy highlights the importance of understanding cellular responses to environmental factors and provides a valuable tool for health preservation and lifespan enhancement by developing therapies and drugs tailored based on the epigenetic expression of cellular processes.

References

1. Bonasio, R., Tu, S. & Reinberg, D. Molecular signals of epigenetic states. Science vol. 330 Preprint at https://doi.org/10.1126/science.1191078 (2010).
2. Nicholl, D. An Introduction to Genetic Engineering. (Cambridge University Press, 2012).
3. Mazzio, E. A. & Soliman, K. F. A. Basic concepts of epigenetics impact of environmental signals on gene expression. Epigenetics vol. 7 Preprint at https://doi.org/10.4161/epi.7.2.18764 (2012).
4. Halušková, J. Epigenetic Studies in Human Diseases (Epigenetics / Human Diseases / Methylation / Histone Acetylation / miRNA / Cancer). Folia Biologica (Praha) vol. 56 (2010).
5. Kanherkar, R. R., Bhatia-Dey, N. & Csoka, A. B. Epigenetics across the human lifespan. Frontiers in Cell and Developmental Biology vol. 2 Preprint at https://doi.org/10.3389/fcell.2014.00049 (2014).
6. Basu, A. & Tiwari, V. K. Epigenetic reprogramming of cell identity: lessons from development for regenerative medicine. Clinical Epigenetics vol. 13 Preprint at https://doi.org/10.1186/s13148-021-01131-4 (2021).
7. Alegría-Torres, J. A., Baccarelli, A. & Bollati, V. Epigenetics and lifestyle. Epigenomics vol. 3 Preprint at https://doi.org/10.2217/epi.11.22 (2011).
8. Heijmans, B. T. et al. Persistent Epigenetic Differences Associated with Prenatal Exposure to Famine in Humans. www.pnas.orgcgidoi10.1073pnas.0806560105 (2008).
9. Tiffon, C. Molecular Sciences The Impact of Nutrition and Environmental Epigenetics on Human Health and Disease. doi:10.3390/ijms19113425.
10. Ford, D., Ions, L. J., Alatawi, F. & Wakeling, L. A. The potential role of epigenetic responses to diet in ageing. doi:10.1017/S0029665111000851.
11. Rö Nn, T. et al. A Six Months Exercise Intervention Influences the Genome-wide DNA Methylation Pattern in Human Adipose Tissue. (2013) doi:10.1371/journal.pgen.1003572.
12. Nitert, M. D. et al. Impact of an Exercise Intervention on DNA Methylation in Skeletal Muscle From First-Degree Relatives of Patients With Type 2 Diabetes. doi:10.2337/db11-1653.
13. Plaza-Diaz, J. et al. Impact of Physical Activity and Exercise on the Epigenome in Skeletal Muscle and Effects on Systemic Metabolism. (2022) doi:10.3390/biomedicines10010126.
14. Baccarelli, A. & Bollati, V. Epigenetics and Environmental Chemicals.

15. Baccarelli, A. et al. Rapid DNA Methylation Changes after Exposure to Traffic Particles. doi:10.1164/rccm.200807-1097OC.

16. Yuan, M. et al. Epigenetic regulation in major depression and other stress-related disorders: molecular mechanisms, clinical relevance and therapeutic potential. doi:10.1038/s41392-023-01519-z.

17. Huang, G. et al. Functional and Biomimetic Materials for Engineering of the Three-Dimensional Cell Microenvironment. Chemical Reviews vol. 117 Preprint at https://doi.org/10.1021/acs.chemrev.7b00094 (2017).

18. Lin, X., Patil, S., Gao, Y.-G. & Qian, A. The Bone Extracellular Matrix in Bone Formation and Regeneration. doi:10.3389/fphar.2020.00757.

19. Kechagia, J. Z., Ivaska, J. & Roca-Cusachs, P. Integrins as biomechanical sensors of the microenvironment. Nat Rev Mol Cell Biol doi:10.1038/s41580-019-0134-2.

20. Leight, J. L., Wozniak, M. A., Chen, S., Lynch, M. L. & Chen, C. S. Matrix rigidity regulates a switch between TGF-β1-induced apoptosis and epithelial-mesenchymal transition. 23, (2012).

21. Kubiczkova, L., Sedlarikova, L., Hajek, R. & Sevcikova, S. TGF-β-an Excellent Servant but a Bad Master. http://www.translational-medicine.com/content/10/1/183 (2012).

22. Migliorini, E., Guevara-Garcia, A., Albiges-Rizo, C. & Picart, C. Learning from BMPs and their biophysical extracellular matrix microenvironment for biomaterial design. Bone vol. 141 Preprint at https://doi.org/10.1016/j.bone.2020.115540 (2020).

23. Zhu, J. & Clark, R. A. F. Fibronectin at select sites binds multiple growth factors and enhances their activity: Expansion of the collaborative ECM-GF paradigm. Journal of Investigative Dermatology vol. 134 895–901 Preprint at https://doi.org/10.1038/jid.2013.484 (2014).

24. Riching, K. M. et al. 3D collagen alignment limits protrusions to enhance breast cancer cell persistence. Biophys J 107, 2546–2558 (2015).

25. Chaubaroux, C. et al. Cell Alignment Driven by Mechanically Induced Collagen Fiber Alignment in Collagen/Alginate Coatings. Tissue Eng Part C Methods 21, 881–888 (2015).

26. Yim, E. K. F., Darling, E. M., Kulangara, K., Guilak, F. & Leong, K. W. Nanotopography-induced changes in focal adhesions, cytoskeletal organization, and mechanical properties of human mesenchymal stem cells. Biomaterials 31, 1299–1306 (2010).

27. Carthew, J. et al. Precision Surface Microtopography Regulates Cell Fate via Changes to Actomyosin Contractility and Nuclear Architecture. (2021) doi:10.1002/advs.202003186.

28. Wang, X., Nyman, J. S., Dong, X., Leng, H. & Reyes, M. Fundamental Biomechanics in Bone Tissue Engineering. (Springer International Publishing, Cham, 2010). doi:10.1007/978-3-031-02579-2.

29. Singh, G. & Chanda, A. Mechanical properties of whole-body soft human tissues: A review. Biomedical Materials (Bristol) vol. 16 Preprint at https://doi.org/10.1088/1748-605X/ac2b7a (2021).

30. Espina, J. A., Marchant, C. L. & Barriga, E. H. Durotaxis: the mechanical control of directed cell migration. doi:10.1111/febs.15862.

31. Substrate stiffness regulates cadherin-dependent collective migration through myosin-II contractility.

32. science.aaf7119.

33. Rita Cantelmo, A. et al. Endothelial Cell Orientation and Polarity Are Controlled by Shear Stress and VEGF Through Distinct Signaling Pathways. (2021) doi:10.3389/fphys.2020.623769.

34. Pagani, S. et al. Uniaxial Cyclic Stretching Promotes Chromatin Accessibility of Gene Loci Associated With Mesenchymal Stem Cells Morphogenesis and Osteogenesis. Frontiers in Cell and Developmental Biology | www.frontiersin.org 1, 664545 (2021).

35. Zhang, J. et al. Electrically Guiding Migration of Human Induced Pluripotent Stem Cells. (2011) doi:10.1007/s12015-011-9247-5.

36. Hernández, D. et al. Electrical Stimulation Promotes Cardiac Differentiation of Human Induced Pluripotent Stem Cells. (2016) doi:10.1155/2016/1718041.

37. Glick, D., Barth, S., Macleod, K. F. & May, B. Autophagy: cellular and molecular mechanisms What is autophagy? INVITED REVIEW Journal of Pathology J Pathol 221, 3–12 (2010).

38. Parzych, K. R. & Klionsky, D. J. An overview of autophagy: Morphology, mechanism, and regulation. Antioxidants and Redox Signaling vol. 20 460–473 Preprint at https://doi.org/10.1089/ars.2013.5371 (2014).

39. Hollenstein, D. M. & Kraft, C. Autophagosomes are formed at a distinct cellular structure. Current Opinion in Cell Biology vol. 65 50–57 Preprint at https://doi.org/10.1016/j.ceb.2020.02.012 (2020).

40. Pattingre, S. et al. Bcl-2 antiapoptotic proteins inhibit Beclin 1-dependent autophagy. Cell 122, 927–939 (2005).

41. Jin, L. et al. YAP inhibits autophagy and promotes progression of colorectal cancer via upregulating Bcl-2 expression. Cell Death Dis 12, 457 (2021).

42. Orii, M., Tsuji, T., Ogasawara, Y. & Fujimoto, T. Transmembrane phospholipid translocation mediated by Atg9 is involved in autophagosome formation. Journal of Cell Biology 220, (2020).

43. Klionsky, D. J. & Eskelinen, E. L. The vacuole versus the lysosome: When size matters. Autophagy vol. 10 185–187 Preprint at https://doi.org/10.4161/auto.27367 (2014).

44. Lőrincz, P. & Juhász, G. Autophagosome-Lysosome Fusion. Journal of Molecular Biology vol. 432 2462–2482 Preprint at https://doi.org/10.1016/j.jmb.2019.10.028 (2020).

45. Dikic, I. & Elazar, Z. Mechanism and medical implications of mammalian autophagy. (2018) doi:10.1038/s41580-018-0003-4.

46. Al-Bari, Md. A. A. et al. Targeting Autophagy with Natural Products as a Potential Therapeutic Approach for Cancer. Int J Mol Sci 22, 9807 (2021).

47. Festuccia, W. T. et al. MINI REVIEW The mTOR-Autophagy Axis and the Control of Metabolism. (2021) doi:10.3389/fcell.2021.655731.

48. Zhou, B. et al. Mitochondrial Permeability Uncouples Elevated Autophagy and Lifespan Extension. Cell 177, 299-314.e16 (2019).

49. Deleyto-Seldas, N. & Efeyan, A. The mTOR–Autophagy Axis and the Control of Metabolism. Front Cell Dev Biol 9, (2021).

50. Ren, H., Zhai, W., Lu, X. & Wang, G. The Cross-Links of Endoplasmic Reticulum Stress, Autophagy, and Neurodegeneration in Parkinson's Disease. Front Aging Neurosci 13, (2021).

51. Karabiyik, C., Lee, M. J. & Rubinsztein, D. C. Autophagy impairment in Parkinson's disease. Essays Biochem 61, 711–720 (2017).

52. Costa, C. A. da, Manaa, W. El, Duplan, E. & Checler, F. The Endoplasmic Reticulum Stress/Unfolded Protein Response and Their Contributions to Parkinson's Disease Physiopathology. Cells 9, 2495 (2020).

53. Daskalaki, I., Gkikas, I. & Tavernarakis, N. Hypoxia and Selective Autophagy in Cancer Development and Therapy. Front Cell Dev Biol 6, (2018).

54. Zaarour, R. F. et al. Role of Hypoxia-Mediated Autophagy in Tumor Cell Death and Survival. Cancers (Basel) 13, 533 (2021).

55. Mazure, N. M. & Pouysségur, J. Hypoxia-induced autophagy: cell death or cell survival? Curr Opin Cell Biol 22, 177–180 (2010).

56. Sukumaran, P. et al. Calcium Signaling Regulates Autophagy and Apoptosis. Cells 10, 2125 (2021).

57. Bootman, M. D., Chehab, T., Bultynck, G., Parys, J. B. & Rietdorf, K. The regulation of autophagy by calcium signals: Do we have a consensus? Cell Calcium 70, 32–46 (2018).
58. Rubinsztein, D. C., Codogno, P. & Levine, B. Autophagy modulation as a potential therapeutic target for diverse diseases. Nat Rev Drug Discov 11, 709–730 (2012).
59. Rana, T. et al. Exploring the Role of Autophagy Dysfunction in Neurodegenerative Disorders. Mol Neurobiol 58, 4886–4905 (2021).
60. Lu, R., Zhang, L. & Yang, X. Interaction between autophagy and the NLRP3 inflammasome in Alzheimer's and Parkinson's disease. Front Aging Neurosci 14, (2022).
61. Zhu, R., Luo, Y., Li, S. & Wang, Z. The role of microglial autophagy in Parkinson's disease. Front Aging Neurosci 14, (2022).
62. Mulcahy Levy, J. M. & Thorburn, A. Autophagy in cancer: moving from understanding mechanism to improving therapy responses in patients. Cell Death Differ 27, 843–857 (2020).
63. Debnath, J., Gammoh, N. & Ryan, K. M. Autophagy and autophagy-related pathways in cancer. Nat Rev Mol Cell Biol 24, 560–575 (2023).
64. Pang, Y., Wu, L., Tang, C., Wang, H. & Wei, Y. Autophagy-Inflammation Interplay During Infection: Balancing Pathogen Clearance and Host Inflammation. doi:10.3389/fphar.2022.832750.
65. Liang, S., Wu, Y.-S., Li, D.-Y., Tang, J.-X. & Liu, H.-F. Autophagy in Viral Infection and Pathogenesis. Front Cell Dev Biol 9, (2021).
66. Jiang, B. et al. The role of autophagy in cardiovascular disease: Cross-interference of signaling pathways and underlying therapeutic targets. Front Cardiovasc Med 10, (2023).
67. Bielawska, M., Warszyńska, M., Stefańska, M. & Błyszczuk, P. Autophagy in Heart Failure: Insights into Mechanisms and Therapeutic Implications. J Cardiovasc Dev Dis 10, 352 (2023).
68. Oka, T. et al. Mitochondrial DNA that escapes from autophagy causes inflammation and heart failure. Nature 485, 251–255 (2012).
69. De Meyer, G. R. Y., De Keulenaer, G. W. & Martinet, W. Role of autophagy in heart failure associated with aging. Heart Fail Rev 15, 423–430 (2010).
70. Canale, E. D., Campbell, G. R., Smolich, J. J. & Campbell, J. H. Cardiac Muscle. (Springer Berlin Heidelberg, Berlin, Heidelberg, 1986). doi:10.1007/978-3-642-50115-9.
71. Odedra, D. et al. Cardiac Tissue Engineering. in Biomaterials for Tissue Engineering Applications 421–456 (Springer Vienna, Vienna, 2011). doi:10.1007/978-3-7091-0385-2_15.
72. Medical gallery of Blausen Medical 2014. WikiJournal of Medicine 1, (2014).

73. Burbaum, L. et al. Molecular-scale visualization of sarcomere contraction within native cardiomyocytes. Nat Commun 12, 4086 (2021).
74. Hamledari, H. et al. Using human induced pluripotent stem cell-derived cardiomyocytes to understand the mechanisms driving cardiomyocyte maturation. Front Cardiovasc Med 9, (2022).
75. Manabe, I., Shindo, T. & Nagai, R. Gene Expression in Fibroblasts and Fibrosis. Circ Res 91, 1103–1113 (2002).
76. Parker, K. K. & Ingber, D. E. Extracellular matrix, mechanotransduction and structural hierarchies in heart tissue engineering. Philosophical Transactions of the Royal Society B: Biological Sciences 362, 1267–1279 (2007).
77. Toole, B. P. Hyaluronan in morphogenesis. Semin Cell Dev Biol 12, 79–87 (2001).
78. Sun, J. et al. hapln1 Defines an Epicardial Cell Subpopulation Required for Cardiomyocyte Expansion During Heart Morphogenesis and Regeneration. Circulation 146, 48–63 (2022).
79. Schenke-Layland, K. et al. Reprogrammed Mouse Fibroblasts Differentiate into Cells of the Cardiovascular and Hematopoietic Lineages. Stem Cells 26, 1537–1546 (2008).
80. Noh, K. M., Park, S.-J., Moon, S.-H. & Jung, S. Y. Extracellular matrix cues regulate the differentiation of pluripotent stem cell-derived endothelial cells. Front Cardiovasc Med 10, (2023).
81. Yamashita, J. et al. Flk1-positive cells derived from embryonic stem cells serve as vascular progenitors. Nature 408, 92–96 (2000).
82. Zeng, D. et al. Collagen/β1 integrin interaction is required for embryoid body formation during cardiogenesis from murine induced pluripotent stem cells. BMC Cell Biol 14, 5 (2013).
83. Park, J. H., Ryu, J. M. & Han, H. J. Involvement of caveolin-1 in fibronectin-induced mouse embryonic stem cell proliferation: Role of FAK, RhoA, PI3K/Akt, and ERK 1/2 pathways. J Cell Physiol 226, 267–275 (2011).
84. Easley, C. A. et al. Laminin activates CaMK-II to stabilize nascent embryonic axons. Brain Res 1092, 59–68 (2006).
85. Khan, S., Downing, K. H. & Molloy, J. E. Architectural Dynamics of CaMKII-Actin Networks. Biophys J 116, 104–119 (2019).
86. Lin, Y.-C. & Redmond, L. CaMKIIβ binding to stable F-actin in vivo regulates F-actin filament stability. Proceedings of the National Academy of Sciences 105, 15791–15796 (2008).
87. Dobaczewski, M., Chen, W. & Frangogiannis, N. G. Transforming growth factor (TGF)-β signaling in cardiac remodeling. J Mol Cell Cardiol 51, 600–606 (2011).

88. Carson, D. et al. Nanotopography-Induced Structural Anisotropy and Sarcomere Development in Human Cardiomyocytes Derived from Induced Pluripotent Stem Cells. ACS Appl Mater Interfaces 8, 21923–21932 (2016).
89. Lundy, S. D., Zhu, W.-Z., Regnier, M. & Laflamme, M. A. Structural and Functional Maturation of Cardiomyocytes Derived from Human Pluripotent Stem Cells. Stem Cells Dev 22, 1991–2002 (2013).
90. Castilho, M. et al. Melt Electrowriting Allows Tailored Microstructural and Mechanical Design of Scaffolds to Advance Functional Human Myocardial Tissue Formation. Adv Funct Mater 28, (2018).
91. Tsui, J. H. et al. Conductive silk–polypyrrole composite scaffolds with bioinspired nanotopographic cues for cardiac tissue engineering. J Mater Chem B 6, 7185–7196 (2018).
92. Allen, A. C. B. et al. Temporal Impact of Substrate Anisotropy on Differentiating Cardiomyocyte Alignment and Functionality. Tissue Eng Part A 25, 1426–1437 (2019).
93. Li, J. et al. Human Pluripotent Stem Cell-Derived Cardiac Tissue-like Constructs for Repairing the Infarcted Myocardium. Stem Cell Reports 9, 1546–1559 (2017).
94. Zhu, C. et al. Increased Cardiomyocyte Alignment and Intracellular Calcium Transients Using Micropatterned and Drug-Releasing Poly(Glycerol Sebacate) Elastomers. ACS Biomater Sci Eng 4, 2494–2504 (2018).
95. Oyunbaatar, N.-E., Lee, D.-H., Patil, S., Kim, E.-S. & Lee, D.-W. Biomechanical Characterization of Cardiomyocyte Using PDMS Pillar with Microgrooves. Sensors 16, 1258 (2016).
96. Castilho, M. et al. Melt Electrowriting Allows Tailored Microstructural and Mechanical Design of Scaffolds to Advance Functional Human Myocardial Tissue Formation. Adv Funct Mater 28, (2018).
97. Ahn, H. et al. Hierarchical Topography with Tunable Micro-and Nanoarchitectonics for Highly Enhanced Cardiomyocyte Maturation via Multi-Scale Mechanotransduction. (2023) doi:10.1002/adhm.202202371.
98. Tsui, J. H. et al. Conductive silk–polypyrrole composite scaffolds with bioinspired nanotopographic cues for cardiac tissue engineering. J Mater Chem B 6, 7185–7196 (2018).
99. LAMMERDING, J., KAMM, R. D. & LEE, R. T. Mechanotransduction in Cardiac Myocytes. Ann N Y Acad Sci 1015, 53–70 (2004).
100. Sun, Z., Costell, M. & Fässler, R. Integrin activation by talin, kindlin and mechanical forces. Nat Cell Biol 21, 25–31 (2019).

101. Liao, H. et al. Mechanotranduction Pathways in the Regulation of Mitochondrial Homeostasis in Cardiomyocytes. Front Cell Dev Biol 8, (2021).
102. Hao Feng, D. E. D. Mechanosensing and Regulation of Cardiac Function. J Clin Exp Cardiolog 05, (2014).
103. Panciera, T., Azzolin, L., Cordenonsi, M. & Piccolo, S. Mechanobiology of YAP and TAZ in physiology and disease. Nat Rev Mol Cell Biol 18, 758–770 (2017).
104. Cai, X., Wang, K.-C. & Meng, Z. Mechanoregulation of YAP and TAZ in Cellular Homeostasis and Disease Progression. Front Cell Dev Biol 9, (2021).
105. Dupont, S. et al. Role of YAP/TAZ in mechanotransduction. Nature 474, 179–183 (2011).
106. Zhang, C. et al. Regulation of Hippo Signaling by Mechanical Signals and the Cytoskeleton. DNA Cell Biol 39, 159–166 (2020).
107. Driscoll, T. P., Cosgrove, B. D., Heo, S.-J., Shurden, Z. E. & Mauck, R. L. Cytoskeletal to Nuclear Strain Transfer Regulates YAP Signaling in Mesenchymal Stem Cells. Biophys J 108, 2783–2793 (2015).
108. Codelia, V. A., Sun, G. & Irvine, K. D. Regulation of YAP by Mechanical Strain through Jnk and Hippo Signaling. Current Biology 24, 2012–2017 (2014).
109. Byun, J. et al. Yes-associated protein (YAP) mediates adaptive cardiac hypertrophy in response to pressure overload. Journal of Biological Chemistry 294, 3603–3617 (2019).
110. Aragona, M. et al. A Mechanical Checkpoint Controls Multicellular Growth through YAP/TAZ Regulation by Actin-Processing Factors. Cell 154, 1047–1059 (2013).
111. Elosegui-Artola, A. et al. Force Triggers YAP Nuclear Entry by Regulating Transport across Nuclear Pores. Cell 171, 1397-1410.e14 (2017).
112. Yamashiro, Y. et al. Matrix mechanotransduction mediated by thrombospondin-1/integrin/YAP in the vascular remodeling. Proceedings of the National Academy of Sciences 117, 9896–9905 (2020).
113. Song, M., Jang, Y., Kim, S.-J. & Park, Y. Cyclic Stretching Induces Maturation of Human-Induced Pluripotent Stem Cell-Derived Cardiomyocytes through Nuclear-Mechanotransduction. Tissue Eng Regen Med 19, 781–792 (2022).
114. Thavandiran, N. et al. Design and formulation of functional pluripotent stem cell-derived cardiac microtissues. Proceedings of the National Academy of Sciences 110, (2013).
115. Sidorov, V. Y. et al. I-Wire Heart-on-a-Chip I: Three-dimensional cardiac tissue constructs for physiology and pharmacology. Acta Biomater 48, 68–78 (2017).

116. Zhao, Y. et al. A Platform for Generation of Chamber-Specific Cardiac Tissues and Disease Modeling. Cell 176, 913-927.e18 (2019).
117. Li, Z. & Guan, J. Hydrogels for Cardiac Tissue Engineering. Polymers (Basel) 3, 740–761 (2011).
118. Kupfer, M. E. et al. In Situ Expansion, Differentiation, and Electromechanical Coupling of Human Cardiac Muscle in a 3D Bioprinted, Chambered Organoid. Circ Res 127, 207–224 (2020).
119. Shin, S. R. et al. Reduced Graphene Oxide-GelMA Hybrid Hydrogels as Scaffolds for Cardiac Tissue Engineering. Small 12, 3677–3689 (2016).
120. Agarwal, A. et al. Micropatterning Alginate Substrates for In Vitro Cardiovascular Muscle on a Chip. Adv Funct Mater 23, 3738–3746 (2013).
121. Testore, D., Zoso, A., Kortaberria, G., Sangermano, M. & Chiono, V. Electroconductive Photo-Curable PEGDA-Gelatin/PEDOT:PSS Hydrogels for Prospective Cardiac Tissue Engineering Application. Front Bioeng Biotechnol 10, (2022).
122. Wang, Z. et al. 3D bioprinting in cardiac tissue engineering. Theranostics 11, 7948–7969 (2021).
123. Sackmann, E. K., Fulton, A. L. & Beebe, D. J. The present and future role of microfluidics in biomedical research. Nature 507, 181–189 (2014).
124. Rexius-Hall, M. L. et al. A myocardial infarct border-zone-on-a-chip demonstrates distinct regulation of cardiac tissue function by an oxygen gradient. Sci Adv 8, (2022).
125. Liu, H. et al. Heart-on-a-Chip Model with Integrated Extra- and Intracellular Bioelectronics for Monitoring Cardiac Electrophysiology under Acute Hypoxia. Nano Lett 20, 2585–2593 (2020).
126. Nunes, S. S. et al. Biowire: a platform for maturation of human pluripotent stem cell–derived cardiomyocytes. Nat Methods 10, 781–787 (2013).
127. Ren, L. et al. Combined Effects of Electric Stimulation and Microgrooves in Cardiac Tissue-on-a-Chip for Drug Screening. Small Methods 4, (2020).
128. Zimmermann, W.-H. et al. Tissue Engineering of a Differentiated Cardiac Muscle Construct. Circ Res 90, 223–230 (2002).
129. Pavesi, A. et al. Controlled electromechanical cell stimulation on-a-chip. Sci Rep 5, 11800 (2015).
130. Kuma, A. et al. The role of autophagy during the early neonatal starvation period. Nature 432, 1032–1036 (2004).

131. Kanamori, H. et al. Functional Significance and Morphological Characterization of Starvation-Induced Autophagy in the Adult Heart. Am J Pathol 174, 1705–1714 (2009).
132. Maruyama, R. et al. Morphological and biochemical characterization of basal and starvation-induced autophagy in isolated adult rat cardiomyocytes. American Journal of Physiology-Heart and Circulatory Physiology 295, H1599–H1607 (2008).
133. Kawaguchi, T. et al. Prior starvation mitigates acute doxorubicin cardiotoxicity through restoration of autophagy in affected cardiomyocytes. Cardiovasc Res 96, 456–465 (2012).
134. Ma, S., Wang, Y., Chen, Y. & Cao, F. The role of the autophagy in myocardial ischemia/reperfusion injury. Biochimica et Biophysica Acta (BBA) - Molecular Basis of Disease 1852, 271–276 (2015).
135. Hamacher-Brady, A., Brady, N. R. & Gottlieb, R. A. Enhancing Macroautophagy Protects against Ischemia/Reperfusion Injury in Cardiac Myocytes. Journal of Biological Chemistry 281, 29776–29787 (2006).
136. Vion, A.-C. et al. Autophagy is required for endothelial cell alignment and atheroprotection under physiological blood flow. Proceedings of the National Academy of Sciences 114, (2017).
137. Santovito, D. et al. Noncanonical inhibition of caspase-3 by a nuclear microRNA confers endothelial protection by autophagy in atherosclerosis. Sci Transl Med 12, (2020).
138. Lo Verso, F., Carnio, S., Vainshtein, A. & Sandri, M. Autophagy is not required to sustain exercise and PRKAA1/AMPK activity but is important to prevent mitochondrial damage during physical activity. Autophagy 10, 1883–1894 (2014).
139. Lin, L. et al. High-density lipoprotein inhibits mechanical stress-induced cardiomyocyte autophagy and cardiac hypertrophy through angiotensin II type 1 receptor-mediated PI3K/Akt pathway. J Cell Mol Med 19, 1929–1938 (2015).
140. Lin, L. et al. Mechanical Stress Triggers Cardiomyocyte Autophagy through Angiotensin II Type 1 Receptor-Mediated p38MAP Kinase Independently of Angiotensin II. PLoS One 9, e89629 (2014).
141. Kanamori, H. et al. The role of autophagy emerging in postinfarction cardiac remodelling. Cardiovasc Res 91, 330–339 (2011).
142. Nakai, A. et al. The role of autophagy in cardiomyocytes in the basal state and in response to hemodynamic stress. Nat Med 13, 619–624 (2007).
143. Matsui, Y. et al. Distinct Roles of Autophagy in the Heart During Ischemia and Reperfusion. Circ Res 100, 914–922 (2007).

144. McMullen, J. R. et al. Inhibition of mTOR Signaling With Rapamycin Regresses Established Cardiac Hypertrophy Induced by Pressure Overload. Circulation 109, 3050–3055 (2004).
145. HA, T. et al. Attenuation of cardiac hypertrophy by inhibiting both mTOR and NFκB activation in vivo. Free Radic Biol Med 39, 1570–1580 (2005).
146. Takemura, G. et al. Autophagic Degeneration and Death of Cardiomyocytes in Heart Failure. Autophagy 2, 212–214 (2006).
147. Gao, W. et al. Inhibiting Receptor of Advanced Glycation End Products Attenuates Pressure Overload-Induced Cardiac Dysfunction by Preventing Excessive Autophagy. Front Physiol 9, (2018).
148. Eskelinen, E.-L., Reggiori, F., Baba, M., Kovács, A. L. & Seglen, P. O. Seeing is believing: The impact of electron microscopy on autophagy research. Autophagy 7, 935–956 (2011).
149. Zhou, C. et al. Monitoring autophagic flux by an improved tandem fluorescent-tagged LC3 (mTagRFP-mWasabi-LC3) reveals that high-dose rapamycin impairs autophagic flux in cancer cells. Autophagy 8, 1215–1226 (2012).
150. Kimura, S., Noda, T. & Yoshimori, T. Dissection of the Autophagosome Maturation Process by a Novel Reporter Protein, Tandem Fluorescent-Tagged LC3. Autophagy 3, 452–460 (2007).
151. Kanamori, H. et al. Autophagic adaptations in diabetic cardiomyopathy differ between type 1 and type 2 diabetes. Autophagy 11, 1146–1160 (2015).
152. Disatnik, M.-H., Hwang, S., Ferreira, J. C. B. & Mochly-Rosen, D. New therapeutics to modulate mitochondrial dynamics and mitophagy in cardiac diseases. J Mol Med 93, 279–287 (2015).
153. Lopez, A., Fleming, A. & Rubinsztein, D. C. Seeing is believing: methods to monitor vertebrate autophagy in vivo. Open Biol 8, (2018).
154. Zhou, X.-L., Wan, X.-M., Fu, X.-X. & Xie, C.-G. Puerarin prevents cadmium-induced hepatic cell damage by suppressing apoptosis and restoring autophagic flux. Biomedicine & Pharmacotherapy 115, 108929 (2019).
155. Kim, K.-R. et al. Zinc enhances autophagic flux and lysosomal function through transcription factor EB activation and V-ATPase assembly. Front Cell Neurosci 16, (2022).
156. Shen, J. et al. An integrated chip for immunofluorescence and its application to analyze lysosomal storage disorders. Lab Chip 12, 317–324 (2012).

157. Karakas, H. E. et al. A microfluidic chip for screening individual cancer cells via eavesdropping on autophagy-inducing crosstalk in the stroma niche. Sci Rep 7, 2050 (2017).
158. Osaki, T., Uzel, S. G. M. & Kamm, R. D. Microphysiological 3D model of amyotrophic lateral sclerosis (ALS) from human iPS-derived muscle cells and optogenetic motor neurons. Sci Adv 4, (2018).
159. Samiei, E., Seyfoori, A., Toyota, B., Ghavami, S. & Akbari, M. Investigating Programmed Cell Death and Tumor Invasion in a Three-Dimensional (3D) Microfluidic Model of Glioblastoma. Int J Mol Sci 21, 3162 (2020).
160. Pestana, C. R., Urbaczek, A. C., Alberici, J. V., Rodrigues, G. J. & Carrilho, E. Metabolic profiling of human endothelial cells during autophagy assessed in a biomimetic microfluidic device model. Life Sci 172, 42–47 (2017).
161. He, Y. et al. Extracellular vesicles produced by human-induced pluripotent stem cell-derived endothelial cells can prevent arterial stenosis in mice via autophagy regulation. Front Cardiovasc Med 9, (2022).
162. Lee, S. et al. Angiogenesis-on-a-chip coupled with single-cell RNA sequencing reveals spatially differential activations of autophagy along angiogenic sprouts. Nat Commun 15, 230 (2024).
163. Lin, L., Tang, C., Xu, J., Ye, Y. & Weng, L. Mechanical Stress Triggers Cardiomyocyte Autophagy through Angiotensin II Type 1 Receptor-Mediated p38MAP Kinase Independently of Angiotensin II. PLoS One 9, 89629 (2014).
164. Drolet, M.-C. et al. Blockade of the acute activation of mTOR complex 1 decreases hypertrophy development in rats with severe aortic valve regurgitation. Springerplus 4, 435 (2015).

Chapter 2:
Microfluidic platform for the microenvironment cues introduction

2.1 Introduction

The study of microfluidics has revolutionized the field of cell culture, offering precise control over the microenvironment that cells are exposed to, thereby significantly influencing their behavior. This control is crucial for deeply understanding cellular mechanisms, drug screening, tissue engineering, and regenerative medicine. Microfluidic devices allow to create well-defined microenvironments that can mimic the *in vivo* conditions that cells naturally experience, providing insights into cellular responses to various stimuli. These devices facilitate the delivery of nutrients, waste removal and application of mechanical forces or chemical gradients, closely replicating the dynamic conditions of the human body.

At the heart of microfluidic device fabrication is the technique of photolithography, a process that plays a pivotal role in patterning substrates to guide cell alignment, among other functionalities. Photolithography, traditionally used in semiconductor manufacturing, has been also used for the creation of microfluidic channels and structures. This technique involves exposing a light-sensitive polymer, or photoresist, to ultraviolet (UV) light through a mask that defines the desired pattern. The exposed areas of the photoresist become soluble (in the case of positive photoresist) or insoluble (in the case of negative photoresist) to a developer solution, allowing for the creation of intricate patterns with high precision. The ability to pattern substrates using photolithography has profound implications for cell culture studies. It enables the design of surfaces with specific geometries and topographies that can direct cell growth, orientation, and differentiation. For instance, by patterning substrates to mimic the ECM or specific tissue architectures, researchers can guide cell alignment, a crucial factor for tissues that require highly organized cell arrangements, such as cardiac and skeletal muscle tissues. Moreover, photolithography's versatility allows for the integration of multiple processes within a single device, enabling the study of complex cell behaviors in response to multifaceted stimuli. By designing microfluidic devices with various microenvironmental conditions, researchers can dissect the roles of biochemical and physical cues in cellular processes such as migration, proliferation, and differentiation.

In summary, the study of microfluidics, supported by sophisticated fabrication techniques like photolithography, is indispensable for advancing our understanding of cell behavior and response to the microenvironment. This field holds the key to unlocking new approaches in biomedical research, drug development and tissue engineering, promising innovative solutions for health challenges and furthering our grasp of life at the cellular level.

Established on the main knowledge about microfluidic device formulations for cell culture manipulation, our μP was designed to introduce a variety of microenvironmental signals that closely simulate the cardiac cell environment. To ensure the efficacy and functionality of our platform, COMSOL simulations were employed, offering a preliminary validation of its design by analyzing the fluid dynamics and mechanical behavior of the device. The experimental testing of both the fluid dynamic and mechanical components of the device confirmed its capability to not only effectively culture cells but also to subject them to equi-biaxial mechanical stimulation. This type of stimulation is particularly relevant for cardiac cells, as it closely mimics the natural mechanical forces these cells experience in the heart, contributing to their proper function and development. Furthermore, our experiments demonstrated that the device could simultaneously deliver both biochemical and mechanical stimuli without one impairing the functionality of the other. This dual-signal delivery is critical for creating a more physiologically relevant environment, enabling the study of cell responses to complex stimuli. A key aspect of our μP is the use of photolithography to fabricate PDMS membranes with micron-scale patterns. These patterned membranes play a pivotal role in guiding cell alignment in the direction of mechanical stimulation, an essential feature for mimicking tissue functionality. Proper alignment of cardiac cells is crucial for the formation of functional cardiac tissue, as it ensures the coordinated contraction and electrical conductivity necessary for heart tissue performance. By controlling cell orientation through engineered topographies, we can influence cell behavior in ways that more accurately reflect their natural environment. The integration of photolithography-fabricated structures into our μP exemplifies the synergy between microfabrication techniques and biological research. Through this platform, we aim to advance the understanding of cardiac cell responses to their microenvironment.

2.2 Materials and Methods

2.2.1 Design and COMSOL simulations of the microfluidic platform

The μP, featuring the fluid flow and mechanical stimulation unit circuitry of micro-channels and chambers, was designed with AutoCAD (Autodesk), a 2D and 3D computer-aided design (CAD) software application. Both 2D and 3D models of the platform were modelled, the first for the fabrication and the second for the simulation. COMSOL Multiphysics software was used to simulate the fluid dynamic and mechanic behavior of the designed μP. It is a finite element analysis software for solving and simulating physics, describing phenomena involving fluid dynamic, mechanic, electric and thermal problems. In our study, 3D simulations of the Fluid Flow physics were performed to mimic culture medium flow with different chamber geometries, in particular round-shaped and high aspect ratio-shaped. Laminar Flow interface was used to solve fluid dynamic equations on the material chosen for the culture medium fluxes, approximated to water for sake of simplicity. Then, the working principle of the mechanical stimulation unit was simulated both in 2D and 3D domain simulations. In both cases, coupling of multiphysics was adopted to combine air flow and flexible membrane deformations. The air flow was modeled with the Laminar Flow interface, assuming that the air was a compressible fluid with Ma<0.3. Whereas, the membrane deformation was modelled with the Structural Mechanics physics, through the Solid Mechanics interface, and the material used was PDMS. The material behavior was approximated to a hyperelastic material, with a Neo-Hookean behavior. Characteristic parameters of the material, e.g. Young's Modulus, density, and Poisson's ratio, were retrieved from previous literature studies [1–3]. The same approach was taken for the Neo-Hookean model parameters, i.e. Bulk modulus and Lamé parameter [2–4].

2.2.2 Fabrication of the microfluidic platform

The microfluidic device was fabricated using a micro-milling machine (Minitech Machinery Corp.), which employs subtractive manufacturing procedures by means of a rotating tool, i.e. the endmill, that removes material from the bulk piece. Computer numerical control (CNC) was used to define the production steps: starting from the CAD models' conversion, the design was converted into the language of the CNC machine control, known as G-code, using the DesKAM CNC software. The G-code provides intermediate steps and instructions for the final fabrication on the workpiece. The material chosen for the milling was the PMMA, a thermoplastic material,

known to be excellent for microfluidic devices production, due to its mechanical properties and optical accessibility [5]. The endmill diameters chosen for the micro-channels and chamber fabrication were of 1 mm and 381 µm. Given the complexity of device's working principle, a fabrication approach involving the separation of different channels for culture medium and air flow was employed, exploiting a layer-by-layer approach. In fact, separate layers of PMMA were milled to realize the channels and chambers and then they were bound together to build up the microfluidics apparatus. The fabricated layers were firstly washed in deionized water to remove residual debris from the milling step and then flushed in dried air. PMMA-PMMA consecutive layers were bound by dissolving the material in the interaction layers using a solvent-based approach, readapting the procedure reported in the work of Bamshad et al. [6]. Isopropyl alcohol (IPA) was used as solvent for PMMA plasticization at 68°C, because of a reduction in the solvent solubility at that temperature, optimal to stay below the glass transition temperature of the material and avoid deformation on the micro-milled structures. The bonding surfaces were washed in pure IPA to remove residuals that could impair the adhesion between the layers. Then, IPA solution in deionized water at the 70% was poured on the surface of one PMMA layer, which was then brought into contact with the other layer for the bonding. After accurate alignment of the layers, clamps were used to press the layers together to improve the integration of the material at the interface between the two layers. After 10 minutes at 68°C, the layers were left to cool down at room temperature and the procedure was repeated for the other PMMA layers.

2.2.3 PDMS membrane fabrication and device integration

A deformable membrane was fabricated and then integrated in the µP to complete the microfluidics-driven mechanical stimulation unit. PDMS was the chosen material due to its adaptable mechanical properties achieved by varying the prepolymer-curing agent ratio. A high ratio of components (prepolymer-curing agent of 20:1 ratio) was chosen to increase the flexibility of the PDMS membrane under deformation. PDMS (Sylgard 184, Dow Corning, MI, USA) was degassed to remove bubbles arising from the mixing step of the components. Then, 2 mL of PDMS 20:1 were poured on the surface of a 500 µm thick layer of PMMA, to facilitate the handling of the thin layer. Subsequently, it was spin-coated in a two-step program, the first at 500 rpm for 5 s and 100 rpm/s of acceleration, the second at 1400 rpm for 1 minutes and 100 rpm/s of acceleration. These parameters were adjusted to obtain a final thickness of spin-coated PDMS of 40 µm. The spun PDMS was then backed at 80°C for 2h to accomplish the final

crosslinking of the material. After cooling down and overnight resting, the membrane was bound to the PMMA microfluidic circuitry by exploiting a PDMS-PMMA bonding technique adapted from a literature method [7]. In more details, an intermediate SiO_2 layer was created at the PMMA-PDMS interface to increase the stickiness between the two parts. A solution based on chloroform, the principal solvent of PMMA, was prepared by mixing 60% ethanol, 20% tetraethyl orthosilicate (TEOS, 99.999% trace metals basis, Sigma-Aldrich), 10% 0.1 M HCl and 10% chloroform. The solution was poured on the surface of cleaned PMMA and spin-coated at 2000 rpm for 1 min at 500 rpm/s. Subsequently, SiO_2 layer was activated on both surfaces of the spun PMMA and PDMS membrane by means of oxygen plasma treatment (Plasma Etch, Thermoservice) carried out for 5 s at a power of 100 W and flux of 15 sccm. The two treated sides were then bound, bringing them in direct contact, applying mechanical compression by clamps and baking in oven at 80°C for 2h. The PMMA-bonded PDMS was then peeled off from the 500 µm PMMA layer, adapting the procedure reported in literature [8]. The free surface of the PDMS was then bound to the other PMMA microfluidic layers to finally seal the platform, following the same procedure described above.
The device was then completed by attaching Nanoport connectors (NanoPort Kit for 1/16" OD tubing, Darwin Microfluidics) to the micro-channels of the platform, for the culture medium and air flow.

2.2.4 Fabrication of patterned PDMS and integration in the platform

The PDMS deformable membrane was enriched with a surface topography. In a first step of micro-pattern design, AutoCAD modeling was used to draw a topography featuring characteristic ridges and grooves in a radial circular pattern. This structure consisted of stripes radially arranged, with a maximum dimension of 5 µm and a minimum interspace between stripes of 1 µm. Lately, the micro-pattern was fabricated exploiting photolithographic techniques. Firstly, a positive photoresist, AZ 1505 (MicroChemicals GmbH), was poured and spin-coated onto the surface of a 500 µm thick PMMA layer. This PMMA layer was previously cleaned with deionized water and IPA, desiccated with dried air, and baked for 5 minutes at 90°C. The photoresist was spun in a two-step process to reach a thickness of 1 µm, by using 500 rpm for 10 s at acceleration 100 rpm/s in a first step and 1000 rpm for 40 s at acceleration 1000 rpm/s in the second step. Suddenly, after spin-coating, the photoresist was soft-backed at 100°C for 50 s and exposed to a high-resolution direct-write laser lithography tool (DWL 66 fs, Heidelberg Instruments), according to the model design. The photoresist was exposed to a laser

with a 395 nm wavelength with precise control in the laser movement above the x-y plane. After the exposure, the sample was pre-backed at 100°C for 1 min, developed using AZ 351B (MicroChemicals GmbH), in a ratio 1:4 in deionized water, for 30 s and then rinsed with deionized water and dried with desiccated air. Due to the kind of photoresist, the development step allowed to remove the photoresist areas solubilized by the laser exposure. Hard-baking at 90°C for 50 s concluded the process. After the micro-pattern master fabrication, PDMS 20:1 was poured and spun on the surface of the micro-patterned photoresist carried by the 500 µm-flexible PMMA layer, maintaining the PDMS spinning parameters of section 2.2.3. The PDMS was cured at 80°C for 2 h. After cooling down at room temperature, the spun PDMS was bound to the PMMA microfluidic circuitry following the PDMS-PMMA SiO_2 treatment previously described in paragraph 2.2.3. Thanks to the transparency of both PMMA and photoresist layer, the micro-pattern was aligned with the underlying microfluidic circuitry at high magnification using a stereomicroscope. Following PDMS-PMMA bonding, the patterned PDMS fixed above the microfluidic apparatus was peeled off from the thin PMMA carrying the patterned photoresist layer and the entire device was sealed with the upper part of the device containing the microfluidic channels and chambers.
The device was again completed by attaching Nanoport connectors, as previously described.

2.2.5 Pressure-controlled deformation and confocal acquisitions

Both the flat PDMS, corresponding to the non-patterned PDMS and micro-pattern-enriched PDMS membrane, embedded in the microfluidic device, were mechanically stimulated by applying flow of air suction. The Nanoport connectors were used to link the device micro-channels to an external pressure controller throughout PTFE tubes. The controller (OB1 MK4, Elveflow) included internal vacuum channels remotely controlled by software, enabling the imposition of different pressure curves for the air flow with limit pressure values of ±1 bar. The system was used to apply continuous and cyclic deformation to the deformable PDMS membrane. For device testing purposes, the PDMS membrane was enriched with fluorescent nanoparticles. The uncured PDMS, consisting of prepolymer-curing agent, was mixed with fluorescent polystyrene nanobeads (Fluoro-Max Dyed Green Aqueous Fluorescent Particles, aqueous suspension at 1% solids, diameter of 0.083 µm, Thermo Scientific), at a concentration of 15 µL/g of PDMS. The PDMS was spin-coated and cured as previously described. After embedding the device, an equi-biaxial deformation was applied to the fluorescence-labeled PDMS using the pressure controller, providing continuous negative pressures in the time. The

PDMS fluorescence was tracked by acquiring its vertical lowering in the mechanical deformation unit chamber by acquiring z-stack images with a Leica TCS SP 5 (Leica Microsystems) and a 10x objective. The sample was excited with a 488 nm laser wavelength and emission was collected in the (495÷515) nm range. In addition, time-lapse images were taken over time by acquiring the fluorescent nanobeads, tracking their position and displacement in the x-y plane during the equi-biaxial deformation in the μP. Confocal images were acquired, with the same, just reported, parameters, with a flow of an aqueous solution of fluorescent nanobeads (1:1000 of nanobeads versus deionized water) in the microfluidic channels of the platform at a flow rate of 200 μL/min, to test the fluid dynamic response and the combination of fluid flow with mechanical deformation in the designed device.

2.2.6 Profilometer measurements

Profilometer measurements of the PDMS membrane and micro-patterned master thickness was performed by using a stylus profilometer (Dektak, Bruker), with a stylus radius of 2.5 μm and force of 1 mg. For the PDMS membrane profiling, a scanning length of 3 mm with a duration of 60 s was applied with a valley profile in a measurement range of 65.5 μm. For the micro-pattern master characterization, a scanning length of 1 mm with duration of 60 s was applied, measuring valleys profile in a range of 6.5 μm.

2.2.7 Scanning electron microscopy characterization

Scanning electron microscopy (SEM) imaging of patterned PDMS was performed with a Zeiss Ultraplus field emission gun (FEG) SEM. Imaging parameters included setting the acceleration voltage of the electron high tension at 5 kV and maintaining the working distance between 8-30 mm. Prior to high vacuum acquisition, the PDMS samples were coated with a conductive gold layer by sputtering 10 nm of thickness.

2.2.8 Image and data analysis

Profilometer curves were reconstructed using MATLAB (MathWorks) built-in plotting functions based on scanning length and vertical displacement coordinates.
Confocal images from device testing were reconstructed and analyzed by ImageJ (Fiji). Z-stacks were reconstructed and the Analyze Line Graph function in ImageJ allowed to retrieve the

coordinates of the fluorescent-labeled PDMS membrane lowering during mechanical stimulation. The coordinates were uploaded and plotted in MATLAB. By retrieving the minimum coordinates reached by the membrane during the vertical lowering as a function of the suction pressure applied by the external pressure controller, calibration curves were built by MATLAB plot.

Starting from confocal time-series of PDMS-embedded fluorescent nanobeads movement under the equi-biaxial stimulation, trajectories of the nanobeads were obtained using a Fiji tracking plugin, MTrackJ. The detector was employed to detect particle positions, by extracting the objects of interest from the image and a tracer linked the extracted objects over time. A semi-automatic detection and manual tracing of the moving beads were therefore performed. The detection algorithm was based on the position calculation of the specified image feature, which can be the choice of maximum and minimum intensity and bright and dark centroid, for a precise mouse cursor positioning. At the end of the tracking process, MTrackJ allowed to measure the feature characteristics in terms of points and tracks, e.g. in terms of number of points per tracks, points coordinates, trajectory length at the current point, velocity of the tracked object, angular displacement of the track segment. The positions of nanobeads over time were used to generate profiles of trajectory orientation in the x-y plane using the Chemotaxis and Migration tool of ImageJ. The latter allowed to plot diagrams in which the start point of cell trajectories were translated in the origin of the x and y axes of the image system to observe their arrangement in the plane. Furthermore, Windrose diagrams were exploited to observe the count of the trajectories number in a specific direction of the same plane. After that, the positions of the nanobeads were also used to reconstruct deformation field and map by MATLAB plotting. In particular, quiver plot defined the displacement field, by using the initial and final position of each nanobead to build arrows in which the direction represents the orientation of movement while the length is the modulus of the displacement. A color map was used to illustrate the progression of the displacement gradient due to equi-biaxial mechanical stimulation applied to the deformable PDMS membrane.

2.3 Results

2.3.1 Computational simulations for microfluidics platform design

With advancements in the creation of new micro-testing systems, computational tools have become increasingly significant. They enhance experimental research by offering an engineering perspective, facilitating the investigation of physical phenomena, evaluating device feasibility, and aiding in device design and optimization for specific purposes. Likewise, numerical simulations in computational fluid dynamics (CFD) assist in the evaluation of critical process parameters that are challenging to measure experimentally, such as pressure, velocity, shear rate, temperature, along with structural mechanical properties and their combinations. This is why, in this study, we integrated numerical methods for a more comprehensive analysis of the μP design and its applicability for our purposes.

The first step involved the design of the unit for introducing the culture medium fluid flow. The culture medium might be introduced on one side and drained on the other side to allow the circulation of nutrients and the disposal of cell respiration products. Channels were designed to meet the microfluidic assumptions, which comprise low Reynold's number (Re), meaning laminar flow conditions with the dominance of viscous forces over inertial forces, absence of gravity forces in the flow equations and incompressibility of the fluid [9]. Regarding the assumption of low Re, this implies that not only inertial terms are neglected, but also that there is no lateral convection in the channels and adjacent layers of fluid do not interfere, preventing mixing. On the contrary, when the Re number increases, turbulence emerges with the amplification of perturbations, curling of field lines and unpredictable development of the velocity field over time. In addition, squared channels were designed with characteristic dimensions below 1 mm to fulfil the microfluidic assumptions. The evaluation of the pressure drop between the inlet and outlet of the microfluidic conduct necessitates consideration of the Poiseuille law, applied to steady-state flow in laminar conditions for an incompressible Newtonian fluid in a constant cross section. The resulting formula originates from Navier-Stokes equations, the system of partial derivative differential equations describing the behavior of fluid considered as a continuum. The generical form is the following:

$$\rho \frac{D\underline{v}}{Dt} = -\underline{\nabla} P + \mu \nabla^2 \underline{v} \qquad (Eq.\ 1)$$

where ρ is the fluid density, $\underline{v}$ is the velocity field that the fluid undergoes during the motion, μ is the fluid viscosity, P is the reduced pressure defined by $P = p + \rho g$ (g is the gravity force). In cylindrical coordinates it appears as:

r component : $\rho\left(\frac{\partial v_r}{\partial t} + v_r\frac{\partial v_r}{\partial r} + \frac{v_\theta}{r}\frac{\partial v_r}{\partial \theta} - \frac{v_\theta^2}{r} + v_z\frac{\partial v_r}{\partial z}\right) = -\frac{\partial P}{\partial r} + \mu\left[\frac{1}{r}\frac{\partial}{\partial r}\left(r\frac{\partial v_r}{\partial r}\right) - \frac{v_r^2}{r} + \frac{1}{r^2}\frac{\partial^2 v_r}{\partial \theta^2} - \frac{2}{r^2}\frac{\partial v_\theta}{\partial \theta} + \frac{\partial^2 v_r}{\partial z^2}\right]$

θ component: $\rho\left(\frac{\partial v_\vartheta}{\partial t} + v_r\frac{\partial v_\vartheta}{\partial r} + \frac{v_\theta}{r}\frac{\partial v_\vartheta}{\partial \theta} + \frac{v_r v_\vartheta}{r} + v_z\frac{\partial v_\vartheta}{\partial z}\right) = -\frac{1}{r}\frac{\partial P}{\partial \vartheta} + \mu\left[\frac{1}{r}\frac{\partial}{\partial r}\left(r\frac{\partial v_\vartheta}{\partial r}\right) - \frac{v_\vartheta^2}{r} + \frac{1}{r^2}\frac{\partial^2 v_\vartheta}{\partial \vartheta^2} + \frac{2}{r^2}\frac{\partial v_r}{\partial \vartheta} + \frac{\partial^2 v_\vartheta}{\partial z^2}\right]$

z component: $\rho\left(\frac{\partial v_z}{\partial t} + v_r\frac{\partial v_z}{\partial r} + \frac{v_\theta}{r}\frac{\partial v_z}{\partial \theta} + v_z\frac{\partial v_z}{\partial z}\right) = -\frac{\partial P}{\partial z} + \mu\left[\frac{1}{r}\frac{\partial}{\partial r}\left(r\frac{\partial v_z}{\partial r}\right) + \frac{1}{r^2}\frac{\partial^2 v_z}{\partial \vartheta^2} + \frac{\partial^2 v_z}{\partial z^2}\right]$

(*Eq. 2*)

Then, making the approximation of hydraulic diameter, the pressure drop evaluation is solved as an equivalent problem in which a circular cross-section of the channels can be used in the Poiseuille law, considering the radius of a circle inscribed in the square with dimension equal to the channel characteristic dimension, following the formula:

$$D_H = \frac{4S}{P} \qquad (Eq.\ 3)$$

with S and P respectively the wet surface and the perimeter of the real channel cross-section. In these conditions, flow through a cylindrical pipe can be considered. Additionally, the formation of a velocity gradient should be taken into account in pipe flow. The hydrodynamic entrance region is defined as the segment within the pipe where the velocity profile of the flowing fluid begins to form as a result of viscous forces exerted by the pipe's inner walls. Initially, the fluid enters with a constant velocity but, when fluid layers encounter the pipe surface, they stop and adhere due to the no-slip condition, i.e. velocity at the wall is zero. Under the effect of fluid viscous forces, the layer touching the pipe slows down the movement of adjacent fluid layers, creating a velocity profile throughout the pipe cross-section. In fact, the fluid layers in the center of the pipe exhibit higher velocities compared to layers closer to the pipe surface, due to the effect of mass conservation.

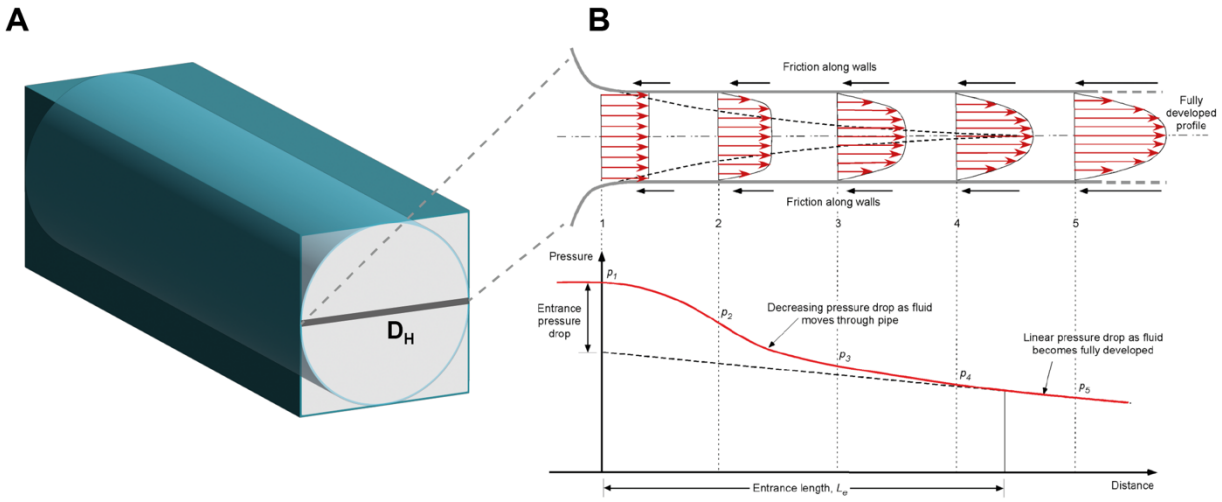

Figure 1 – The theory of flow in a pipe is based on the definition of hydraulic diameter D_H (A) and velocity gradient in conditions of fully-developed flow (B). Image in (B) adapted from https://eaglepubs.erau.edu/introductiontoaerospaceflightvehicles/chapter/internal-flows/.

In the previously described assumptions for the fluid properties and in conditions of fully-developed flow, the velocity is changing only along the main axis of the pipe, while there is not a variation in the velocity along the circumferential (θ) and radial components (r), meaning that:

$$\underline{v} = (0,0,v_z(r)) \qquad (Eq.\ 4)$$

and the Navier-Stokes equations become:

$$0 = -\frac{\partial P}{\partial z} + \mu\left[\frac{1}{r}\frac{\partial}{\partial r}\left(r\frac{\partial v_z}{\partial r}\right)\right] \qquad (Eq.\ 5)$$

For Poiseuille flow, the velocity is:

$$v_z(r) = \frac{R^2}{4\mu}\frac{\Delta P}{L}\left(1 - \frac{r^2}{R^2}\right) \qquad (Eq.\ 6)$$

That integrated between 0 and R, i.e. hydrodynamic radius, gives the flow rate and, consequently, the pressure drop in the pipe:

$$Q = 2\pi\int_0^R v_z(r)rdr = \pi\frac{\Delta P R^4}{8\mu L} \qquad (Eq.\ 7)$$

To compute velocity and pressure drop profiles following the previously discussed assumptions, laminar flow might be fulfilled in the design of the channels and chambers of the μP. To meet these requirements, CFD simulations were implemented with COMSOL Multiphysics, which is a software for finite element analysis, solving and simulating a wide range of physics and engineering problems, with a particular focus on interacting phenomena and multiphysics applications, integrating coupled systems of partial differential equations. In our application, since the microfluidic assumption deals with low Reynolds number, which means laminar flows, the design of the chambers was done by exploiting the physics corresponding to *Single-Phase Fluid Flow*, with a particular focus on *Laminar Flow* physics (*spf* module) to compute velocity and pressure fields. Table 1 illustrates the main parameters and assumptions adopted to simulate the fluid dynamic working of the proposed platform. In more details, for sake of simplicity, water was chosen as the material for the fluid to approximate the culture medium, whose main component is water. To better simulate cell culture conditions, water density and dynamic viscosity values were considered at 37°C and were directly extrapolated from the COMSOL library of materials. In the *Laminar Flow* physics, the boundary slip conditions at the pipe walls were considered to suppose a velocity gradient build up during the water flow. The inlet boundary conditions were chosen to accomplish the fully developed flow hypothesis, and flow rate was simulated as inlet parameter. At the pipe outlet, null pressure was imposed to establish a pressure-driven flow, with a suppress backflow assumption to fix unidirectional flow conditions. Shear stress quantification was also considered in the simulation (τ) and was computed by the proportion with the velocity gradient through water viscosity. The simulations on the fluid flow behavior in the designed channels were carried out in *Stationary Study* conditions, meaning that all the time-dependent terms in the model differential equations were null.

Fluid Dynamics (spf): Water (Materials) **Laminar flow**			
Fluid Properties		**From material (37°C)**	
Dynamic viscosity (37°C)	μ_{water}	From library	Pa·s
Density (37°C)	ρ_{water}	From library	kg/m^3
Wall		**Boundary condition: No slip**	
Inlet	Flow rate	Q1 = 1	µL/min
		Q2 = 10	µL/min
		Q3 = 100	µL/min
		Q4 = 1000	µL/min
		Boundary condition: Fully-developed flow	
Outlet	Pressure	0	Pa
		Pressure conditions: Suppress backflow	
Additional Parameters	Velocity gradient	spf.sr	1/s
	Shear Stress	$\tau = \mu * spf.sr$	Pa·s

Table 1 – Simulation parameters for the fluid dynamic operation of the platform microfluidic channels and chambers.

The initial simulations included the study of the fluid dynamic behavior of two different configurations for the cell culture chamber. The chamber shape was thought to avoid turbulences and, consequently, bubble formations. Bubbles in the cell culture medium can compromise the homogeneity of oxygen and nutrients availability, along with changes in interfacial tension and stress increase, all of which could impair cells viability during the seeding process. Both designed configurations included two square channels with a width of 500 µm each, one for the inlet and one for the outlet. To separate the inlet and outlet, a central chamber was designed to host the cell culture and collect the culture medium from the feeding channels, providing cells with the nutrient necessary for their viability. Two chamber designs were simulated: a circular one (*Fig. 2A*) and one with a high-aspect ratio geometry (length over width) (*Fig. 2B*). This was

done to test which configuration provided the best conditions for cell survival. Four separate simulations were executed for each geometry by varying the inlet flow rates. The initial flow rate was set at the lowest (1 μL/min) to create conditions conducive to cell culture survival, as the mild flow effect improves cell adhesion to the substrate without detaching them or significantly altering cell behavior with high shear stresses. For the other three flow rates, their values were increased by one order of magnitude each time to prove the effect of fluid velocity on the laminar nature of the flow. The flow rate values are reported in Table 1. From the stationary simulations, it was observed that the velocity increased linearly with the flow rate (*Fig. 2C-D*) and the laminar flow conditions were mantained up to a flow rate of 1000 μL/min, beyond which turbulence arose in the cell seeding chamber for both circular and high-aspect ratio geometries. This was evident from the fluid flow streamlines shown in *Fig. 2C* and *Fig. 2D*. A comparison of the two geometries revealed that, at the highest flow rate, turbulence was more pronounced in the case of circular shape. Sharp corners in the channels leading to the cell culture chamber, as in the case of rounded-shape chamber, increased the likelihood to creating discontinuities and cavitation phenomena. On the other hand, the high-aspect ratio shape, with mild discontinuities, maintained the fluid flow direction avoiding bubble formation.

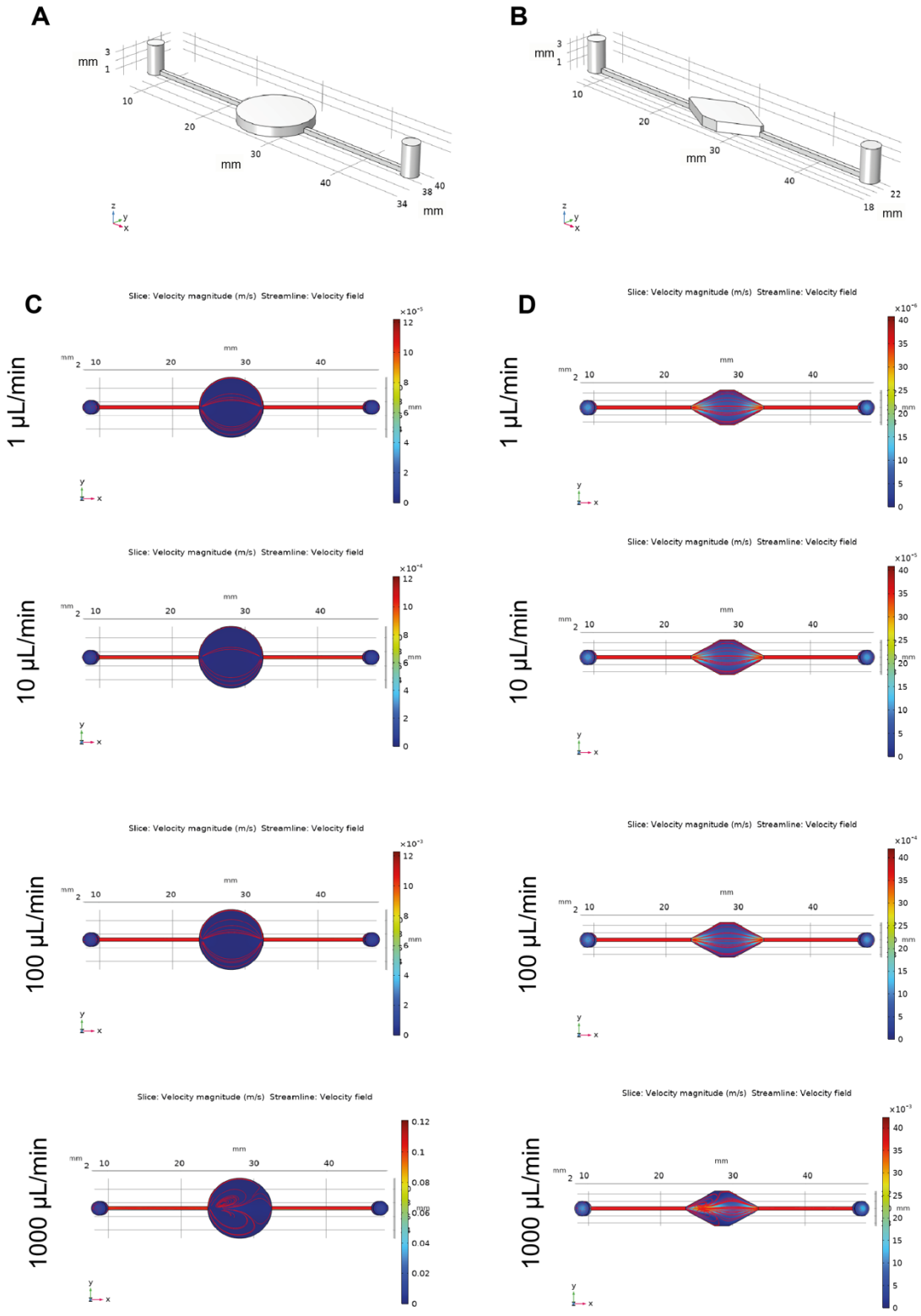

Figure 2 – COMSOL simulations of fluid flow evolution by changing the shape of the cell culture chamber. Two different geometries were tested, one rounded-shaped (A) and one squared and high-aspect ratio shaped (B). Velocities field and streamlines were simulated and plot for both the geometries (C and D, respectively).

Concurrently with the characterization of the velocity field, the distribution of shear stresses on the surface of the cell seeding area demonstrated the impact of flow rates, geometry and their combination on the concentration of stresses on the top of cell culture (*Fig. 3*). This aimed to simulate what happens during culture medium exchange and treatments, providing insights to prevent cell detachment from the adhesion substrate and enhance cell survival, eluding deleterious fluid flows. The simulations showed that round-shaped geometries gave higher shear stress values with respect to squared geometries at the same flow rate values. The superior performance of high-aspect ratio chambers was further confirmed by the ability to create a central area of low shear rates. This ensures the presence of regions with high cell viability and protection against sharp, potentially harmful flows, thereby providing optimal culture conditions.

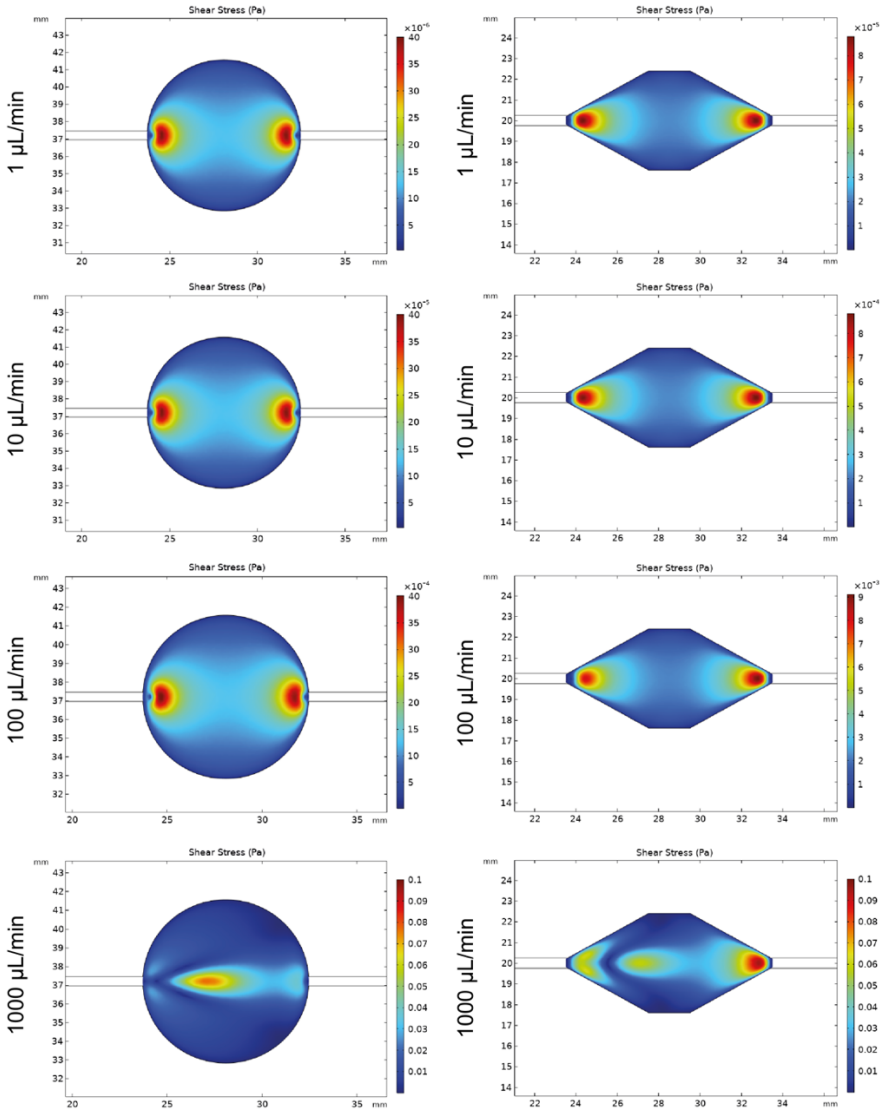

Figure 3 – COMSOL simulations of shear stress maps for circular (left panels) and squared (right panels) cell culture chambers, in dependence of the flow rate values.

Following the characterization of fluid flow, CFD simulations were performed to design the mechanical deformation chamber. The platform's working principle was based on the concept of stretching a deformable membrane on top of a hollowed circular chamber with a fixed central pillar (*Fig. 4*). Stimulation was induced by applying vacuum in the hollow cavity of the chamber throughout some holes in its basis. The vacuum lowered the membrane into the cavity, causing its vertical movement. However, the circular pillar stopped the lowering of the membrane and, instead, induced a planar biaxial stretch due to the sliding of the membrane on its surface. By applying the suction in four specular points on the chamber basis, a planar equi-biaxial stretch arises on the surface of the flexible membrane corresponding to the fixed circular pillar.

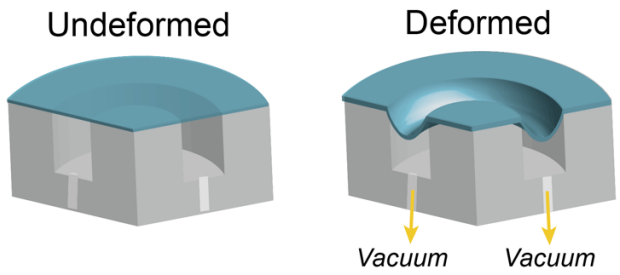

Figure 4 – Mechanical stimulation unit working principle. A deformable membrane is bound on the top of a hollowed cavity, at the center of which a fixed pillar limits the vertical movement of the flexible membrane that, instead, lowers in the free cavity. The vacuum is applied on the basis of the hollowed chamber through small holes applied to increase the pressure for the suction.

To test this proposed working principle, 2D COMSOL simulations were applied to the lateral section of the deformation chamber, exploiting the *Structural Mechanics* physics. In particular, the *Solid Mechanics* interface (*solid* module) was employed to compute the structural analysis of the proposed geometry, by computing displacements, stresses and strains field on the structure. For these purposes, multiphysics coupling was used to combine the air flow, to simulate the negative pressure applied to the flexible membrane in the air domain (*Fig. 5A*, top-right panel), and structural mechanics, to simulate the deformation on the membrane due to the air suction in the PDMS membrane domain (*Fig. 5A*, bottom-right panel). Hence, in combination with the Solid Mechanics interface, the Fluid Dynamics interface (*spf* module) was applied to the air as flowing material, as reported in Table 2. In this case, the incompressibility hypothesis cannot be applied to the model since air changes its density as a function of temperature. The Mach number (Ma) is a critical parameter in determining the compressibility effects of air and other fluids. Compressibility effects become significant in air when the Ma approaches and exceeds 0.3. As the Ma increases, the density of the air can no longer be considered constant due to the increasing influence of the object's speed on the air pressure and

temperature around it. In our study, a compressible flow with Ma<0.3 was considered for the flow of air in the channels. No-slip boundary conditions were applied to the chamber walls, while the inlet parameter was a negative pressure, along with the hypothesis of backflow suppression and normal flow. The simulated pressures applied at the inlet of the chamber remained in the order of mbar to be consistent with plausible values that can be employed through the aid of external air flow control systems. To build a pressure difference, an outlet with a pressure equal to 0 was applied, at which the same pressure conditions of the inlet were applied. The air inlet was applied at the base of a vacuum camera underlying the deformation chamber to better distribute the suction at the bottom of the hollow cavity (*Fig. 5B*, left panel). The outlet of the air fluid flow was the contact surface between the air camera and the bottom of the PDMS membrane (*Fig. 5B*, right panel).

Fluid Dynamics (spf): Air (Materials) **Laminar flow**			
Fluid Properties		**From material (37°C)**	
Dynamic viscosity (37°C)	μ_{air}	From library	Pa·s
Density (37°C)	ρ_{air}	From library	kg/m^3
Physical model		**Compressibility: Compressible flow (Ma<0.3)**	
Wall		**Boundary condition: No slip**	
Inlet	Pressure	P1 = -1	mbar
		P2 = -5	mbar
		P3 = -10	mbar
		Pressure condition 1: Suppress backflow	
		Pressure condition 2: Normal flow	
Outlet	Pressure	0	Pa
		Pressure conditions 1: Suppress backflow	
		Pressure condition 2: Normal flow	

Table 2 – Simulation parameters for the fluid dynamic operation on the air suction in the deformation chamber.

PDMS domain deformation was simulated in the Solid Mechanics interface. The equilibrium equations start from the Newton's second law:

$$\rho \frac{\partial^2 u}{\partial t^2} = \nabla_x \sigma + f_V \qquad (Eq.\ 8)$$

where σ is the Cauchy stress tensor, f_V is a body force per unit volume. In terms of second Piola-Kirchhoff stress tensor S, the equation becomes:

$$\rho_0 \frac{\partial^2 u}{\partial t^2} = \nabla_x (FS) + F_V \qquad (Eq.\ 9)$$

in which ρ_0 is the initial mass density (before deformation), F is the deformation gradient, F_V is a body force with components in the current configuration but given with respect to the undeformed volume.

The hyperelastic material model is instead characterized by the elastic strain energy density W_S, function of the elastic strain state. In this case, the relation between stress and strain is nonlinear. In the assumption of nearly incompressible material, the total strain energy density W_S splits into an isochoric and volumetric strain energy density:

$$W_S = W_{iso} + W_{vol}. \qquad (Eq.\ 10)$$

Depending on the elastic strain energy, different hyperelastic material models can be distinguished. In the case of the Neo-Hookean model, W_S is a function of the elastic volume ratio J_{el} and the first invariant of the elastic right Cauchy-Green deformation tensor $I_1(C_{el})$ in the form:

$$W_S = \frac{1}{2}\mu(I_1 - 3) - \mu \ln(J_{el}) + \frac{1}{2}\lambda[\ln(J_{el})]^2 \qquad (Eq.\ 11)$$

with λ and μ Lamé parameters. In the nearly incompressible case, the elastic volume ratio J_{el} and bulk modulus κ define the volumetric strain energy density W_{vol}, while the isochoric invariant $I_1(\overline{C_{el}})$ define the isochoric strain energy density W_{iso}:

$$W_{iso} = \frac{1}{2}\mu\left(\overline{I_1} - 3\right). \qquad (Eq.\ 12)$$

The material chosen from the library set was the PDMS, and its density, Poisson's ratio and Young's modulus were added following data from the literature [1–3]. In the solid mechanics interface, PDMS was simulated with a Neo-Hookean model, considering PDMS as a hyperelastic material, nearly incompressible. This constitutive model characterizes the response of rubber-like materials in the small strain hypothesis, and parameters were retrieved from previous literature studies [2–4]. In the structural analysis, the load on the bottom and top side of the PDMS membrane was the pressure exerted by the suction air flow in the underlying deformation chamber and the static air flow on the top, respectively (*Fig. 5C*). Some fixed constraints for the PDMS membrane movement were considered during the simulation, i.e. null displacements on the top of the pillar surface and on the side of the PDMS membrane (*Fig. 5D*).

Structural Mechanics (solid): PDMS (Materials) **Solid Mechanics**			
Material: PDMS		**From library**	
Density	ρ	970	kg/m^3
Young's modulus	E	600	kPa
Poisson's ratio	ν	0.49	N.D.
Hyperelastic Material		**Material model: Neo-Hookean**	
		Compressibility: Nearly incompressible	
		Volumetric strain energy: Quadratic	
Lamé parameter	μ	1e5	N/m^2
Bulk modulus	κ	5e8	Pa
Density	ρ	From library	kg/m^3
Load on the boundary		Pressure	From spf
Fixed constraints		Pillar surface	
		PDMS membrane sides	

Table 3 – Simulation parameters for the structural mechanics module operation on the PDMS membrane deformation.

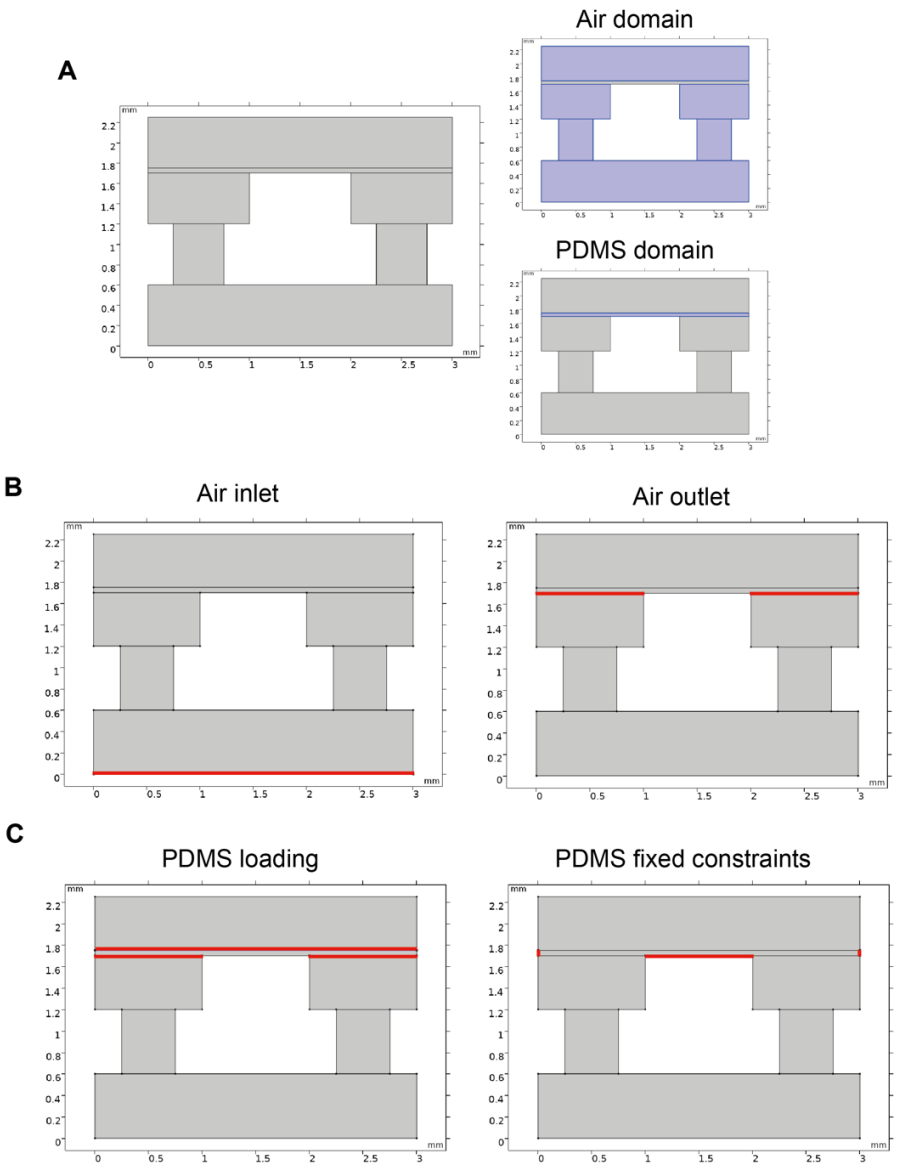

Figure 5 – Mechanical stimulation unit. It is modelled in two separate domains: the air domain and PDMS membrane domain (A). B) Air inlet and outlet are the lower and upper boundaries of the mechanical stimulation unit. C) The pressure p retrieved from the fluid dynamic simulation of air flow is the stimulus introduced to the PDMS membrane for the deformation.

The simulations of the fluid dynamic part of the deformation chamber are reported in *Fig. 6A*. The highest velocities values were reached in the channel sections with the small characteristic dimension, while symmetry in air flow was evident in the deformation area underlying the PDMS membrane. Regarding the structural mechanics module, the pressure exerted by the air suction lowered the PDMS in the deformation chamber, as expected. Thanks to the multiphysics simulations coupling between the fluid dynamics module and structural mechanics module, it is possible to notice that the vertical lowering of the membrane had a peak corresponding to the maximum air velocity and pressure and there was a non-linear trend of PDMS vertical displacement between the three values of air suction pressure.

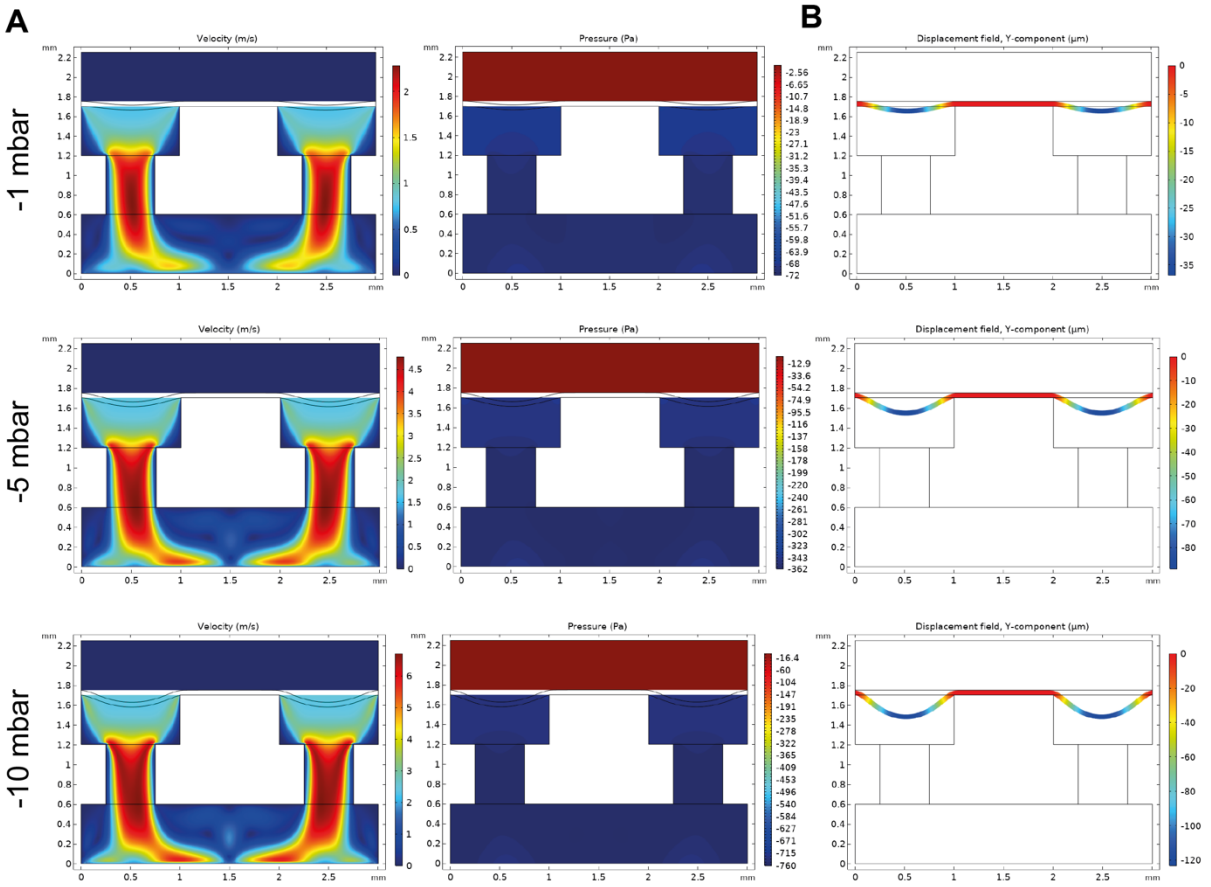

Figure 6 – Mechanical stimulation unit simulations. A) Fluid dynamic simulations of air flow suction under three different values of inlet pressure. B) Structural mechanics module allowed to simulate the vertical lowering of the PDMS in the deformation chamber under the action of air vacuum.

After the 2D validation of the model's response to mechanical stimulation, the interaction between the fluid dynamic channel for air suction and the PDMS membrane deformation was assessed by a 3D stimulation. The design introduced a single long micro-channel for air flow, which was intended to withdraw air from the bottom of the deformation chamber to the connector hole for the connection of the µP to the external pumping control system. At the end of the air channel, a circular chamber was thought and designed to apply a flux distribution under the deformation chamber, accomplishing its dimension. Then, on the upper part, air flux split was applied to increase air pressure in four small symmetric and equidistant holes, distributed at four points on the basis of the largest deformation chamber to apply a symmetric equi-biaxial stretch on the upper membrane with respect to the pillar center. In the simulation, the membrane was modelled as a cylinder with height of 40 µm and a diameter equal to that of the deformation chamber. On the top of the membrane, another chamber was modeled to replicate the culture medium chamber; however, for these simulations, for sake of simplicity, only air flow was considered here. In *Fig. 7A,* the two domains are represented, as before; the

fluid flow domain (top left panel) was used to simulate air fluxes, while structural mechanics physics (bottom left panel) modeled the PDMS membrane deformation under the action of air suction. For the fluid flow and structural mechanics physics, a laminar flow and solid mechanics interface were again used, respectively, with the same parameters reported in Table 2 and Table 3. The inlet of the air flow was the entrance of the microfluidic channel, and here a negative pressure was applied to simulate the vacuum application, while the output was placed at the interface deformation chamber-membrane, in particular at the bottom of the PDMS membrane. The results of the fluid dynamic simulations are reported in *Fig. B-C*. The velocity profile demonstrated high speed suction in the small microfluidic channel, and in the small holes of air splitting, as expected. The pressure profile shows a difference in pressure between the inlet of the micro-channel and the outlet underlying the PDMS membrane, demonstrating that a negative pressure was applied under the membrane. As a consequence, the solid mechanics simulation on the PDMS membrane presented a vertical displacement field along the z-direction in the hollowed cavity of the deformation unit. The displacement was maximum at the center of the circular hollowed crown, delimited by the external deformation chamber and the central pillar, and was minimum in the lateral fixed constraints. On the top of the pillar, the vertical displacement field gave null values, since the pillar was considered a fixed constraint for z-motion but not for x-y displacement.

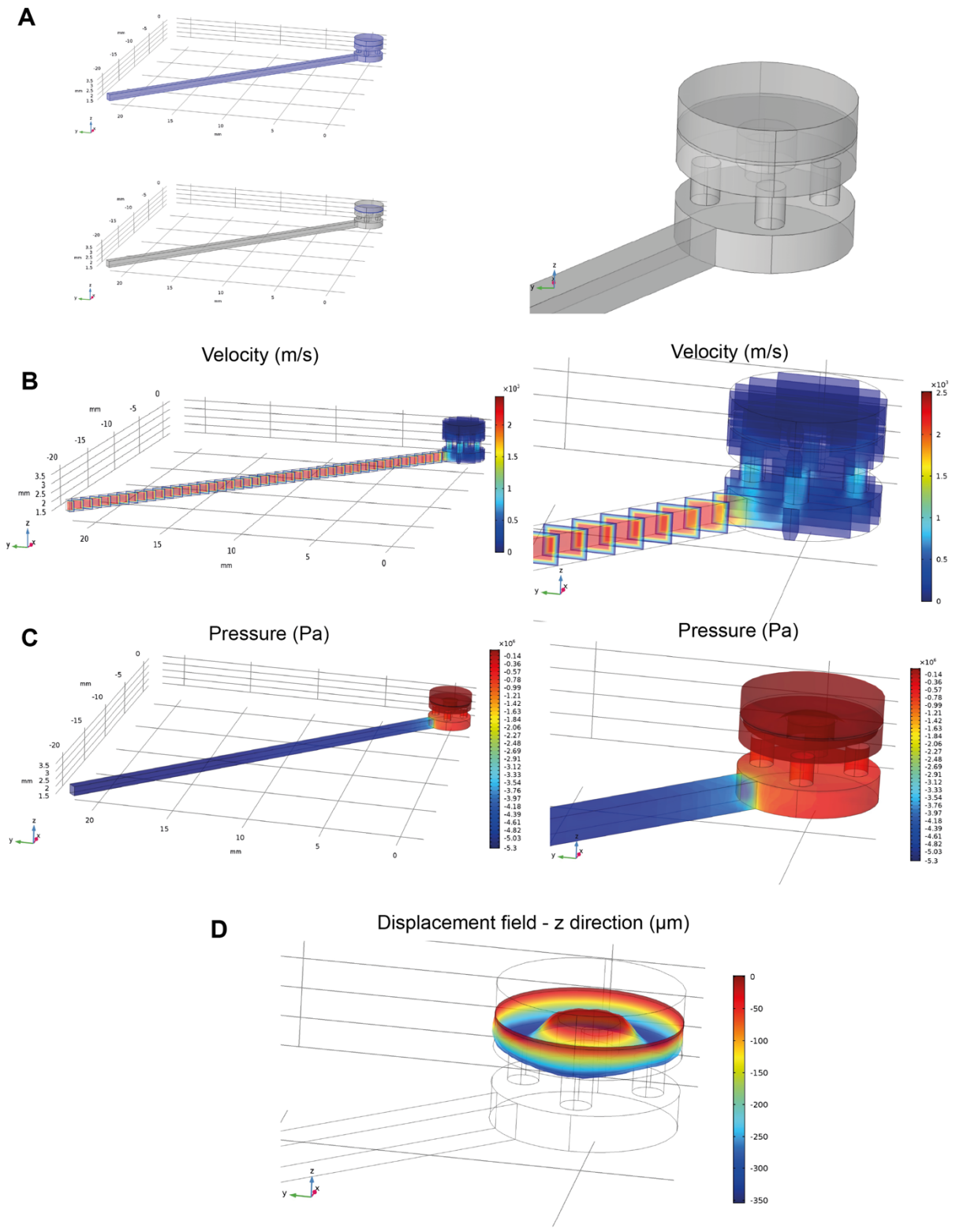

Figure 7 – 3D simulations of the membrane deformation under the action of vacuum applied by air suction. A) Fluid flow domain (top panel) was used for air flow simulations, while structural mechanics domain (bottom panel) was emulating the PDMS membrane movement due to the air flow. An inset on the complete mechanical deformation unit is reported on the right. Velocity field (B) and pressure field (C) are represented to represent the air movement during the suction. D) The interaction between air suction and the structural element simulated the membrane displacement in the hollowed cavity.

In the structural mechanics theory, stress and strain representation is important to highlight the response of the structure to the applied load and how the stimulation influences the mechanical nature of the deformed object. In this representation, Von-Mises stresses help to give information on the yielding of the structure to the external applied load. The 3D representation of Von-Mises stress map on the PDMS membrane demonstrated that the structure underwent high stresses on the boundary, in agreement with the fixed constraints, and slightly on the side of the pillar, onto which the PDMS membrane bends (*Fig. 8A*). Principal stresses, which, differently from Von-Mises stresses, give the measure of the actual stresses acting on the material, were separated into first, second and third principal stress evaluation. The map of the first principal stresses qualitatively represents the tensile maximum value of stress induced in the plane. As expected, the highest tension can be found on the constrained boundaries and on the side of the pillar surface where the PDMS membrane bends and stretches (*Fig. 8B*- left plot). The third principal stress is the maximum value of compressive stress in the system and from the map in *Fig. 8B* (right plot), it is evident that the maximum compressions are reached at the point of membrane-wall interaction, i.e. on the sides and at the points where the membrane bends on the pillar. Second principal stresses have values that are a combination of first and third principal stresses. In the same way, principal strains give information on material deformation, particularly explaining how much a material stretches or compresses under the applied load (*Fig. 8C*).

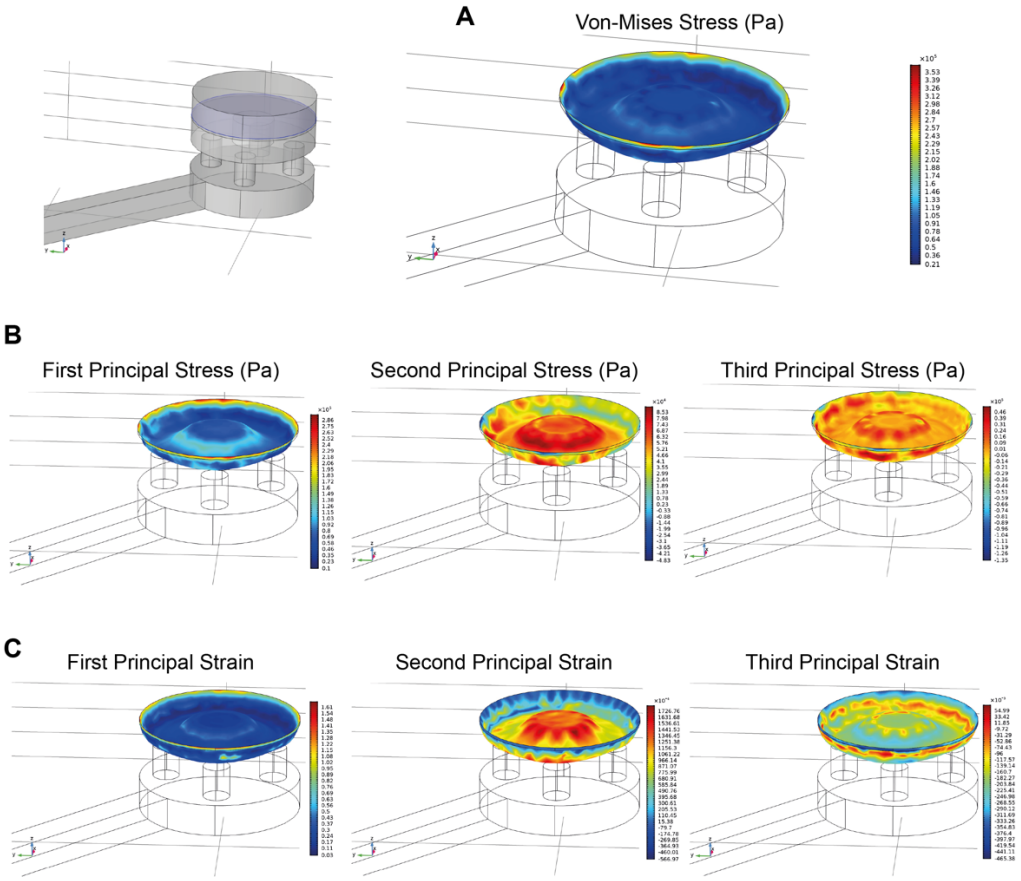

Figure 8 – Mechanical characterization of the deforming PDMS membrane. A) Von-Mises stress field explains the yielding of the structure under the mechanical load. Principal stresses (B) and principal strains (C) characterize the mechanical response in terms of stress field and deformation field arising on the structure by the application of the external loading.

With a particular focus on the pillar surface, the principal strain map was also assessed to observe the PDMS deformation on the area interested by the loading significant for our application. Here, a gradient of deformations arose from the center towards the boundaries of the pillar, quantified by arrows in which the orientation pointed to the deformation direction, and the modulus represented the deformation intensity in a specific point of the membrane undergoing loading. In addition, the observed deformation is visibly equi-biaxial and symmetric in all orientations (*Fig. 9*). In fact, another method for the quantification of deformation and strain in continuum mechanics is the deformation gradient representation [10]. The latter is a mathematical representation that describes the transformation of a material body from its initial undeformed configuration (X) to its current deformed configuration (x). It is a measurement of the rotation and stretch that a material element has experienced during the loading. The deformation gradient (F) is defined as the gradient of the deformation mapping function Φ, which maps points in the initial configuration X to points in the current configuration x. F is a 3x3 matrix in the space, in the form:

$$F = \begin{bmatrix} \frac{\partial x}{\partial X} & \frac{\partial x}{\partial Y} & \frac{\partial x}{\partial Z} \\ \frac{\partial y}{\partial X} & \frac{\partial y}{\partial Y} & \frac{\partial y}{\partial Z} \\ \frac{\partial z}{\partial X} & \frac{\partial z}{\partial Y} & \frac{\partial z}{\partial Z} \end{bmatrix} \quad (Eq.\ 13)$$

We computed the corresponding deformation gradient of the PDMS membrane structure under the deformation applied by the air suction. The study focused on the area of the PDMS membrane top side corresponding to the pillar, to quantify the deformation gradient arising under the equi-biaxial mechanical deformation on the cell seeding zone (*Fig. 10A*). This provides a measurement of the kind of substrate transformation experienced by the cells when undergoing deformation. The 2D surface simulations of deformed PDMS on the pillar showed that the only non-null components were those on the principal diagonal of the deformation gradient matrix, i.e. xX-, yY- and zZ-component (*Fig. 10B*). This was also proven by the 1D plot, as it is possible to observe in *Fig. 10C*. In these line plots, the x-axis represents the Arc Length, which is the length of a cutline chosen to compute the deformation components point-by-point. Four different cutlines on the surface of the PDMS were chosen to prove the equi-biaxial nature of the deformation. By quantifying the deformation gradient for different cutlines, it did not change its values, meaning that the deformation was symmetric on the surface on the pillar. The result, indicating that the reconstructed deformation gradient has only elements on the principal diagonal, demonstrated that rotations and shear forces did not contribute to the deformation of the PDMS, while the only consistent transformation on the membrane was in the x-, y- and z-direction with pure stretching.

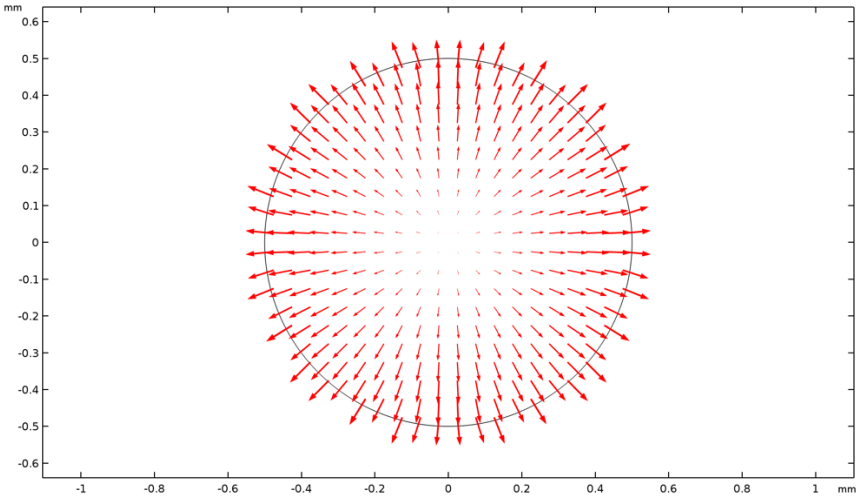

Figure 9 – The equi-biaxial deformation field and a deformation gradient were proved by the quantification of the principal strains on the surface of the PDMS deforming on the pillar surface.

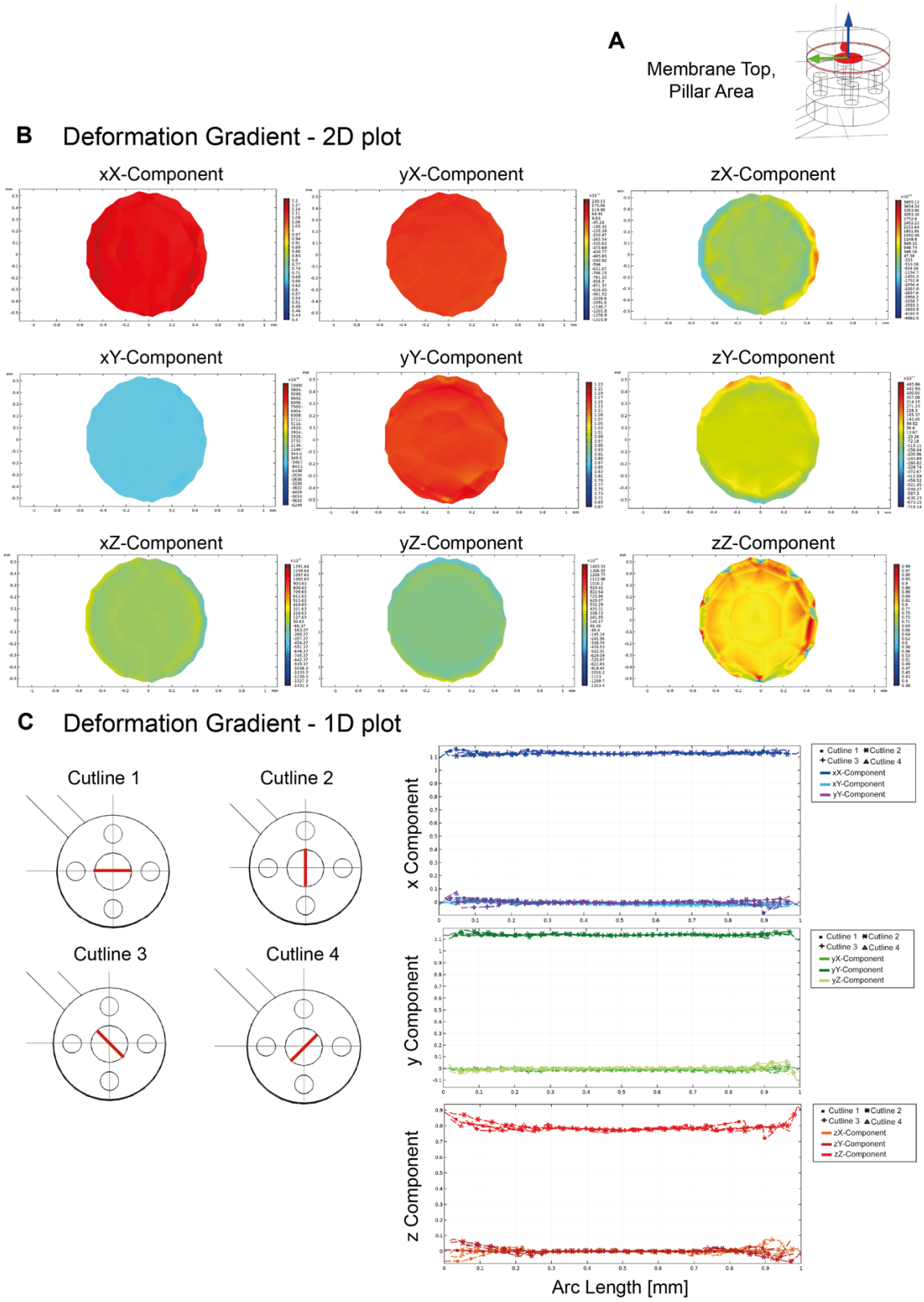

Figure 10 – The deformation gradient of the PDMS membrane under loading gave a measurement of the transformation arising in the structure. A) The deformation matrix was computed on the surface of the PDMS lying on the pillar. B) 2D plots of deformation gradient demonstrated that the non-zero components were those on the principal diagonal of the matrix, result confirmed by 1D line graphs (C), plotted along four cutlines to prove the equi-biaxial stretching of the PDMS on the surface of the pillar.

2.3.2 Design, fabrication and testing of the microfluidic platform

The CFD simulations allowed to validate the platform's working principle and to test the device's functionality. The results confirmed that the fluid dynamic design of the chamber and channels effectively facilitated the flow of culture medium for cell feeding without compromising cell survival, thanks to the maintenance of low shear stresses. Additionally, the mechanical stimulation unit was able to deliver equi-biaxial stimulation to the flexible PDMS membrane, positioned on the top of the cylindric pillar. This complex setup required a multi-layer structure to separately deliver air and culture medium flow that could also withstand the pressure reached without collapsing or changing channels and chamber cross-sections. Moreover, the device was designed as a two-chamber configuration aiming to simultaneously test the stimulated cell culture and the control cell culture. For these reasons, the material choice for the μP fell on poly(methyl methacrylate) (PMMA), a thermoplastic transparent plastic that is tough and lightweight, able to withstand to deformation, temperature and solvent variations, allowing the implementation the multi-layer logic without impairing the structure and shape of channels and chambers [5]. The use of this transparent material for the workpiece ensured a great accessibility to common microscopy instruments for real-time fluorescence checking of cell culture response/condition. The microfluidic device was produced with the aid of the micro-milling machine, which uses subtractive manufacturing procedures by means of a rotating tool, the endmill, that removes material from the bulk PMMA piece. The single PMMA layers were fabricated and then together bound together to build up the microfluidic elements of the device (*Fig. 11A-B*). The first layer of the platform was composed by the air flow channel and chamber to deliver the vacuum from the outside to the stimulation chamber and to distribute the negative pressures under the mechanical stimulation unit. The second layer comprised the small four channels for air splitting and enhancement of negative air pressures, and it was aligned with the underlying air vacuum chamber and the upper circular and hollowed chamber to position the holes on the symmetric side of the central rigid pillar of the deformation chamber. The last one was hollowed out in the third layer, onto which the deformable PDMS membrane was bound. The last layer was the ensemble of culture medium flow channels and chambers for both test sample and control sample. The test sample chamber was designed to align with the mechanical deformation unit so that the central area of the chamber fitted with the pillar surface: in this way, cells seeded and stimulated on the top of the deformable PDMS membrane sensed low shear stresses due to fluid flow, as already described in *Fig. 3*.

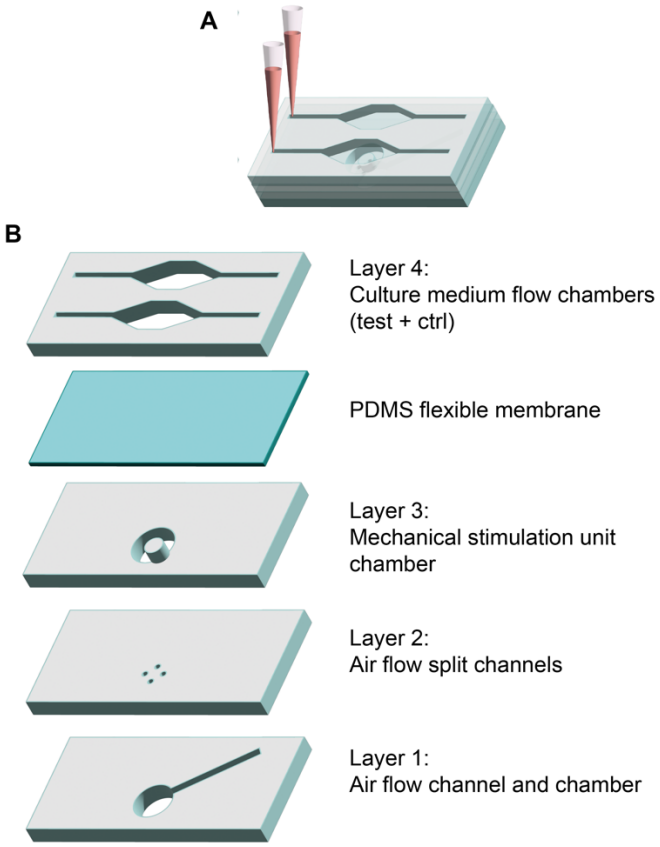

Figure 11 – μP fabrication working principle. A) The device was thought to analyze both tested cell culture and control cell culture in two separate chambers. B) The multi-layer logic was the ground of the fabrication. Different separate layers were fabricated and bound one on top of each other, to separate air flow for mechanical stimulation and liquid flow for cell culture seeding and feeding.

The mechanical part of the device consisted of a deformable membrane stimulated by the actuation of vacuum in the chamber below the membrane, as before mentioned. The chosen membrane material is polydimethylsiloxane (PDMS), a viscoelastic silicon-based polymer with good properties in terms of mechanical stability, chemical inertness, and non-toxicity, as well as transparency, biocompatibility and gas permeability [11]. All these features make PDMS a good candidate for the base material of a deformable membrane, as it might enhance cell survival with improved adhesion and oxygen exchange. It must also be transparent for bright field or laser-based imaging to track cell behavior directly in the microfluidic device. However, PDMS surface hydrophobicity represents a main drawback in its implementation in cell biology applications. Surface modifications or functionalization was addressed to improve PDMS hydrophilicity and adhesion to biomolecules [12], as explained in Chapter 3. The degree of polymerization affects its mechanical properties and different ratio of prepolymer/crosslinker should be used to obtain diverse elastic moduli. To achieve a large deformation range, a monomer/curing agent ratio of 20:1 (w/w) was chosen and a thin membrane was obtained by

spin-coating non-polymerized solution that was then cured at 80°C for 2 hours, completing the polymerization. By changing spin-coating parameters, e.g. speed, acceleration, and time [13], the membrane was characterized in terms of thickness, ultimately reaching a thickness of 40 µm (*Fig. 12*).

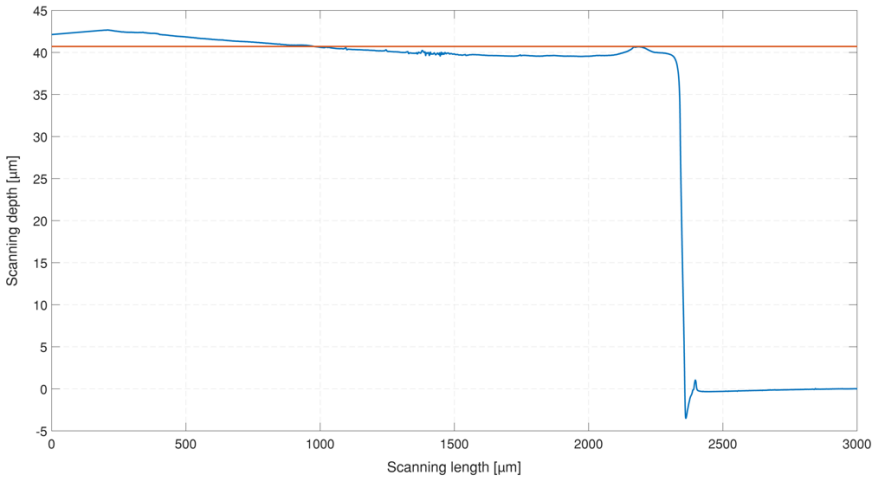

Figure 12 – Profilometer characterization of PDMS thickness after spin-coating on a rigid substrate.

To test the fluid dynamic shape of the culture medium chambers, a solution of water and fluorescent nanoparticles was flushed in the microchannels with a flow rate of 200 µL/min. From the panels in *Fig. 13* it is possible to appreciate that the high aspect ratio shape with mild discontinuities accomplished the fluid flow direction avoiding bubble formation both at the inlet and at the outlet of the culture medium chamber.

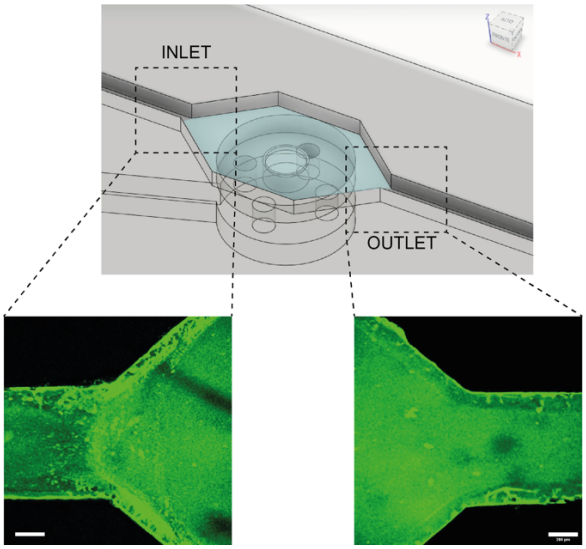

Figure 13 – The chamber shape accomplished the flow of fluorescent nanoparticles in water solution, avoiding the formation of bubbles. Scale bar 200 µm.

The mechanical properties of the deformed PDMS membrane were also evaluated. Initially, fluorescent nanoparticles were embedded in the uncured formulation of the PDMS 20:1. The resulting fluorescently labeled PDMS membrane was then bound with the PMMA microfluidic layers and sealed with the upper fluid flow chamber. An external setup for pressure control was used to deform the PDMS membrane through air suction and both brightfield (*Fig. 14A*) and fluorescence images (*Fig. 14B*) of the membrane deformation were acquired by confocal imaging. In particular, z-stacks and subsequent image reconstruction, along with data quantification (*Fig. 14C*) allowed computing the vertical lowering of the PDMS membrane in the hollowed cavity of the deformation chamber. By varying the inlet pressure of the pressure control system, a calibration curve was retrieved (*Fig. 14D*). It is noteworthy that the relationship between pressure and vertical displacement is not a linear function; instead, it can be described by a second-order polynomial curve.

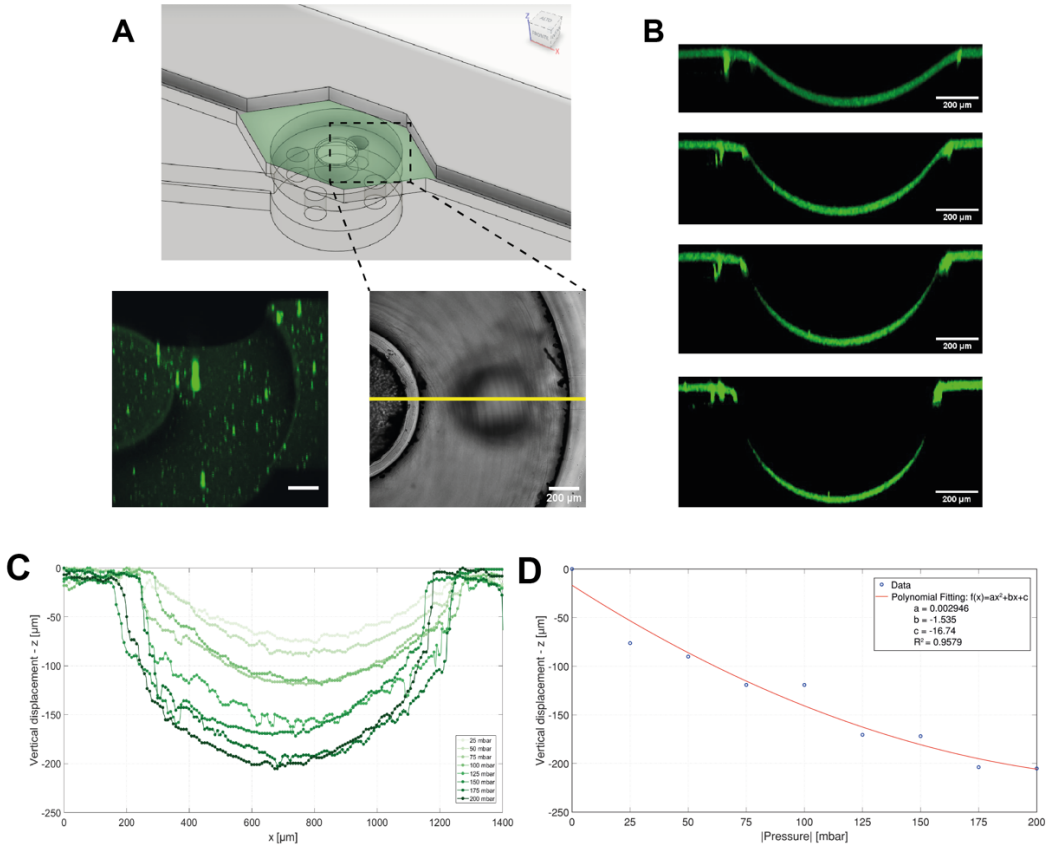

Figure 14 – The membrane lowering was assessed by embedding fluorescent nanoparticles in the uncured PDMS. By focusing the observation on a side of the deformation unit (A), confocal images of the membrane lowering can be reconstructed by changing the inlet pressure (B). C) Different vertical displacement values can be retrieved in dependence of the inlet pressure. D) A calibration curve vertical displacement-inlet pressure can be built to reconstruct the behavior of the PDMS membrane under deformation. Values of pressure are negative and considered in absolute value. Scale bar 200 µm.

Moreover, the device was able to couple biophysical signal to fluxes of substances. By flushing a water solution of fluorescent nanoparticles, the confocal acquisitions confirmed that the flow of fluorescent dye did not impair the deformability of the PDMS.

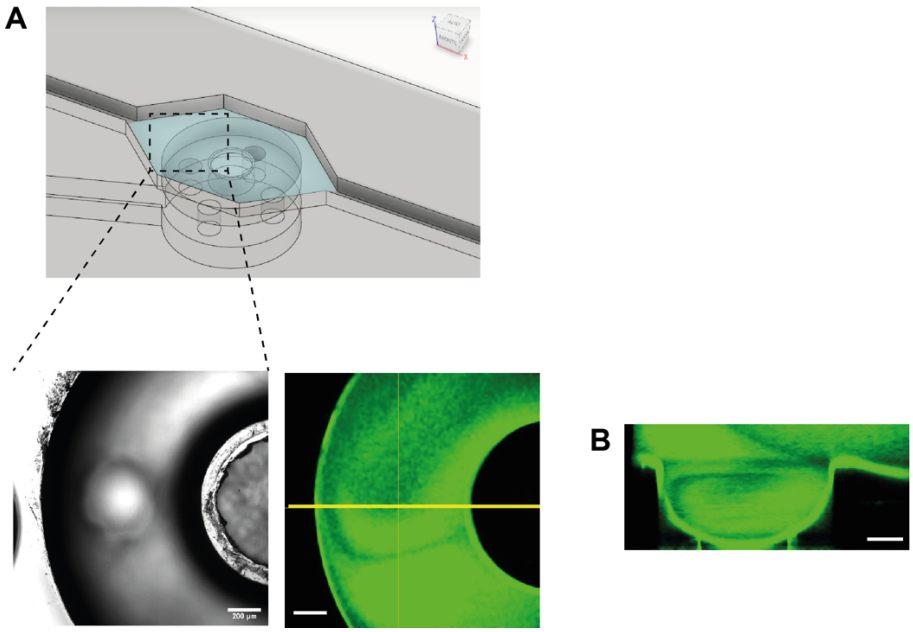

Figure 15 – The membrane lowering was assessed while flushing a water solution of fluorescent nanoparticles. B) The flux did not impair the PDMS membrane deformation. Scale bar 200 µm.

Regarding the deformation field developed on the surface of the pillar in the mechanical stimulation unit, after embedding fluorescent nanoparticles in the PDMS, their displacements on the device pillar were assessed over time. The deformation was imposed by an external pressure of withdraw equal to 200 mbar, and confocal images of the PDMS-embedded nanoparticle positions were acquired every minute for a total observation interval of 10 minutes. Tracking of the nanoparticle positions over time was performed through subsequent data analysis from confocal images (*Fig. 16A*). Windrose plots of the trajectories were built to observe the direction of movement of the nanoparticles, and consequently, the PDMS membrane, during the deformation. By translating all the trajectories to a common origin, which is the x-y axes origin in *Fig. 16B*, Windrose plots showed that the nanoparticles moved equally in radial directions in space, reveling the formation of an equi-biaxial deformation on the surface of the PDMS. To further confirm this result, Windrose diagrams of trajectory orientation occurrences were plotted both in a circular form in the x-y plane and in dependence on the mean orientation angle of the trajectory. The occurrences were distributed all above the x-y plane, with existing peaks due to the higher number of particles tracked in that region with respect to others. Consequently, a deformation map was generated from the initial and final positions of the

nanoparticle trajectories on the pillar surface, referring to the mechanical definition of strain as the difference between the initial and final length of the deformed object (*Fig. 16C, left panel*). In arrow representation, it is evident that the direction of the deformation followed the equi-biaxial stimulation, distributed in the θ-direction on the circular pillar, while the variable length of the arrows in the r-direction indicated variability in the deformation entity. A map of the displacements starting from the trajectories of the nanoparticles demonstrated that a displacement, i.e. deformation gradient, arose during the PDMS membrane deformation, with lower values at the center and higher values at the boundaries of the pillar moving in the r-direction (*Fig. 16C, right panel*). These results are validated by the simulation reported in *Fig. 9* and *Fig. 10*, respectively.

In conclusion, the presented setup achieved pure stretching stimulation on the deformable membrane, which could be tracked, enabling a detailed analysis of the stretching forces exerted on the cells seeded on this deformable membrane area.

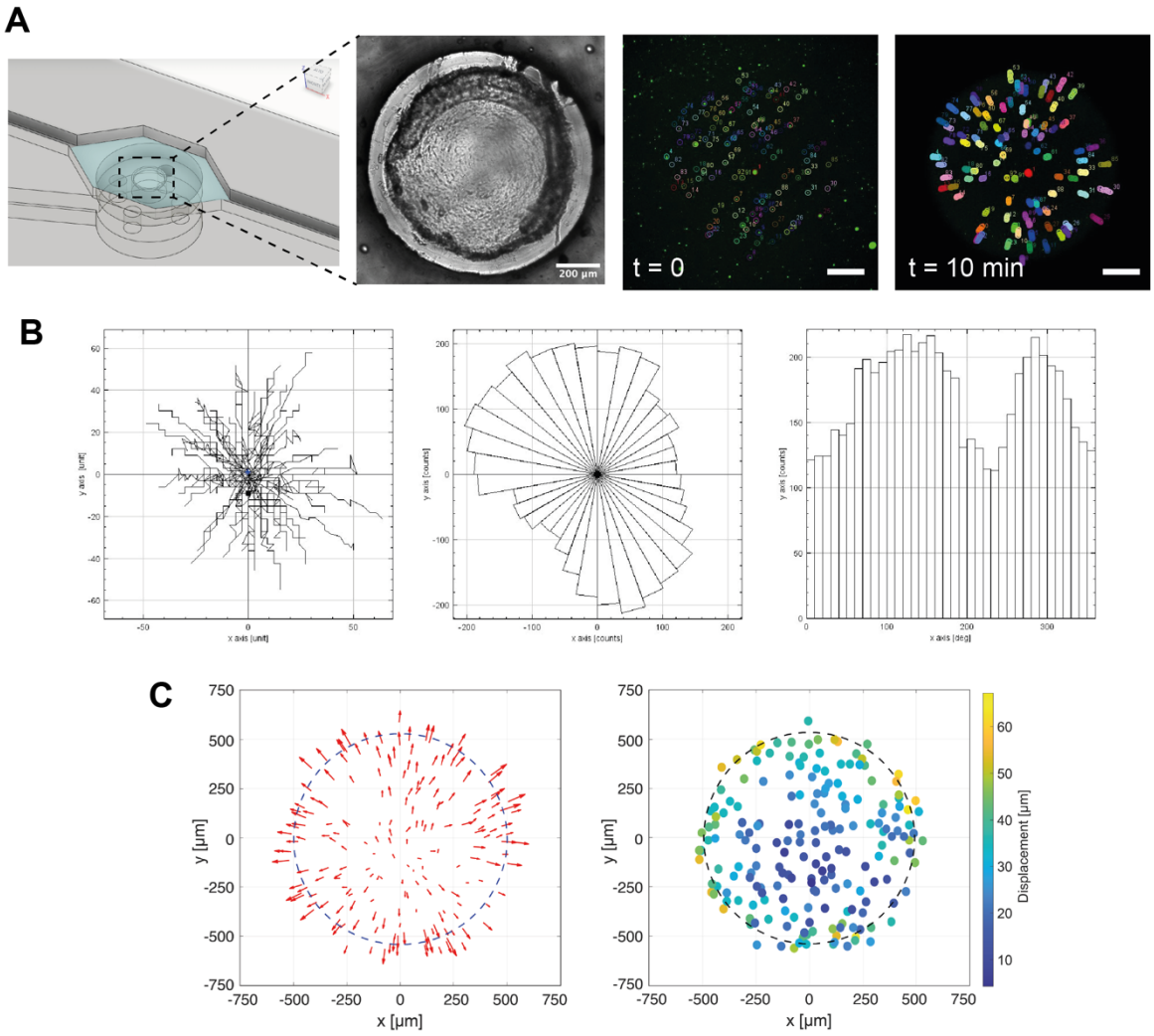

Figure 16 – The membrane deformation was tracked on the surface of the pillar, to find out an equi-biaxial deformation field on its surface. A) Nanoparticles embedded in the deformed PDMS were tracked in the time. The last two images are confocal representations of the particles position at time 0 and after 10 minutes of deformation. B) Position tracking in time allowed to reconstruct the orientation and distribution of the nanoparticle trajectories during the deformation. C) A deformation gradient was generated on the surface of the PDMS membrane over the device central pillar. Arrows represented the difference between the initial and final position of the trajectories during the tracking. The displacement map showed the difference in deformation values from the center to the boundary of the pillar. Scale bar 200 μm.

2.3.3 Design, fabrication and characterization of the micro-pattern

The topography of the cardiac microenvironment plays a crucial role in heart function and development, impacting cell behavior, tissue formation, and the overall physiological response of cardiac cells, as already described in Chapter 1. Topographic signals refer to the physical cues provided by the micro and nano-scale features of the cardiac extracellular matrix (ECM) and surrounding environment. In the heart, the precise alignment of CMs is critical for efficient heart contractions and electrical conductivity. Topographic cues from the ECM guide the orientation and alignment of these cells, ensuring that they contract in a coordinated manner to promote effective heart pumping. Given these considerations, a micro-pattern was reproduced on the surface of the PDMS to align the cardiac cell line in a proper manner, that reproduced the mechanical and topographic characteristics of cardiac tissue. A radial pattern was designed and fabricated using photolithography techniques to reproduce a precise geometry. The characteristic pattern structure consisted of a series of alternated ridges and grooves with maximum and minimum widths of 5 μm and 1 μm, respectively. The radial symmetry of the structure dictated the alternating arrangement of the stripes, giving an ordered pattern divided into sectors along the r-direction, where a specific organization was equally reproduced along the θ-direction. The thickness of the stripes was regulated by the photoresist spin coating and corresponded to 1 μm (*Fig. 17C*). The master micro-pattern was fabricated on a flexible substrate to facilitate handling during the alignment and peel-off procedure of the thin PDMS membrane in the microfluidic device bonding step. A positive photoresist was poured and spin-coated on a thin and flexible PMMA layer, cured and exposed to UV laser to reproduce the design of the desired micro-pattern. After exposure, the photoresist area exposed to the UV laser became soluble to the positive photoresist solvent, i.e. the developer, leaving only the unexposed areas after the development step. Subsequently, the non-crosslinked PDMS was poured, spin-

coated and cured on the surface of the micro-pattern master to obtain the thin 40 µm membrane. The flow chart of the master and PDMS molding fabrication is reported in *Fig. 17A*.

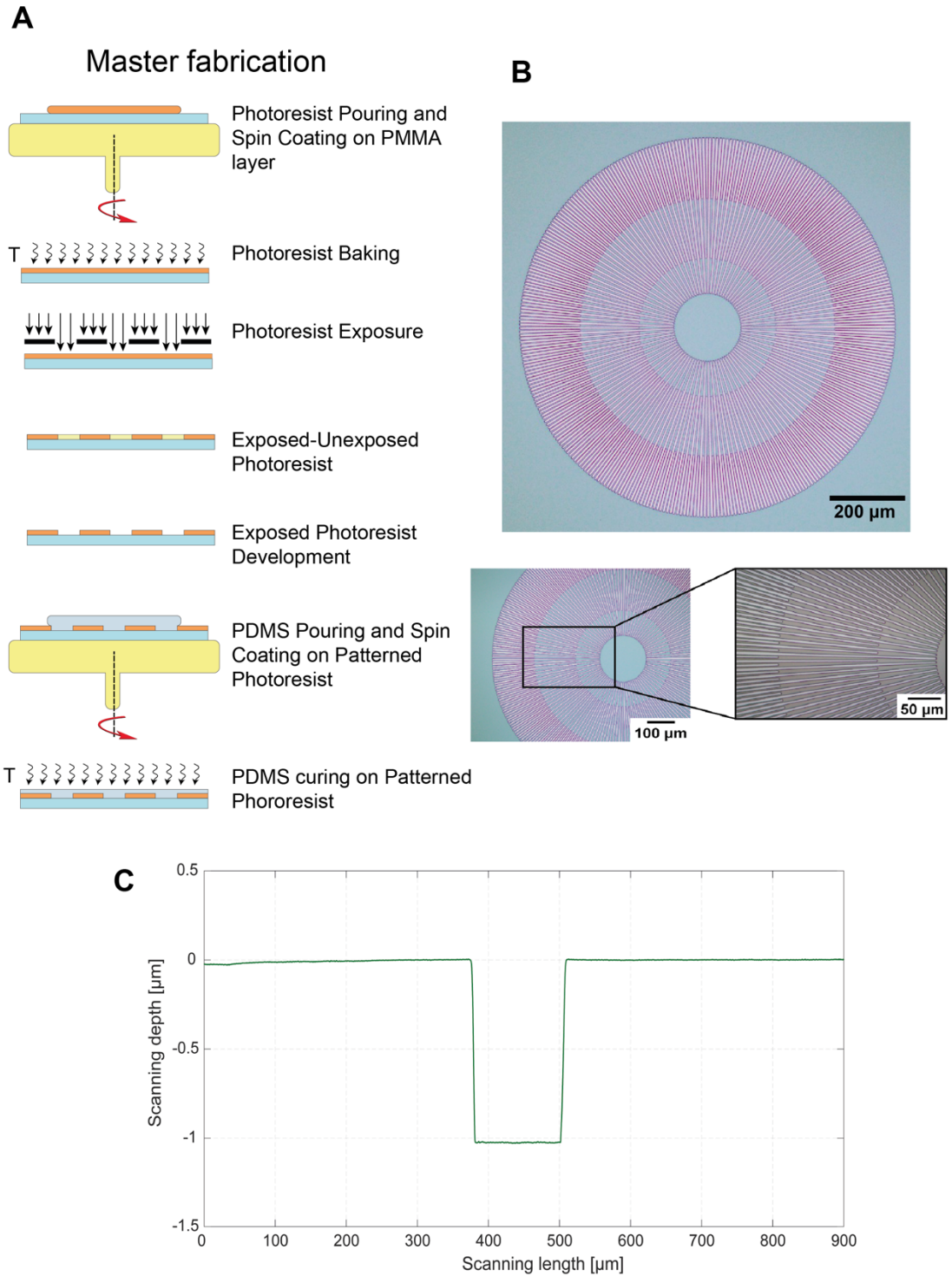

Figure 17 – Micro-pattern fabrication. A) Flow chart of the master and PDMS mold fabrication steps. B) Micro-pattern images of the master demonstrated the particular arrangement of the ridges and grooves along the r- and θ-direction. C) Profilometer measurement of the photoresist thickness after the spin-coating on the PMMA flexible substrate.

After the PDMS micro-patterned membrane fabrication, it was integrated in the μP (*Fig. 18A*). In particular, the circular pattern was aligned with the circular boundaries of the pillar in the mechanical deformation unit, allowing the application of the deformation field along the pattern direction. As already mentioned, the thin PMMA layer carrying the PDMS membrane facilitated both handling and alignment to the small area of the central pillar. After aligning the device and bonding it to the PMMA microchannels assembly, the PDMS membrane was peeled-off the PMMA-carrying layer, and the device was sealed with the top circuitry of micro-channels and chamber for culture medium fluid flow. Stereomicroscope images of the device-bound micro-patterned PDMS membrane are shown in *Fig. 18C,* illustrating the good alignment of the radial pattern with the underlying pillar circular surface. SEM imaging allowed the characterization of the morphology and dimensionality of the micro-patterned PDMS mold (*Fig. 18B-D)*. The front view of the micro-pattern revealed that the radial stripes were accurately reproduced during the molding step, with characteristic dimension of the stripes' width close to 5 μm. In contrast, a side view of the micro-pattern was captured to evaluate the height of the stripes, with a mean value around 1 μm. In conclusion, the fabrication technique employed for the micro-patterned PDMS membrane successfully produced a precise and well-defined structure, which can be easily introduced in a complex device to enrich the cell seeding chamber with different micro-environment signals, including mechanical and topographical stimulation in our case study.

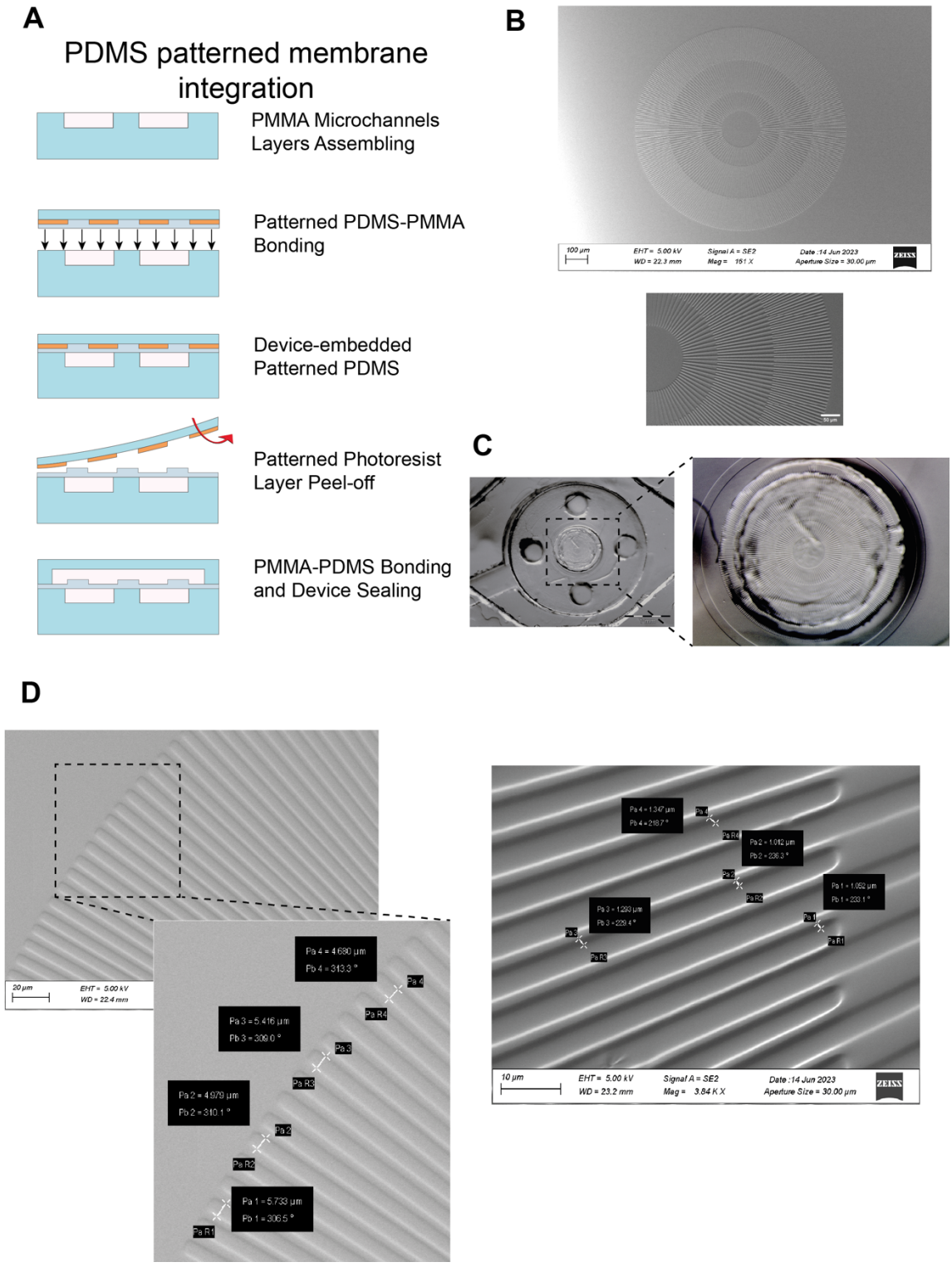

Figure 18 – Micro-pattern integration in the μP. A) Flow chart of the PDMS membrane bonding, peeling and embedding in the microfluidic device. B) SEM images of the whole micro-patterned PDMS and some details of the same PDMS mold. C) Stereomicroscope images of the patterned membrane directly in the μP, with a inset on the alignment to the circular pillar of the deformation chamber. D) SEM images and characterization of PDMS mold stripes width and height, which were well-reproducing the designed master micro-pattern.

References

1. Ho, K. K. Y., Wang, Y. L., Wu, J. & Liu, A. P. Advanced Microfluidic Device Designed for Cyclic Compression of Single Adherent Cells. Front Bioeng Biotechnol 6, (2018).
2. Zhang, D. et al. Microfabrication of polydimethylsiloxane–parylene hybrid microelectrode array integrated into a multi-organ-on-a-chip. Jpn J Appl Phys 62, 017002 (2023).
3. Briones, J. et al. A design and optimization of a high throughput valve based microfluidic device for single cell compartmentalization and analysis. Sci Rep 11, 12995 (2021).
4. Kim, T. K., Kim, J. K. & Jeong, O. C. Measurement of nonlinear mechanical properties of PDMS elastomer. Microelectron Eng 88, 1982–1985 (2011).
5. Faghih, M. M. & Sharp, M. K. Solvent-based bonding of PMMA–PMMA for microfluidic applications. Microsystem Technologies 25, 3547–3558 (2019).
6. Bamshad, A., Nikfarjam, A. & Khaleghi, H. A new simple and fast thermally-solvent assisted method to bond PMMA–PMMA in micro-fluidics devices. Journal of Micromechanics and Microengineering 26, 065017 (2016).
7. Norouzi, A. R., Nikfarjam, A. & Hajghassem, H. PDMS–PMMA bonding improvement using SiO2 intermediate layer and its application in fabricating gas micro valves. Microsystem Technologies 24, 2727–2736 (2018).
8. Criscuolo, V. et al. Double-Framed Thin Elastomer Devices. ACS Appl Mater Interfaces 12, 55255–55261 (2020).
9. Tabeling, P. Introduction to Microfluidics. (Oxford University PressOxford, 2023). doi:10.1093/oso/9780192845306.001.0001.
10. Fridtjov Irgens. Continuum Mechanics. (Springer Berlin Heidelberg, Berlin, Heidelberg, 2008). doi:10.1007/978-3-540-74298-2.
11. Seghir, R. & Arscott, S. Extended PDMS stiffness range for flexible systems. Sens Actuators A Phys 230, 33–39 (2015).
12. Akther, F., Yakob, S. B., Nguyen, N.-T. & Ta, H. T. Surface Modification Techniques for Endothelial Cell Seeding in PDMS Microfluidic Devices. Biosensors (Basel) 10, 182 (2020).
13. Vannozzi, L. et al. Self-assembly of polydimethylsiloxane structures from 2D to 3D for bio-hybrid actuation. Bioinspir Biomim 10, 056001 (2015).

Chapter 3:
Cardiomyocytes response to the microenvironment cues in microfluidics

3.1 Introduction

Replicating the cardiac cell microenvironment *in vitro* is a pivotal work in the field of cardiovascular research, offering profound insights into the fundamental mechanisms of heart function and disease. Microfluidic technology plays a crucial role in this pursuit, providing a versatile platform for recreating and precisely controlling the complex array of signals that cardiac cells encounter *in vivo*. By mimicking the native cardiac environment, researchers can gain a deeper understanding of cardiac cell behavior, paving the way for novel therapeutic strategies and advancing tissue engineering. Cardiac cells are highly responsive to their extracellular environment, with ECM composition, mechanical forces, and electrical signals all playing integral roles in determining their function, morphology, and fate. The ECM not only provides structural support but also influences cell orientation, crucial for the contraction of cardiac tissue, which is dependent on the tissue anisotropic directionally. The alignment of CMs, in concert with fibroblasts and other cardiac cells, is essential for the synchronized contraction that leads blood efficiently through the heart and vascular system. In addition, the complex 3D arrangement of the cardiac tissue from the endocardium to the epicardium faces a total helicoidal arrangement of cardiac fibers and cells, which cannot be properly recapitulated *in vitro* by uniaxial geometries for CMs alignment. In fact, the cardiac tissue functionality and contractility depends on the combination of local anisotropy of the myocardial fibers arrangement and total helicoidal organization of the 3D structure [1,2].

Mechanical signals, arising both from the contractile activity of the heart itself and from external forces applied to the cardiac tissue, further regulate CMs behavior. These signals include shear stress from blood flow, stretching due to the heart's filling and contracting, and compression forces. CMs respond to these mechanical cues through mechanotransduction pathways, leading to changes in gene expression, protein synthesis and cell morphology. This adaptive response is critical for the maintenance of cardiac function and the heart's ability to respond to physiological and pathological stimuli. Moreover, due to this complex interplay of cells, ECM and external environment, the mechanical machinery of the heart is a combination of longitudinal,

circumferential and radial components of the myocardial tissue deformation field [3], adding further complexity to the recapitulation of the mechanical identity of the cardiac microenvironment, which cannot be well represented by simple uniaxial stretching. Microfluidics offers the opportunity to study these complex interactions by enabling the creation of defined, controllable microenvironments. This technology allows for the precise application of mechanical stimuli, such as cyclic stretch, and the presentation of ECM components in defined orientations and compositions. Furthermore, the integration of μPs with live-cell imaging and biosensors enables real-time monitoring of CMs behavior and function in response to environmental cues. This dynamic observation sheds light on the immediate and long-term effects of mechanical and biochemical signals on cardiac cells, offering a window into the cellular processes that underlie cardiac physiology and pathology.

In our μP, we have successfully demonstrated that CMs can grow aligned according to the specifically designed micropatterns. These patterns were engineered to achieve anisotropic alignment at the cellular level and radial organization at the population level, and to align the CMs along the stretching direction, mimicking the natural orientation, structure and behavior of cardiac tissue. This structured environment enables CMs to migrate in a directed manner when subjected to mechanical stimuli on the pattern, showing persistent movement during deformation attributable to the designed pattern. Further investigations into the CMs functional responses revealed significant insights into their beating activity, particularly in terms of calcium influx, under mechanical stimulation. We evaluated the effects of both continuous and cyclic mechanical stimulation on CMs cultured on flat and patterned substrates. The results indicated that cyclic stimulation notably enhances the CMs' contractile activity. Moreover, the presence of the micropattern facilitated the propagation of calcium waves across the cell population. This phenomenon underscores the importance of physical cues in modulating the physiological responses of cardiac cells, with the pattern playing a crucial role in synchronizing and amplifying their contractile behavior. This intricate interplay between mechanical stimulation and pattern-induced alignment offers a powerful tool for dissecting the mechanobiological processes underlying cardiac function. In fact, by closely simulating the physical and mechanical cues present in the cardiac environment, our μP provides a valuable model for studying cardiomyocyte behavior in a controlled setting.

3.2 Materials and Methods

3.2.1 Device sterilization and functionalization

The microfluidic device underwent sterilization by flushing different solutions after fabrication, sealing and prior to cell seeding and culture. This process included flushing the inlet and outlet micro-channels, as well as the cell seeding chamber, to sterilize the area where the culture medium flows. In the first step of the sterilization, 70% ethanol was flushed and left for 5 minutes, followed by three washes with deionized water to remove the excess ethanol. After that, a solution of the antibiotic Penicillin-Streptomycin (P/S) (Merck) in phosphate buffer saline (PBS) with a 1:2 ratio was used to rinse three times the channels and chambers and at the fourth flush it was left in the channels for 6 minutes. This step was repeated three times, and after that two washes with PBS were performed to completely remove the antibiotic solution. The device and its micro-channels were left to dry under laminar flow in a biological hood under sterile conditions and were further exposed to UV light for 1 h to sterilize the external surfaces of the platform.

After the complete evaporation of the solvents, the functionalization of the device-embedded PDMS was performed using a protein from the ECM, specifically fibronectin, just before cell seeding. A solution of 0.1% fibronectin from human plasma (Merck) in sterile PBS at different final concentrations was prepared and flushed into the micro-channels. The device was then sealed with custom-made sterile connectors and incubated at 37°C for 1 h, leaving the fibronectin protein to precipitate and rinse the inner surface of the PDMS. After the fixed incubation time, the fibronectin solution was removed, and the channels and chambers were washed twice with complete cell culture medium. Then, complete culture medium was left in the device that was incubated at 37°C until the cell seeding procedure, enabling other proteins from the culture medium to precipitate on the surface of the functionalized PDMS.

3.2.2 HL-1 cell culture

HL-1 CMs were seeded according to the protocols reported in the work of Claycomb et al. [4]. They were seeded and left to grow in T-25 flask, supplementing their culture medium with Claycomb medium (Merck), 10% fetal bovine serum (FBS), 1% P/S at a final concentration of 100 units penicillin/mL and 100 µg streptomycin/mL, 1% L-glutamine 200 mM (Biowest) at a final concentration of 2 mM, and 1% norepinephrine solution at a final concentration of 0.1 mM.

The norepinephrine solution was used to maintain the contractility phenotype of the HL-1 CMs and was prepared dissolving 80 mg of norepinephrine powder in 20 mL of a 30mM ascorbic acid aqueous solution. Prior to culture medium addition, the norepinephrine solution was filtered with a 0.22 µm syringe filter, similarly to the complete culture medium. After medium preparation, it was stored in the dark and used to feed cells every two days and let them grow in the incubator set at 37°C, 5% CO_2 and 95% humidity. When cells reached 80% confluency on the culture substrate, they were detached with 0.25% Trypsin-EDTA (Merck) through incubation for 5 minutes at 37°C. They were then collected with complete culture medium to inactivate the enzymatic activity of the Trypsin and transferred to a tube for centrifugation at 1000 rpm for 5 minutes. Lastly, the supernatant was removed and exchanged with pre-warmed culture medium to resuspend the cell pellet. For cell seeding, cell numbers were manually counted using a Neubauer chamber.

3.2.3 Cells seeding in the microfluidic platform

After device sterilization and functionalization as already described in paragraph 3.2.1, HL-1 cells were detached from T-25 flask, counted, and resuspended in pre-warmed culture medium to accomplish the desired seeding density for the programmed experiment. A cell suspension of 300 µL was introduced into the inlet channel of the device to completely fill the seeding chamber, outlet and inlet channels. The seeded device was sealed with sterile connectors, incubated at 37°C, 5% CO_2 and 95% humidity, allowing cells to adhere to the functionalized PDMS for 4 h. After, the first medium exchange was performed with pre-warmed complete culture medium, and, lately, it was performed every day.

3.2.4 Cells stimulation

For experiments related to topography alignment quantification, HL-1 cells were seeded on micro-patterned PDMS, embedded in the device, at a concentration of $2 \cdot 10^5$ cells/mL. Morphologic alignment was quantified after 24 h of cell seeding by fixing the samples and staining f-actin and nuclei, as reported in section 3.2.5.

In migration experiments, HL-1 cells were seeded on devices enriched with flat and patterned PDMS at a density of $2 \cdot 10^5$ cells/mL. After 24 h of cell seeding, the devices were moved to a microscope-associated incubation chamber with controlled temperature, maintained at 37°C during the stimulation experiments. To maintain pH conditions suitable for cell culture and

sustain the CO_2 level sustenance, Hepes solution 1M (Merck) was added to the complete culture medium. The air flow channel was connected to the external pressure controller and a continuous pressure of -200 mbar was delivered for 1 h to the device, in order to the deform the PDMS substrate and subsequently apply equi-biaxial stimulation to the HL-1 cells seeded on top of the pillar area. Nuclei were stained and tracked as reported in section 3.2.5 and 3.2.7.
In contractility experiments, HL-1 CMs were seeded in the device with an increased cell density of $2.5 \cdot 10^5$ cells/mL to improve the cell-cell communication and propagation of calcium wave. Both flat and patterned PDMS were used, and stimulation was applied after 24 h of seeding, under the same conditions as the migration experiments. The pressure controller deformed the substrate, applying both continuous and cyclic pressure profiles. The cyclic deformation followed a sinusoidal waveform at a frequency of 0.1 Hz and amplitude equal to -200 mbar. Stimulation was applied for 1 h, 2 h and 3 h for cells seeded on patterned PDMS, both in continuous and cyclic deformation. The samples were stained following the Calcium imaging protocol in section 3.2.5.

3.2.5 Cells staining and confocal imaging

Cells were stained and their behavior was tracked by acquiring images with confocal microscopes. For the results regarding the response of the HL-1 cells to fibronectin functionalization, cells were stained with Hoechst 33342. Culture medium was removed, cells were washed twice in PBS to remove medium residuals and rinsing the sample for 10 minutes in a solution of Hoechst-PBS (1:10000). The solution was removed, washed twice in PBS and samples were rinsed in culture medium. Subsequently, they were acquired with a 10x objective of an EVOS microscope (FL Cell Imaging System, Thermo Fisher Scientific) under live-imaging acquisitions. The procedure was repeated at 24, 48 and 72 h after substrate functionalization and cell seeding. The same staining procedure with Hoechst 33342 was applied to track HL-1 cells' migration on flat and patterned device-embedded PDMS under mechanical deformation for 1 h. Live-imaging of cell nuclei was applied through acquisition made by a confocal Laser Scanning Microscope (LSM) 900 model (Zeiss), with a 10x objective. Hoechst was excited with a 350 nm laser, and brightfield images of the PDMS membrane on the device pillar were acquired to track the precise positions of cells during the migration.
For live-dead assay, HL-1 cells were stained to detect vital and non-vital cells in response to topographic signal. This was done with simultaneous staining through Calcein AM and Propidium Iodide (PI), respectively. Calcein AM is a non-fluorescent dye that selectively labels

cells in vital conditions, converting into a green-fluorescent probe after cleavage of acetoxymethyl ester by intracellular esterases. PI is used to detect dead cells through its binding with DNA. Samples were washed twice in PBS and incubated for 15 minutes with a solution of the probes in PBS. In particular, Calcein AM was used in a proportion 1:1000 (final concentration 1 µg/mL) and PI in 1:100, from 1 mg/mL of PI stock solution (final concentration 10 µg/mL). Then, the samples were washed twice in PBS and rinsed in culture medium for live-imaging acquisition, performed by a Leica TCS SP 5 (Leica Microsystems). Calcein AM was excited with a 488 nm laser, emitting in the range (495-515) nm, while PI was excited at 555 nm and read in the range of emission (528-617) nm. Samples were taken in both fluorescence and with the brightfield acquisition for micro-patetrn detection, all with a 10x objective.
For alignment experiments on patterned PDMS, cells were seeded for 24 h and then fixed, following the procedure reported below. Culture medium was removed and washed twice with pre-warmed PBS. Afterwards, cells were fixed in 4% paraformaldehyde (PFA) in PBS for 15 minutes at room temperature. PFA was removed and washed three times in PBS. To permeabilize the cells and provide stain access to the cell membrane, 0.1% Triton X-100 in PBS was used for 10 minutes at 4°C. Samples were washed twice in PBS and stained. A solution of Hoechst 33342 in PBS 1:10000 was used to rinse the fixed samples for 20 minutes, avoiding direct exposure to light. Then, the solution was removed and washed with PBS. A solution of Phalloidin 555 (Abcam) in PBS 1:1000 was exposed to the sample for 1 hour in light-shielded environment, and the samples were then washed and preserved in PBS under humid conditions at 4°C. Imaging of the samples was carried out through a confocal Laser Scanning Microscope (LSM) 900 model (Zeiss) with a 10x objective. Phalloidin was excited with a 555 nm wavelength laser and acquired in the range (570÷600) nm, while Hoechst was excited with a 350 nm wavelength and acquired up to a maximum wavelength of 461 nm. Brightfield images were also acquired to define the precise position and orientation of the cells above the micro-pattern.

3.2.6 Calcium imaging

HL-1 cells Ca^{2+} imaging experiments were conducted to deeply study the dynamics of ions in the cells after the application of topographical and mechanical stimulations. Cells seeded on flat and patterned PDMS membranes, outside the device and directly in the µP, were washed twice in PBS and incubated with a 2 µM Fluo-4 AM (Thermo Fisher Scientific) in PBS for 30 minutes, following the stimulation times fixed in the paragraph 3.3.2 . After the incubation under cell culture conditions, the staining solutions was washed twice in PBS and incubated for 30 minutes

in complete culture medium prior to imaging. Time-series live imaging was applied to the stained and stimulated samples with the LSM 900. Ca^{2+} flux was tracked by exciting with a 488 nm laser and reading in the range of emission (495÷515) nm. Images were taken with a 10x objective for 30 s, fixing the frame time to 200 ms and utilizing a high scan speed of acquisition to capture, in different time points, the intracellular beating and the wave progression at the cell population level.

After the acquisition of time frames, the beating activity and propagation wave of Ca^{2+} were analyzed by developing suitable MATLAB codes. Images were extracted and analyzed first with ImageJ, where the intracellular beating activity was computed by selecting areas of the cell cytoplasm (region of interest, ROI). Z-axis profiling was employed to evaluate fluorescence intensity oscillation over time by providing the mean value within the selected ROI for every slice in the stack. Values were extracted and plotted with MATLAB. The frequency of beating was computed for each sample by extracting and counting the peak values of fluorescence intensity from the previous plots. The propagation wave was quantified by extracting activation maps from the confocal time series of 30 s for each sample of interest. First, an image scaling was carried out to retrieve images that could be easily managed during data analysis and to reduce the area of a cell to a single pixel. For instance, a 256x256 pixel image was reduced to a 55x55 pixel image, utilizing a bicubic interpolation method, in which the pixel output is the weighted mean of the pixel in a region made by a 4x4 pixels matrix. Afterwards, the mean fluorescence intensity of each frame in time was computed to extract the so-called events, defined as the number of time frames of maximum intensity. Practically, the events were extracted as the values of fluorescence intensity above a certain threshold, which is the activation threshold. An array of events was built, in which each element was a single matrix containing fluorescence intensity values of the event and the corresponding frames. From this matrix, the activation map was retrieved by computing the frame at which the activation wave reached each pixel of the image. An image for each event was retrieved and it was represented as a 2D map of pixels in which the pixel color indicated the frame number activated in that pixel during the wave progression. By multiplying the frame number for the period of observation between frames (200 ms), the activation time was retrieved, and the activation map was represented in function of the activation time. The propagation velocity was computed for each event by extracting the centroid of each area of activation and by computing the vectorial distance between two consecutives centroids.

3.2.7 Images and data analysis

All the confocal images were extracted and analyzed by ImageJ and quantification plots were performed by exploiting MATLAB codes.

Curves of cell proliferation in the time were built by automatically counting nuclei after image thresholding, using the ImageJ Analyze particles command. Percentage values of cell proliferation were extracted from the cell number count normalized with respect to the number of seeded cells at time zero.

Live-dead quantification was performed by exploiting ilastik, an open-source software for learning and segmentation of images. The pixel classification unit was used to assign labels to the pixel of the image based on some features. The training of the classifier allowed iterative drawing of the objects to be recognized, including the single labels, i.e. pixel class that should be separated from other, for live cells (in green), dead cells (in red), and background (in black). Then, by running the feature selection and extracting the automatic segmentation, green and red cells were separated in different images and counted with the Analyze particles tool of ImageJ. Their values were normalized with respect to the total number of the cells, considering both live and dead cells, and plotted in percentage.

Orientation maps of cell f-actin on the micro-patterned PDMS substrates were extracted using the OrientationJ plugin of ImageJ. This plugin calculated the structure tensor of the image, retrieving orientation, coherency and energy from the images. At the end, the image analysis generated a color map of the cells f-actin, in which the color tonality indicates the orientation, following the color-coded map reported in Fig. 3. The occurrences of the orientations were also counted and plotted to highlight the preferential orientations of the actin fibers distribution among the micro-pattern.

From the single images of nuclei and f-actin per cell, Directionality plugin of ImageJ allowed the extraction of the dominant orientation of these structures within the provided image. It generated a histogram that displays the distribution of structures according to their orientation, with the highest peak modeled using a Gaussian function. The Direction values retrieved from the analysis are the Gaussian's central points, providing information on the mean orientation of the structure. By extracting these values of Direction and by plotting their histogram by MATLAB, a fitting with a Gaussian distribution was performed to assess the angular alignment mean orientation. This orientation is the difference between the mean orientation of nucleus or f-actin of the cells contained in a single sector with respect to the sector orientation, as explained

in 3.3.2. A linear fit with MATLAB code was also applied to the orientation of nuclei and f-actins with respect to the sector orientation.

TrackMate is an ImageJ tracking tool utilized in our application to automate the segmentation and tracking of HL-1 cell migration on the deformed PDMS under equi-biaxial mechanical stimulation. The first step of the tracking involves selecting the detector for spots research, where the LoG Detector is employed. This detector applies a plain Laplacian of a Gaussian filter to the image: it is obtained by summing the second order spatial derivatives of the image filtered by the Gaussian (operator G). Cell detection was performed by local maxima recognition in the filtered image. After this, a mapping is performed to retrieve the physical coordinates of the cell in the source image. Regarding the selection of the tracker, in TrackMate the detected spots are linked by exploiting a two-steps algorithm: segments of the trajectory that link the spots from a frame to the next one are created, followed by the segments connection in order to reach the closing of potential gaps between consecutive segments. When the tracking is completed, the Analysis button of TrackMate allows for a review of key parameters. After the extraction of trajectories positions in time, Chemotaxis and Migration tool of ImageJ was used to build Windrose diagrams. They were exploited to observe the count of the trajectories number in a specific direction of the same plane, to determine the directionality adopted by the cells during the migration phenomenon on both flat and patterned substrates under deformation. Mean cell velocities were retrieved from the positions and plotted following Lognormal distributions of probability density function in MATLAB. The peak values of the probabilities distributions were considered the mean velocities of migrating cells per group.

Statistical parameters of the migration were also retrieved from the tracking parameters. In particular, mean squared displacement (MSD) was computed from the cell trajectories, as:

$$MSD(t_i) = \langle [(x(t + t_i) - x(t))^2 + (y(t + t_i) - y(t))^2] \rangle \qquad (Eq.\ 1)$$

MSD was plotted against the lag times (t_i) in log-log representation, which are the time points of the acquisitions, and the slope was computed from linear curve fitting, to demonstrate the super-diffusive, sub-diffusive or simple diffusive behavior of migrating cells. In its general definition:

$$MSD = 6\,\mathcal{D}\tau \qquad (Eq.\ 2)$$

Where $\mathcal{D}$ is the diffusion coefficient of the moving elements, τ is the lag time and α is the slope of the MSD curve respect to the lag time. This kind of proportionality between MSD and the time lag allowed to retrieve diffusion coefficient as another statistical parameter of HL-1 migration.

3.2.8 Statistical data analysis

The experiments were performed three times per group and the results were statistically tested by using t-test in MATLAB to find out significant differences in each group. Statistical significance was set by fixing p at 0.05. p values less than 0.05 were considered significant.

3.3 Results and discussion

3.3.1 HL-1 cells survival in the microfluidic platform

HL-1 CMs were seeded onto the stimulation platform after the functionalization with ECM proteins to enhance the compatibility of the PDMS substrate for cell adhesion and survival. Fibronectin was chosen as the ECM protein for HL-1 attachment, and three different concentrations of the macromolecule in PBS were tested within 72 h to determine the concentration that yielded the highest cell survival and proliferation percentage. Results indicated that the lowest fibronectin concentration (1 μg/mL) decreased HL-1 proliferation percentage within 24 h after seeding, but slightly increased cell survival after 48 and 72 h. This effect was likely due to the shedding of non-adherent cells, resulting in negative proliferation after 24 h and increased proliferation at longer times due to duplication of residual adherent cells (*Fig. 1B*). In contrast, the other two concentrations significantly improved HL-1 proliferation on PDMS. A fibronectin concentration of 10 μg/mL doubled the cell number after 72 h, while the concentration of 100 μg/mL doubled the proliferation percentage already within 24 h after cell seeding. Considering the physiologic behavior of HL-1 cells in conventional culture plate, with a cell doubling time of 48 h, an intermediate concentration of fibronectin (50 μg/mL) was chosen to appropriately enhance HL-1 cells adherence to PDMS substrates. Literature studies demonstrated that fibronectin treatment is the most effective for HL-1 cells survival, ensuring the highest levels of both cell adhesion and proliferation compared to other ECM proteins, such as collagen, gelatin and laminin, which instead exhibited lower performances in terms of cell proliferation [5]. This cell response to fibronectin is likely associated with the enhanced exposure of fibronectin cell-adhesive motifs on the PDMS surface, related to an index of fibronectin orientation at the outermost surface. This orientation is directly related to the nanoscale surface stiffness of PDMS, which demonstrated to be relatively high in PDMS with 20:1 ratio of prepolymer to crosslinker in previous studies [6].

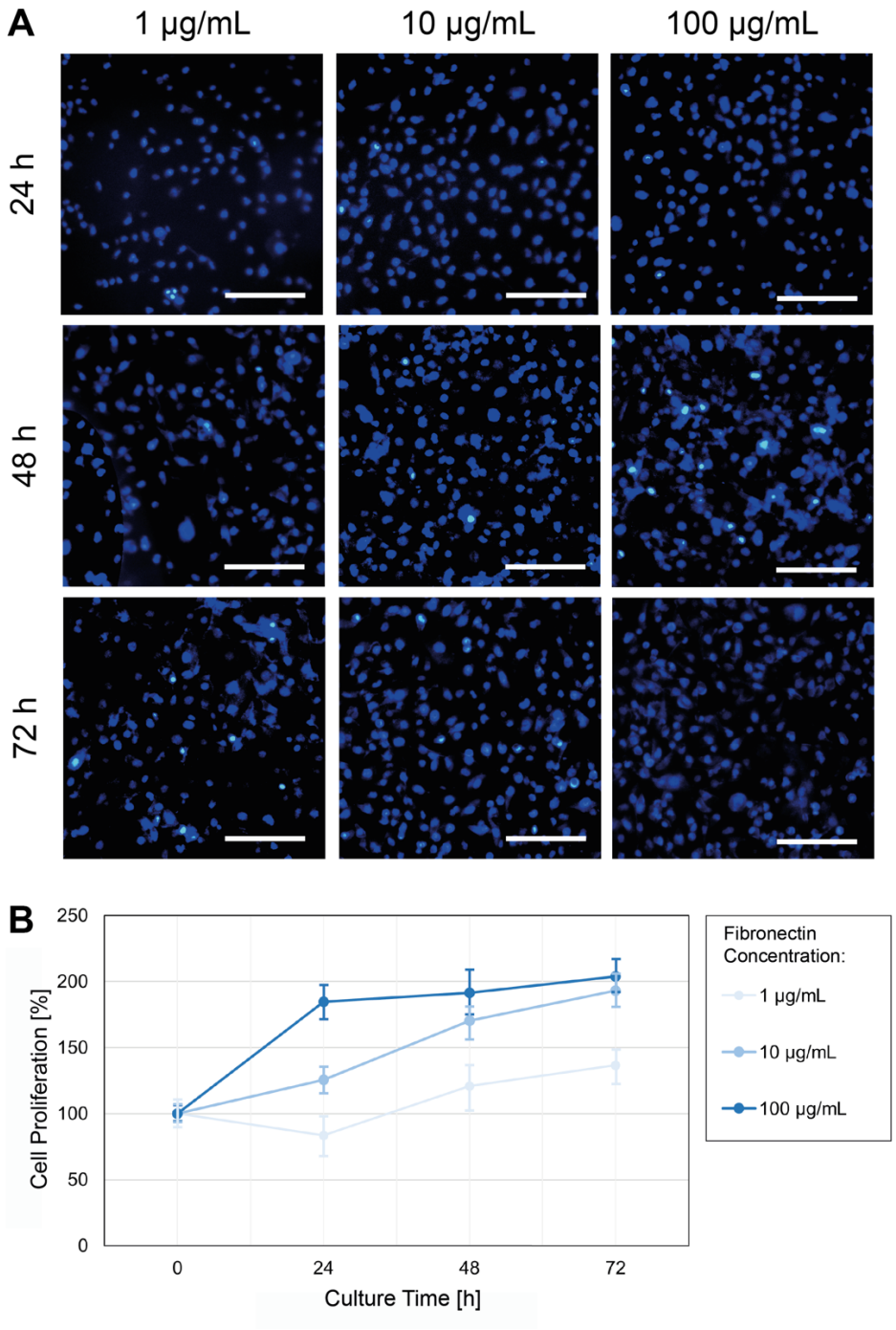

Figure 1 – Fibronectin PDMS functionalization improved cell proliferation. A) EVOS images of time evolution from 24 h to 72 h of HL-1 nuclei stained with Hoechst 33342 (blue) and seeded on PDMS functionalized with different concentrations of fibronectin. B) By varying fibronectin concentration the proliferation rate changed, leading to impaired HL-1 survival and proliferation at low concentration (1 µg/mL) and enhanced vitality for both 10 and 100 µg/mL of fibronectin concentration. Values of proliferation related to 100% corresponded to the cells seeding density at the starting point (time 0). Scale bar equal to 200 µm.

Cell survival was assessed using a live-dead assay, where HL-1 cells were stained with both Calcein-AM and PI to determine the percentage of cell survival over mortality resulting from

interaction with the PDMS substrate. The assay on flat substrate demonstrated the device's potentiality to support cell survival after fibronectin functionalization and 24 h of seeding (*Fig. 2 – CTRL samples*). Moreover, to test the ability of the device to improve cell survival, live-dead assay was repeated by changing the cell seeding density. The results showed that cell vitality was not impaired, even at half of the seeding density. For comparison, HL-1 survival was also tested on patterned PDMS after 24 h of seeding and the enhanced predominance of vital cells over death cells is evident also on patterned PDMS, as shown from bar plot in *Fig. 2 -Pattern samples*.

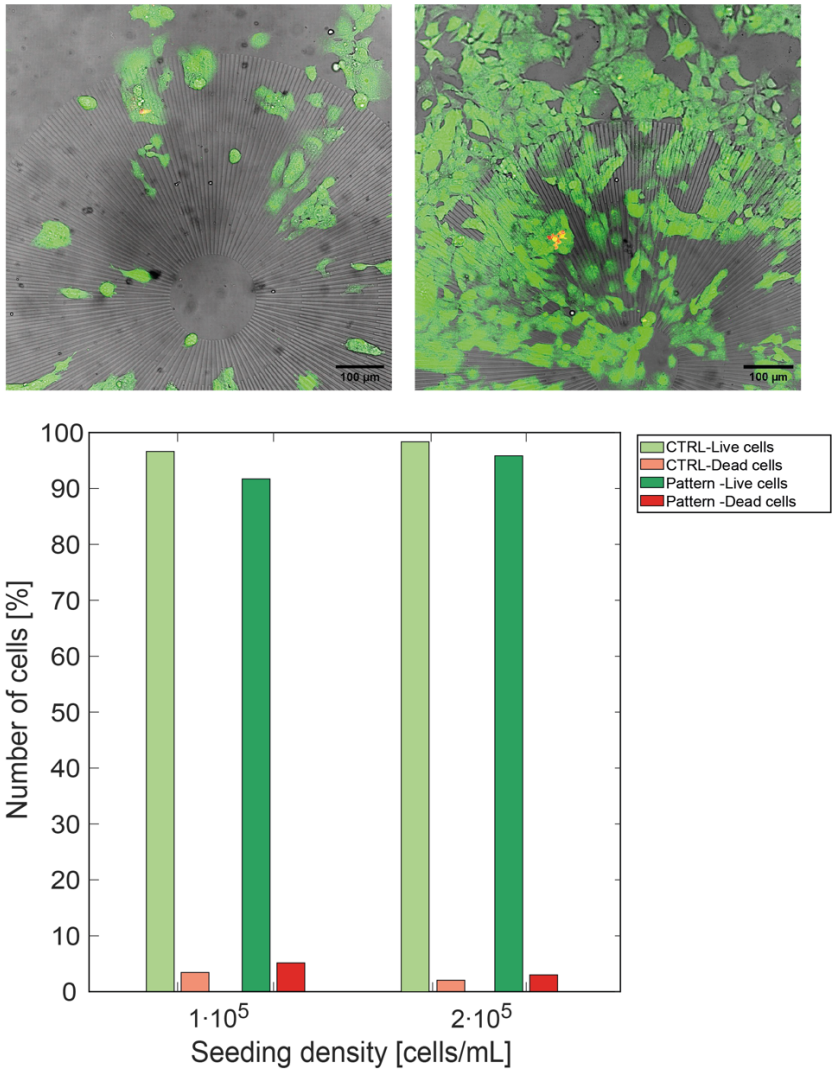

Figure 2 – Live/dead assay to assess the capability of the PDMS substrate to support HL-1 vitality. On the top panel, Hl-1 cells seeded on patterned PDMS at two seeding densities, $1{\cdot}10^5$ cells/mL on the left and $2{\cdot}10^5$ cells/mL on the right. In brightfield there is the micro-pattern, live cells are stained with Calcein AM (green) and dead cells with Propidium Iodide (PI) (red). On bottom panel, quantification of percentage of live cells over dead cells on flat PDMS (CTRL) and patterned PDMS seeded with a density of $1{\cdot}10^5$ cells/mL and $2{\cdot}10^5$ cells/mL. in all of the four cases, cell viability was supported over cell mortality. Scale bar equal to 100 µm.

3.3.2 HL-1 cells response to radial pattern topographical cue

As previously detailed in the 2.2 section, a radial pattern was designed and fabricated to align the cell population variably in orientation across the space and to guide the cells along mechanical stimulation direction. A comparison of f-actin and nuclei images of HL-1 cells cultured for 24 h on patterned and non-patterned PDMS reveals a noticeable difference in orientation and order. Initially, a color map was developed to visually represent the orientation of cells in relation to the adhesion patterned substrate. In the map, each orientation was associated with a specific color, as outlined in the color legend in *Fig. 3*. Analysis of HL-1 cells cultured for 24 h on the radial pattern showed colors corresponding to the orientation of f-actin in cell population, indicating effective alignment across the full 360° range of the pattern orientation.

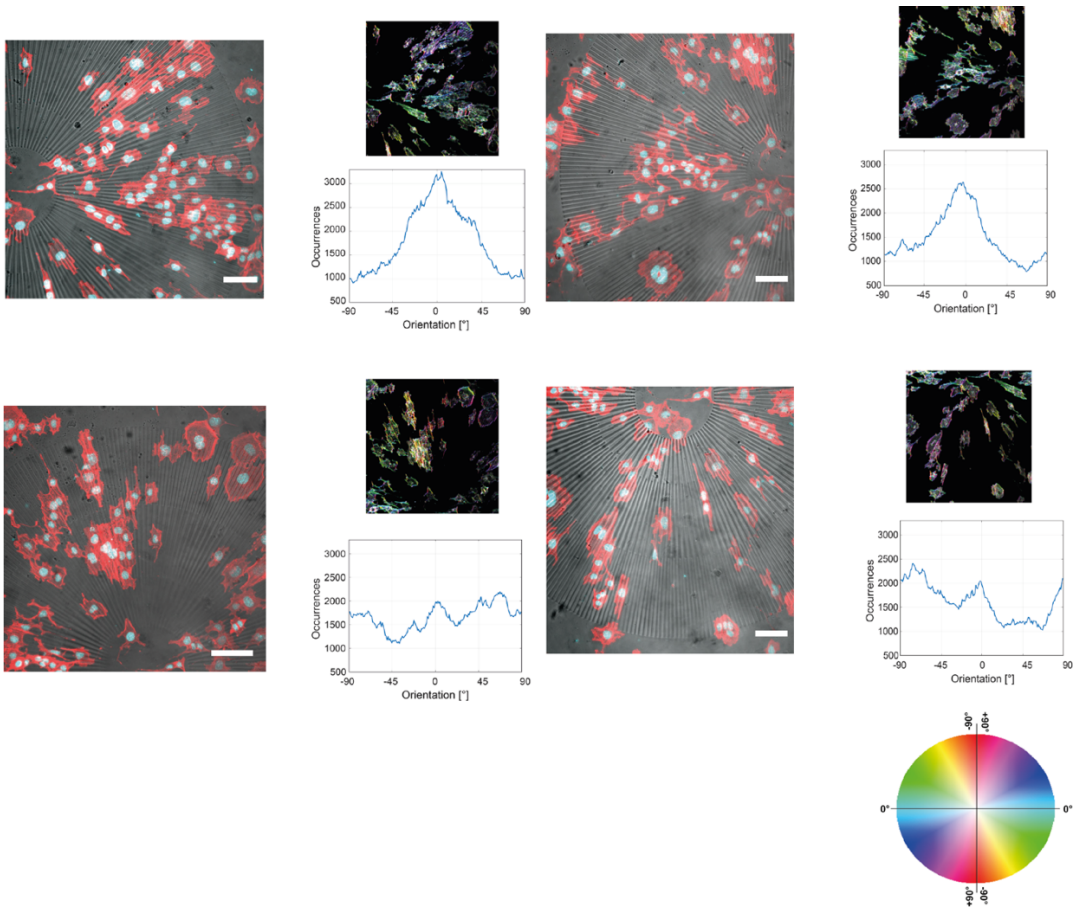

Figure 3 – Orientation of HL-1 cells on micro-patterned PDMS was assessed by staining f-actin with Phalloidin 555 (red) and nuclei with Hoechst 33342 (cyan). The orientation distribution of the cells above the pattern was characterized with ImageJ plugin "OrientationJ", qualitatively with the color-coded map and quantitatively with the distribution of f-actin fibers throughout the structure tensor of the image, as described in section 3.2.7. Scale bar equal to 100 µm.

To go deeply into the characterization, a circle was identified at the external boundary of the pattern design and a spherical coordinate system was centered in the circle's center. Sectors of 10° were isolated by varying the θ direction of the spherical coordinates in a value range of [10°, 360°]. Then, the θ-sector orientation was quantified for each of the 10° sectors as the middle angle, within a value range of [5°, 355°]. Within each sector, the orientation of the cells relative to the pattern was precisely measured by detecting the tilting of nuclei and f-actin with respect to the stripes of the PDMS ridges and grooves, specifically to the single θ-sector orientation. The alignment of nuclei and f-actin per each θ-sector was calculated as angular alignment γ, representing the difference between the single cell nucleus orientation and the sector orientation for nuclei angular alignment and as the difference between the single cell f-actin mean orientation and the sector orientation for actin filaments angular alignment.

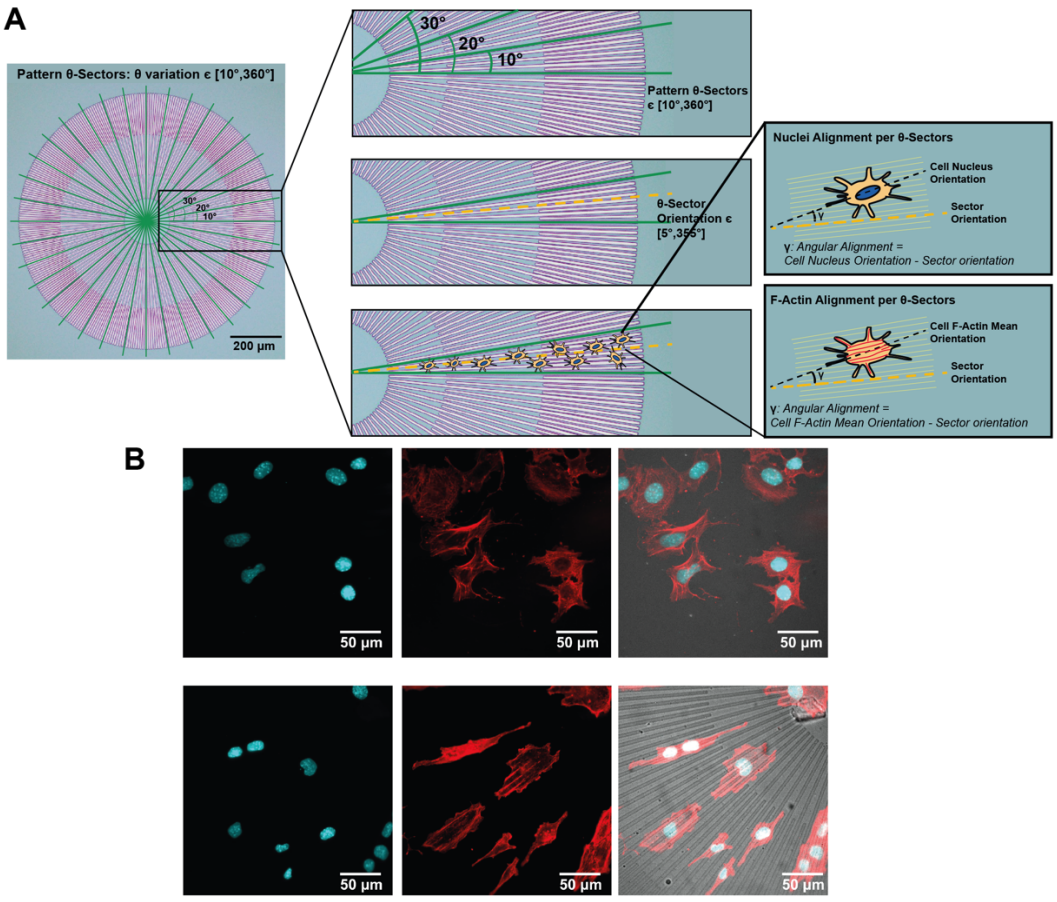

Figure 4 – A) Logic of actin and nuclei alignment data analysis. The radial micro-pattern was divided in sectors of 10° and in each sector nuclei and f-actin orientation was compared to the mean orientation of the belonging sector, retrieving in this way the angular alignment for the cell. B) Representative confocal images of HL-1 cells on flat non-patterned PDMS (top row) and patterned PDMS (bottom row) demonstrate the differences in alignment and orientation between the two samples. Cells were stained with Hoechst 33342 for nuclei (cyan) and Phalloidin 555 for actin fibers (red). Scale bar equal to 50 µm.

The histogram of nuclei and f-actin angular alignment over the cell population appeared as a distribution peaked around 0, and it can be fitted in both cases by a normal distribution with mean equal to -1.294° for nuclei angular alignment (*Fig. 5A* - left panel) and equal to -1.419° for f-actin angular alignment (*Fig. 5B* - left panel). These results demonstrated that the radial pattern was able to align both nuclei and actin filaments, since their average orientation value did not deviate from the sector orientation. Additionally, to further verify the alignment ability of the designed pattern, the nuclei mean orientation of all the cells belonging to each single θ-sector was plotted against the mean orientation of the corresponding θ-sector. The values plotted for all the pattern, i.e. for pattern orientation values varying in the range [5, 355], were fitted by a linear model, which resulted to have a slope equal to 0.8596 for the nuclei plot (*Fig. 5A* - right panel). This means that there was a univocal correspondence between nuclei mean orientation and pattern mean orientation for each θ-sector. The same was replicated for f-actin orientations, and the results showed that a linear curve slope of 0.9431 was picked up, confirming the outcome obtained for the nuclei alignment characterization (*Fig. 5B* - right panel).

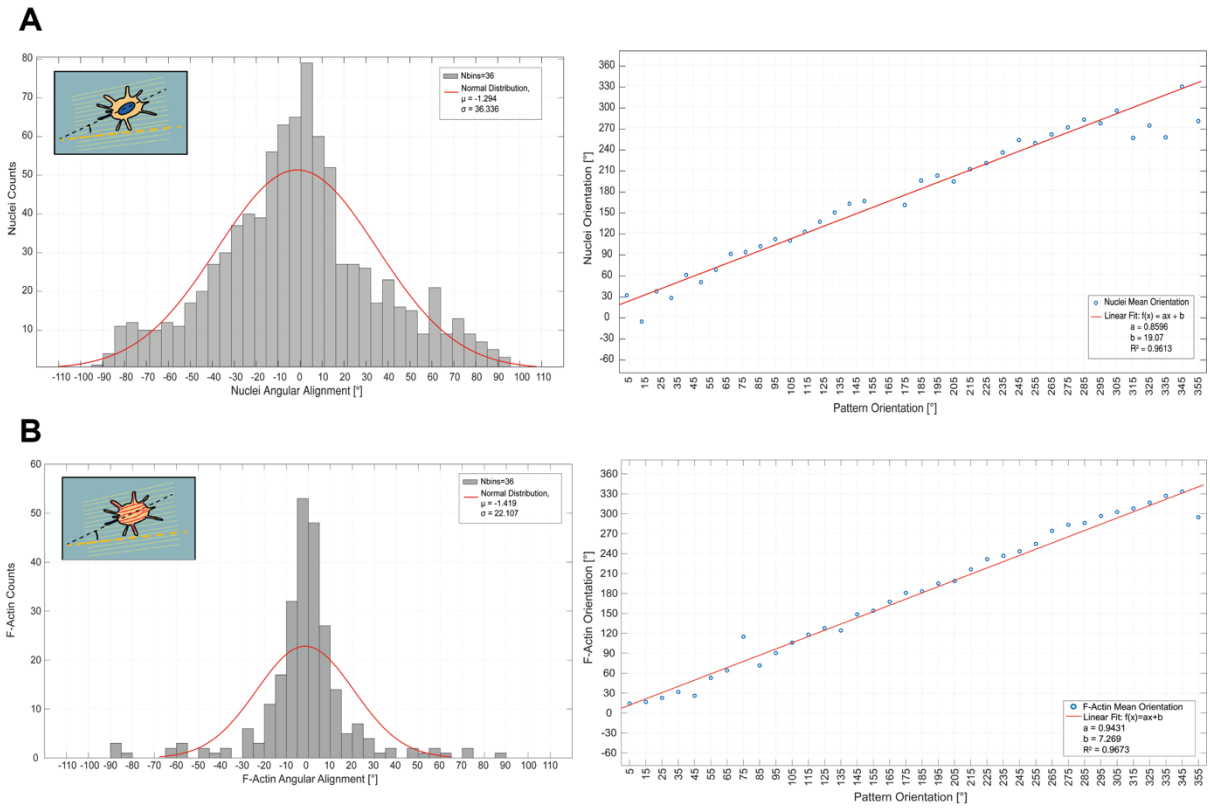

Figure 5 – The micro-pattern was able to align both HL-1 cells nuclei and f-actin along its geometry. Distributions of cells angular alignment in the θ-sectors and fitting curves of cells orientation versus pattern orientation in each θ-sector were derived for nuclei (A) and f-actin (B) demonstrating the ability of the pattern to align HL-1 CMs.

The geometric design of the radial pattern necessitated a peculiar symmetrical arrangement. Consequently, there is a noticeable gradient of alternating ridges and grooves extending along the r-direction of the spherical coordinate system. Due to this arrangement and given the specific design of the radial pattern, a question arose regarding the orientation of cell nuclei and actin filaments, that is whether their alignment shifted in accordance with the gradient inherent in the pattern design. Trying to unravel this concern, the same quantification of nuclei/f-actin angular alignment histogram, applied to the θ-sectors, was performed on the three sectors identified by the gradient arising from the pattern symmetry and changing in the r-direction (*Fig. 6A*). The results demonstrated that the alignment of nuclei was not impaired by the gradient logic, since the histograms of nuclei angular alignment were again fitted by normal distributions with means of -5.3094°, -0.8072° and -0.8692° for r-sectors starting from the inner part going to the boundaries of the pattern, respectively (*Fig. 6B* – left panels). Accordingly, nuclei mean orientation was again compared in scatter plot with the mean orientation of pattern in each θ-sector, this time dividing the quantification for each of the three r-sectors. What could be observed by the resulting plots was that the linear trend and the univocal correspondence were maintained even along the r-direction, with slopes equal to 0.8997 for the inner most sector, 0.9417 for the middle sector, and 0.9417 for the outer sector (*Fig. 6B* – right panels).

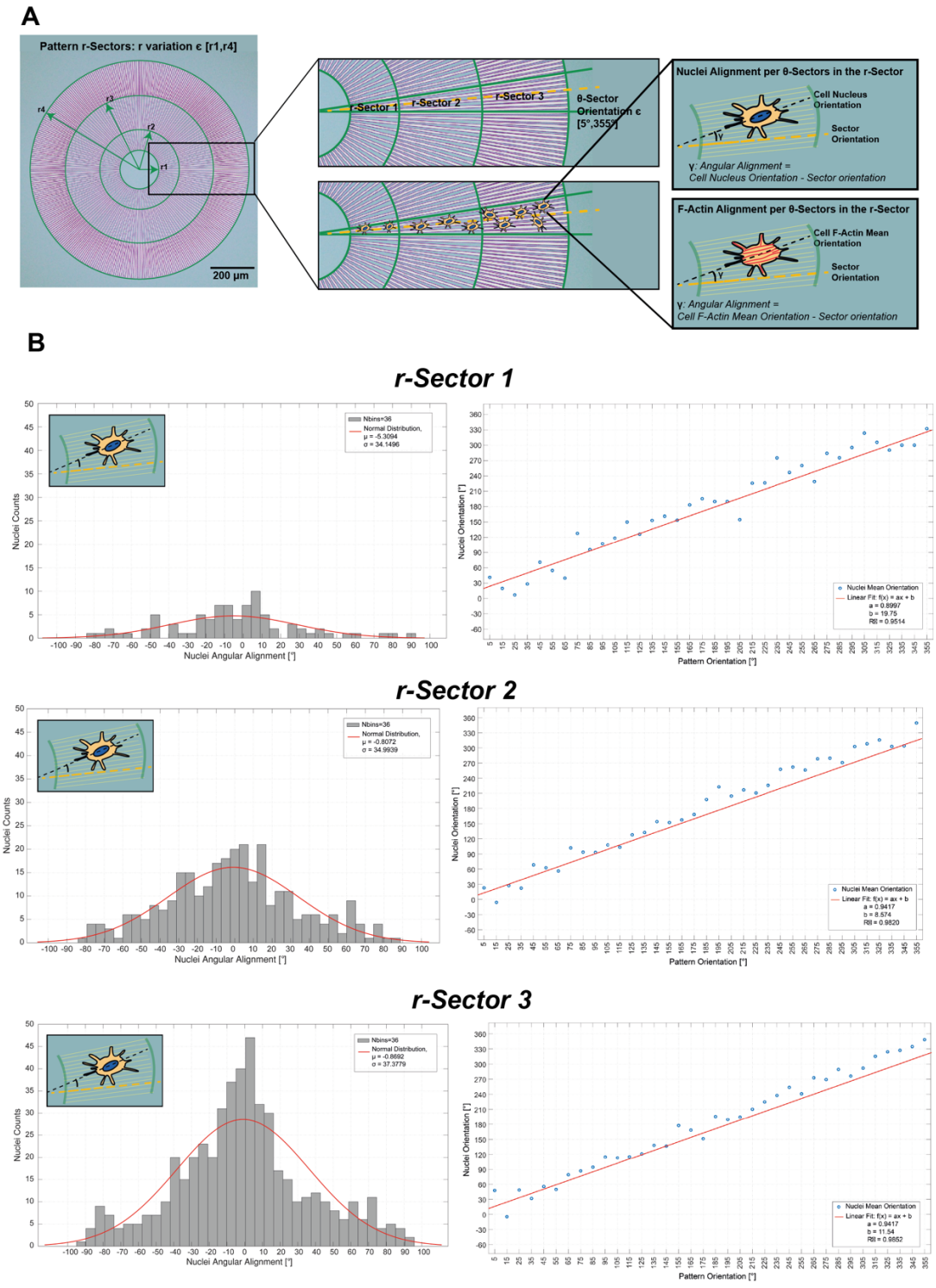

Figure 6 – The micro-pattern was able to align HL-1 cells nuclei along its geometry also in the r-direction. A) Logic of nuclei alignment data analysis. The radial micro-pattern was divided in sectors of 10° and in each of them sectors along the r-direction were recognized from the gradient symmetric structure of the same pattern. Here nuclei orientation was compared to the mean orientation of the belonging sector, retrieving in this way the angular alignment for the cell. B) Distributions of cells angular alignment in the r-sectors and fitting curves of cells orientation versus pattern orientation in each θ-sector for the three r-sectors were derived for nuclei demonstrating the ability of the pattern to align HL-1 CMs, despite a geometrical gradient arised in the r-direction.

These outcomes collectively indicate that the proposed pattern effectively aligned HL-1 CMs in terms of both nuclei and f-actin, which are essential players of mechanotransduction pathways, in every characteristic dimension of the PDMS ridge and groove pattern, namely θ and r of the spherical coordinate system. Recent advancements in micro- and nano-fabrication technologies enabled the implementation of topographies that closely replicate the geometry and scale of native tissues, particularly guiding cellular alignment in highly oriented tissues such as the cardiac environment [7]. On the microscale, features comparable to the size of a cell can influence its alignment and elongation through the contact guidance of the whole cell cytoskeleton mediated by the underlying microtopography [8]. Conversely, nanoscale features, comparable in size to individual cell receptors, such as integrins and FA complexes, allow cells to interact with these structures, potentially influencing new functions and determining cell fate [9,10]. Filopodia serve as the cell's sensing machinery for material surface, composed of actin filaments with a typical length of about 5 μm [11]. Surface features extending above this length might not be easily detected by filopodia. Upon contacting a surface, filopodia facilitate the spreading of the cell membrane and initiate the development of cellular adhesions. In addition, previous research proved that the formation of FAs on surface protrusions higher that 1 μm discouraged the formation of the complexes in the pits of the structures [12]. The work of Ventre et al. demonstrated that on patterns with ridge and groove geometry and a characteristic dimension of 5 μm, cells aligned and migrated along the pattern direction, exhibiting a coherent alignment of actin fibers influenced by pattern geometry [13]. The results of our study (*Fig. 6*) are strongly supported by the aforementioned literature reports, confirming that the radial pattern presented and employed in the platform effectively aligned HL-1 cells through mechanotransduction phenomena.

3.3.3 HL-1 cells response to mechanical stimulation

The impact of equi-biaxial deformation on CMs seeded in the μP was evaluated by examining the migratory ability of the cells on the deformed substrate. Continuous mechanical deformation was applied for 1 h and HL-1 cells trajectories were tracked by recording their nuclei positions every minute on the surface of the pillar. This experiment was conducted on both flat and patterned PDMS substrates embedded in the platform on the pillar surface (*Fig. 7A*). The results revealed a noticeable difference in the distribution of cell trajectories on the two substrates (*Fig. 7B*). Cells on the flat PDMS showed a more uniform distribution of trajectories compared to the corresponding undeformed substrate. On the other hand, cells on the patterned PDMS exhibited an even more increased uniform distribution of trajectories in the x-y plane of migration during deformation compared to the flat deformed PDMS. As the distribution of cell trajectories followed the radial conformation of the patterned PDMS, these findings indicated that mechanical deformation and the introduction of substrate micro-patterning can significantly influence cell movement under mechanical stress. The study further evaluated the response of cells to mechanical deformation by examining their migration velocity (*Fig. 7C*). It was found that the velocity distribution of HL-1 cells, described using a lognormal probability density function, peaked at a higher value for cells migrating on the radial patterned PDMS that had undergone 1 h of continuous deformation. This suggests that the mechanical deformation applied to patterned cells not only guides the orientation of cell movement but also significantly influences the migration speed.

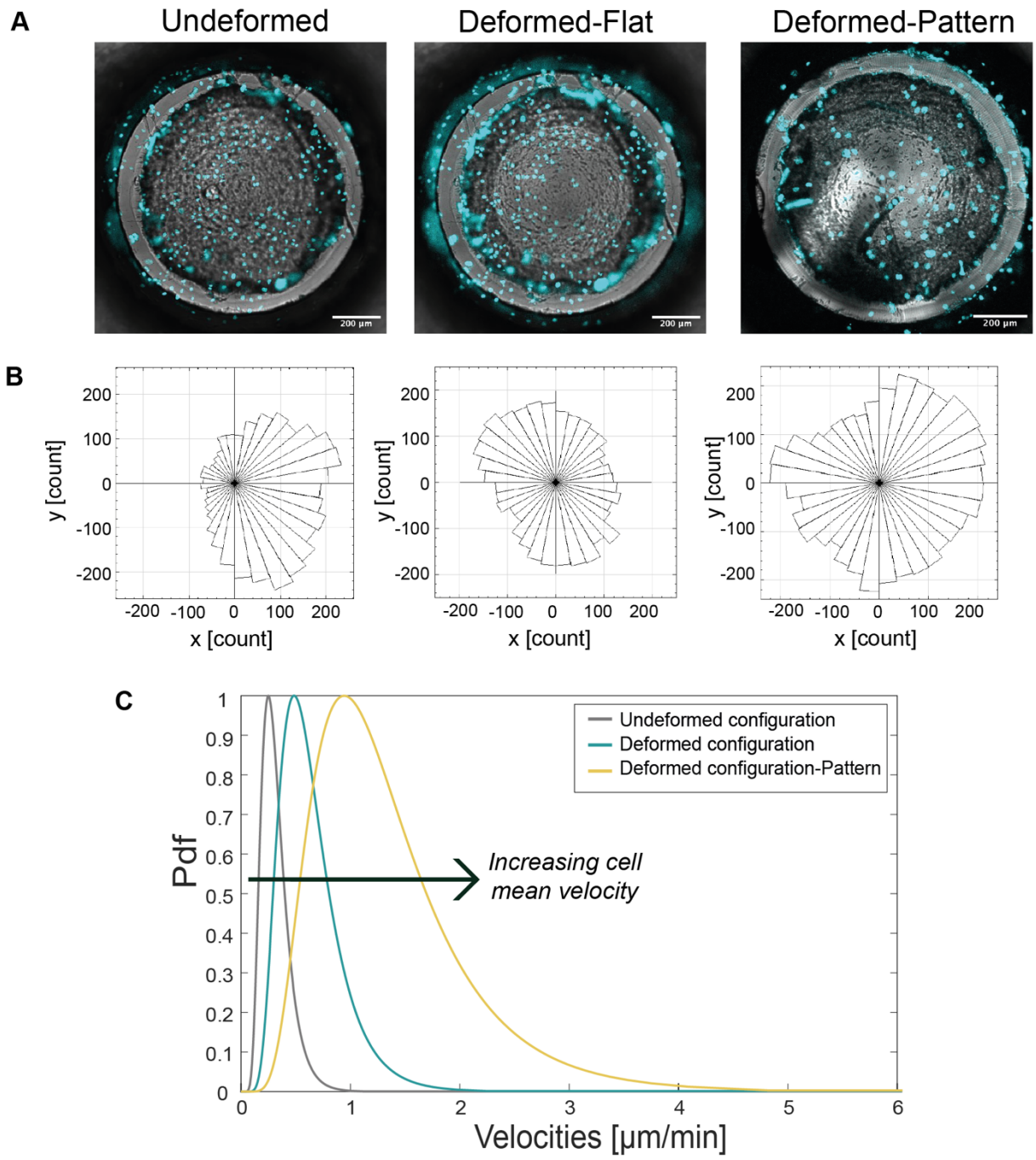

Figure 7 – HL-1 migration changed upon equi-biaxial mechanical deformation and on pattern. A) Confocal images of platform-seeded HL-1 cells on undeformed flat PDMS (left), deformed flat PDMS (middle) and deformed patterned PDMS (right). Cells were stained with Hoechst 33342 (cyan) and tracked for 1 h. B) Migration trajectories distribution changed in 1 h from randomly arranged for HL-1 cells migrating on flat undeformed PDMS (left panel), to increasingly ordered for HL-1 cells migrating on the flat PDMS, deformed on the surface of the pillar (middle panel), to completely ordered following and spreading on the pattern geometry for HL-1 cells migrating on patterned PDMS deformed on the surface of the pillar (right panel). C) Migration speed increased when HL-1 migrated on deformed PDMS and patterned deformed PDMS with respect to the control undeformed. Scale bar equal to 200 µm.

Another quantification of HL-1 migration parameters under mechanical deformation was performed over the turning angles distribution, that gave an indication of the persistence of the cell motion (*Fig. 8A*). Turning angles represent the angles between two consecutive polar angles or two consecutive segments of the trajectory. A turning angle approaching to 0 indicates that consecutive segments are parallel, suggesting guided and persistence cell motion. Histograms of turning angles for flat PDMS (*Fig. 8B* – top panel) and patterned PDMS (*Fig. 8B* – bottom panel) demonstrated increased persistence in cell migration on deformed pattern, as the distribution was more peaked around 0° compared to the flat counterpart.

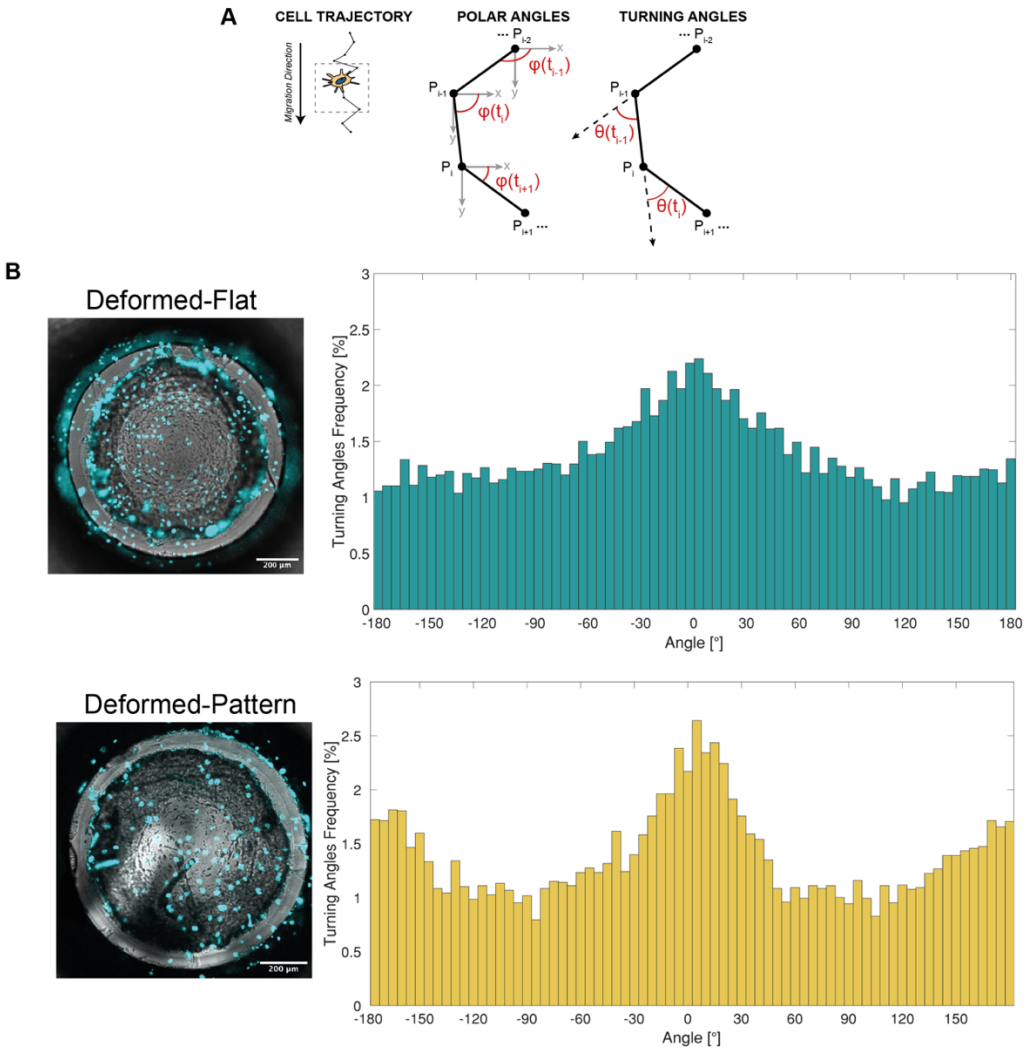

Figure 8 – Turning angles are a measurement of the persistence of HL-1 cells migration. A) Turning angles are defined as the different between two consecutive polar angles, i.e. the difference between two consecutive segments of cell trajectory. B) Histograms of turning angles demonstrated that the HL-1 cells migrating on pattern experienced a more persistent motion with respect to cells migrating on flat substrate when both the sample were undergoing to an equi-biaxial mechanical deformation.

In the study by Takemoto et al., mechanical stimulation, applied in the form of continuous and cyclic stretch, increased migration velocity and cell alignment compared to the non-stretched cells [14]. These outcomes can be explained highlighting the role of stress on cell integrins, which plays a key role in the activation of calcium responses and FAK. Mechanical stimulation on integrins also triggers factors like Rho GTPase family, known to enhance cell migration by promoting forward elongation and posterior contraction [15,16]. Therefore, mechanical stimulation intensifies these pathways, leading to pronounced migration with increased velocity. The results on the role of pattern in the enhancement of migration persistence and velocity are supported by previous literature studies, where micro-pattern and nano-pattern with characteristic feature of 5 μm or above guide a directed migration of cell trajectories [13,17]. Migration speed increased in the presence of the pattern, as confirmed by the study of Nam et al., where migration speed increased compared to the control non-patterned substrate, and by decreasing the characteristic dimension of the ridge, the migration velocity significantly increased [17]. In addition, the study of Slater et al. suggested that in endothelial cells, restricting the growth of cell adhesion sites led to smaller, more dynamic adhesions, enhancing cell movement by bypassing the slow process of disassembling larger, mature adhesions [18]. This likely explain the high speed of migration observed on patterned PDMS with respect to flat substrate.

The influence of mechanical stretching on migration phenomena was also statistically assessed. Mean Squared Displacement (MSD) was computed starting from cell positions derived during the 1 h of migration tracking on both flat and patterned deformed substrate. MSD curves exhibited different behaviors for HL-1 migrating on flat and patterned PDMS (*Fig. 9B*). The linear plot of MSD against the time lag of migration on non-patterned substrate demonstrated an initial linear trend followed by a switch towards decreasing slopes after 50 minutes of tracking. After 60 minutes, a stabilization towards increasing slopes arose again from the MSD plot. In contrast, on patterned substrate, the MSD slope was linear for the first 50 minutes of tracking, whereas it tended to increase the slope after 60 minutes of tracking. This behavior may underlie an adaptive mechanism in the HL-1 migration in response to mechanical deformation in the first case, and in response to both pattern and mechanical stretching in the second case. In fact, the formation of cell-matrix adhesions involves a stepwise process. In the initial steps, the sensing machinery is activated to perceive the physical environments. Subsequently, actin polymerization enhances the early adhesion formation, which plays a role in assessing substrate rigidity. On soft substrates, these early adhesions exhibit random motility, while on rigid substrates, adhesions are transient. After the maturation of the adhesion on softer surfaces, cells form podosomes in about 40 minutes, playing a crucial role in invasion processes [19,20]. On rigid

surfaces, mature FAs develop alongside stress fibers, exerting force and enabling mechanotransduction. In this context, MSD is a measure of the deviation of the position of a cell with respect to the reference position over different time lags. Its quantification determines if a walker is moving solely due to diffusion or if other forces contribute to the motion. Unlike normal or free diffusion, in which the MSD grows linearly with the time lag, in anomalous diffusion MSD grows as a power of the time interval. On 2D and 1D confined paths, super-diffusive cells possess lognormal MSD curves with slopes greater than 1. In 3D conditions, the embedded structure provides immobile and ballistic motion to the cell population, with lognormal MSD curves possessing slopes smaller than 1 [21,22]. In our study, MSD plots of HL-1 migrating on both non-patterned and patterned PDMS showed a linear random motion in the first 50 minutes. After this time, comparable to the mechanosensing processes for podosomes formation, in the first case of simple mechanical deformation, an adaptive response in cells can be observed, underlying a first phase of constrained subdiffusive motion, followed by a final linear trend. This is probably due to the mechanosensing adaptive phenomena to the externally applied stimulation, during which an increase in substrate rigidity arises in the cell adhesion loci when continuous mechanical stimulation is applied. Instead, in patterned PDMS combined with mechanical stimulation, after the initial adaptation, a persistent and superdiffusive behavior can be observed by the MSD curve, meaning that alongside mechanosensing processes, contact guidance imparted by the micro-pattern is acting on the conditioning of HL-1 cell migration.

The slope of both curves was also determined from the log-log MSD-time lag plots, demonstrating that the migration on flat PDMS undergoing mechanical deformation was totally a random motion, with a slope approximatively equal to 1. Conversely, the HL-1 behavior on patterned PDMS confirmed to be persistent, with the slope greater than 1 (*Fig. 9C*). The diffusion coefficient, a measure of the area covered by the cell during the motion, was one order of magnitude greater in flat deformed substrate with respect to patterned deformed PDMS, indicating that HL-1 cells adopted a persistent motion configuration moving on straight lines in the latter case (*Fig. 9D*).

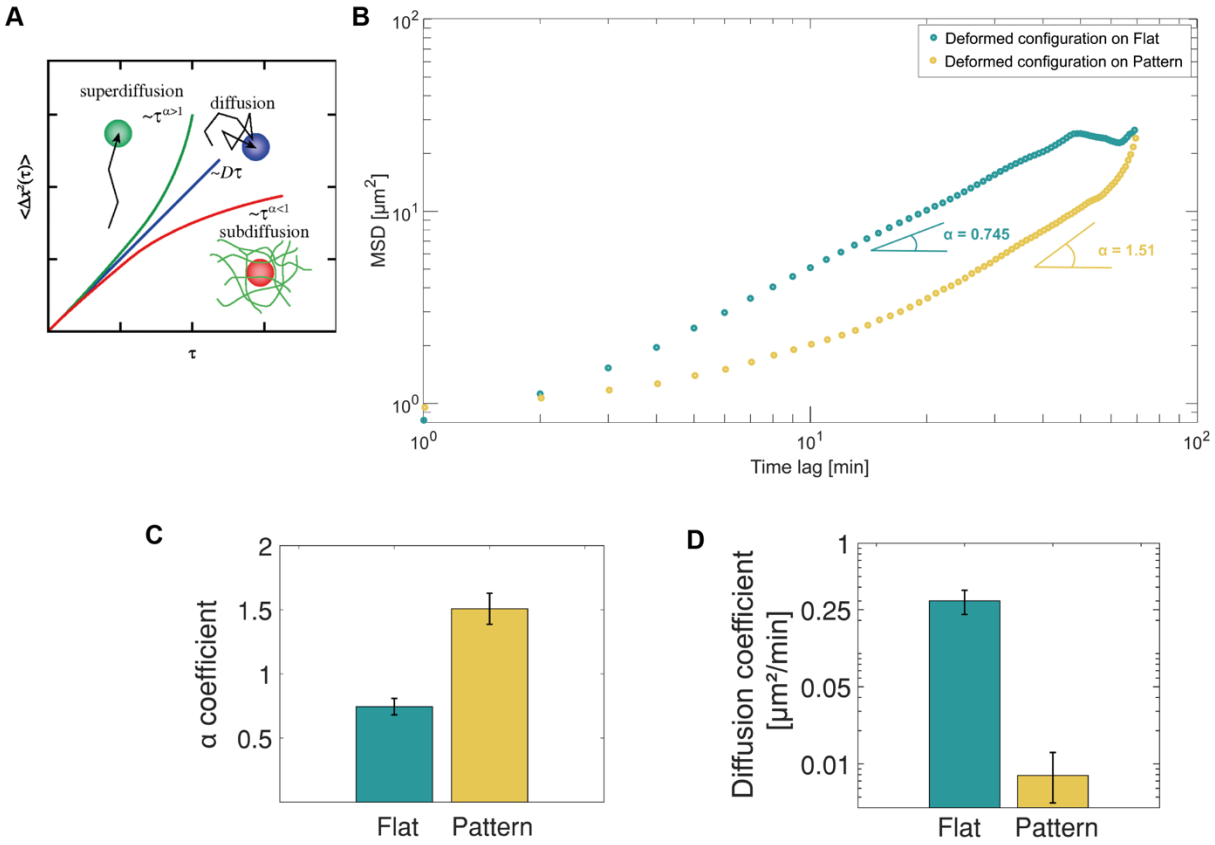

Figure 9 – Statistical analysis of HL-1 cells migration is based on the persistent random walk model (PRW). A) Depending on the MSD trend with respect to time lag, superdiffusive, subdiffusive and diffusive behaviors can be observed in the tracked object [21]. B) MSD was computed for cells migrating on flat and pattern PDMS undergoing an equi-biaxial stimulation. By linear curve fitting of the first order the slopes of the MSD curves were retrieved with R^2 equal to 0.9451 for flat and 0.9542 for pattern. Slope values are reported in C). D) Knowing the MSD trend allowed to compute the diffusion coefficient of migrating cells, that is a quantification of the area covered by the cells during the motion.

3.3.4 HL-1 cells contractility in response to mechanical and topographical cues

The heart's contraction mechanism is based on the interaction between myosin and actin within the sarcomeres. As described in section 1.6, contraction involves myosin heads binding to actin, leading to sarcomere shortening and muscle contraction. The contraction is initiated by electrical action potential (AP) signals that stimulates Ca^{2+} release from the sarcoplasmic reticulum. The released ions bind to troponin, causing a shift in tropomyosin and enabling myosin-actin interaction. CMs are interconnected by intercalated discs and gap junctions, facilitating synchronized contractions throughout the heart. Commonly used techniques to analyze the ability of CMs to withstand this vital electrophysiological activity include calcium imaging, patch clamping, and microelectrode array.

Calcium imaging is a technique that tracks fluctuations in cellular Ca^{2+} levels using fluorescent dyes. These indicators illuminate changes in intracellular Ca^{2+} concentration, enabling visualization and measurement of dynamics within the cell. In fact, in the excitation/contraction-coupling events, after cytosolic Ca^{2+} has activated the contractile units, it is carried outside the cytosol, awaiting the activation of the next electric AP. Key Ca^{2+} efflux mechanisms involve the sarco/endoplasmic reticulum Ca^{2+} ATPase (SERCA) pump and the plasma membrane Na^{+}/Ca^{2+} exchanger (NCX) [23]. During the heartbeat, there is a time-dependent increase in Ca^{2+} concentration, known as Ca^{2+} transient, which activates contraction during the excitation-contraction coupling. Spontaneous sparks in CMs occur independently of Ca^{2+} entry through L-type Ca^{2+} channels. Instead, in excitation-contraction coupling, L-type channel-mediated Ca^{2+} influx triggers the synchronized activation of sparks. The collective action of these sparks across the myocyte results in a cohesive Ca^{2+} transient [24].

Advancements in Ca^{2+} fluorescence technology and confocal microscopy led to the discovery of new chemical labeling to detect Ca^{2+} sparks in CMs. These chemical indicators have the ability to chelate Ca^{2+}. Fluo-3 and Fluo-4 are preferred indicators for Ca^{2+} spark experiments due to their excellent signal-to-noise ratio, and quick response to Ca^{2+} changes. These chemical fluorescent indicators, typically impermeable to cells, are often modified with acetoxymethyl (AM) ester groups at their chelator carboxyl groups to enhance their ability to cross cell membranes, making the molecules lipophilic. Once inside a cell, enzyme esterases activity removes the AM groups, releasing the carboxyl groups and allowing the fluorescent indicator to bind Ca^{2+} and effectively trap the cell-impermeant indicator within the cellular environment. Upon Ca^{2+} binding, the indicator experiences an increase in fluorescence quantum yield and shift in its emission/excitation wavelengths [25].

In this study, Ca^{2+} transients and sparkling activity of HL-1 cells were measured through confocal acquisition of Fluo-4 intracellular Ca^{2+} binding. The beating activity of CMs was recorded to determine whether both mechanical stimulation and topographic guidance of cell alignment conditioned the beating response of cardiac cells in the designed control platform.

Frame acquisition every 200 ms for a total duration of 30 s enabled the tracking of Ca^{2+} sparkling activation following different AP activations. Confocal images and retrieved qualitative activation maps of pixel fluorescence switching during the 30 s of acquisition, showed the trend of the Ca^{2+} oscillation across the total cell population. Activation maps were constructed based on the confocal images, as explained in section 3.2.6. Initially, contraction events were identified, representing consecutive frames during which the pixel mean fluorescence intensity exceeds a predefined threshold. Then, the map was created by quantifying the time at which the

activation wave reached each pixel in the image for every single event. In a first experiment, HL-1 beating activity was detected when cells were seeded on non-patterned PDMS (*Fig. 10A*). In addition, they were stimulated with a continuous equi-biaxial mechanical deformation applied for 1 h, achieved through flexible PDMS deformation induced by air suction with a negative pressure of 300 mbar. Control samples, consisting of cells seeded on flat undeformed PDMS outside the microfluidic device, and cells seeded on the flat device-embedded PDMS, before undergoing mechanical deformation, exhibited a random and non-synchronized activation of Ca^{2+} oscillation in the cell population (*Fig. 10B*). Analysis of intracellular fluorescence intensity oscillation over time and subsequent quantification of beating frequency revealed that the control exhibited heterogeneity in beating frequency among the cell population, while the cell population corresponding to the pillar surface in undeformed configuration showed a reduction in beating variability among cells (*Fig. 10C*). After 1 h of continuous equi-biaxial deformation, Ca^{2+} wave propagation above the deformation area became more coordinated, with a coherent movement of the fluorescence signal starting from the bottom to the top of the x-y acquisition plane, as demonstrated by corresponding activation maps (*Fig. 10B*). Beating frequency quantification showed a decrease in sparkling occurrence in the single cell compared to the time zero of stimulation and the control. Literature studies reported the importance of cyclic mechanical stimulation compared to the continuous one, from both biomimetic and physiologic response point of view. For this reason, the response of HL-1 cells to cyclic equi-biaxial deformation was tested using a stimulus guided by a sinusoidal wave, with period of 10 s (frequency of 0.1 Hz) and an amplitude of -300 mbar. The cyclic deformation was applied continuously for 1 h, after which Ca^{2+} wave movement of HL-1 on the surface of the deformation pillar was tracked for 30 s every 200 ms. The frames demonstrated that the guided propagation was still present under cyclic deformation conditions, with the fluorescent Ca^{2+} wave moving from the bottom to the top of the x-y plane (*Fig. 10B*). The intracellular beating activity remained paced: in the cell population, frequencies of fluorescence oscillation were reduced compared to 1 h of continuous deformation and were even halved with respect to control sample (*Fig. 10C-D*).

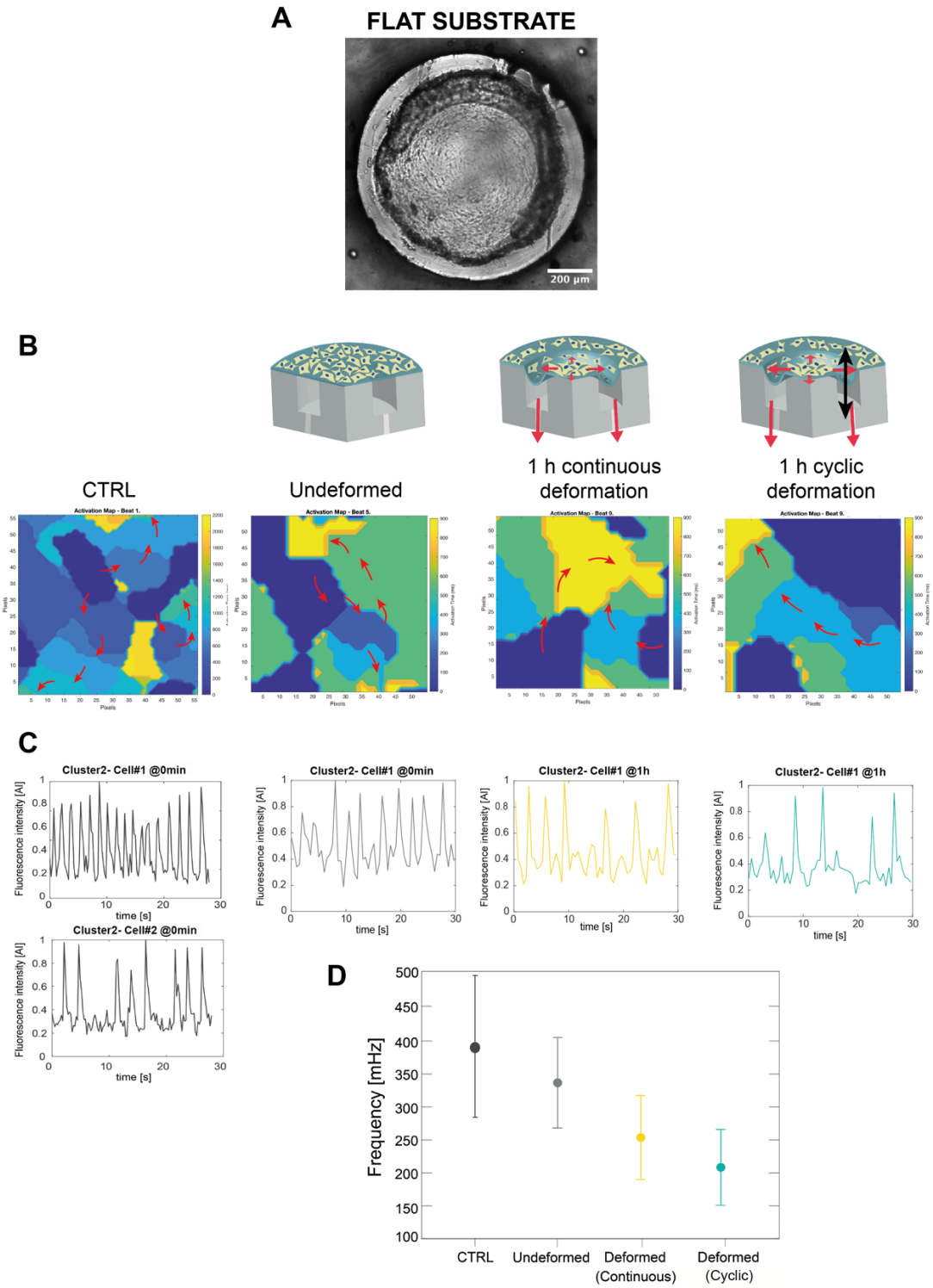

Figure 10 – Quantification of beating activity of HL-1 cells on flat PDMS under mechanical deformation. A) Brightfield image of the un-patterned PDMS corresponding to the deformation area, which is the pillar surface where equi-biaxial deformation field arises. B) Activation map of fluorescence propagation on CTRL substrates (PDMS out of the device), on undeformed PDMS (device-embedded), after 1h of continuous deformation and 1h of cyclic deformation at 1 Hz. C) Sparkling of intracellular Ca^{2+}, from left to right: CTRL, undeformed PDMS, 1h of continuous and 1h of cyclic mechanical stimulation. The plots correspond to the fluorescence oscillation in the same cell. D) Quantification of frequency of Ca^{2+} sparkling demonstrated a pacing activity of HL-1 cells when a cyclic deformation was applied. Scale bar 200 µm.

Afterwards, a radial micro-pattern was introduced in the Ca^{2+} handling experiments (*Fig. 11A*). Like before, the activity of HL-1 cells at the time zero stimulation was recorded within the control platform for 30 s with time frames of 200 ms. It was found that the HL-1 cells seeded on micro-pattern in undeformed configuration exhibited a coordinated propagation of Ca^{2+} that seemed to follow the radial arrangement of the micro-structure. The wave originated from a right corner of the pattern and moved toward the center, then propagating along the boundaries of the circular pillar along the r and θ direction. In the presence of the sole micro-pattern, the cytoplasmic cell beating frequency was reduced with respect to the response under the same culture conditions on flat undeformed PDMS (*Fig. 11B-C* versus *Fig. 10C*). This suggests that the topographic signal influenced the beating activity of HL-1 cells. When continuous and cyclic (sinusoidal, at 0.1 Hz) deformation was applied for 1 h to the patterned PDMS, the propagation wave of Ca^{2+} for the HL-1 population on the pillar surface appeared increasingly ordered by the underlying pattern. This was evident in the activation maps, where the fluorescence signal started from the center of the pattern and propagated toward the boundaries following the radial direction of the ridges and grooves (*Fig. 11B*).

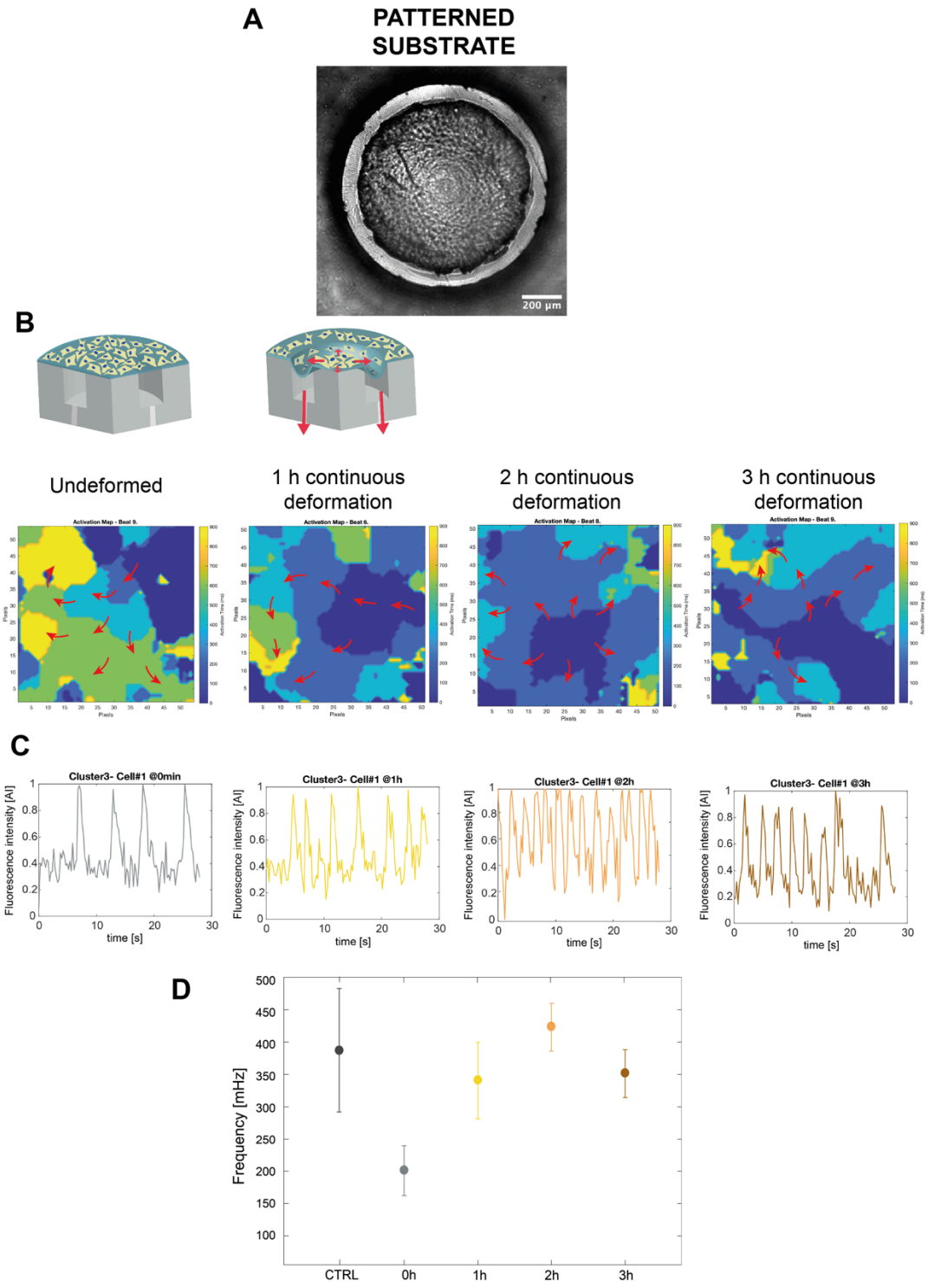

Figure 11 – Quantification of beating activity of HL-1 cells on patterned PDMS under continuous mechanical deformation. A) Brightfield image of the patterned PDMS corresponding to the deformation area, which is the pillar surface where equi-biaxial deformation field arises. B) Activation map of fluorescence propagation on undeformed PDMS (device-embedded) and after 1h, 2h and 3h of continuous deformation. C) Sparkling of intracellular Ca^{2+}, from left to right: undeformed PDMS, and 1h, 2h and 3h of continuous mechanical stimulation. The plots correspond to the fluorescence oscillation registered in the same cell. D) Quantification of frequency of Ca^{2+} sparkling demonstrated an enhanced activity by increasing the deformation time, although at 3h a pacing phenomenon started. Scale bar 200 µm.

To further confirm the role of the micro-pattern in guiding Ca^{2+} wave propagation, both continuous (*Fig. 11B*) and cyclic mechanical stretching (*Fig. 12B*) were applied for 2 h and 3 h. Activation maps were then reconstructed from fluorescence frames of 200 ms at these time points. The influence of the radial micro-pattern on synchronized propagation of Ca^{2+} is even more evident for longer stimulations, particularly in the presence of cyclic deformation (*Fig. 11B* versus *Fig. 12B*). Regarding beating frequencies, different phenomena occurred in the case of continuous and cyclic deformation (*Fig. 11C* versus *Fig. 12C*). After 1 h of deformation in both cases the beating activity increased, showing higher frequencies than the undeformed patterned configuration but similar between the two types of deformation. In addition, the beating frequencies were higher also respect to the flat PDMS case at the same time points. After 2 h of deformation, the frequency increased further in both continuous and cyclic stretching. However, after 3 h a difference emerged. In fact, while pattern in continuous deformation led to a decrease in HL-1 beating activity, the same pattern in cyclic deformation at 0.1 Hz sustained the beating stimulation by increasing the frequency of internal Ca^{2+} oscillation. The observed difference in both propagation and beating frequency of Ca^{2+} in stimulated HL-1 underlies the crucial role of the micro-pattern in the response of CMs to external mechanical stimulation. Additionally, to prove the synchronization effect of the pattern in combination with mechanical stimulation, we assessed the Ca^{2+} wave propagation velocity in both continuous and cyclic deformation (*Fig. 13B-C*). The results revealed that after 3 h of stimulation, the mean propagation speed significantly increased over the control, with higher values in the case of cyclic stimulation at 0.1 Hz. This indicates an enhancement in synchronization due to the pattern and mechanical stretch.

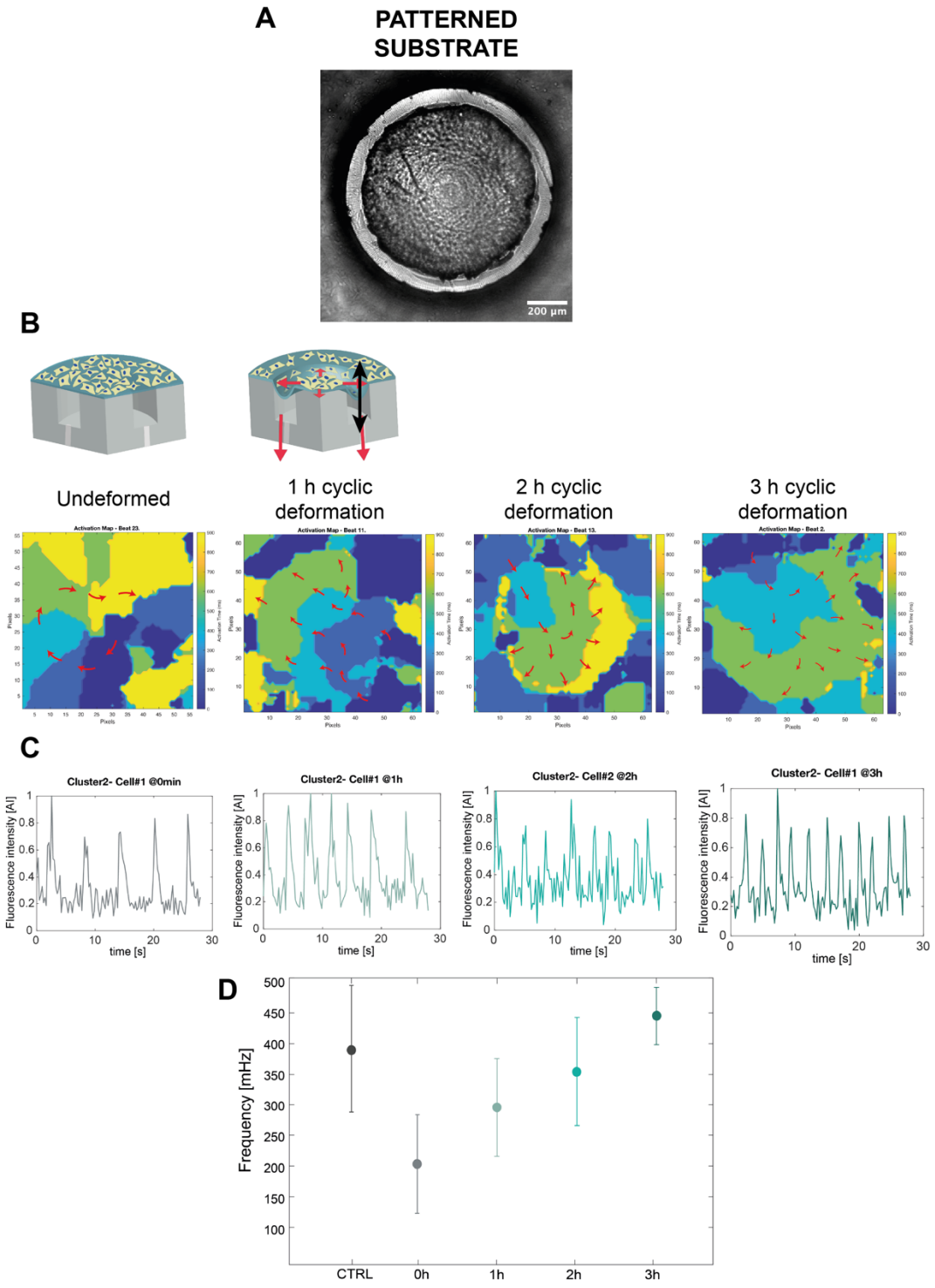

Figure 12 – Quantification of beating activity of HL-1 cells on patterned PDMS under cyclic mechanical deformation at 0.1 Hz. A) Brightfield image of the patterned PDMS corresponding to the deformation area, which is the pillar surface where equi-biaxial deformation field arises. B) Activation map of fluorescence propagation on undeformed PDMS (device-embedded) and after 1h, 2h and 3h of cyclic deformation. C) Sparkling of intracellular Ca^{2+}, from left to right: undeformed PDMS, and 1h, 2h and 3h of cyclic mechanical stimulation. The plots correspond to the fluorescence oscillation registered in the same cell. D) Quantification of frequency of Ca^{2+} sparkling demonstrated an enhanced activity by increasing the deformation time, with 3h demonstrating the higher frequency of beating. Scale bar 200 µm.

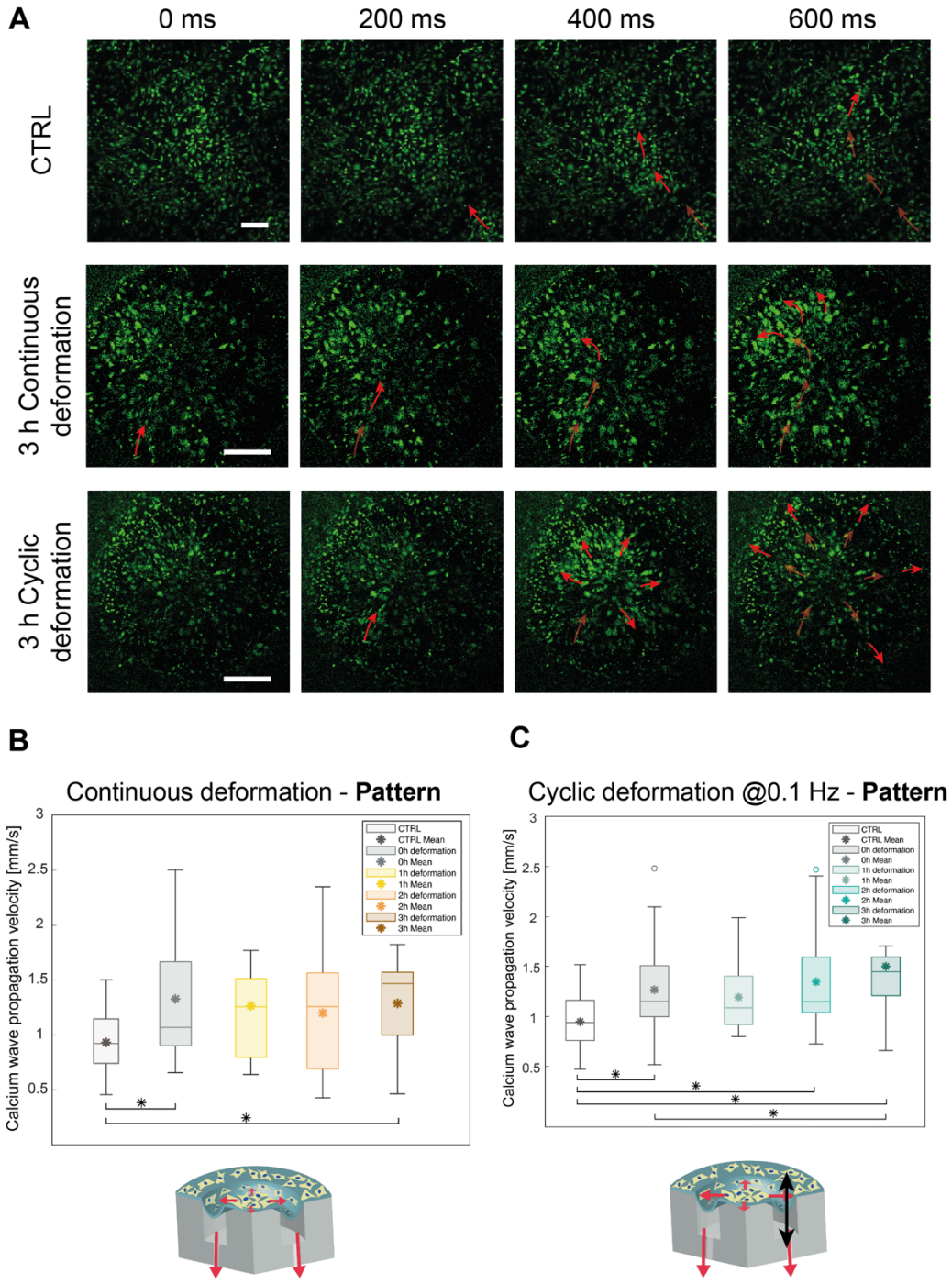

Figure 13 – Representative images of Ca2+ wave propagation in time and quantification of propagation velocity. A) Time frame of 200 ms describing the different propagation phenomenon arising between the CTRL substrate and the continuous and cyclic deformation applied to cell seeded on patterned PDMS. While the CTRL demonstrated no guided propagation, 3h of cyclic deformation gave high synchronization between HL-1 cells, probably related to the presence of the radial micro-pattern. This is increasingly evident even compared to the continuous deformation. B) Calcium wave propagation quantification demonstrated that the mechanical deformation on pattern significantly increased the speed of the spreading of beating signal among the cell culture, both in continuous and cyclic deformation, with higher values in the cyclic one. Scale bar 200 μm.

Literature studies have reported both pacing and enhanced contraction frequency in mechanically stimulated cardiac cell lines. Different studies report that the cyclic mechanical stimulation can pace the CMs activity synchronizing their beating with the deformation of the substrate [26,27]. Instead, other studies indicate that acute mechanical deformation may induce arrhythmias, significantly increasing the beating activity of CMs [28]. As already highlighted by previous studies and our findings, mechanical stretching profoundly impacts cardiac cell behavior, contributing to increased adhesion substrate rigidity and the continuous assembly and disassembly of FAs on the adherent substrate. Integrins, which are receptors linked to mechanosensing and mechanotransduction activity, play a role in controlling calcium response pathways. The mechanical stimulation in CMs, due to substrate deformation, involves activation of stress-sensitive ion channels, enhancing Ca^{2+} trafficking, or cell signaling pathways, induced by stress sensors responding to mechanical variations. In this study, sole mechanical stimulation on flat PDMS substrate appeared to pace the HL-1 cell activity, with beating frequency approaching the stimulation frequency of 0.1 Hz.

The presence of a pattern significantly influenced HL-1 activity. Previous studies reported that CMs cultured on nanofibrous aligned electrospun patches exhibited a significant increase in both beating rate and amplitude compared to those cultured on random patches, influencing in this way not only the morphology but also the cellular behavior of CMs [29]. In another study, nanopatterned polystyrene substrates demonstrated to induce CMs enhanced contraction, due to the higher tenacity of CMs and stability of f-actin seeded on patterns that likely contributed to the prolonged integrity of myofibrils, thereby maintaining the beating function longer than flat substrates [30]. In our study, the undeformed pattern demonstrated a paced frequency of Ca^{2+} oscillation cells. In fact, the samples were probed with Ca^{2+} indicators 24 h after the seeding, favoring in this way cells adaptation to conformational changes induced by the patterned substrate, which results in a pacing of the cell activity with reduced beating frequency in undeformed pattern configuration. When mechanical perturbation was introduced on patterned cells, they firstly responded by coordinating the propagation of Ca^{2+} signal within cell population, due to the presence of the pattern, and later adapted to the mechanical constraints. Continuous deformation provided more stability to cell anchoring sites with respect to cyclic stretch, which instead induced a continuous assembly and disassembly of adhesions. After 3 h of continuous deformation, HL-1 cells started to adapt and pace their activity, decreasing beating frequency. In contrast, after 3 h of cyclic stretch, the oscillation frequency continued to increase, suggesting that CMs sustained their adaptation related to mechanosensing and mechanotrasduction pathways. In a first attempt to go deeply in these findings, the study of

Jeong et al. highlighted that CMs seeded on Au-deposited nano-grooved PDMS if exposed to mechanical stimulation at 1 Hz increased their beating rate in 48 h of stimulation. Then, the activity decreased indicating maturation, which was confirmed by immunofluorescent staining of α-actinin and Cx43 resulting enhanced in mechanically stimulated cells [31].

While the presented results on HL-1 CMs' contractility and Ca^{2+} wave propagation in response to mechanical stimulation and topographic micro-pattern offer insightful findings, more comprehensive studies are needed to deepen our understanding of these phenomena. Herein, we showed the potentiality of the presented μP to replicate behaviors typically associated to cardiac cell, suggesting that future investigations should include extended stimulation periods to observe cellular adaptation over time. Additionally, immunostaining techniques could be implemented as a crucial element to evaluate the maturation level of cardiac cells under various stimulation conditions. In this study, the investigation focused on unraveling the autophagy response of HL-1 CMs to the previously characterized stimuli, as a step forward to prove the μP's capability to monitor cell health when influenced by various signals from the surrounding microenvironment.

References

1. Dwyer, K. D. & Coulombe, K. L. K. Cardiac mechanostructure: Using mechanics and anisotropy as inspiration for developing epicardial therapies in treating myocardial infarction. Bioact Mater 6, 2198–2220 (2021).
2. Navaee, F. et al. Toward a Physiologically Relevant 3D Helicoidal-Oriented Cardiac Model: Simultaneous Application of Mechanical Stimulation and Surface Topography. Bioengineering 10, 266 (2023).
3. Bijnens, B., Cikes, M., Butakoff, C., Sitges, M. & Crispi, F. Myocardial Motion and Deformation: What Does It Tell Us and How Does It Relate to Function? Fetal Diagn Ther 32, 5–16 (2012).
4. Claycomb, W. C. et al. HL-1 cells: A cardiac muscle cell line that contracts and retains phenotypic characteristics of the adult cardiomyocyte. Proceedings of the National Academy of Sciences 95, 2979–2984 (1998).
5. Choi, S. et al. Effects of Various Extracellular Matrix Proteins on the Growth of HL-1 Cardiomyocytes. Cells Tissues Organs 198, 349–356 (2013).
6. Seo, J.-H., Sakai, K. & Yui, N. Adsorption state of fibronectin on poly(dimethylsiloxane) surfaces with varied stiffness can dominate adhesion density of fibroblasts. Acta Biomater 9, 5493–5501 (2013).
7. Ahn, H. et al. Hierarchical Topography with Tunable Micro- and Nanoarchitectonics for Highly Enhanced Cardiomyocyte Maturation via Multi-Scale Mechanotransduction. Adv Healthc Mater 12, (2023).
8. Guvendiren, M. & Burdick, J. A. Stem Cell Response to Spatially and Temporally Displayed and Reversible Surface Topography. Adv Healthc Mater 2, 155–164 (2013).
9. Dalby, M. J., Gadegaard, N. & Oreffo, R. O. C. Harnessing nanotopography and integrin–matrix interactions to influence stem cell fate. Nat Mater 13, 558–569 (2014).
10. Park, J., Bauer, S., von der Mark, K. & Schmuki, P. Nanosize and Vitality: TiO 2 Nanotube Diameter Directs Cell Fate. Nano Lett 7, 1686–1691 (2007).
11. Schäfer, C., Faust, U., Kirchgeßner, N., Merkel, R. & Hoffmann, B. The filopodium. Cell Adh Migr 5, 431–438 (2011).
12. Seo, C. H., Jeong, H., Furukawa, K. S., Suzuki, Y. & Ushida, T. The switching of focal adhesion maturation sites and actin filament activation for MSCs by topography of well-defined micropatterned surfaces. Biomaterials 34, 1764–1771 (2013).

13. Ventre, M., Natale, C. F., Rianna, C. & Netti, P. A. Topographic cell instructive patterns to control cell adhesion, polarization and migration. J R Soc Interface 11, 20140687 (2014).
14. Takemoto, F., Uchida-Fukuhara, Y., Kamioka, H., Okamura, H. & Ikegame, M. Mechanical stretching determines the orientation of osteoblast migration and cell division. Anat Sci Int 98, 521–528 (2023).
15. Raftopoulou, M. & Hall, A. Cell migration: Rho GTPases lead the way. Dev Biol 265, 23–32 (2004).
16. Gardel, M. L., Schneider, I. C., Aratyn-Schaus, , Yvonne & Waterman, C. M. Mechanical Integration of Actin and Adhesion Dynamics in Cell Migration. Annu Rev Cell Dev Biol 26, 315–333 (2010).
17. Nam, K.-H. et al. Multiscale Cues Drive Collective Cell Migration. Sci Rep 6, 29749 (2016).
18. Slater, J. H. et al. Modulation of Endothelial Cell Migration via Manipulation of Adhesion Site Growth Using Nanopatterned Surfaces. ACS Appl Mater Interfaces 7, 4390–4400 (2015).
19. Changede, R. & Sheetz, M. Integrin and cadherin clusters: A robust way to organize adhesions for cell mechanics. BioEssays 39, 1–12 (2017).
20. Linder, S., Cervero, P., Eddy, R. & Condeelis, J. Mechanisms and roles of podosomes and invadopodia. Nat Rev Mol Cell Biol 24, 86–106 (2023).
21. MacKintosh, F. C. Active diffusion: The erratic dance of chromosomal loci. Proceedings of the National Academy of Sciences 109, 7138–7139 (2012).
22. Luzhansky, I. D. et al. Anomalously diffusing and persistently migrating cells in 2D and 3D culture environments. APL Bioeng 2, (2018).
23. Fearnley, C. J., Roderick, H. L. & Bootman, M. D. Calcium Signaling in Cardiac Myocytes. Cold Spring Harb Perspect Biol 3, a004242–a004242 (2011).
24. Guatimosim, S., Guatimosim, C. & Song, L.-S. Imaging Calcium Sparks in Cardiac Myocytes. in 205–214 (2011). doi:10.1007/978-1-60761-950-5_12.
25. Grienberger, C., Giovannucci, A., Zeiger, W. & Portera-Cailliau, C. Two-photon calcium imaging of neuronal activity. Nature Reviews Methods Primers 2, 67 (2022).
26. Nitsan, I., Drori, S., Lewis, Y. E., Cohen, S. & Tzlil, S. Mechanical communication in cardiac cell synchronized beating. Nat Phys 12, 472–477 (2016).
27. Marsano, A. et al. Beating heart on a chip: a novel microfluidic platform to generate functional 3D cardiac microtissues. Lab Chip 16, 599–610 (2016).

28. Galie, P. A., Byfield, F. J., Chen, C. S., Kresh, J. Y. & Janmey, P. A. Mechanically Stimulated Contraction of Engineered Cardiac Constructs Using a Microcantilever. IEEE Trans Biomed Eng 62, 438–442 (2015).
29. Lin, Y.-D. et al. A nanopatterned cell-seeded cardiac patch prevents electro-uncoupling and improves the therapeutic efficacy of cardiac repair. Biomater Sci 2, 567 (2014).
30. Wang, P.-Y., Yu, J., Lin, J.-H. & Tsai, W.-B. Modulation of alignment, elongation and contraction of cardiomyocytes through a combination of nanotopography and rigidity of substrates. Acta Biomater 7, 3285–3293 (2011).
31. Jeong, Y.-J. et al. On-stage bioreactor platform integrated with nano-patterned and gold-coated PDMS diaphragm for live cell stimulation and imaging. Materials Science and Engineering: C 118, 111355 (2021).

Chapter 4:
HL-1 response to microenvironment-induced autophagy in microfluidics

4.1 Introduction

Replicating CMs autophagy *in vitro* is a critical area of research in cardiovascular biology, especially to unravel the autophagic progression under the action of diverse extracellular signals from the microenvironment. Autophagy, a cellular degradation and recycling process, plays a vital role in maintaining cellular homeostasis, responding to stress, and regulating cell death. In CMs, autophagy is essential to handle the high metabolic demands and to withstand stress conditions that these cells often face, such as mechanical stress, hypoxic conditions, and nutrient level oscillation. Understanding how CMs regulate autophagy in response to these stimuli is crucial for uncovering the mechanisms underlying heart disease and developing therapeutic strategies. Starvation-induced autophagy is a well-established method, mimicking the conditions of nutrient deficiency that occur in pathological states. In the adult heart, autophagy plays a crucial role in preserving cardiac functionality, particularly during periods of starvation. Blocking autophagy results in marked cardiac impairments and reduced performances, highlighting its essential function in supplying amino acids for energy production. Recent studies have highlighted that autophagy plays a crucial role in translating mechanical forces from the surrounding microenvironment into biological responses. This process is particularly important in muscles during physical activities, where stretching-induced autophagy contributes to muscle health by managing mitochondrial quality. Cardiac cells also experience enhanced autophagy in response to increased mechanical stress, such as during myocardial infarction, systemic hypertension, and pulmonary embolism. Research has shown that mechanical tension can trigger autophagy in heart cells, with evidence from cases of myocardial infarction and pressure overload scenarios like transverse aortic constriction. While autophagy provides protective benefits to CMs during ischemia and can mitigate ventricular hypertrophy, thereby improving heart function, its excessive activation in failing hearts may lead to cell death. This highlights the debated role of autophagy in cardiac cells, serving as both a protective mechanism and a potential contributor to cellular death, depending on its level and the context of its activation.

Microfluidics emerges as a powerful tool in the analysis of autophagy, providing a controlled and precise platform to simulate the cardiac microenvironment and apply various extracellular cues. The ability of microfluidic devices to generate gradients of nutrients, apply mechanical forces, and manipulate the chemical environment allows researchers to study autophagy under conditions closely mimicking those *in vivo*. Several studies have exploited microfluidics to induce autophagy in CMs, many of them trying to recapitulate the cardiovascular system and its response in autophagy induction. Other studies tried to replicate the induction of autophagy in response to mechanical stimulation by employing deformation platforms. However, these efforts often fall short of accurately mimicking cardiac physiological conditions. The limitation primarily stems from the inability of these platforms to integrate the appropriate fluxes of nutrients and other critical signals that constitute the complete cardiac microenvironment. While these platforms can simulate mechanical stress, they lack the complexity to replicate the multifaceted nature of the environment surrounding cardiac cells, which includes not just mechanical but also biochemical and topographical cues. In addition, studies on the role of topography in autophagy induction are reduced and applied to different cell application, like osteogenic differentiation [1,2] and neurogenesis [3], but less is known on the role of topographical controlled arrangement of cardiac cells on the autophagy induction.

For these reasons, in the last part of the work we used the μP to study autophagy modulation following the integration of nutrient flux, mechanical deformation, and the guided alignment of the cardiac cells. Initially, HL-1 cells were electroporated to incorporate a plasmid carrying a tandem reported that targets autophagic vacuoles, specifically labeling autophagosomes and autolysosomes with the combined and selective GFP-mRFP fluorescent signal to visualize the two stages of the autophagic flux. To validate the platform ability to monitor autophagy, a starvation signal was applied to cells seeded within the device. This step confirmed that autophagy could be affectively detected within the microfluidic environment. Subsequent experiments involved applying mechanical stimulation over extended periods, both in the absence and presence of micro-patterns designed to align the cells. These experiments revealed a notable observation: while the induction of autophagy appeared to be enhanced by mechanical stress, the degradation final step seemed to be inhibited. In particular, in the presence of cell-aligning patterns, the accumulation of autophagic vacuoles seemed to increase with respect to the non-patterned deformed cell culture. Further investigation using a live-dead assay demonstrated that cell survival was not adversely affected, despite the apparent blockage in the autophagy flux. This result suggests that while the μP can effectively simulate biochemical stimuli relevant to the cardiac microenvironment by inducing autophagy, the presence of cyclic

mechanical stretching and patterns may interfere with the later stages of autophagy, specifically the degradation process within autolysosomes, even if these stimulations avoided to harm the cardiac cell vitality.

4.2 Materials and Methods

4.2.1 HL-1 cells electroporation

The read-out of autophagy induction was carried out by exploiting a reporter targeting the LC3 proteins on the surface of both autophagosomes and autolysosomes. A mRFP-GFP-LC3 reporter was used to detect the autophagy flux, following the working principle already described in paragraph 1.8.2.1. The plasmid carrying the tandem fluorescent probes was introduced into HL-1 cells by exploiting the electroporation technique. Electroporation involves the application of an electrical field to cells to enhance the permeability of their membranes, allowing the entry of large, highly charged molecules, which cannot naturally diffuse through the hydrophobic core of the bilayer. This process enables the transfection, i.e. the introduction of external substances, such as DNA, into the cell. Electroporation causes lipid molecules to reposition without chemical damage, forming conductive pore filled with water. The outcome of electroporation depends on achieving a specific transmembrane voltage threshold that, if it is surpassed, leads to the compromission of cell viability. Electroporation is a multi-step process initiated by a short electrical pulse that charges the membrane like a capacitor through ion migration. Upon reaching a critical field, a rapid lipid rearrangement leads to the formation of a first pore structure across the membrane, which then transitions to a conductive pore. These conductive pores may either heal, resealing the bilayer, or expand and potentially rupture it.

HL-1 cells were detached from T-25 flask to undergo electroporation. They first were counted to seed a final cell density of $2.5 \cdot 10^6$ cells in the chamber of a 6 well plate. They were centrifugated at 1000 rpm for 5 minutes and the cells pellet was resuspended in 1 mL of PBS. They were centrifugated again at 1000 rpm for 5 minutes and supernatant was removed and replaced with a reagent buffer (buffer R, Neon™ Transfection System 10 µL Kit, ThermoFisher) and complemented with the right quantity of the plasmid. After a first phase of plasmid purification, leading to a concentration of 1 µg/µL, the quantity of plasmid chosen for a proper electroporation was 0.5 µg, meaning 2 µL. The cells suspended in the buffer R and the final quantity of the plasmid were transferred in a tip enriched with an inner core of gold that was submerged in an electroporation cuvette filled with an electrolytic buffer throughout a Neon™ Pipette. The cuvette and the gold tip were properly contacted in the Neon™ Pipette Station, allowing the contact of the electrodes of the cuvette and the Station. The Neon™ Device was then programmed to deliver two pulses with electric field of 1700 V of the duration of 10 ms was run. The electroporated cells were transferred from the Neon™ Pipette Station to the

chamber of the 6 well plate, enriched with HL-1 culture medium deprived of P/S and norepinephrine. After 24 h, the culture medium was complemented with the last two components. After 48 h from electroporation and seeding, HL-1 cells were detached from the 6 well plate and treated. Images of electroporated HL-1 cells with the mRFP-GFP tandem fluorescent-tagged LC3 are reported in *Fig. 1*.

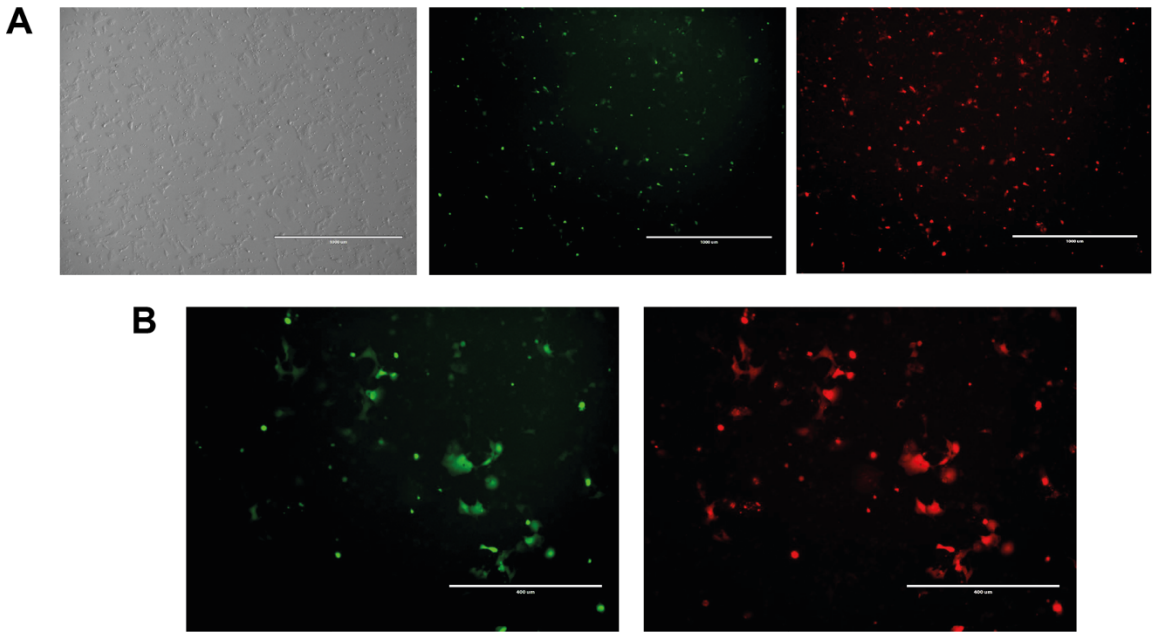

Figure 1 – Electroporated HL-1 cells with the mRFP-GFP tandem fluorescent-tagged LC3 (tfLC3) at 48 h. Images were acquired by an EVOS microscope, and the same field was represented in brightfield, GFP channel and TRITC channel with 4x objective (A) and GFP channel and TRITC channel with 10x objective (B), to highlight the success of the tandem plasmid introduction in the cell culture. Scale bar 1 mm (A) and 400 μm (B).

4.2.2 Cells seeding in the microfluidic platform

After 48 h from electroporation, HL-1 cells were detached from the 6 well plate, counted and seeded in the previously sterilized and functionalized μP (as described in paragraph 3.2, see 3.2.1, 3.2.2 and 3.2.3 for more details) at a density of $2.5 \cdot 10^5$ cells/mL. The chosen cell density was higher with respect to the validation experiments of the platform described in the Chapter 3. This adjustment was made because electroporation resulted in a higher degree of cell mortality with respect to non-electroporated cells. Consequently, the platform was seeded with the same number of cells.

4.2.3 Cells stimulation

For starvation experiments, electroporated HL-1 were detached 48 h after the plasmid tfLC3 introduction and seeded in the μP. After 24 h of seeding into the device, Hank's Balanced Salt Solution (HBSS) was flushed into the micro-channels and chamber to fill and treat the cell culture with starvation medium. This was done after two washes with PBS to remove the culture medium and residuals of nutrients from the chamber. In the control chamber, cells were similarly washed two times with PBS and complete culture medium was again introduced.

To study the effect of mechanical stimulation and micro-pattern on the autophagy induction and flux, HL-1 electroporated cells were seeded after 48 h from the electroporation treatment in the μP, enriched with both a flat PDMS membrane and a patterned PDMS membrane. After 24 h of device seeding, cells were transferred in microscope-associated incubation chamber under controlled temperature conditions, maintained at 37°C during the stimulation experiments. To maintain pH conditions suitable for cell culture and thus substitute CO_2 levels, Hepes solution (Merck) was incorporated into the complete culture medium. Additionally, the air flow channel was linked to the external pressure controller, which applied a continuous pressure of -200 mbar for 12 and 24 h to the device. This pressure was used to deform the PDMS substrate, thereby providing equi-biaxial stimulation to the HL-1 cells seeded on the surface of the PDMS flat or patterned on the pillar area.

4.2.4 Cells staining and confocal imaging

Electroporated cells exhibited intracellular fluorescence due to the introduction of the tandem plasmid, allowing direct imaging with LSM 900 acquisitions. A 40x water objective was used to capture the autophagic vacuoles in a more defined way, in order to well distinguish their number progression in response to the applied stimulations. Intracellular GFP and mRFP tagged vacuoles were respectively excited with 488 nm and 555 nm lasers and z-stack of the single cell or small group of cells were acquired to accurately count the right number of vacuoles in the 3D space of the cell.

For live-dead assay, HL-1 cells were stained to detect vital and non-vital cells in response to the prolonged mechanical stimulation using Calcein AM and Propidium Iodide (PI) for simultaneous staining. Device-seeded cells were washed twice in PBS and incubated for 15 minutes with a solution containing both probes in PBS. In particular, Calcein AM was used in a proportion of 1:1000 (final concentration 1 μg/mL) and PI in 1:100, from 1 mg/mL of PI stock

solution (final concentration 10 µg/mL). Then, the samples were washed twice in PBS and rinsed in culture medium for live-imaging acquisition, performed by LSM 900 with a 10x objective to capture the cell culture above the deformation pillar surface. Calcein AM was excited with a 488 nm laser, while PI was excited at 555 nm.

4.2.5 Focused ion beam scanning electron microscope (FIBSEM) analysis

Samples with cells were prepared for FIBSEM imaging using the ROTO and ultra-thin plasticization protocol (https://doi.org/10.1038/s41596-019-0161-7). Briefly, samples were fixed in 2.5% glutaraldehyde in 0.1M sodium cacodylate buffer at 4°C overnight. After rinsing in sodium cacodylate samples were quenched in a chilled solution of 20 mM glycine, then rinsed again in the washing buffer. A RO step was carried out by using of 1% osmium tetroxide and 1% potassium ferrocyanide for 1 hour in the dark on ice. After washing three times in sodium cacodylate, samples were incubated with 1% thiocarbohydrazide at room temperature for 20 min (T step), washed (3 × 5 min) in distilled water and fixed in 2% osmium tetroxide aqueous solution for 1 h at room temperature (O step). After rinsing with distilled water, specimens were incubated overnight in a solution of 1% uranyl acetate at 4°C. The samples were washed in chilled water and stained with 0.15% acid tannic aqueous solution for 3 min. Samples were dehydrated by increasing concentration of ethanol each step of 15 min on ice, the last step of absolute ethanol was performed at room temperature. Specimens were infiltrated with increasing concentration of Spuur'r resin in absolute ethanol at a room temperature. Finally, samples were embedded in absolute resin overnight. Excess of resin was removed by ethanol washing and the samples were mounted vertically for 3 h, then put in oven at 70°C. After 24 h of polymerization samples were mounted on 12 mm aluminum pin stub by using silver paste and sputtered (sputter coater 208HR cressington) with a layer of 20 nm of gold before FIBSEM imaging. For the imaging the Helios CX 5 (Themofisher) was used at 3kV in a range of magnification between 5 kX and 80kX.

4.2.6 Images and data analysis

Confocal images were processed and analyzed using ImageJ, while quantification plots were generated using MATLAB codes.

Confocal images of HL-1 cells undergoing autophagy were extracted and modified by using ImageJ. Single cell images were extracted from the acquisition and separately analyzed with

ilastik, a tool for automatic segmentation and separation of yellow puncta and red puncta within the single cell. In this way the separate count of autophagosomes and autolysosomes was carried out in a precise, controlled, and reproducible manner, avoiding potential errors due to the user-dependent detection and counting of the autophagic vacuoles. Segmented images were retrieved by training the classifier, iteratively drawing the labels of interest, i.e. yellow puncta, red puncta, and cell/black background. Then, feature selection and segmentation allowed to obtain the segmented images of yellow and red puncta, which were counted with the Analyze particles command of ImageJ. For experimental reason, cells on the boundaries of the pillar surface (50 μm from the external diameter of the pillar) were not accounted in the autophagy induction analysis, since these were areas experienced maximum stress due to the bending of the membrane over the pillar, rendering the equi-biaxial planar hypothesis for the stress and deformation field not valid anymore.
The same approach was followed for live-dead assay results, as already reported in paragraph 3.2.6.

4.2.7 Statistical analysis

The experiments were conducted in triplicate for each group, and statistical analysis was carried out using the t-test in MATLAB to identify significant differences among the groups. A p-value threshold of 0.05, 0.01 and 0.001 was established for statistical significance, with values below this threshold believed significant. For the analysis of autophagic vacuoles count at least 30 cells per sample were detected, analyzed and quantified to obtain a significant number of cells for the analysis.

4.3 Results and discussion

4.3.1 Effect of nutrient starvation on autophagy in HL-1 cells

Nutrient starvation is a well-studied autophagy inducer in human cell lines. In this study, HL-1 CMs were stimulated by replacing the feeding culture medium with HBSS, a salt solution enriched with calcium, magnesium, and other bulk inorganic ions essential for normal cell metabolism but deprived from basal nutrients and amino acids. The autophagic response of the HL-1 cells was investigated after exposure to HBSS directly within the μP, specifically using the flat configuration, (non-patterned) of PDMS substrate. After cells transfection with a tandem fluorescent plasmid and seeding into the microfluidic device, the starvation medium (HBSS) was introduced into the culture chamber, and the autophagy activation was monitored for 30 minutes, 1 h, 2 h and 3 h (*Fig. 2*). Confocal live imaging allowed the real-time monitoring of autophagic puncta in the same cells population for the whole range of times, distinguishing between yellow puncta, representing the autophagosome vesicles, and red puncta, indicating the final stage of the autophagic flow, including the fusion of autophagosomes with lysosomes to form autolysosome vesicles. This assay revealed the complete autophagic flow, involving the accumulation of both autophagosomes and autolysosomes during the stimulation period. After an initial autophagosome increase within the first hour of stimulation, it followed a gradual increase in autolysosomes significant ($p<0.05$) at 3 h of starvation. Autophagosomes number decreased while autolysosome increased, meaning that autophagy induction was directed by nutrient deprivation within the observation period. Control samples, the untreated cells in the device, underwent an initial burst of autophagosomes, likely related to environmental condition oscillations at the start of observation. After 1 h, the control decreased significantly ($p<0.05$) and stabilized throughout the experiment. Autolysosome percentage relative to the total number of puncta per cell was quantified and plotted (*Fig. 3*), confirming the enhanced autophagic flow in HL-1 cells during the 3-hour of exposure to HBSS.

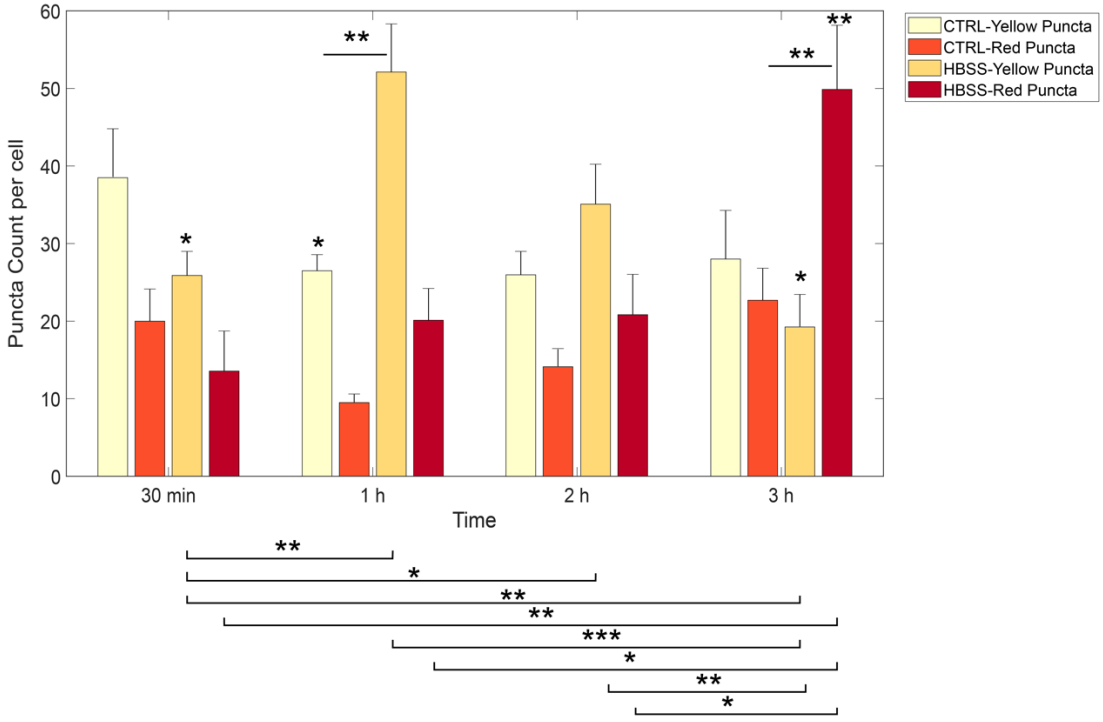

Figure 2 – Starvation induced autophagy in HL-1 cell line. Autolysosome significantly increased at 3 h of starvation, while autophagosomes started to increase at 1 h and suddenly decreased in the next time points. Analysis performed on n = 30 cells per sample (experiment in triplicate). Data represented as (mean ± SEM). * statistical analysis versus CTRL at 30 minutes; _* statistical analysis versus CTRL of the corresponding group (1h, 2h or 3h); |_* statistical analysis of stimulated samples versus the other stimulated groups. * $p<0.05$ ** $p<0.01$ *** $p<0.001$.

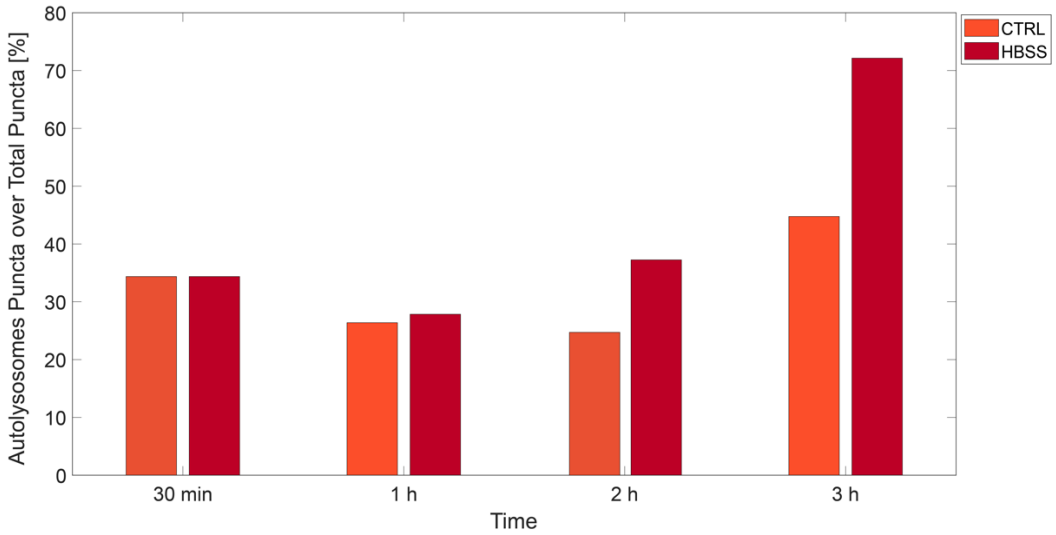

Figure 3 – Starvation induced autophagy in HL-1 cell line is proved by autolysosome quantification relatively to the total number of puncta per cells. Autolysosome significantly increased at 3 h of starvation. Analysis performed on n = 30 cells per sample. Data represented as percentage of the mean values.

Literature studies reported that the activity and response of HL-1 cells in autophagy are complex and differ from other cardiac cell lines. While it is well known that autophagy is strongly enhanced upon nutrient deprivation, a study of Brady et al. reported that in HL-1 cells, autophagy was induced after 3.5 h of nutrient deprivation, but the activity remained down-regulated with low autophagosome levels [4]. The authors suggested that this autophagic response could be attributed to either high lysosomal turnover, a characteristic of HL-1 cells, or to low autophagic flux. In another study by Yuan et al., autophagy enhancement was detected in HL-1 cells after 3.5 h of starvation when an inhibitor of lysosomal degradation (Bafilomycin A1) was used in conjunction with starvation medium [5]. Another study revealed that in HL-1 cells, starvation notably increased LC3-II levels during the initial 2 h of starvation, followed by a gradual decrease in LC3-II levels over the remaining period of starvation, up to 24 h [6]. In our work, we focused on observing autophagy induction by nutrient deprivation at time points previously studied in the literature. This prior knowledge guided our use of starvation as a calibration signal to assess the potential of the μP in handling biochemical stimulations and to test the autophagy detection technique used to monitor the cells response to the applied stimulation. HL-1 cells responded to the starvation insult up-regulating the autophagic turnover of autolysosomes, confirming that autophagy could be induced and studied effectively in the designed platform.

4.3.2 Effect of mechanical stimulation and topography on HL-1 cells autophagy induction

Once ensured that HL-1 CMs can be studied in terms of autophagy induction, the investigation focused on unraveling the role of both mechanical deformation and micro-pattern in modulating autophagic flux. Cells transfected with the mRFP-GFP-LC3 plasmid were used to monitor autophagy progression directly in the μP. Since literature studies have reported that, by exploiting commercial and microscopic platform for cell stretching, mechanical stimulation can activate autophagy in intervals ranging from 12 h to 48 h, and no information was available on the autophagy response when combined with a pattern, we first focused our detection on the initial 12 h and 24 h of stimulation. In addition, cyclic mechanical deformation, often preferred over continuous deformation, was chosen for the experiments, as different studies have reported its induction of autophagy upon cyclic substrate stretching. This is why the first experiments on autophagy-biophysical signals correlation were performed in the frequency domain. HL-1 cells were seeded, after plasmid transfection, in the μP and subjected to mechanical stimulation

implemented on both flat and micro-patterned PDMS substrates. After 24 h of seeding, the stimulation was applied by stretching the deformable PDMS substrate. Vacuum was applied to the deformable area by means of an external pressure controller, which actuated a sinusoidal waveform suction of air with amplitude of -300 mbar and period of 10 ms (frequency of 0.1 Hz), lasting 24 h. Intermediate time points were used to check autophagy progression. Quantification of autophagic puncta per cell showed that mechanical deformation applied on HL-1 cells spread on non-patterned (flat) PDMS (first two boxes of each time point) lead to a decrease the red puncta per cell, while yellow puncta remained unaltered. This was proved by the autolysosomes quantification per cell, showing a significant decrease in autolysosomes production at 12 h ($p<0.05$) and 24 h ($p<0.001$) with respect to unstimulated cells (time 0). Differently, autophagosomes number appeared unaltered by mechanical stimulation until 24 h of stretching, suggesting a block in autophagosomes fusion with lysosomes (*Fig. 4*, first two boxes per time point). It is reasonable to suppose a block in the fusion since the intracellular accumulation of autophagosomes became apparent from plot of autophagosomes puncta over the total puncta number, showing a significant increase of autophagosomes at 12 h ($p<0.01$) and 24 h ($p<0.001$) of mechanical stimulation with respect to undeformed sample. In addition, the reduction in autolysosomes number was confirmed by the plot of autolysosomes puncta number relative to the total number of puncta (*Fig. 5*). The increase in autophagosomes' relative number and the decrease of autolysosomes' relative number from 12 h to 24 h of mechanical stimulation are statistically significant ($p<0.05$ both). The plots of autophagosome and autolysosome puncta normalized with respect to the total number of puncta of the cell were necessary to understand their relative fraction and oscillation during the stimulation period.

The presence of the micro-pattern seemed to induce an increase in autophagosomes at 12 h and even more at 24 h ($p<0.01$) and a steady-state of autolysosomes number in the count of the overall puncta per cell, leading to the conception that the autophagic block persisted also in HL-1 cells stimulated when seeded in anisotropic orientation (*Fig. 4*, last two boxes per time point). Also, in the case of patterned substrate, autophagosomes increased relative to the total number of puncta, with an enhancement from the undeformed configuration to deformation endured for 24 h ($p<0.01$). Moreover, the relative number of autolysosomes decreased with respect to the total number of puncta from time 0 to 24 h of stimulation ($p<0.01$) (*Fig. 5*). In addition, by observing the total number of puncta per cell, it is conceivable that a huge and significant increase in total puncta number occurred when HL-1 cells were stimulated at 12 h and 24 h on micro-patterned substrates compared to the corresponding flat substrate. This can be explained considering either that the fusion of autophagosomes with lysosomes can be blocked, leading to

a consequent accumulation, or that autophagic induction was enhanced when HL-1 cells were aligned by the micro-pattern under deformation. If the latter hypothesis is valid, only the combination of mechanical stimulation and micro-pattern led to this achievement since at time 0, which is the undeformed configuration, there was no significant difference between flat and pattern in autophagosomes and autolysosomes numbers over the total number of puncta.

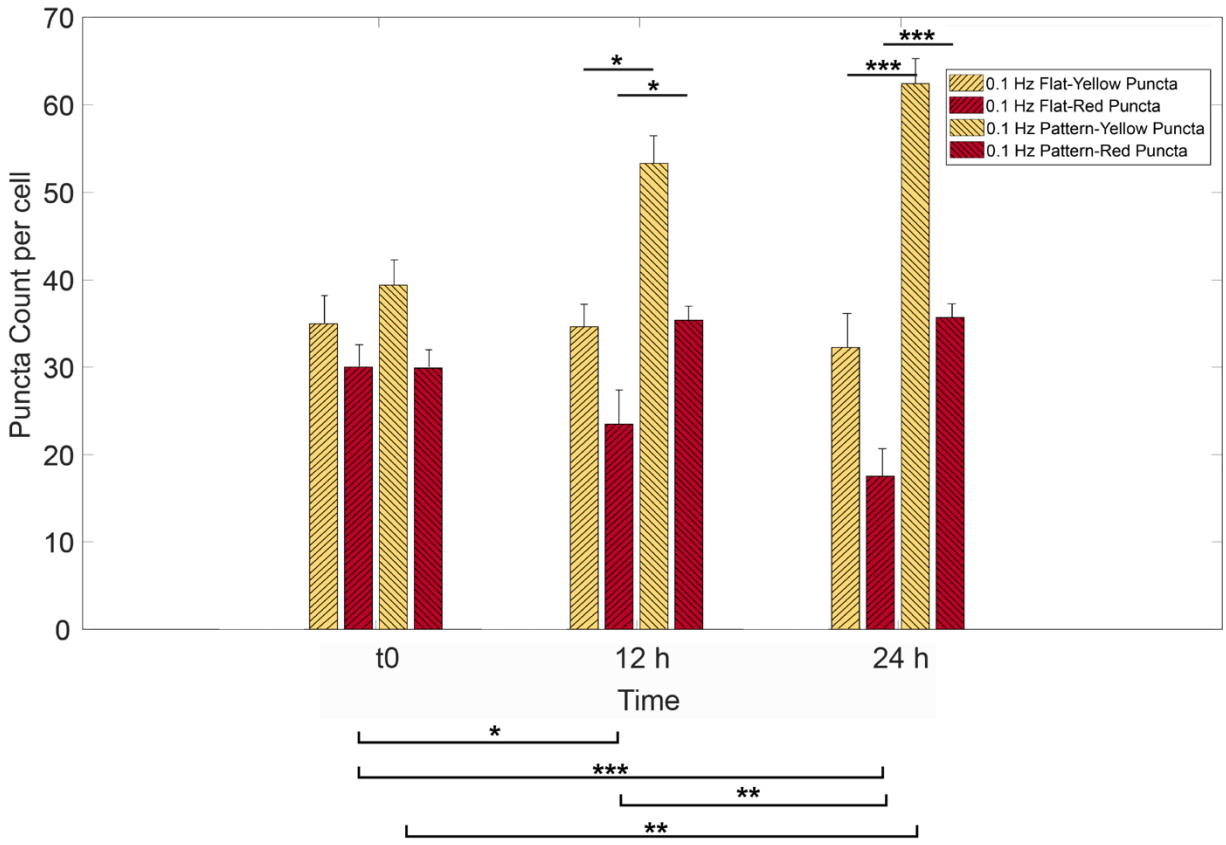

Figure 4 – Mechanical stimulation and topographic alignment effect on autophagy flux in HL-1 CMs. Plot of count on puncta per cell demonstrated that upon mechanical stimulation the autophagosomes number remained unchanged, while a decrease of autolysosomes occurred. With the introduction of the pattern, the autophagosome puncta count at 24 h significantly increased respect to the undeformed control and the corresponding at 12 h. Analysis performed on n = 30 cells per sample (experiment in triplicate). Data represented as (Mean ± SEM). _* statistical analysis in the group (t0, 12h or 24h); |_* statistical analysis of stimulated samples versus the other stimulated groups. * $p<0.05$ ** $p<0.01$ *** $p<0.001$.

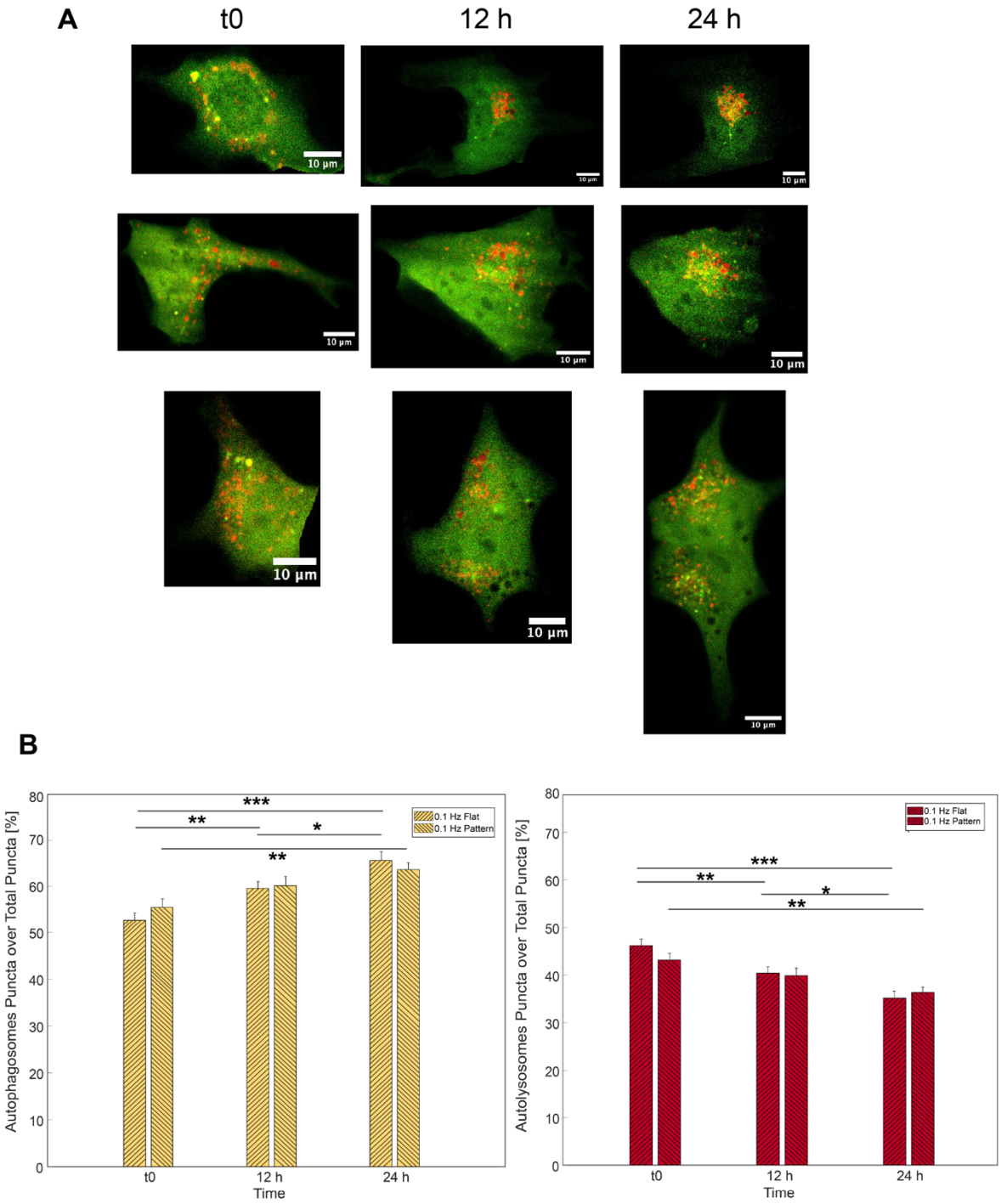

Figure 5 – Autophagosome puncta count (left panel) and autolysosome puncta count (right panel) were normalized relatively to the total number of puncta per cell. A) Example of three cells undergoing their evolution in autophagy read-out during 24 h of mechanical stimulation on patterned PDMS. B) Autophagosomes appeared to increase, while autolysosome decreased during the stimulation, in both flat and patterned PDMS substrates. Scale bar 10 µm. Data represented as (Mean ± SEM). * $p<0.05$ ** $p<0.01$ *** $p<0.001$.

To further confirm the capability of our platform to enhance the autophagic activity, FIBSEM cross-section images of stimulated HL-1 cells were acquired, since electron microscopy is a effective approach for the validation of autophagic vesicles recognition. FIBSEM cross-section images of HL-1 cells, seeded in the μP (*Fig. 6A*) and stimulated for 24 h on flat PDMS membrane, demonstrated different ultrastructure composition with respect to control samples, which are HL-1 seeded in device-integrated flat PDMS in undeformed configuration. The control samples display normal morphology, with few small compartments probably related to autophagosomes formation due to physiologic autophagy induction (*Fig. 6B*). In the deformed cells, 24 h of cyclic deformation at 0.1 Hz clearly increased the autophagic activity, demonstrating an increased number of autophagosomes that are enclosing the autophagic cargo undergoing the degradative process (*Fig. 6C*). Vacuoles sectioning allowed to recognize electron dense spherical bodies and even rough endoplasmic reticulum as autophagic cargoes (*Fig. 6D*).

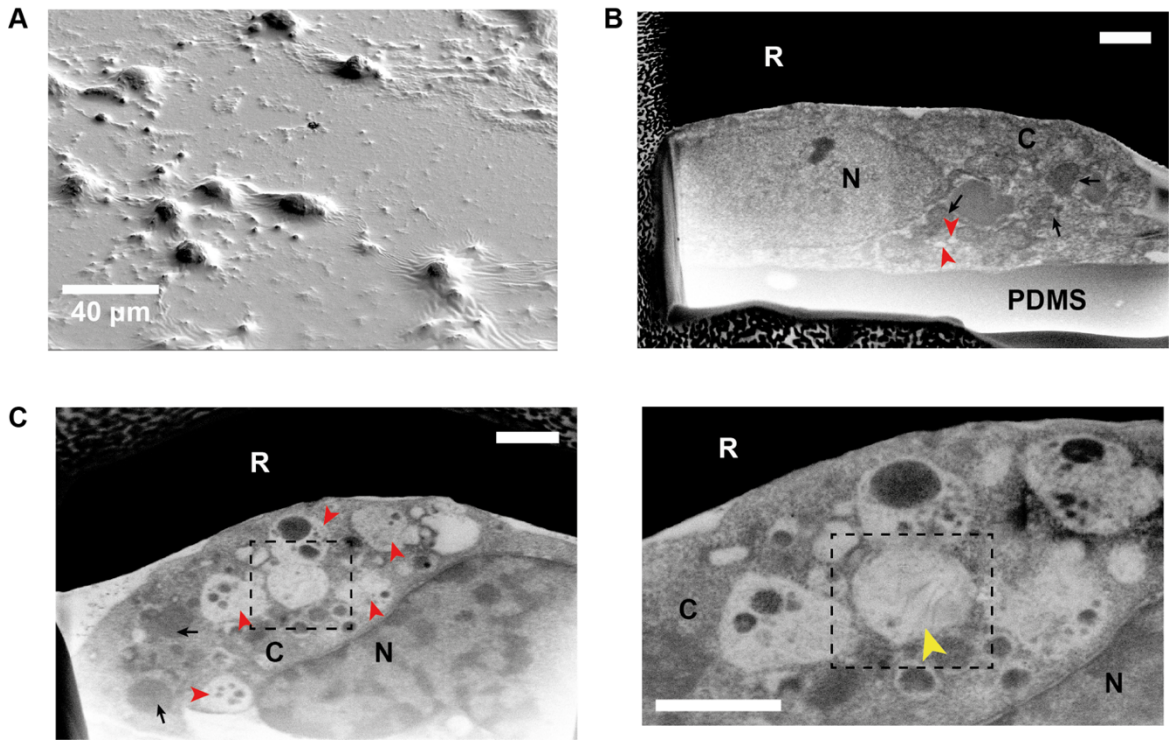

Figure 6 – FIBSEM images of HL-1 cells deformed for 24 h on flat PDMS. A) Images of resin-embedded HL-1 cells on flat PDMS. B) Sectioning of the control cells, so the undeformed population, allowed to reveal cell embedded in resin (R) and seeded on PDMS, where it can be recognized nucleus (N), cytoplasm (C) with interspersed mitochondria (black arrows), but no variation in the autophagic activity, unless few and very small vesicles probably associated to autophagosomes can be observed (red arrows).C) Sectioning of the deformed cell population demonstrated an important increase in autophagic vesicles, indicated by red arrows, containing the cargoes of the degradation, highlighted by black bodies embedded in white vacuoles. A zoom evidences the presence of rough endoplasmic reticulum in autophagic vacuole (right panel, yellow arrow). Where not specified, images scale bar is of 1 μm.

To further elucidate these preliminary results, additional studies are necessary to unravel the role of both mechanical and topographical stimulation on the HL-1 cell line. As reported in the work of Brady et al., the low autophagic activity of HL-1 revealed a response to nutrient deprivation that was not associated with the behavior of common cell lines, probably associated to the enhanced lysosomal activity of HL-1 CMs [4]. This could explain the decrease in autolysosomes numbers when autophagy is highly induced under mechanical deformation and especially in the case of deformed patterned substrate. Regarding the hypothesis of lysosomal fusion block, different studies reported that this behavior can be associated with a type of autophagy-induced cell death called autosis [7], related to main cases of I/R. During such events, autophagosomes accumulate due to the blockade of autophagic flux, accompanied by enhanced upregulation of Beclin 1 [8,9]. In the study of King et al., the accumulation of autophagosomes during compression of MDA-MB-231 cells was explained by treating them with Bafilomycin A, which impairs lysosomal activity. The accumulation of autophagosomes upon Bafilomycin treatment occurred much faster when cells were compressed, suggesting that this stimulation induced the formation of new autophagosomes [10]. On the other hand, FAK serves as a crucial downstream controller of cardiac integrins and growth factor receptors, both of which are recognized for their capacity to suppress autophagy [11]. Notably, cell-matrix adhesion can directly influence mTOR activity by involving FAK. FAK, a pivotal player in adhesion-related signaling, is activated in mechanosensing pathways for substrate recognition, migration, response to durotaxis, and in mechanotransduction pathways, directing YAP/TAZ complex [12]. FAK has also the capability to phosphorylate TSC2, an upstream regulator of mTOR, inhibiting its function and sustaining mTOR activation. When FAK activity is hindered, it leads to mTOR inhibition and autophagy induction [13]. For instance, a study on HL-1 CMs proved that FAK inhibited autophagy by phosphorylating Beclin1, and this mechanism was the cause of the induction of cardiac hypertrophy driven by PE/FAK signaling [14]. In this work, the authors confirmed the suppression of autophagic flux: by blocking autophagy at the substrate degradation stage, they observed a reduction in LC3-II production. This may explain the changes in autophagy found in the response of cardiac cells to the combination of micro-pattern and mechanical stimulation, which, together, can actively upregulate FAK, leading to autophagy blockade. Therefore, our work should be complemented with additional findings on lysosomal activity, autophagosome-lysosome fusion, and FAK activity quantification during mechanical stimulation coupled with topographic alignment of CMs.

Considering that autophagic activity is strictly related to the cell survival and health, we tested the viability of HL-1 undergoing mechanical deformation. In section 3.3.1 we already mentioned

the survival capability of the micro-pattern to enhance HL-1 cells vitality through a live-dead assay. Similarly, after 12 h and 24 h of mechanical stimulation, HL-1 CMs were stained with Calcein AM and PI to determine the percentage of live and dead cells. The results demonstrated that cyclic deformation did not affect the vitality of HL-1 cells. At 24 h of stimulation, a slight increase in dead cells was visible, mainly at the boundary of the pillar, where stresses increased due to the extension and bending of the PDMS deformable membrane over the pillar walls (*Fig. 7B*). For this reason, cells seeded on the PDMS in correspondence to the pillar boundaries were not accounted in the quantification of autophagic puncta count. It is then conceivable that the possible blockade of autophagic flux did not affect the vitality of the HL-1 cells, which was instead preserved during the extended deformation period of 24 h.

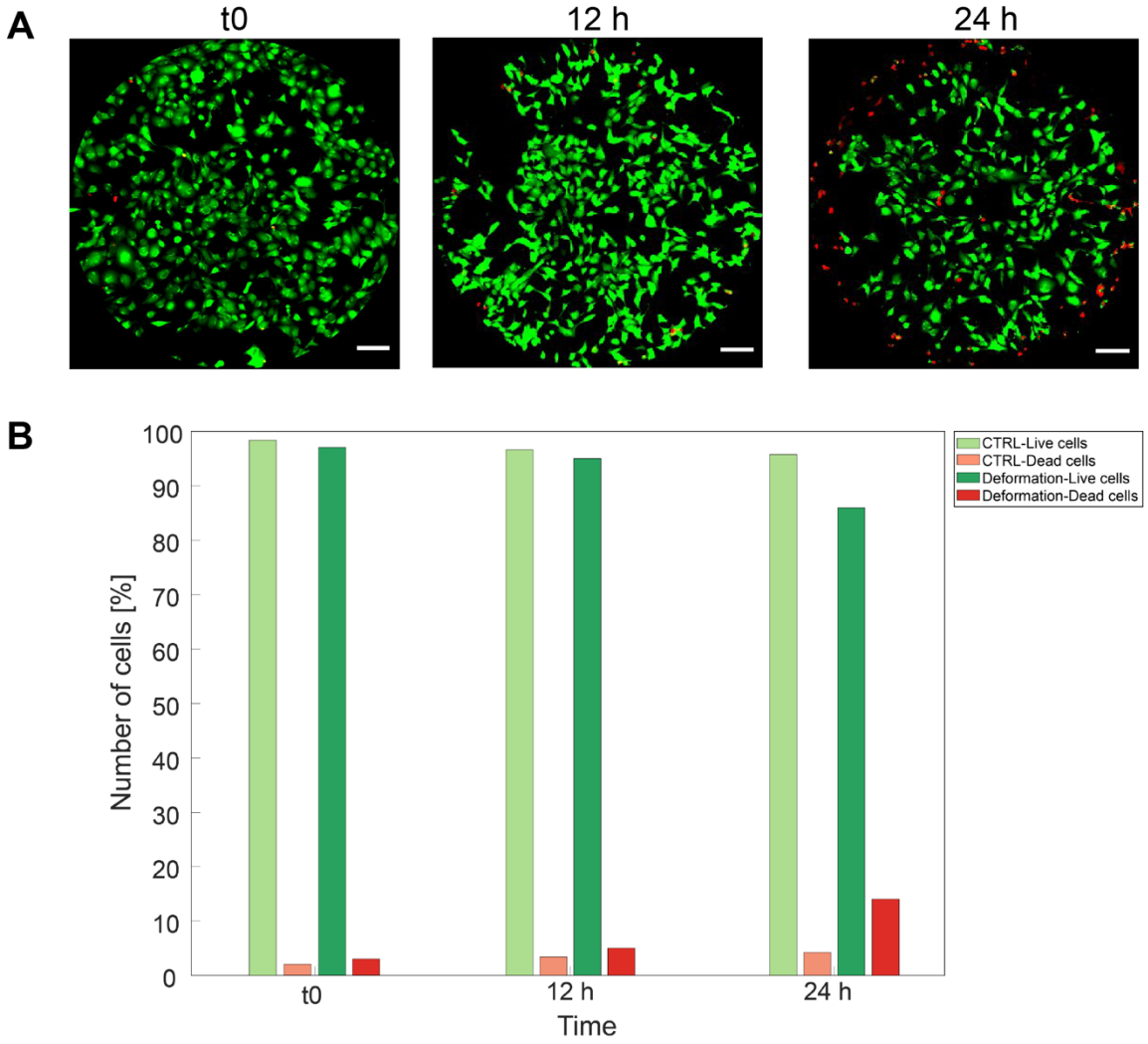

Figure 7 – Live/dead assay on HL-1 cells seeded on deformed and non-patterned PDMS. A) Representative images of HL-1 cells at time 0, which corresponded to the undeformed configuration, 12h and 24 h of cyclic mechanical stimulation at 0.1 Hz. Calcein AM stained live cells (green), while PI stained dead cells (red). B) The mechanical stimulation was not affecting cell viability during the deformation, but at 24 h the percentage of dead cells increased slightly with respect to the corresponding at 12 h and controls. Scale bar 100 μm.

A final step in the characterization of HL-1 CMs autophagy response to external physical fields was carried out to determine whether a sector analysis could change the autophagy quantifications. Indeed, the identification of pattern sectors along the r-direction of the radially symmetric geometry, as discussed in Paragraph 3.3.2, and the corresponding deformation gradient on the surface of the PDMS during the mechanical equi-biaxial deformation could lead to a differentiation in autophagy induction. The field of cell analysis was restricted to each single area delimited by the pattern's geometrical gradient along the r-direction and the variation in displacements registered in the map of deformation field performed in Paragraph 2.3.2 (*Fig. 8A*). In this way, four different sectors were distinguished, from sector 1 (the inner non patterned area) to sector 4 (the most external part of the pattern). Puncta count was accomplished between cells belonging to the same sector, repeating the same measurements for all four sectors. What emerged was that there was no evident difference in autophagy induction between sectors (*Fig. 8B*). The same trend of autophagosomes increase and autolysosomes decrease during the mechanical deformation above the 24 h remained unchanged when checking the puncta per sectors. This means that the CMs' response to mechanical stretching was homogenous above the surface of the pillar, likely due to the presence of the underlying micro-patterned PDMS. Hence, the alignment role of the topography played a crucial role not only in the CMs' response in terms of migration and contractility but also in the uniformity of the autophagic response following mechanical deformation. This allows us to take a step forward in the recapitulation of the cardiac microenvironment, in which the combined influence of topographical and mechanical cues orchestrates the behavior of CMs in a guided and organized manner, in a type of hierarchical organization that can be found *in vivo*, where a group of cells composing the same tissue fulfils specific functions and behaves in the same way.

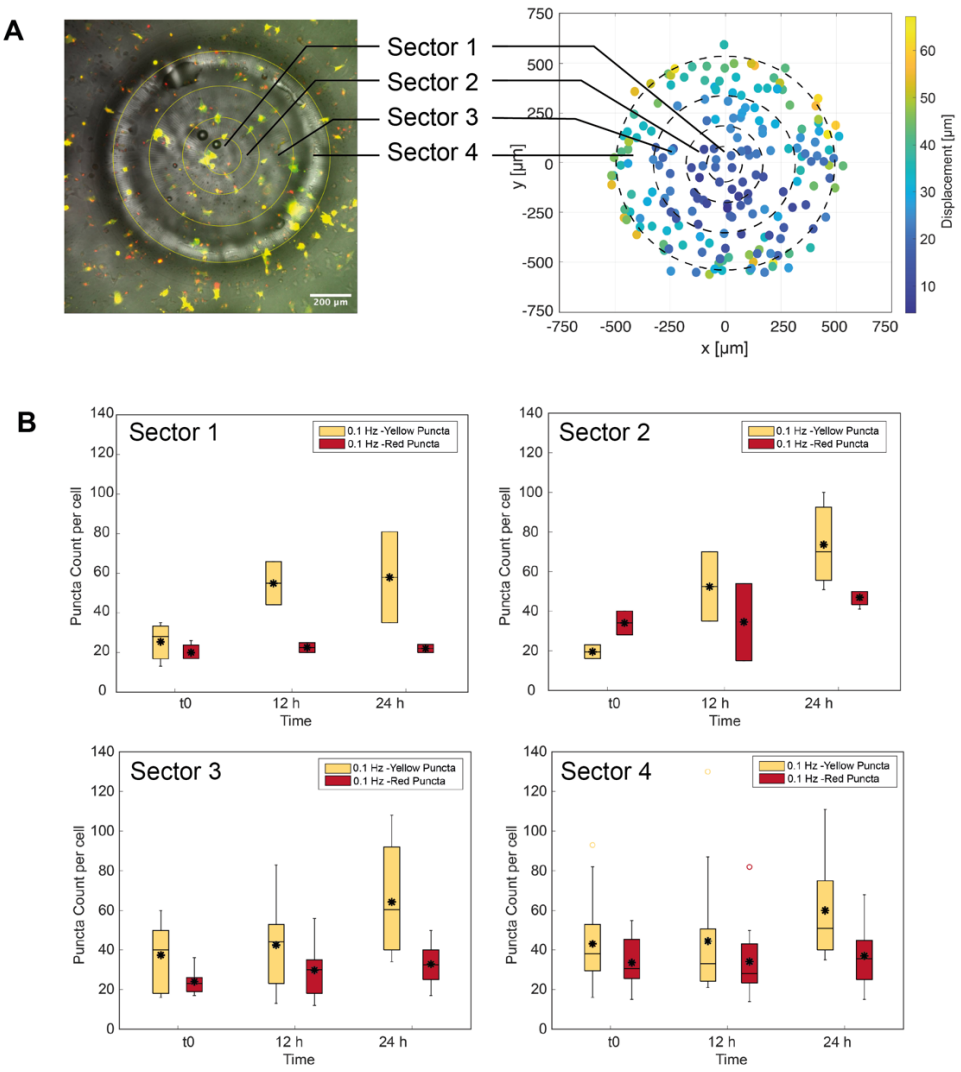

Figure 8 – Analysis per pattern sector on autophagy flow after mechanical stimulation implementation on HL-1 cells. A) The sectors were chosen from the geometry of the micro-pattern, which gave rise to a gradient due to symmetry, and from the deformation gradient arising on the surface of PDMS when mechanical bi-axial deformation is applied. B) The results previously discussed regarding autophagy modulation by mechanical stimulation combined to micro-pattern did not change when the analysis was limited to the single sector. Scale bar 200 µm. Data in B) expressed as *mean, -median, box bottom and top edges are lower and upper quartiles, ⊥ lower and upper bars are the endpoints of the range of values, ° outliers.

References

1. Zhang, Q., Zhang, Q., Yan, X., Wang, L. & Yuan, X. Wrinkled topography regulates osteogenesis via autophagy-mediated Wnt/β-catenin signaling pathway in MC3T3-E1 cells. Arch Oral Biol 151, 105700 (2023).
2. Song, W., Shi, M., Dong, M. & Zhang, Y. Inducing Temporal and Reversible Autophagy by Nanotopography for Potential Control of Cell Differentiation. ACS Appl Mater Interfaces 8, 33475–33483 (2016).
3. He, L. et al. Electrical stimulation at nanoscale topography boosts neural stem cell neurogenesis through the enhancement of autophagy signaling. Biomaterials 268, 120585 (2021).
4. Li, X. et al. A nanostructure platform for live-cell manipulation of membrane curvature. Nat Protoc 14, 1772–1802 (2019).
5. Brady, N. R., Hamacher-Brady, A., Yuan, H. & Gottlieb, R. A. The autophagic response to nutrient deprivation in the hl-1 cardiac myocyte is modulated by Bcl-2 and sarco/endoplasmic reticulum calcium stores. FEBS J 274, 3184–3197 (2007).
6. Yuan, H. et al. LPS-induced autophagy is mediated by oxidative signaling in cardiomyocytes and is associated with cytoprotection. American Journal of Physiology-Heart and Circulatory Physiology 296, H470–H479 (2009).
7. Samokhvalov, V. et al. Epoxyeicosatrienoic acids protect cardiac cells during starvation by modulating an autophagic response. Cell Death Dis 4, e885–e885 (2013).
8. Ikeda, S., Zablocki, D. & Sadoshima, J. The role of autophagy in death of cardiomyocytes. J Mol Cell Cardiol 165, 1–8 (2022).
9. Nah, J. et al. Upregulation of Rubicon promotes autosis during myocardial ischemia/reperfusion injury. Journal of Clinical Investigation 130, 2978–2991 (2020).
10. Matsui, Y. et al. Distinct Roles of Autophagy in the Heart During Ischemia and Reperfusion. Circ Res 100, 914–922 (2007).
11. King, J. S., Veltman, D. M. & Insall, R. H. The induction of autophagy by mechanical stress. Autophagy 7, 1490–1499 (2011).
12. Lock, R. & Debnath, J. Extracellular matrix regulation of autophagy. Curr Opin Cell Biol 20, 583–588 (2008).
13. Martino, F., Perestrelo, A. R., Vinarský, V., Pagliari, S. & Forte, G. Cellular Mechanotransduction: From Tension to Function. Front Physiol 9, (2018).

14. Gan, B., Yoo, Y. & Guan, J.-L. Association of Focal Adhesion Kinase with Tuberous Sclerosis Complex 2 in the Regulation of S6 Kinase Activation and Cell Growth. Journal of Biological Chemistry 281, 37321–37329 (2006).
15. Cheng, Z. et al. Focal Adhesion Kinase-mediated Phosphorylation of Beclin1 Protein Suppresses Cardiomyocyte Autophagy and Initiates Hypertrophic Growth. Journal of Biological Chemistry 292, 2065–2079 (2017).

Conclusions

With the development of progress and the necessity to find a solution to the main pathologies affecting human wellness, considerable efforts are focused on researching, designing, and testing new strategies to extend human lifespan under optimal conditions. Nevertheless, a comprehensive understanding of how to achieve these targets remains elusive, necessitating further research on biological processes at cell level. Given the significant impact of cardiac pathologies on human health, understanding how to enhance cardiac cell states is crucial, considering also that different factors can influence this result. Between the others, the composition and the impact of the surrounding environment on cell behavior are central for these response mechanisms. These signals, encompassing biochemical, biophysical, and topographical cues, play a pivotal role in modulating cellular behavior by altering epigenetic pathways. Such epigenetic modifications often manifest in autophagy modulation, highlighting autophagy not only as a marker of cellular health but also as an indicator of disease states. Autophagy, a critical process for maintaining cellular homeostasis, can reflect the cell response to its surroundings and its overall wellness. However, the investigation on these cell conditions necessitates the adoption of tool that can implement the microenvironment control in a biomimetic fashion, as close as possible to the *in vivo* physiologic contest.

Therefore, our research attempted to elucidate the influence of the microenvironment on cellular states and functions, with a particular focus on a cardiac cell line. In fact, we aimed to investigate the relationship between cell states and autophagic activity in response to external microenvironmental stimuli. By doing so, we sought to uncover whether a direct correlation exists between the levels of autophagy and the state of cardiac cells under specific environmental conditions, applied in a controlled μP, in the attempt to provide further insights into the cellular mechanisms underlying cardiac health and disease.

In the design of the μP, we considered the possibility to introduce diverse stimuli of the cardiac microenvironment, notably through fluid flow for biochemical fluxes and a mechanical stimulation unit for equi-biaxial planar stretching of seeded cardiac cells. To refine the platform's design and ensure its functionality, COMSOL simulations were integral, revealing that chambers with a high aspect ratio of dimensions effectively accommodate fluxes while mitigating turbulence and shear stresses that could potentially compromise cell culture integrity. Furthermore, the designed stimulation unit achieved an equi-biaxial stretch above the surface of a thin flexible membrane, which slide and deform on the top of a circular fixed pillar. This pure

stretch was symmetric in all the direction and was characterized by a gradient of deformation from the center to the boundaries of the pillar surface.

The μP was fabricated using a layer-by-layer approach, effectively separating different channels to isolate various applied signals, specifically, air flux for membrane deformation and fluid flow for cell feeding. A deformable PDMS membrane was integrated into the platform. The platform's capability for equi-biaxial deformation was evaluated, confirming the COMSOL simulations along with the achievement of a uniform deformation gradient on the pillar surface. To enhance the platform's ability to replicate the highly organized structure of cardiac tissue, a radial micro-topography was introduced. The PDMS patterned membrane was integrated on the deformation pillar within the μP. This strategic configuration facilitated the alignment of cells along the pattern prior to subjecting them to equi-biaxial stimulation in alignment with their orientation. Through this comprehensive design and testing process, the platform not only emulated the mechanical and biochemical cues of the cardiac microenvironment but also incorporated a micro-topographical feature that tried to mimic the natural alignment found in cardiac tissue.

By seeding HL-1 CMs in the μP, we have effectively shown that they can align following the micro-pattern, achieving anisotropic arrangement at cell level and radial organization at population level, in the attempt to emulate the natural structure and orientation of cardiac tissue. This arrangement not only supports directed cell migration under mechanical stress but also enhances CMs functional responses, particularly in beating activity and Ca^{2+} influx during mechanical stimulation. Notably, cyclic mechanical stimulation was found to significantly boost contractile activity, with the micro-pattern aiding in the propagation of calcium waves, highlighting the critical role of physical cues in cardiac cell physiology.

In the final phase of our study, we utilized the μP to examine how autophagy modulation in cardiac cells is influenced by integrating nutrient flux, mechanical deformation, and cell alignment. Using HL-1 cells electroporated with a plasmid targeting the autophagic vacuoles, we were able to visualize autophagosomes and autolysosomes progression, marking the stages of autophagic flux. The application of a starvation signal confirmed the platform's capability to detect autophagy. With the introduction of mechanical stimulation, both with and without cell-aligning micro-pattern, while autophagy initiation was promoted, the degradation phase seemed to be inhibited, especially in pattern-aligned cultures where autophagosome vacuoles accumulation was more pronounced. Despite this, a live-dead assay showed that cell viability remained unaffected, suggesting that while the platform can mimic cardiac microenvironmental stimuli and induce autophagy, the mechanical and topographical cues could disrupt the autophagy degradation process, without compromising cardiac cell survival. This led to

correlate a particular cell state to a related modulation of autophagy induction, by the application of single signals or their combinatory activity.

In conclusion, this work demonstrated that the synergy between mechanical stimuli and pattern-induced alignment provides a profound insight into both mechanobiological processes, essential for cardiac function, and autophagy alteration, crucial for cardiac cell survival and healthy state, making our platform a valuable tool for in-depth study of CMs behavior under the conditioning action of the microenvironment modulation.

Future perspectives

The reported results demonstrated the potentiality of the μP in the mimicking of the cardiac microenvironment and paves the way to additional experimental proof to further characterize the CMs state and response to the surrounding environmental conditions. Pivotal issues still need to be addressed, such as the mechanical identity of cardiac cells under deformation and in combination with the micro-pattern. As reported in chapter 1, the mechanical interaction of the cells with the underlying substrate is crucial for cardiac cells maturation and functionality, as stress and strain field are directly responsible of the structural organization of the mechanosensing and mechanotransduction main actors in CMs. For these reasons, it is important to assess the mechanical properties of cell cytoskeleton in response to the applied biophysical stimulations. In addition, the organization of cell on the micro-patterned membrane needs to be characterized, in the perspective to assess the morphological evolution of cell binding domains due to the topographic confinement. This is important to address whether the cell alignment on this geometry is due not only to actin fibers level orientation but also to FAs confinement.

The potentiality of the μP and the control imposed by the mechanical deformation allow to replicate the previous testing in the case of a dynamic deformation at the heart beating frequency. This is crucial to study CMs functionality and then autophagy in both physiologic and pathologic conditions, such as in the simulation of arrhythmias and HF. In the perspective of the implementation of a pathologic cardiac model, the microfluidic circuitry related to fluid flow unit can be useful to test drugs and treatment coupled to mechanical and topographical cues, to understand the effect of the healing strategy on the cardiac cell culture in *in vivo*-like conditions. In this work the cardiac environment was designed and tested on rat CMs, HL-1 cells, indeed. This cardiac cell line was used to simplify the model and the μP testing. In fact, immortalized cell lines can be easily handled as do not undergo managing issues related to limited passages and undesired differentiation. In the future, given the potentiality of the model, it will be possible to test human primary cells or human-derived stem cells, to increase the impact of this approach in the control of cell fate by microenvironment conditioning.

Moreover, the microfluidic circuitry can be easily coupled to automated systems for programmed extracellular stimuli delivery to the cell culture. For instance, the dose of biophysical, as long as biochemical stimuli, can be modulated by an automated system applied to the platform to reach a defined cell state, both in terms of cell health and defined autophagy level. In this automated approach, the implementation of control theory plays a crucial role since the combined effect of a plethora of microenvironment signals could be handled by an

automated logic. In this way, multiple signals can be tested on the same platform and the control system could help in the modulation of the stimuli level, in response to the read-out of the autophagy cell state in terms of fluorescence detection of the autophagic cytoplasmic vesicles. The automated platform could be conceived to find out which signal or combination of signals, at which concentration/level, will give to the cell a healthy condition in fast and precise analytic approach.